

2006

Experimental study of turbulent mixing in a rectangular reactor

Hua Feng
Iowa State University

Follow this and additional works at: <https://lib.dr.iastate.edu/rtd>

 Part of the [Mechanical Engineering Commons](#)

Recommended Citation

Feng, Hua, "Experimental study of turbulent mixing in a rectangular reactor " (2006). *Retrospective Theses and Dissertations*. 1510.
<https://lib.dr.iastate.edu/rtd/1510>

This Dissertation is brought to you for free and open access by the Iowa State University Capstones, Theses and Dissertations at Iowa State University Digital Repository. It has been accepted for inclusion in Retrospective Theses and Dissertations by an authorized administrator of Iowa State University Digital Repository. For more information, please contact digirep@iastate.edu.

Experimental study of turbulent mixing in a rectangular reactor

by

Hua Feng

A dissertation submitted to the graduate faculty
in partial fulfillment of the requirements for the degree of
DOCTOR OF PHILOSOPHY

Major: Mechanical Engineering

Program of Study Committee:
Michael G. Olsen, Co-major Professor
Rodney O. Fox, Co-major Professor
James C. Hill
Francine Battaglia
Richard H. Pletcher

Iowa State University

Ames, Iowa

2006

Copyright © Hua Feng, 2006. All rights reserved.

UMI Number: 3229071

INFORMATION TO USERS

The quality of this reproduction is dependent upon the quality of the copy submitted. Broken or indistinct print, colored or poor quality illustrations and photographs, print bleed-through, substandard margins, and improper alignment can adversely affect reproduction.

In the unlikely event that the author did not send a complete manuscript and there are missing pages, these will be noted. Also, if unauthorized copyright material had to be removed, a note will indicate the deletion.

UMI[®]

UMI Microform 3229071

Copyright 2006 by ProQuest Information and Learning Company.

All rights reserved. This microform edition is protected against unauthorized copying under Title 17, United States Code.

ProQuest Information and Learning Company
300 North Zeeb Road
P.O. Box 1346
Ann Arbor, MI 48106-1346

Graduate College
Iowa State University

This is to certify that the doctoral dissertation of
Hua Feng
has met the dissertation requirements of Iowa State University

Signature was redacted for privacy.

Co-major Professor

Signature was redacted for privacy.

Co-major Professor

Signature was redacted for privacy.

For the Major Program

TABLE OF CONTENTS

LIST OF TABLES	vii
LIST OF FIGURES	viii
CHAPTER 1 INTRODUCTION	1
General Introduction	1
Dissertation Organization	3
CHAPTER 2 INVESTIGATION OF TURBULENT MIXING IN A CON-	
FINED PLANAR-JET REACTOR	5
Introduction	5
Experimental Apparatus and Methodology	9
Flow Facility	9
Velocity Measurements	10
Concentration Measurements	11
Overview of CFD Models	12
Scalar Moment Transport Model	14
Transported PDF Model	15
Simulation Conditions	17
Results and Discussion	18
Experimentally Measured Mean Velocities and Reynolds Stresses	18
CFD Predictions for Mean Velocity	19
CFD Predictions for Turbulent Kinetic Energy	20
Experimentally Measured Scalar Mean and Scalar Variance	20
CFD Predictions for Mean Mixture Fraction	21

CFD Predictions for Mixture-Fraction Variance	21
Dissipation Rate	24
Conclusions	25
CHAPTER 3 TURBULENT MIXING IN A CONFINED RECTANGULAR WAKE	
Introduction	41
Experimental Apparatus and Methodology	45
Flow Facility	45
Velocity Measurements	46
Concentration Measurements	47
Overview of CFD Models	48
Inert Scalar Moment Transport Model	49
Transported PDF Model	51
Simulation Conditions	52
Results and Discussion	53
Mean Velocities and Reynolds Stresses	54
Self-Similarity of the Rectangular Wake	55
Turbulent Kinetic Energy	56
Turbulent Dissipation Rate	56
Mixture-Fraction Mean and Variance	57
One-Point Composition PDF	60
Conclusions	62
CHAPTER 4 SIMULTANEOUS VELOCITY AND CONCENTRATION FIELD MEASUREMENTS OF PASSIVE-SCALAR MIXING IN A CONFINED RECTANGULAR JET	
Introduction	81
Experimental Apparatus and Methodology	84
Flow Facility	84

Velocity Measurements	85
Concentration Measurements	87
Combined PIV and PLIF System	89
Stochastic Estimation of Velocity and Concentration Fields	90
Stochastic Estimation of Concentration Fields	91
Stochastic Estimation of Velocity Fields	92
Results and Discussion	92
Mean Velocities, Reynolds Stresses and Turbulent Kinetic Energy	93
Self-similarity of the Rectangular Jet	94
Concentration Mean and Variance	96
Turbulent Fluxes and Velocity-Concentration Correlation Coefficients	97
Turbulent Viscosity and Turbulent Diffusivity	99
Two-Point Spatial Correlations	101
Linear Stochastic Estimation	103
Conclusions	105

**CHAPTER 5 SIMULTANEOUS VELOCITY AND CONCENTRATION
FIELD MEASUREMENTS OF PASSIVE SCALAR MIXING IN A CON-
FINED PLANE WAKE 127**

Introduction	128
Experimental Apparatus and Methodology	130
Flow Facility	130
Combined PIV and PLIF system	132
Stochastic Estimation of Concentration and Velocity Fields	134
Linear Stochastic Estimation of Concentration Fields	134
Linear Stochastic Estimation of Velocity Fields	135
Results and Discussion	136
Evolution of Wakes	136
Turbulent Fluxes	137

Turbulent Viscosity and Turbulent Diffusivity	139
Two-point Spatial Correlations	140
Linear Stochastic Estimation	142
Conclusions	143
CHAPTER 6 CONDITIONAL STATISTICS FOR PASSIVE-SCALAR MIX-	
ING IN A CONFINED RECTANGULAR TURBULENT JET	162
Introduction	162
Experimental Details and Conditions	164
Results and Discussion	166
Probability Densities	166
Conditional Mean Velocities	167
Scalar Mean Conditioned on Velocities	171
Conclusions	172
CHAPTER 7 CONCLUSIONS AND FUTURE DIRECTIONS	188
Summary and Conclusions	188
Confined Jet	188
Confined Wake	191
Conditional Statistics	192
Future Directions	193
BIBLIOGRAPHY	195
ACKNOWLEDGEMENTS	210

LIST OF TABLES

Table 2.1	Estimated Error of PLIF Variance Measurements	27
Table 3.1	Kolmogorov Length Scale and Spatial Resolution of PIV Measurements.	64
Table 3.2	Batchelor Length Scale and Spatial Resolution of PLIF Measurements.	64
Table 3.3	Estimated Variance Unresolved by PLIF at the Peak of the Variance Profile.	64
Table 4.1	Estimated Komolgorov time scale, length scale and spatial resolution of PIV measurements.	108
Table 4.2	Estimated Batchelor length scale and spatial resolution of PLIF measurements.	108
Table 5.1	Komolgorov time scale, length scale and spatial resolution of PIV measurements.	146
Table 5.2	Batchelor length scale and spatial resolution of PLIF measurements. .	146

LIST OF FIGURES

Figure 2.1	Flow facility used in the PIV and PLIF experiments.	28
Figure 2.2	Confined planar-jet test section.	28
Figure 2.3	Top vies of the optical setup for the PIV and PLIF experiments. . . .	29
Figure 2.4	(a) Mean streamwise velocity and (b) turbulent kinetic energy at the entrance plane of the confined planar jet. —, Simulations; ●, PIV data.	29
Figure 2.5	Sample instantaneous velocity field.	30
Figure 2.6	Sample instantaneous concentration field.	30
Figure 2.7	Normalized mean streamwise velocity at various downstream locations as measured by PIV. ×, $x/d = 0$; ■, $x/d = 1$; △, $x/d = 4.5$; ▼, $x/d = 7.5$; ◆, $x/d = 12$; ○, $x/d = 15$	31
Figure 2.8	Streamwise Reynolds normal stress at various downstream locations as measured by PIV. ×, $x/d = 0$; ■, $x/d = 1$; △, $x/d = 4.5$; ▼, $x/d = 7.5$; ◆, $x/d = 12$; ○, $x/d = 15$	31
Figure 2.9	Cross-stream Reynolds normal stress at various downstream locations as measured by PIV. ×, $x/d = 0$; ■, $x/d = 1$; △, $x/d = 4.5$; ▼, $x/d = 7.5$; ◆, $x/d = 12$; ○, $x/d = 15$	32
Figure 2.10	Reynolds shear stress at various downstream locations as measured by PIV. ×, $x/d = 0$; ■, $x/d = 1$; △, $x/d = 4.5$; ▼, $x/d = 7.5$; ◆, $x/d = 12$; ○, $x/d = 15$	32
Figure 2.11	Comparison of the mean streamwise velocity profiles measured by PIV (symbols) and calculated from the RANS code (solid line) for (a) $x/d = 1$, (b) $x/d = 4.5$, (c) $x/d = 7.5$, (d) $x/d = 15$	33

Figure 2.12	Comparison of the turbulent kinetic energy profiles measured by PIV (●) and calculated from RANS code (—) for (a) $x/d = 1$, (b) $x/d = 4.5$, (c) $x/d = 7.5$, (d) $x/d = 15$	34
Figure 2.13	Comparison of mean mixture fraction profiles for (a) $x/d = 1$, (b) $x/d = 4.5$, (c) $x/d = 7.5$, (d) $x/d = 15$. ●, PLIF; —, RANS, $Sc_T = 0.7$; - - -, RANS, $Sc_T = 0.5$; ▲, PDF, $Sc_T = 0.7$; Δ, PDF, $Sc_T = 0.5$	35
Figure 2.14	Comparison of mixture-fraction variance profiles (a) $x/d = 1$, (b) $x/d = 4.5$, (c) $x/d = 7.5$, (d) $x/d = 15$. ●, PLIF; —, RANS, $Sc_T = 0.7$; - - -, RANS, $Sc_T = 0.5$; ▲, PDF, $Sc_T = 0.7$; Δ, PDF, $Sc_T = 0.5$	36
Figure 2.15	Comparison of analytical solution to mixture-fraction variance and calculated mixture-fraction variance. - - -, Analytical solution; ○, RANS; Δ, PDF at $x/d = 7.5$; —, analytical solution; ●, RANS; ▲, PDF at $x/d = 15$	37
Figure 2.16	Effect of C_ϕ ($C_\phi = 2.5$) on the prediction of mixture-fraction variance profiles at (a) $x/d = 1$, (b) $x/d = 4.5$, (c) $x/d = 7.5$, (d) $x/d = 15$. ●, PLIF; —, RANS, $Sc_T = 0.7$; - - -, RANS, $Sc_T = 0.5$; ▲, PDF, $Sc_T = 0.7$; Δ, PDF, $Sc_T = 0.5$	38
Figure 2.17	Turbulence dissipation rate at various downstream locations measured by PIV: (a) estimated by Sheng's method; (b) estimated with nine terms. ■, $x/d = 1$; Δ, $x/d = 4.5$; ▼, $x/d = 7.5$; ◆, $x/d = 12$; ○, $x/d = 15$	39
Figure 2.18	Comparison of dissipation profiles measured Sheng's method (●), method 2 (○), and calculated from the RANS code (---) for (a) $x/d = 1$, (b) $x/d = 4.5$, (c) $x/d = 7.5$, (d) $x/d = 15$	40
Figure 3.1	Schematic of the flow facility and the optical setup used in the PIV and PLIF experiments.	65
Figure 3.2	Schematic of the confined rectangular-wake reactor.	65

Figure 3.3	(a) Mean streamwise velocity, (b) turbulent kinetic energy and (c) dissipation at the entrance plane of the wake. —, inlet boundary conditions for simulations; ●, PIV data.	66
Figure 3.4	An instantaneous velocity field as measured by PIV.	66
Figure 3.5	An instantaneous concentration field as measured by PLIF.	66
Figure 3.6	Comparison of the mean streamwise velocity profiles measured by PIV (●) and calculated from RANS code (—) for (a) $x/d = 1$, (b) $x/d = 4.5$, (c) $x/d = 7.5$, (d) $x/d = 12$, (e) $x/d = 15$ and (f) $x/d = 30$	67
Figure 3.7	Normalized Reynolds stresses measured by PIV. ■, $x/d = 0$; □, $x/d = 1.0$; ▲, $x/d = 4.5$; A, $x/d = 7.5$; ▼, $x/d = 12$; B, $x/d = 15$; ×, $x/d = 30$	68
Figure 3.8	Normalized velocity defect measured by PIV (left) and predicted by RANS (right). □, $x/d = 1.0$; ▲, $x/d = 4.5$; A, $x/d = 7.5$; ▼, $x/d = 12$; B, $x/d = 15$	69
Figure 3.9	Comparison of the turbulent kinetic energy profiles measured by PIV (●) and calculated from RANS code (—) for (a) $x/d = 1$, (b) $x/d = 4.5$, (c) $x/d = 7.5$, (d) $x/d = 12$, (e) $x/d = 15$ and (f) $x/d = 30$	70
Figure 3.10	Comparison of dissipation rate profiles as measured by PIV (●) and as calculated from RANS code (—) for (a) $x/d = 1$, (b) $x/d = 4.5$, (c) $x/d = 7.5$, (d) $x/d = 12$, (e) $x/d = 15$ and (f) $x/d = 30$	71
Figure 3.11	Comparison of mixture-fraction mean profiles measured by PLIF (●) and calculated from RANS code (—), IEM model (Δ) and EMST model (○) for (a) $x/d = 1$, (b) $x/d = 4.5$, (c) $x/d = 7.5$, (d) $x/d = 12$, (e) $x/d = 15$ and (f) $x/d = 30$	72
Figure 3.12	Comparison of mixture-fraction variance profiles measured by PLIF (●) and calculated from RANS code (—), IEM model (Δ) and EMST model (○) for (a) $x/d = 1$, (b) $x/d = 4.5$, (c) $x/d = 7.5$, (d) $x/d = 12$, (e) $x/d = 15$ and (f) $x/d = 30$	73

Figure 3.13	Comparison of one-point composition PDF measured by PLIF and calculated from PDF code for $x/d = 1$ at transverse distances from the centerline by (a) $3\delta/2$, (b) $5\delta/4$, (c) $9\delta/8$, (d) δ , (e) $7\delta/8$, (f) $3\delta/4$, (g) $\delta/2$ and (h) 0.	74
Figure 3.14	Comparison of one-point composition PDF measured by PLIF and calculated from PDF code for $x/d = 4.5$ at transverse distances from the centerline by (a) $3\delta/2$, (b) $5\delta/4$, (c) $9\delta/8$, (d) δ , (e) $7\delta/8$, (f) $3\delta/4$, (g) $\delta/2$ and (h) 0.	75
Figure 3.15	Comparison of one-point composition PDF measured by PLIF and calculated from PDF code for $x/d = 7.5$ at transverse distances from the centerline by (a) $3\delta/2$, (b) $5\delta/4$, (c) $9\delta/8$, (d) δ , (e) $7\delta/8$, (f) $3\delta/4$, (g) $\delta/2$ and (h) 0.	76
Figure 3.16	Comparison of one-point composition PDF measured by PLIF and calculated from PDF code for $x/d = 12$ at transverse distances from the centerline by (a) $3\delta/2$, (b) $5\delta/4$, (c) $9\delta/8$, (d) δ , (e) $7\delta/8$, (f) $3\delta/4$, (g) $\delta/2$ and (h) 0.	77
Figure 3.17	Comparison of one-point composition PDF measured by PLIF and calculated from PDF code for $x/d = 15$ at transverse distances from the centerline by (a) $3\delta/2$, (b) $5\delta/4$, (c) $9\delta/8$, (d) δ , (e) $7\delta/8$, (f) $3\delta/4$, (g) $\delta/2$ and (h) 0.	78
Figure 3.18	Comparison of one-point composition PDF measured by PLIF and calculated from PDF code for $x/d = 30$ at transverse distances from the centerline by (a) $3\delta/2$, (b) $5\delta/4$, (c) $9\delta/8$, (d) δ , (e) $7\delta/8$, (f) $3\delta/4$, (g) $\delta/2$ and (h) 0.	79
Figure 4.1	Schematic of the flow facility and the optical setup used in the combined PIV and PLIF experiments.	109
Figure 4.2	Photograph and schematic of the confined rectangular-jet test section.	110

Figure 4.3	(a)An instantaneous velocity field as measured by PIV, and(b)the corresponding instantaneous concentration field as measured by PLIF. . .	110
Figure 4.4	Normalized mean streamwise velocity and Reynolds stresses at different streamwise locations. (a) Mean velocity; (b) longitudinal stress; (c) lateral stress; (d) shear stress. \square , $x/d = 0$; \blacksquare , $x/d = 1.0$; \triangle , $x/d = 4.5$; \times , $x/d = 7.5$; \blacktriangledown , $x/d = 12$; z , $x/d = 15$; \circ , $x/d = 30$	111
Figure 4.5	Normalized turbulent kinetic energy at different streamwise locations. \blacksquare , $x/d = 1.0$; \triangle , $x/d = 4.5$; \times , $x/d = 7.5$; \blacktriangledown , $x/d = 12$; z , $x/d = 15$; \circ , $x/d = 30$	112
Figure 4.6	Self-similar of mean streamwise velocity and Reynolds stresses. (a) Mean velocity; (b) longitudinal stress; (c) lateral stress; (d) shear stress. Symbols, experimental data (\blacksquare , $x/d = 1.0$; \triangle , $x/d = 4.5$; \times , $x/d = 7.5$; \blacktriangledown , $x/d = 12$; z , $x/d = 15$; \circ , $x/d = 30$.); line, Eqn. 4.16.	113
Figure 4.7	Normalized concentration mean and variance at different streamwise locations. (a) Mean concentration; (b) concentration variance. \blacksquare , $x/d = 1.0$; \triangle , $x/d = 4.5$; \times , $x/d = 7.5$; \blacktriangledown , $x/d = 12$; z , $x/d = 15$; \circ , $x/d = 30$	114
Figure 4.8	Orientation of the gradient vector of mean concentration at different streamwise locations. \blacksquare , $x/d = 1.0$; \triangle , $x/d = 4.5$; \times , $x/d = 7.5$; \blacktriangledown , $x/d = 12$; z , $x/d = 15$; \circ , $x/d = 30$	114
Figure 4.9	Turbulent fluxes at different streamwise locations. (a) Longitudinal flux; (b) lateral flux. \blacksquare , $x/d = 1.0$; \triangle , $x/d = 4.5$; \times , $x/d = 7.5$; \blacktriangledown , $x/d = 12$; z , $x/d = 15$; \circ , $x/d = 30$	115
Figure 4.10	Velocity-concentration correlation coefficients at different streamwise locations. (a) Longitudinal coefficient; (b) lateral coefficient. \blacksquare , $x/d = 1.0$; \triangle , $x/d = 4.5$; \times , $x/d = 7.5$; \blacktriangledown , $x/d = 12$; z , $x/d = 15$; \circ , $x/d = 30$	115

Figure 4.11	Orientation of the turbulent flux vector at different streamwise locations. \triangle , $x/d = 4.5$; \times , $x/d = 7.5$; \blacktriangledown , $x/d = 12$; \mathbf{z} , $x/d = 15$; \circ , $x/d = 30$	116
Figure 4.12	Dimensionless turbulent viscosity at different streamwise locations. \blacksquare , $x/d = 1.0$; \triangle , $x/d = 4.5$; \times , $x/d = 7.5$; \blacktriangledown , $x/d = 12$; \mathbf{z} , $x/d = 15$; \circ , $x/d = 30$	116
Figure 4.13	Dimensionless cross-component of the turbulent diffusivity tensor. \blacksquare , $x/d = 1.0$; \triangle , $x/d = 4.5$; \times , $x/d = 7.5$; \blacktriangledown , $x/d = 12$; \mathbf{z} , $x/d = 15$; \circ , $x/d = 30$	117
Figure 4.14	Dimensionless turbulent diffusivity. \blacksquare , $x/d = 1.0$; \triangle , $x/d = 4.5$; \times , $x/d = 7.5$; \blacktriangledown , $x/d = 12$; \mathbf{z} , $x/d = 15$; \circ , $x/d = 30$	117
Figure 4.15	The ratio of the two components of turbulent diffusivity tensor. \blacksquare , $x/d = 1.0$; \triangle , $x/d = 4.5$; \times , $x/d = 7.5$; \blacktriangledown , $x/d = 12$; \mathbf{z} , $x/d = 15$; \circ , $x/d = 30$	118
Figure 4.16	Turbulent Schmidt number at different streamwise locations. \times , $x/d = 7.5$; \blacktriangledown , $x/d = 12$; \mathbf{z} , $x/d = 15$; \circ , $x/d = 30$	118
Figure 4.17	Contours of two-point spatial correlation $R_{w'\phi'}$	119
Figure 4.18	Contours of two-point spatial correlation $R_{v'\phi'}$	120
Figure 4.19	Contours of two-point spatial correlation $R_{\phi'\phi'}$	121
Figure 4.20	Linear stochastic estimate of a concentration field given an event of $\phi'(\mathbf{x}_o) = 2\phi'_{rms}(\mathbf{x}_o)$	122
Figure 4.21	Linear stochastic estimate of a concentration field given an event of $\phi'(\mathbf{x}_o) = -2\phi'_{rms}(\mathbf{x}_o)$	123
Figure 4.22	Estimated velocity fields given an event of $\phi'(\mathbf{x}_o) = 2\phi'_{rms}(\mathbf{x}_o)$, with $U(\mathbf{x}_o)$ subtracted from each vector.	124
Figure 4.23	Estimated velocity fields given an event of $\phi'(\mathbf{x}_o) = -2\phi'_{rms}(\mathbf{x}_o)$, with $U(\mathbf{x}_o)$ subtracted from each vector.	125

Figure 4.24	Large-structure size based on estimated velocity fields at the measured downstream locations in the flow. The dashed line represents the linear-fit trend line.	126
Figure 5.1	Schematic of the flow facility and the optical setup used in the combined PIV and PLIF experiments.	147
Figure 5.2	Schematic of the confined rectangular-wake reactor.	148
Figure 5.3	(a) An instantaneous velocity field as measured by PIV, and (b) the corresponding instantaneous concentration field as measured by PLIF.	148
Figure 5.4	Normalized mean streamwise velocity and Reynolds stresses. \blacksquare , $x/d = 0$; \square , $x/d = 1.0$; \blacktriangle , $x/d = 4.5$; A , $x/d = 7.5$; \blacktriangledown , $x/d = 12$; B , $x/d = 15$; \times , $x/d = 30$	149
Figure 5.5	Concentration mean and variance. \square , $x/d = 1.0$; \blacktriangle , $x/d = 4.5$; A , $x/d = 7.5$; \blacktriangledown , $x/d = 12$; B , $x/d = 15$; \times , $x/d = 30$	150
Figure 5.6	Orientation of the mean concentration gradient at different streamwise locations. \square , $x/d = 1.0$; \blacktriangle , $x/d = 4.5$; A , $x/d = 7.5$; \blacktriangledown , $x/d = 12$; B , $x/d = 15$; \times , $x/d = 30$	150
Figure 5.7	Turbulent fluxes. \square , $x/d = 1.0$; \blacktriangle , $x/d = 4.5$; A , $x/d = 7.5$; \blacktriangledown , $x/d = 12$; B , $x/d = 15$; \times , $x/d = 30$	151
Figure 5.8	Mass transport correlation coefficients coefficients. \square , $x/d = 1.0$; \blacktriangle , $x/d = 4.5$; A , $x/d = 7.5$; \blacktriangledown , $x/d = 12$; B , $x/d = 15$; \times , $x/d = 30$	151
Figure 5.9	Orientation of the turbulent flux vector at different streamwise locations. \blacktriangle , $x/d = 4.5$; A , $x/d = 7.5$; \blacktriangledown , $x/d = 12$; B , $x/d = 15$; \times , $x/d = 30$	152
Figure 5.10	Dimensionless turbulent viscosity. \square , $x/d = 1.0$; \blacktriangle , $x/d = 4.5$; A , $x/d = 7.5$; \blacktriangledown , $x/d = 12$; B , $x/d = 15$; \times , $x/d = 30$	152
Figure 5.11	Cross-component of the turbulent diffusivity tensor. \square , $x/d = 1.0$; \blacktriangle , $x/d = 4.5$; A , $x/d = 7.5$; \blacktriangledown , $x/d = 12$; B , $x/d = 15$; \times , $x/d = 30$	153

Figure 5.12	Dimensionless turbulent diffusivity. \square , $x/d = 1.0$; \blacktriangle , $x/d = 4.5$; A , $x/d = 7.5$; \blacktriangledown , $x/d = 12$; B , $x/d = 15$; \times , $x/d = 30$	153
Figure 5.13	Ratio of Γ_{12} and Γ_{22} . \blacktriangle , $x/d = 4.5$; A , $x/d = 7.5$; \blacktriangledown , $x/d = 12$; B , $x/d = 15$; \times , $x/d = 30$	154
Figure 5.14	Turbulent Schmidt number. \blacktriangle , $x/d = 4.5$; A , $x/d = 7.5$; \blacktriangledown , $x/d = 12$; \times , $x/d = 30$	154
Figure 5.15	Contours of two-point spatial correlation $R_{u'\phi'}$	155
Figure 5.16	Contours of two-point spatial correlation $R_{v'\phi'}$	156
Figure 5.17	Contours of two-point spatial correlation $R_{\phi'\phi'}$	157
Figure 5.18	Linear stochastic estimation of a concentration field given an event of $\phi'(\mathbf{x}_o) = 2\phi'_{rms}(\mathbf{x}_o)$	158
Figure 5.19	Linear stochastic estimation of a concentration field given an event of $\phi'(\mathbf{x}_o) = -2\phi'_{rms}(\mathbf{x}_o)$	159
Figure 5.20	Estimated velocity fields given an event of $\phi'(\mathbf{x}_o) = 2\phi'_{rms}(\mathbf{x}_o)$, with $U(\mathbf{x}_o)$ subtracted from each vector.	160
Figure 5.21	Estimated velocity fields given an event of $\phi'(\mathbf{x}_o) = -2\phi'_{rms}(\mathbf{x}_o)$, with $U(\mathbf{x}_o)$ subtracted from each vector.	161
Figure 5.22	Dimensionless large-scale structure size based on estimated velocity fields at the measured downstream locations in the flow. The dashed line represents the linear-fit trend line.	161
Figure 6.1	Schematic of the confined rectangular-jet test section.	174
Figure 6.2	Normalized mean streamwise velocity and Reynolds stresses at different streamwise locations. \square , $x/d = 0$; \blacksquare , $x/d = 1.0$; \triangle , $x/d = 4.5$; \times , $x/d = 7.5$; \blacktriangledown , $x/d = 12$; z , $x/d = 15$; \circ , $x/d = 30$	175
Figure 6.3	Normalized concentration mean and variance at different streamwise locations. \blacksquare , $x/d = 1.0$; \triangle , $x/d = 4.5$; \times , $x/d = 7.5$; \blacktriangledown , $x/d = 12$; z , $x/d = 15$; \circ , $x/d = 30$	176

Figure 6.4	Turbulent fluxes at different streamwise locations. \blacksquare , $x/d = 1.0$; \triangle , $x/d = 4.5$; \times , $x/d = 7.5$; \blacktriangledown , $x/d = 12$; z , $x/d = 15$; \circ , $x/d = 30$	176
Figure 6.5	The comparison of the experimental probability densities (symbols) and beta-PDFs (lines) at various positions. $y = 0$, \times , thin line; $y = -\delta/2$, \square , dotted line; $y = -3\delta/4$, \blacktriangle , short-dash-dot line; $y = -7\delta/8$, \triangle , short-dash line; $y = -\delta$, \blacktriangledown , long-dash line; $y = -9\delta/8$, ∇ , dash-dot-dot line; $y = -5\delta/4$, \diamond , long-dash-dot line; $y = -3\delta/2$, \blacksquare , bold line.	177
6.6	Scatter plots of velocity fluctuations for various downstream locations at $y = 0$ and $y = -\delta$. Line with triangle, $\langle u v \rangle$; line with cross, $\langle v u \rangle$. The lines represent the weighted smoothing splines to the data points.	178
Figure 6.7	Scatter plots for various downstream locations at $y = 0$. Line with triangle, $\langle \mathbf{u} \psi \rangle$; line with cross, $\langle \phi \mathbf{u} \rangle$. The lines represent the weighted smoothing splines to the data points.	179
Figure 6.8	Scatter plots for various downstream locations at $y = -\delta$. Line with triangle, $\langle \mathbf{u} \psi \rangle$; line with cross, $\langle \phi \mathbf{u} \rangle$. The lines represent the weighted smoothing splines to the data points.	180
Figure 6.9	The conditional mean streamwise velocity from the experimental data at various positions normalized according to Eq.6.1. Symbols are the same as in Fig. 6.5.	181
Figure 6.10	The conditional mean transverse velocity from the experimental data at various positions normalized according to Eq.6.1. Symbols are the same as in Fig. 6.5.	182
Figure 6.11	The comparison of conditional mean streamwise velocity from the experimental data (symbols) and from the gradient PDF model (lines). Symbols and lines are the same as in Fig. 6.5. The thin dashed line are the results of the linear model.	183

6.12	The comparison of conditional mean streamwise velocity from the experimental data (symbols) and from the improved gradient PDF model (lines). Symbols and lines are the same as in Fig. 6.5.	184
Figure 6.13	The comparison of conditional mean transverse velocity from the experimental data (symbols) and from the gradient PDF model (lines). Symbols and lines are the same as in Fig. 6.5.	185
Figure 6.14	The mean scalar conditioned on the streamwise velocity at various positions normalized according to Eq.6.14. Symbols are the same as in Fig. 6.5.	186
Figure 6.15	The mean scalar conditioned on the transverse velocity at various positions normalized according to Eq.6.14. Symbols are the same as in Fig. 6.5.	187

CHAPTER 1 INTRODUCTION

General Introduction

The study of turbulent shear flows, such as turbulent jets and wakes, is of great importance due to the presence of turbulent shear flows in a very wide variety of engineering applications. In the chemical process industry, turbulent shear flows prominently appear because of their ability to transport and mix chemical species, momentum, and energy much faster than molecular diffusion. Since the product distribution of chemical processes is significantly affected by turbulent transport, a detailed understanding of the mixing properties in turbulent shear flows is crucial for the development of environmentally benign, commercially efficient chemical processing technologies.

There are many different techniques being used to address different questions concerning turbulent mixing. By virtue of its ability to quickly generate flow field predictions in complex geometries at a relatively low cost, computational fluid dynamics (CFD) has become a promising tool in recent years for chemical process engineers to study turbulent flows and to design reactors[Fox (2003)]. However, in order to avoid costly mistakes on scale up, it is vital that CFD models be validated against experimental data. Therefore, experimental studies are still of great importance not only in advancing turbulent theory, but also in the development and validation of CFD models.

In the past decade, with the advancement of flow visualization techniques, particle image velocimetry (PIV) and planar laser-induced fluorescence (PLIF) have become attractive experimental techniques for the measurements of the instantaneous velocity and scalar (concentration or temperature) distribution in turbulent flows. Due to their non-intrusive character, both PIV and PLIF are capable of providing high-quality measurements. Moreover, as whole-field mea-

surement techniques, both PIV and PLIF are superior to pointwise measurements, such as laser Doppler velocimetry (LDV), because flowfield data can be simultaneously collected at a large number of points over an extended planar domain, and the two-dimensional nature of the data allow the identification and characterization of coherent structures. With the rapid development of optical diagnostics in recent years, it has become possible to create combined PIV and PLIF systems for the simultaneous measurements of velocity and concentration (or temperature) fields in turbulent flows.

There are many examples of earlier work on simultaneous measurements of velocity and concentration fields using combined PIV and PLIF techniques in a number of flow-field geometries. Such combined PIV and PLIF experiments introduce a number of challenges that are not encountered in non-simultaneous studies. For example, Carter et al. (1998) were among the first researchers to report the influence of particle scattering on the PLIF images in the simultaneous PIV and PLIF measurements. They employed optical filters to reject the strong particle scattering and developed a combined PIV and PLIF system for the measurements of turbulent nonpremixed flames. Another example of early combined PIV/PLIF work was performed by Aanen et al. (1999) who investigated the fully developed liquid-phase axisymmetric turbulent flow in a smooth pipe and found that the experimental results agreed well with those of a direct numerical simulation (DNS) and the analytical result. Law and Wang (2000) investigated the potential interference effect between PIV and PLIF techniques and found that the interference of the fluorescent tracer on PIV is negligible, whereas the effect of the seeding particles on PLIF can be attributed to three factors: the attenuation of the laser light that can be described by the Beer-Lambert law, the interaction with the dye tracer leading to a small increase of local fluorescence, and the residual Mie scattering light that passes the PLIF filter. For this reason, optical filters were employed in most reported combined PIV and PLIF systems to reject the PIV particle scattering on the PLIF images in the simultaneous PIV and PLIF measurements.

Despite the large volume of experimental data that exists concerning various aspects of turbulent mixing in shear flows, instantaneous whole-field measurements of velocity and con-

centration fields are lacking. Detailed studies involving simultaneous whole-field velocity and concentration measurements are even scarcer. The objectives of the present study are to develop both conventional PIV and PLIF and simultaneous PIV and PLIF systems and to obtain a comprehensive view of the velocity and concentration fields in liquid-phase confined turbulent shear flows, including a rectangular jet and a plane wake. These experimental results have also been used to validate CFD models.

Dissertation Organization

The remainder of this thesis is organized as follows:

In Chapter 2, the PIV and PLIF measurements of the velocity and concentration fields in a confined rectangular jet will be introduced. The flow system and the measurement methodology are described. The experimental results will be analyzed to characterize the behavior of the confined turbulent jet. Flow statistics are presented, including mean velocity, Reynolds stresses, turbulent kinetic energy and dissipation rate, and concentration mean and variance. These data are also compared with CFD results.

By changing the incoming flow conditions, a rectangular-wake flow may be obtained in the rectangular reactor described in Chapter 2. Chapter 3 presents the results from the investigation of the confined wake flow as measured by non-simultaneous PIV and PLIF. The evolution of the wake is analyzed by quantifying the typical flow statistics of the velocity and concentration fields in the flow. The self-similarity of the wake is also examined. Some CFD models are tested against the experimental data.

On the basis of the experiments introduced in previous chapters, a combined PIV and PLIF system is developed. Chapter 4 describes this combined PIV and PLIF diagnostic system and the simultaneous measurements of the confined rectangular jet. More in-depth analysis of the jet flow is presented in this chapter. Spatial correlations of turbulent fluxes and concentration fluctuation and linear stochastic estimate (LSE) are used to reveal the characteristics of the large-scale structures in the jet.

Chapter 5 presents the investigation of the confined wake flow using the combined PIV

and PLIF system. A similar analysis has been performed with the simultaneously measured experimental data of the wake flow as in Chapter 4. Some of the results are also compared with those of the jet study.

Although conditional statistics data, such as the conditional velocities and the conditional concentration, are important for the development and validation of PDF models and conditional moment closure (CMC) models, such existing experimental data are scarce. The conditional statistics of the obtained experimental data in this study is presented and analyzed in Chapter 6. Some existing models of the conditional velocity and the conditional concentration are tested against the experimental data.

Finally, summary and conclusions are given in Chapter 7. Some future work is also briefly discussed.

CHAPTER 2 INVESTIGATION OF TURBULENT MIXING IN A CONFINED PLANAR-JET REACTOR

A paper published by *AIChE Journal*

Hua Feng, Michael G. Olsen, Ying Liu, Rodney O. Fox and James C. Hill

(Ying Liu is responsible for the simulation work in this paper)

Abstract

The velocity and concentration fields in a liquid-phase confined planar-jet reactor were measured using particle image velocimetry (PIV) and planar laser-induced fluorescence (PLIF). Measurements were taken at downstream distances from the jet splitter plates of 0, 1, 4.5, 7.5, 12, and 15 jet widths for a Reynolds number of 50,000 based on the distance between two sidewalls of the test section. The velocity and concentration field data were analyzed for such flow statistics as mean velocity, Reynolds stresses, turbulent kinetic energy, and scalar mean and variance. The turbulence dissipation rate was also estimated based on a large-eddy PIV approach using the strain-rate tensors computed from velocity fields and the sub-grid scale (SGS) stress obtained from the Smagorinsky model. Computational fluid dynamics (CFD) models including a two-layer $k - \varepsilon$ turbulence model, gradient-diffusion models and a scalar dissipation rate model were validated against experimental data collected from this facility. The experimental and computational results were found to be in good agreement.

Introduction

Because of their ability to transport and mix chemical species, momentum, and energy much faster than molecular diffusion, turbulent flows are widely used in the chemical process

industry. For example, most chemical reactors are designed to operate in the turbulent regime in order to maximize throughput. It follows that a detailed understanding of turbulent mixing is necessary for the proper design and optimization of chemical reactors, making turbulent mixing the topic of numerous experimental and computational studies over the years [Mehta and Tarbell (1987); Pipino and Fox (1994); Baldyga and Pohorecki (1995); Baldyga and Bourne (1999)]. One objective in studying turbulent mixing is to develop computational fluid dynamics (CFD) models for turbulent reacting flows [Fox (2003)]. By virtue of its potential for quickly generating flow field predictions in complex geometries at a relatively low cost, CFD can be a useful tool in reactor design and analysis [Ranade (2002)]. One key component of a successful CFD model is the model used to characterize turbulent mixing at the microscale [Jiménez et al. (1997); Vreman et al. (1997); Langford and Moser (1999); Fox (2003)]. Both the development and validation of sub-grid scale models require comparison with experimental data [Sohankar et al. (1999); Friberg and Hjertager (1999)]. Accordingly, experimental studies can be of great importance in both advancing turbulence theory and in the development and validation of CFD micromixing models. The primary objective of this work is to implement state-of-the-art experimental techniques in order to validate CFD models for turbulent mixing in a well-defined flow geometry: a confined planar-jet reactor.

In the present study, velocity and concentration fields in a turbulent flow have been measured using two non-intrusive optically based techniques: particle image velocimetry (PIV) and planar laser induced fluorescence (PLIF). After their rapid development in the recent years, both PIV and PLIF have been proven to be capable of providing high-quality measurements. Aanen et al. [Aanen et al. (1999)] tested the reliability and precision of the techniques of PIV and PLIF. They measured the mixing of fluorescein emitted from a point source placed in the center of a fully developed turbulent flow in a smooth pipe and found that the experimental results agreed well with those of a direct numerical simulation (DNS) and the analytical results. In their paper on the mixing in a self-preserving axisymmetric turbulent jet, Fukushima et al. [Fukushima et al. (2000)] compared their results obtained from PIV and PLIF techniques with not only the results from DNS, but also with point velocity measurements and combined

PIV, particle tracking velocimetry (PTV), or laser Doppler velocimetry (LDV) with laser induced fluorescence (LIF) measurements, and found satisfactory agreement between the DNS simulations and the data collected using each technique. Meyer et al. [Meyer et al. (2000)] also measured the velocity field and concentration field using PIV and PLIF. They considered the mixing of a jet in a crossflow in a square duct and compared their results with measurements in the same setup by the use of pointwise LIF and laser Doppler anemometry (LDA). They found that PIV and PLIF gave results in good agreement with those from single-point techniques. Furthermore, as whole-field measurement techniques, both PIV and PLIF have distinct advantages over single-point measurement techniques, especially in their ability to give instantaneous spatial information. For this reason, PIV and PLIF have been employed to investigate the spatial structure of turbulent velocity and concentration fields [Kawaguchi et al. (2002); Olsen and Dutton (2002); Crimaldi and Koseff (2001)].

In collecting experimental data to develop or validate computational models, one would like to perform experiments with enough spatial resolution to accurately determine flow quantities such as Reynolds stresses and dissipation rates. According to classical turbulence theory [Kolmogorov (1941)], the smallest spatial scales of motion in the flow are set by the Kolmogorov scale, which is defined by

$$\eta = \left(\frac{\nu^3}{\varepsilon} \right)^{1/4}, \quad (2.1)$$

where ν is the molecular kinematic viscosity and ε is the rate of dissipation of turbulent kinetic energy per unit mass.

Mixing layer growth and fluid entrainment are dominated by large-scale turbulent structures [Brown and Roshko (1974); Mankbadi (1992); Lesieur et al. (1995)]. Large-scale structures absorb energy from the mean flow and are usually flow-dependent, while small-scale structures mainly dissipate the energy provided by larger eddies and are more universal than the large scales [Pope (2000)]. For high Reynolds number flows, only the large-scale turbulent structures need to be resolved to determine the Reynolds stresses and turbulent kinetic energy since they are the energy containing structures. For example, Law and Wang [Law and Wang (2000)] studied turbulent mixing using PIV with a spatial resolution of about 16η and

obtained turbulence intensities in good agreement with results from fine scale measurements. Smaller scales must be resolved if one desires to measure or estimate turbulence dissipation. Tennekes and Lumley [Tennekes and Lumley (1972)] suggested that the spatial resolution of the velocity measurement be no more than 5η where the dissipation of the turbulence has a maximum. Tsurikov and Clemens [Tsurikov and Clemens (2002)] found that kinetic energy dissipative structures have thicknesses ranging from approximately 1η to 10η and a mean thickness of 4η after processing the PIV data at a few different resolutions.

In homogeneous and isotropic turbulence, the mean turbulence dissipation rate, ϵ , can be approximated by

$$\epsilon \simeq A \frac{u_0'^3}{l}, \quad (2.2)$$

where u_0' is the characteristic fluctuating velocity, l represents the integral length scale of turbulence, and A is a constant [Batchelor (1953); Tennekes and Lumley (1972)]. Antonia et al. [Antonia et al. (1980)] found that the value of A is approximately equal to one if Eq. diss appro is applied to planar jets. In practice, the integral length scale is not a constant and varies throughout the flow field so that Eq. diss appro cannot be used to describe the local dissipation rate. Numerous methods have been suggested to estimate the local dissipation rate from hot wire or laser Doppler anemometry data [Browne et al. (1987); Elsener and Elsner (1996)]. However, these methods are limited due to their being single-point velocity techniques. Because of the planar nature of the collected data, PIV offers the possibility of estimating the distribution of the dissipation rate over a large flow region. Based on a large-eddy PIV approach, Sheng et al. [Sheng et al. (2000)] showed that the turbulence dissipation rate could be approximated by computing the Reynolds averaged sub-grid-scale (SGS) dissipation rate

$$\epsilon \simeq -2\langle \tau_{ij} \bar{S}_{ij} \rangle \quad (2.3)$$

where \bar{S}_{ij} is the filtered rate-of-strain tensor defined by

$$\bar{S}_{ij} = \frac{1}{2} \left(\frac{\partial \bar{U}_j}{\partial x_i} + \frac{\partial \bar{U}_i}{\partial x_j} \right), \quad (2.4)$$

where \bar{U} is the filtered velocity field. To close the SGS stress, , various SGS models have been proposed. The Smagorinsky model [Smagorinsky (1963)] is one of the simplest models, which gives

$$\tau_{ij} = -C_s^2 \Delta^2 |\bar{S}| \bar{S}_{ij}, \quad (2.5)$$

where $C_s = 0.17$ is the Smagorinsky constant, Δ is the filter width, and $|\bar{S}| = (2\bar{S}_{ij}\bar{S}_{ij})^{1/2}$. Although a large body of experimental data exists for turbulent flows, no detailed experimental data for both the turbulent flow field and concentration field inside of a liquid-phase, confined planar jet are available for model validation. The objective of the present study is to investigate turbulent mixing in a confined planar jet using both PIV and PLIF. The velocity and concentration fields are analyzed to provide insight into the characteristics of turbulent mixing and to validate the results of CFD models.

Experimental Apparatus and Methodology

Flow Facility

The experimental setup is shown in Figs. 2.1 and 2.2. The flow system is designed to provide a shear flow for Reynolds numbers, based on the distance between two sidewalls, in the range 5,000-100,000. The measurements are carried out in a Plexiglas test section (Fig. 2.2) with a rectangular cross-section of 60 mm by 100 mm and an overall length of 1 m. The test section is mounted in an adjustable cage so that it can be moved up and down to change the interrogation region without moving the lasers and cameras. The width of each of the three inlet channels is 20 mm. Three feedback control systems (Fieldvue DVC6000, Fisher Controls International Inc.) with flow accuracy of 0.5% are used to supply constant flow rates to the inlet channels.

Before they enter the test section, uniform flow and reduced free-stream turbulence intensities are imparted on the incoming flow by flow conditioning consisting of a packed bed, turbulence reducing screens, and a 16:1 contraction. For the present study, the flow rates of each inlet channel were 1.0, 2.0 and 1.0 liter/sec, thus the free-stream velocities were 0.5 m/s,

1 m/s and 0.5 m/s, respectively. The Reynolds number based on the distance between two sidewalls was 50,000. The coordinate system in plots presented here is such that x - is in the downstream direction and y - is in the transverse direction. The cross-stream direction (z -) is assumed to be nearly homogeneous (except near the front and back walls), and no data were taken in that direction.

Velocity Measurements

PIV was used to measure the instantaneous velocity field in a planar cross section of the observed flow. A schematic depicting the PIV (and also the PLIF) experimental setup is shown in Fig. 2.3. The flow was seeded with hollow glass spheres (Spherical, Potters Industries Inc.) with a nominal diameter of $11.7 \mu\text{m}$ and a density of 1.1 g/cm^3 . The particles were added to the feed tanks and mixed until they were distributed homogeneously. About 120 grams of seed particles were added to the total reservoir volume of 3500 liters.

Illumination was provided by a New Wave Research Gemini PIV laser. The Gemini is a double-pulsed Nd:YAG laser that emits two independent 532 nm light pulses at a frequency of 15 Hz. The maximum pulse energy is 120 mJ and the pulse duration is about 5 ns. A time delay between the two laser pulses of $600 \mu\text{s}$ was used in the present study. Using a series of mirror and cylindrical and spherical lenses, the laser beam was formed into a thin light sheet with a thickness of about 0.5 mm passing through the reactor at the centerline of the cross-stream direction. The waist of the light sheet was located near the centerline in the y -direction.

Images of the seeded flow were obtained at a frame rate of 8 images/sec using a 12-bit LaVision Flowmaster 3S CCD camera with a resolution of 1280×1024 pixels. The laser and cameras were connected to a host computer that controlled the timing of laser illumination and image acquisition. Two images were captured per realization, and the corresponding velocity field was computed using a cross-correlation technique [Westerweel (1993); Kompenhans et al. (1998)]. A multi-pass interrogation scheme with decreasingly smaller window sizes was used with a final interrogation spot size measuring 16 by 16 pixels, corresponding to 0.9 mm

on a side. With 50% overlap between adjacent interrogation spots, the spatial resolution was 0.45 mm in both the x and y directions. The only post-processing performed on the vector fields was the removal of bad vectors. No smoothing of vector fields was performed. At each observed location, 2500 image pairs were taken and then analyzed.

Using the exit width of the jet as the characteristic length scale, the Kolmogorov scale in the present study was estimated to be approximately $75 \mu\text{m}$ based on Eqs. 2.1 and 2.2. The spatial resolution of the PIV measurements is about 6η ; therefore, the measurements cannot adequately resolve the smallest scales of the flow. However, since the primary interest in this study is in the determination of the first- and second-order flow statistics such as mean velocity and turbulence intensity, the loss of the fine-scale information should not affect the results.

Uncertainties in the velocity measurements include errors introduced during the recording of the images and bias introduced by large velocity gradients [Keane and Adrian (1992)]. The maximum uncertainty of the measurements can be estimated as one-tenth of the particle image diameter [Prasad et al. (1992)]. The centerline free-stream velocity corresponds to a displacement of $600 \mu\text{m}$ and the side free-stream velocities correspond to a displacement of $300 \mu\text{m}$; thus, the maximum experimental uncertainty is $\pm 1.3\%$ for the center free-stream and $\pm 2.7\%$ for the side free streams.

Concentration Measurements

A similar optical setup was used for the PLIF measurements, except the camera was placed closer to the reactor than in the PIV measurements, giving a smaller field of view. Based on the area imaged per pixel, the spatial resolution for PLIF measurements was 0.026 mm. However, the diffraction-limited spot size for the lens was 0.035 mm; this is a better estimate of the PLIF spatial resolution. Rhodamine 6G was used as the passive scalar. In the center stream, the source concentration of Rhodamine 6G was $45 \mu\text{g/liter}$, whereas the other two streams were pure water. Rhodamine 6G emits broadband fluorescence with a peak emission around 555 nm when excited by light from an Nd:YAG laser [Penzkofer and Leupacher (1987)]. To ensure that reflected or scattered laser light does not interfere with the fluorescence measurements,

the camera lens was fitted with a long-pass (i.e., low pass for frequency) optical filter that blocked light below 555 nm. The concentration field images were captured at a frame rate of 8 images/sec. Since the flow could not be re-circulated during PLIF measurements, the number of images that could be collected per run was limited by the volume of feed tanks. For the data presented here, 1500 images were taken at each observed location.

Nd:YAG lasers have a Gaussian energy distribution, so it is impossible to obtain a uniform energy distribution throughout the entire light sheet. This drawback can be significant for PLIF that is based on light intensity [Law and Wang (2000)]. Furthermore, the intensity of a laser beam decays as it passes through the dye solution due to absorption. Crimaldi and Koseff [Crimaldi and Koseff (2001)] that under appropriate experimental conditions, the local intensity of the fluoresced light, F , is proportional to the local intensity of the excitation source, I , and to the local concentration of the dye, C , so that F is given by

$$F(x, y) = \alpha I(x, y) C(x, y), \quad (2.6)$$

where α is a constant that can be determined empirically. In the present study, we found that this relationship was valid for dye concentrations up to 100 $\mu\text{g}/\text{liter}$ with our experimental setup.

To eliminate any variation of the local intensity of the excitation source, we employed the following procedure for the calibration of the concentration measurements. A series of 1000 dark images were taken and averaged at each pixel to measure the gray offset value distribution in the interrogation field, and this was used to remove the dark field component from each PLIF image. Variations in illumination intensity were accounted for by filling up the test section with the source dye solution and recording a series of 200 in-situ calibration images at each measurement location. The instantaneous PLIF images at each measurement location were then normalized for illumination variations using the ensemble mean of the calibration images.

Overview of CFD Models

Turbulent flows are governed by conservative equations of mass, momentum and energy [Pope (2000)]. In most applications of CFD models, the Reynolds equations are closed

either by turbulent-viscosity models or by Reynolds-stress models. In this work, we adopt a turbulent-viscosity-based model that is widely used in industry, that is, the $k - \varepsilon$ model [Jones, W .P. and Launder, B. E. (1972)]. All the model constants adopt their standard values [Launder and Sharma (1974)]. The $k - \varepsilon$ model is generally regarded as being easy to implement and computationally inexpensive [Pope (2000)]. However, $k - \varepsilon$ calculations in the near-wall region can be computational intensive due to two principal difficulties: (i) sharp gradients in k and ε , and (ii) source terms becoming very large. In order to obtain the desired accuracy with reasonable computational cost, a two-layer $k - \varepsilon$ model (see Appendix for details) has been implemented in our finite-volume Reynolds-averaged Navier-Stokes (RANS) code [Wilcox (1998); Harvey (2003)]. The performance of this model is evaluated by comparing predicted single-point turbulence statistics with time-averaged PIV data.

While turbulent transport of an inert scalar can be successfully described by a small set of statistical moments, the same is not true for reactive scalar fields, which are strongly coupled through the chemical-source term [Fox (2003)]. According to how they treat the sub-grid-scale concentration fluctuations in the closure for the chemical source term, CFD models for liquid-phase turbulent reacting flows can be roughly classified into four general categories: moment methods, conditional moment methods, multi-environment presumed probability density function (PDF) methods and transported PDF methods [Fox (1996, 1998, 2003)]. In the moment methods, the sub-grid-scale fluctuations are represented by a mean-field approximation involving low-order moments. No attempt is made to represent the entire PDF that is present at the mesoscopic level. In general, these models are insufficient for predicting byproduct selectivity in chemical reactors [Chakrabarti et al. (1997)]. Conditional moment methods use a presumed PDF model to account for the sub-grid-scale fluctuations of the mixture fraction. The reaction progress variables are modeled in terms of their mean values conditioned on the value of the mixture fraction. The conditional moments can be found either by a linear interpolation procedure [Baldyga (1994)] or by solving a transport equation [Bilger (1993)]. Multi-environment presumed PDF methods assume that the joint PDF of the sub-grid-scale fluctuations can be represented by a small number of environments, each of which is parameter-

ized by its probability and its chemical composition [Fox (1998, 2003); Wang and Fox (2004)]. In this work, we will validate both a moment model for the mean and variance of an inert scalar and a transported PDF model for the scalar PDF. Although the transported PDF model is not strictly required to describe mixing of inert scalars, it will be needed in our future work with reacting scalars.

Scalar Moment Transport Model

Turbulent mixing encountered in chemical process equipment is almost always inhomogeneous. The most frequently employed inert scalar statistics are the scalar mean and the scalar variance, where ϕ represents an inert scalar and ϕ' is its fluctuation. Denoting the Reynolds average velocity and the fluctuation velocity as U_j and u'_j , respectively, the transport equations of an inert scalar mean and variance are [Fox (2003)]

$$\frac{\partial \langle \phi \rangle}{\partial t} + \langle U_j \rangle \frac{\partial \langle \phi \rangle}{\partial x_j} = \Gamma \nabla^2 \langle \phi \rangle - \frac{\partial \langle u'_j \phi \rangle}{\partial x_j} \quad (2.7)$$

and

$$\frac{\partial \langle \phi'^2 \rangle}{\partial t} + \langle U_j \rangle \frac{\partial \langle \phi'^2 \rangle}{\partial x_j} = \Gamma \nabla^2 \langle \phi'^2 \rangle - \frac{\partial \langle u'_j \phi'^2 \rangle}{\partial x_j} + \mathcal{P}_\phi - \varepsilon_\phi, \quad (2.8)$$

where Γ is the molecular diffusivity and repeated indices imply summation. The scalar-variance-production term \mathcal{P}_ϕ is defined by

$$\mathcal{P}_\phi \equiv -2 \langle u'_j \phi \rangle \frac{\partial \langle \phi \rangle}{\partial x_j}. \quad (2.9)$$

Thus, Eqs. 3.6 and 3.8 have three unclosed terms: the scalar flux $\langle u'_j \phi \rangle$, the scalar-variance flux $\langle u'_j \phi'^2 \rangle$, and the scalar dissipation rate ε_ϕ , which is defined by

$$\varepsilon_\phi \equiv 2\Gamma \left\langle \frac{\partial \phi'}{\partial x_i} \frac{\partial \phi'}{\partial x_i} \right\rangle. \quad (2.10)$$

To be consistent with the $k - \varepsilon$ model used to close the Reynolds stresses, the scalar and scalar-variance fluxes in this study are closed by invoking a gradient-diffusion model [Taylor (1921)], resulting in

$$\langle u'_j \phi \rangle = -\Gamma_T \frac{\partial \langle \phi \rangle}{\partial x_j} \quad (2.11)$$

and

$$\langle u'_j \phi'^2 \rangle = -\Gamma_T \frac{\partial \langle \phi'^2 \rangle}{\partial x_j}, \quad (2.12)$$

with $\Gamma_T = \nu_T / S_{CT}$. ν_T is the eddy viscosity and S_{CT} is the turbulent Schmidt number that equals 0.7 in this study unless specified elsewhere. The scalar dissipation rate is related to the turbulent frequency ε/k by the equation [Spalding (1971)]

$$\varepsilon_\phi = C_\phi \frac{\varepsilon}{k} \langle \phi'^2 \rangle \quad (2.13)$$

with the empirical constant C_ϕ taken to be 2.0 throughout this work unless specified otherwise. The RANS code solves Eqs. 2.7 and 2.8 with closures Eqs. 2.11, 2.12 and 2.13, the accuracy of which is validated by comparing the simulated scalar mean and variance fields with PLIF data.

Transported PDF Model

Transported PDF methods simulate a transport equation for the joint PDF of the sub-grid-scale fluctuations of all concentrations [Pope (1985)]. They are the most computationally intensive of the PDF models. However, they offer the distinct advantage that chemical source terms appear in closed form and require no modeling. Therefore, transported PDF methods are powerful methods for treating the complex (finite-rate) chemistry that is often associated with minor species formation. With the development of detailed chemical kinetics based on molecular-level simulations [Tirtowidjo (1997)], transported PDF methods are an attractive macroscopic simulation technique for probing turbulence-chemistry interactions. Moreover, transported PDF simulations can be employed to validate the assumptions made in simpler closures, and to suggest alternative closures for particular kinetic schemes [Wang and Fox (2004)].

Taking the molecular transport coefficients for all species to be equal, the transport equation of the joint scalar PDF denoted by f_ϕ is [Pope (1985)]

$$\frac{\partial f_\phi}{\partial t} + \frac{\partial}{\partial x_j} (\langle U_j \rangle f_\phi) + \frac{\partial}{\partial x_j} [\langle u'_j | \psi \rangle f_\phi] = -\frac{\partial}{\partial \psi_\alpha} [\langle \Gamma \nabla^2 \phi'_\alpha | \psi \rangle f_\phi] - \frac{\partial}{\partial \psi_\alpha} \{ [\Gamma \nabla^2 \phi_\alpha + S_\alpha(\psi)] f_\phi \} \quad (2.14)$$

where ϕ and ψ represent the composition vector and the composition field, respectively. $S_\alpha(\psi)$ is the chemical source term of species α . $\langle \cdot | \psi \rangle$ denotes the Reynolds average conditioned on $\phi = \psi$. The scalar-flux term $\langle u'_j \phi' \rangle$ can be closed by the gradient-diffusion model [Pope (1985)] as

$$\langle u'_j | \psi \rangle f_\phi = -\Gamma_T \frac{\partial f_\phi}{\partial x_j} \quad (2.15)$$

The micromixing term $\langle \Gamma \nabla^2 \phi_\alpha | \psi \rangle$ may be represented by a micromixing model [Pope (1985)]. The interaction-by-exchange-with-the-mean (IEM) model [Villermaux and Devillon (1972)] is used in this study. For our case, that of an inert scalar, only one composition variable ϕ is needed, and the chemical source term $S_\alpha(\psi)$ is null. However, we retain $S_\alpha(\psi)$ for future reference.

In our Lagrangian PDF code [Raman et al. (2001, 2003, 2004)], Eq. 2.14 is expressed in terms of stochastic differential equations for “notional” particles. The position and composition of a notional particle are given by \mathbf{X}^* and ϕ^* , respectively, the particles are governed by equations [Fox (2003)]

$$d\mathbf{X}^* = [\langle \mathbf{U} \rangle (\mathbf{X}^*, t) + \nabla \Gamma_T (\mathbf{X}^*, t)] dt + \sqrt{2\Gamma_T (\mathbf{X}^*, t)} d\mathbf{W} (t) \quad (2.16)$$

and

$$d\phi^* = \frac{C_{\phi\varepsilon}}{2k} (\langle \phi \rangle (\mathbf{X}^*, t) - \phi^*) dt + \mathbf{S} (\phi^*) dt, \quad (2.17)$$

where $d\mathbf{W} (t)$ is a multi-variate Wiener process, and $\mathbf{S} (\phi^*)$ is the chemical source term. $\langle \mathbf{U} \rangle (\mathbf{X}^*, t)$ and $\langle \phi \rangle (\mathbf{X}^*, t)$ are the mean velocity and the estimated scalar mean at the particle location. The scalar mean and variance are estimated from the compositions of the particles. In the non-reacting flow investigated in this study, $\mathbf{S} (\phi^*)$ is null. The turbulence statistics appearing in Eqs. 2.16 and 2.17 are taken from the RANS code. Details on the coupling between the flow field and the particle fields in the Lagrangian PDF code can be found elsewhere [Fox (2003)]. The turbulent transport closure defined by Eq. 2.15 can be validated by agreement of the scalar mean and variance predicted by the PDF code with PLIF data.

Simulation Conditions

The performance of the confined planar-jet reactor was simulated using the RANS and PDF models described above. Since no chemical reactions occur, the scalar is inert. The distribution of the experimental data was found to be slightly asymmetric with respect to the centerline due to the jet growing slightly towards one of the walls of the test section. To provide inlet boundary conditions for the simulations, the experimental data of mean velocity and turbulent kinetic energy at the entrance plane of the jet were made symmetric with respect to $y/d = 0$ by averaging and then interpolated linearly between data points. The PIV data for the mean velocity and turbulent kinetic energy at the jet exit and the corresponding inlet boundary conditions for the RANS code are shown in Fig. 2.4. In this study, the PIV data for the turbulent kinetic energy were derived from the streamwise and transverse velocity fluctuations, u' , v' , through Eq. 2.18

$$k = \frac{\langle u'^2 \rangle + \langle v'^2 \rangle}{2}. \quad (2.18)$$

More details can be found in the discussion of the CFD predictions for turbulent kinetic energy. The inlet values of dissipation rate were estimated by

$$\varepsilon = A \frac{k^{3/2}}{l_m}, \quad (2.19)$$

where l_m is a characteristic length scale. The length scales l_m were set equal to 0.0035 m for the inner jet and 0.002 m for the outer jets after trial and error investigation that produced a turbulent kinetic energy at $x/d = 0.5$, which agreed with the PIV measurements. Note that these values are smaller than the jet widths, as expected, adopting the value suggested by Antonia, et al. [Antonia et al. (1980)]. By comparing Eqs. 2.2 and 2.19, it is known that $l_m/l = (3/2)^{3/2}$.

Because the flow statistics at the centerline of the channel are only slightly affected by the front and back walls, all simulations were performed on a two-dimensional grid by neglecting gradients in the spanwise direction. An 81×121 Cartesian grid was generated for the computational domain. The grid has non-uniform cells with denser grid points near stream

interfaces and walls to capture more details associated with sharp gradients. The grid was chosen fine enough to ensure a grid-independent solution. However, its resolution is lower than the spatial resolution in the PIV/PLIF measurements. Thus, the inlet boundary conditions shown in Fig. 2.4 effectively cut off the high gradients measured in the shear layers due to the difference in resolution. This was found to have no impact on the predicted flow statistics. A fixed time step that equals 0.005 s was used in the transported PDF code.

Results and Discussion

A typical velocity field from PIV measurements is shown in Fig. jet instant velocity. To aid in the visualization of turbulent structures, a convective velocity of 0.75 m/s has been subtracted from each vector in this figure. As a reminder, the coordinate system used in Fig. 2.5 is such that the tips of the splitter plates are located at $x = 0$ and $y = \pm 10$, and the centerline between two side walls is along $y = 0$. Similarly, Fig. 2.6 shows an instantaneous concentration field. The contour levels represent mixture fraction, which is the concentration normalized by the concentration of the dye in the inner feed stream C_0 . In Figs. 2.7-2.12, $\langle U \rangle$ and $\langle V \rangle$ denote the streamwise and transverse mean velocity components, respectively.

Experimentally Measured Mean Velocities and Reynolds Stresses

The ensemble averaged streamwise velocity profiles for six representative downstream locations are shown in Fig. 2.7. The mean velocity components are normalized by $U_c = 0.5$ m/s, which is the difference between the inlet free-stream velocities of the center and side streams. The y -axis has been normalized by the inlet jet width, $d = 20$ mm. This normalization of the transverse coordinate is used throughout the presented work. As Fig. 2.7 shows, at the inlet level ($x/d = 0$), the velocity profile is fairly symmetric with two mixing layers growing from the tips of the splitter plates, and this symmetry is maintained in each of the downstream velocity profiles. However, these mixing layers are short lived, and they quickly grow together as the flow convects downstream. Indeed, the potential core in the center jet has completely disappeared at $x/d = 4.5$. As the flow progresses downstream, the potential cores in the outer

streams also disappear, and the flow continues its development towards channel flow.

Reynolds stress profiles, normalized by U_c^2 , for the same six locations are shown in Figs. 2.8-2.10. At all six measurement locations, $\langle u'u' \rangle$ (Fig. 2.8) is approximately twice as large as the $\langle v'v' \rangle$ (Fig. 2.9), and both are approximately symmetric about the jet centerline. The stresses are highest just downstream of the tip of the splitter plates, just after the incoming boundary layers have merged to form the initial mixing layers, and the stresses decay as the mixing layers grow. After the two mixing layers have grown together, the peak values remain almost constant while the valley between the two peaks fills up. However, the two peaks in the Reynolds stress profiles remain distinct even at the farthest downstream measurement location, $x/d = 15$. Also note that because of the boundary layers developing along the sidewalls of the test section, the values of the Reynolds normal stresses increase as the observation point moves towards the wall.

The Reynolds shear stress, $\langle u'v' \rangle$, shown in Fig. 2.10, is asymmetric around the centerline, positive where the mean flow shear stress is negative, and negative where the mean flow shear stress is positive. Along the centerline of the reactor, which is a plane of symmetry, the Reynolds shear stress is zero. Due to the turbulent boundary layers, the values of shear stress in the regions near walls are nonzero. Moreover, the boundary layers developing along both sides of the splitter plate cause the sign change of Reynolds shear stress in the mixing layers at locations near the tips (such as $x/d = 0$ and $x/d = 1$). The peak Reynolds shear stress is highest just downstream of the splitter plate tips, and decreases with increasing downstream distances.

CFD Predictions for Mean Velocity

The mean streamwise velocity predicted by the RANS code with the two-layer $k - \varepsilon$ model is compared with PIV measurements in Fig. 2.11. Comparisons are shown for downstream locations $x/d = 4.5, 7.5$ and 15 . The comparisons are good, although the spreading rate of the jet is slightly lower than that measured by PIV, and this characteristic becomes more pronounced as the downstream distance increases. This smaller spreading rate in the RANS

calculations is most likely due to a lower diffusion rate of the turbulent kinetic energy, as discussed in the next section.

CFD Predictions for Turbulent Kinetic Energy

The PIV velocity fields are 2-D measurements, containing only streamwise and transverse velocity components. In order to obtain the turbulent kinetic energy from the 2-D PIV measurements, the spanwise (that is, out-of-plane) velocity fluctuation must be estimated based on the measured x - and y - fluctuations. The spanwise fluctuation was assumed to be equal in magnitude to the cross-stream fluctuation (Eq. 2.18). This assumption is expected to be valid near the inlet since the flow there resembles a pair of mixing layers, and turbulence in mixing layers has this characteristic [Pope (2000)]. Fully developed turbulent channel flow also has this characteristic, so the assumption of comparable transverse and spanwise velocity fluctuations is expected to yield reasonable results. Also recall that PIV measures a filtered velocity field due to the measurement volume being larger than the Kolmogorov scale. However, since the larger energy containing eddies are fully resolved, errors from the filtered velocity field should not significantly affect the measured turbulent kinetic energy.

Turbulent kinetic energy predicted by the RANS code with a two-layer $k - \varepsilon$ model is compared with PIV measurements in Fig. 2.12 for downstream locations $x/d = 1, 4.5, 7.5$ and 15. The RANS code predicts a slightly higher turbulent kinetic energy than that measured by PIV, but in general, the agreement between the two is excellent at all downstream locations.

Experimentally Measured Scalar Mean and Scalar Variance

Figure 2.13 shows the transverse profiles of the ensemble-averaged mixture fraction across the channel at four downstream locations: $x/d = 1, 4.5, 7.5,$ and 15. The mean mixture fraction at $x/d = 1$ is very nearly a top-hat function, with all of the dye located in the center stream. However, as the downstream distance increases, the mean mixture fraction in the center stream decreases and the mean mixture fractions in the outer streams increase because of mass transport of the dye due to both turbulent mixing and molecular diffusion. As in the

mean velocity profiles, the plots are slightly asymmetric due to the jet growing slightly towards one of the walls of the test section.

The mixture-fraction variance is shown in Fig. 2.14. Note that as the mixing layers develop and begin to grow into one another, the peaks of the variance move towards the walls. Also, the experimentally measured peak value of the variance initially increases with increasing distance from the tip of the splitter plate, but after $x/d = 7.5$, it begins to decrease. Since a fully mixed fluid would have a mixture-fraction variance of zero, this behavior after $x/d = 7.5$ is expected. Note also that just as for the Reynolds stresses, two distinct peaks remain in the plots of mixture-fraction variance even at the farthest downstream measurement location.

CFD Predictions for Mean Mixture Fraction

The mean mixture-fraction fields predicted by the RANS and transported PDF codes are compared with the experimental results at various downstream locations in Fig. 2.13, and they agree quite well with the PLIF data. The results indicate that the gradient-diffusion model (Eqs. 2.11 and 2.15) accurately predicts the scalar flux for this flow geometry. The lower spreading rate of the mean mixture fraction in the simulations suggest that the turbulent Schmidt number required in Eqs. 2.11 and 2.15 is slightly less than the typical value of 0.7. By adopting $Sc_T = 0.5$ the agreement between the CFD simulations and PLIF data improves as shown in Fig. 2.13.

CFD Predictions for Mixture-Fraction Variance

The profiles of the mixture-fraction variance as predicted by the RANS and the transported PDF codes are compared with experimental data at various downstream locations in Fig. 2.14. The RANS code and the PDF code yield similar results except at $x/d = 1$, where the PDF code predicts a higher variance than the RANS code. In theory, grid-independent solutions for the mean and variance should be exactly the same for both codes. Thus, the higher values observed near the inlet with the PDF code are an indication that a much smaller time step is required in that region where turbulent mixing is slow. In general, both codes predict a higher

mixture-fraction variance in the shear layers, where the variance peaks in value, than was measured experimentally. As seen in Fig. 2.14, the agreement cannot be improved by reducing the turbulent Schmidt number to 0.5. Instead, due to the higher turbulent diffusivity, the mixture-fraction variance at each streamwise position reaches a maximum value that is even higher than that given by $Sc_T = 0.7$ at a cross-section position that is further from the centerline. If the scalar dissipation term, ε_ϕ , is set to zero (this is equivalent to turning off the micromixing model in the PDF code), the analytical solution to Eq. scalar variance becomes

$$\langle \phi'^2 \rangle = (1 - \langle \phi \rangle) \langle \phi \rangle. \quad (2.20)$$

The numerical simulation results show (Fig. 2.15) that the PDF code and the RANS code predict this analytical solution accurately. Thus, the scalar-variance flux (Eq. 2.12) was correctly implemented in the RANS code and the grid density at downstream locations was fine enough to ensure that both codes predict consistent results.

Figure 2.13 shows that the mixture-fraction mean (and thus the production of mixture-fraction variance defined by Eq. 2.9) is accurately predicted. Therefore, the discrepancies of the model predictions and experimental results observed in Fig. 2.14 indicate either inaccuracy in the closure for the scalar dissipation rate (Eq. 2.13), which is determined by the mixing timescale k/ε , or experimental limitations (due to finite resolution of PLIF at high Sc), or both. Near walls, $k \sim O(y^2)$ and $\varepsilon \sim O(1)$ as $y \rightarrow 0$. This results in a very small mixing timescale and thus a scalar dissipation rate that is so large that the mixture-fraction variance is forced to zero in the near-wall regions. Therefore, in the near-wall regions the predicted mixture-fraction variance shows insufficient diffusion. In fact, Eq. 2.13 is actually a model for the scalar spectral energy transfer rate through the inertial-convective sub-range in homogeneous turbulence, and thus cannot be expected to be accurate in the near-wall regions.

For inhomogeneous turbulence, it can be expected that ε_ϕ depends on the degree of turbulent anisotropy and the mean shear rate. Near the reactor entrance ($x/d = 1$) where the turbulence is neither fully developed nor isotropic, this closure cannot represent the entire energy transfer rate from large to small scales. Nevertheless, this closure is valid in fully developed turbulence when the dissipation scales are in spectral equilibrium with the energy-

containing scales. With the development of the flow, the performance of the model improves gradually resulting in better agreement of the predicted variance and PLIF data (Figs. 2.14(b) and (c)). The insufficient diffusion at near-wall regions is overshadowed by the more uniform scalar concentration indicated by the PLIF data at those downstream locations. At $x/d = 15$, where the non-zero near-wall mixture-fraction variance shown by PLIF data indicates that the scalar concentration is not uniform near walls, the underestimation by the model is significant. Therefore the performance of the model does not improve in the near-wall region at downstream locations (Fig. 2.14(d)). Further work will be required to improve the closure for the scalar dissipation rate for this region.

Another factor that must be considered is that the PLIF measurements underestimate the scalar variance due to the spatial resolution being insufficient to resolve the smallest mixing scales. By definition, the scalar variance can be found directly from the scalar energy spectrum $E_\phi(\kappa, t)$ by integrating over the space of the wavenumber κ :

$$\langle \phi'^2 \rangle = \int_0^\infty E_\phi(\kappa) d\kappa. \quad (2.21)$$

The spatial resolution of the PLIF measurements is limited by the thickness of the laser sheet. The laser-sheet thickness represented by L^* ($L^* = 5 \times 10^{-4}$ m in this study) determines a cut-off wavenumber

$$\kappa^* = \frac{1}{L^*}. \quad (2.22)$$

Consequently, the scalar variance measured by PLIF decreases to

$$\langle \phi'^2 \rangle^* = \int_0^{\kappa^*} E_\phi(\kappa) d\kappa. \quad (2.23)$$

Using the model scalar spectrum [Fox (2003)], Table 2.1 shows the percentage of scalar variance missed by the PLIF measurements, defined as $1 - \langle \phi'^2 \rangle^* / \langle \phi'^2 \rangle$, at each downstream location. The missing variance decreases from 12.68% at $x/d = 1$, to about 5.98% at the furthest downstream distance where the Kolmogorov scale of the turbulence is largest, and thus less of the scalar energy spectrum is cut-off. This may account for some of the discrepancies between the experimental results and the simulations.

Nevertheless, even after accounting for the PLIF resolution, Fig. 2.14 indicates that the missing mixture-fraction variance is larger than expected. For example, the maximum variance predicted and measured at $x/d = 4.5$ are 0.048 and 0.035, respectively. Thus, the scalar variance missed by the PLIF measurement is 27%, rather than 9.36%, if the exact scalar variance is 0.048. We are therefore motivated to investigate the effect of C_ϕ on the mixture-fraction variance prediction. From direct numerical simulations [Yeung et al. (2002)], it is known that C_ϕ can vary in the range of 2.0-2.5 for inert scalar mixing in stationary turbulence. Moreover, at large Reynolds numbers, C_ϕ will approach a Schmidt number-independent limiting value of 2.43 [Fox (2003)], which is the ratio of the Kolmogorov and the Obukhov-Corrsion constants. By taking $C_\phi = 2.5$ the predicted mixture-fraction variance (Fig. 2.16) matches the PLIF data much better at all downstream locations except for $x/d = 1$. This result is quite interesting because it is usually assumed that C_ϕ in liquid-phase flows should be smaller than in gas-phase flows due to the larger Schmidt number effects [Fox (2003)]. Under these flow conditions, however, it appears that the Reynolds number is high enough to make Schmidt-number effects negligible.

Dissipation Rate

One of the primary advantages of PIV over pointwise velocity measurement techniques is the capability of measuring vorticity and rate-of-strain fields [Adrian (1991)]. This enables us to evaluate the dissipation rate in the flow field. However, in 2D-PIV measurements, the out-of-plane component of velocity is not measured. Therefore only four terms of velocity gradient, $\partial\bar{U}/\partial x$, $\partial\bar{U}/\partial y$, $\partial\bar{V}/\partial x$ and $\partial\bar{V}/\partial y$, can be computed directly. Another term, $\partial\bar{W}/\partial z$, may also be determined by using the incompressible continuity equation. Here, \bar{U} , \bar{V} and \bar{W} are the x , y and z components of filtered velocity. Since the other four terms are still missing, some researchers have computed only the so-called 2-D dissipation rate [Saarenrinne and Piirto (2000); Tsurikov and Clemens (2002)]. To estimate the turbulence energy dissipation rate using 2D-PIV data, Sharp et al. [Sharp et al. (1998)] assumed that the unknown terms were statistically isotropic and thus derivable from the known ones. For a complicated 3-D

flow in a stirred vessel, Sheng et al. [Sheng et al. (2000)] applied a similar assumption that approximated the dissipation rate by multiplying the sum of the known components of Eq. 2.3 by a factor of $9/5$. In the present study, two methods were used to estimate the dissipation rate: 1) Sheng's method; 2) assuming $w = v$ and $\partial/\partial z = \partial/\partial y$ to obtain nine terms. Because of the nature of the flow (i.e., shear layers and wall-bounded flow), we expect that the second method most closely corresponds to our conditions.

The results of the estimations at five downstream locations can be seen in Fig. 2.17. Notice that the dissipation rates calculated using Sheng's method are smaller than those from the second method. However, both methods show that the distribution of the dissipation rate in the reactor is highly inhomogeneous. These graphs also indicate the general trend that the profile of dissipation rate becomes more uniform in the y -direction as the observation location moves downstream, and the peak values in dissipation decay very quickly at positions nearer the inlet. In comparing with the distributions of energy dissipation rate and turbulent kinetic energy, it is also seen that regions of high values of these quantities coincide, implying a strong correlation between these two properties. The dissipation rate predicted by the $k - \varepsilon$ model is compared with that estimated from PIV measurements in Fig. 2.18. The predicted dissipation rate agrees better with that calculated using nine terms (that is, method 2) than with that found using Sheng's method.

Conclusions

In the present study, velocity and concentration measurements were made for turbulent mixing in a confined planar-jet reactor using PIV and PLIF techniques. The measurements were carried out at six downstream locations with a Reynolds number of 50,000 based on the distance between sidewalls. Statistics of mean velocity, Reynolds stresses, turbulent kinetic energy, mixture-fraction mean and mixture-fraction variance were calculated. It was observed that two mixing layers grow symmetrically about the centerline of the reactor from the tips of the splitter plates, but these merged together very quickly, and the flow continued its development towards channel flow. It was also noticed that the values of turbulent kinetic

energy and Reynolds stress are nonzero in regions near the walls, which indicates that unlike free jets, the boundary layer developing along sidewalls in the confined jet plays a significant role in the mixing, especially after the potential cores in the outer streams disappear.

The planar velocity data from PIV measurements were also used for estimating the turbulence dissipation rate by computing the Reynolds-averaged SGS dissipation rate. Because the out of plane component of velocity fluctuations is unachievable in the present study, some terms of the velocity gradient were not measured. Therefore, two methods were tested to approximate the missing terms using known ones. The results of the dissipation rate from the two methods were compared and showed that the dissipation rate decayed rapidly close to the tips of the splitter plates. It was noted that the distribution of the dissipation rate was symmetric around the centerline and inhomogeneous in the reactor. As expected, the distribution of the dissipation rate also suggested strong correlation with the turbulent kinetic energy.

CFD models were validated against the experiments by comparing computed mean velocity and turbulence fields, and the mixture-fraction mean and variance with PIV/PLIF data. The Reynolds stresses were closed by a two-layer $k - \varepsilon$ model that predicted the turbulent kinetic energy and dissipation rate successfully with reasonable computational cost even in near-wall regions. The scalar fluxes were closed by gradient-diffusion models. The accurately computed mixture-fraction mean indicates that the scalar flux was well represented by the gradient-diffusion model. The analytical solution to the transport equation of mixture-fraction variance with no dissipation was predicted exactly by both scalar transport models, illustrating that the solutions were grid independent. The scalar dissipation rate was over-predicted by the equilibrium closure in near-wall regions, suggesting that this quantity might be better approximated by solving its transport equation. Elsewhere, ε_ϕ was underpredicted by the equilibrium model with $C_\phi = 2$, but well predicted with $C_\phi = 2.5$. In general, the overall agreement between the CFD models and the experimental data is excellent for this rather complex flow.

Table 2.1 Estimated Error of PLIF Variance Measurements

x/d	1	4.5	7.5	12	15
Error(%)	12.68	9.36	8.01	7.75	5.98

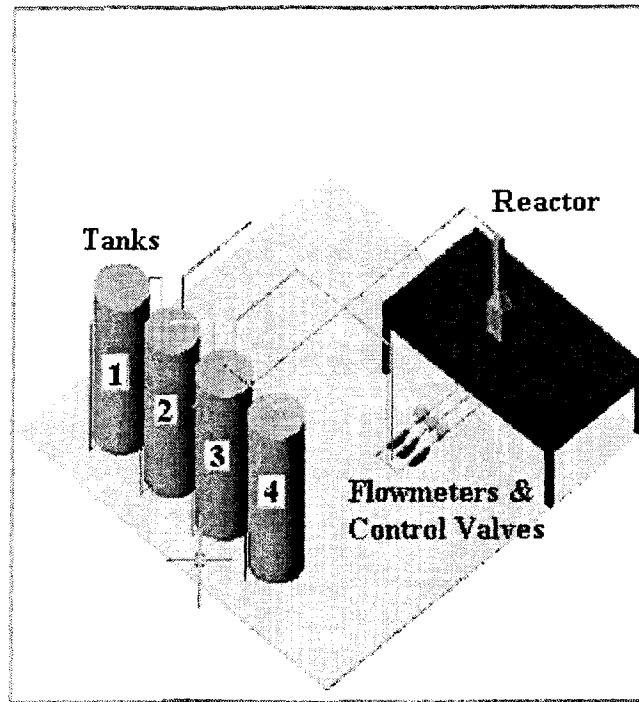


Figure 2.1 Flow facility used in the PIV and PLIF experiments.

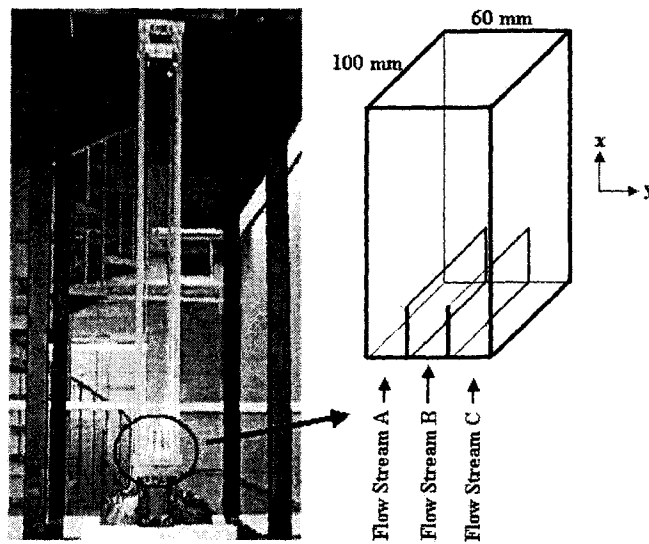


Figure 2.2 Confined planar-jet test section.

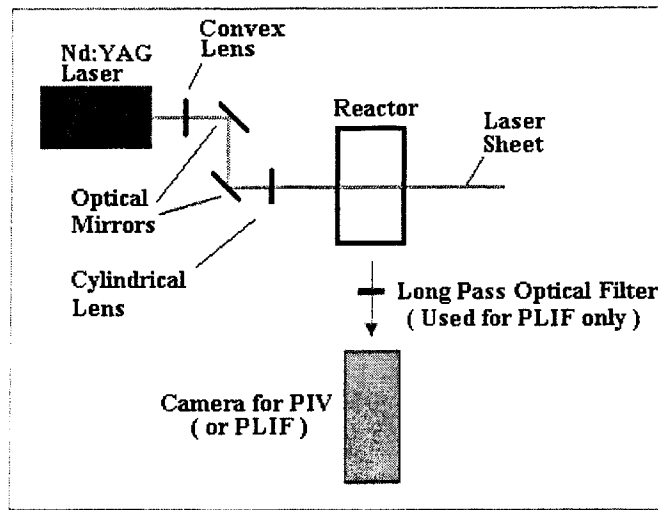


Figure 2.3 Top views of the optical setup for the PIV and PLIF experiments.

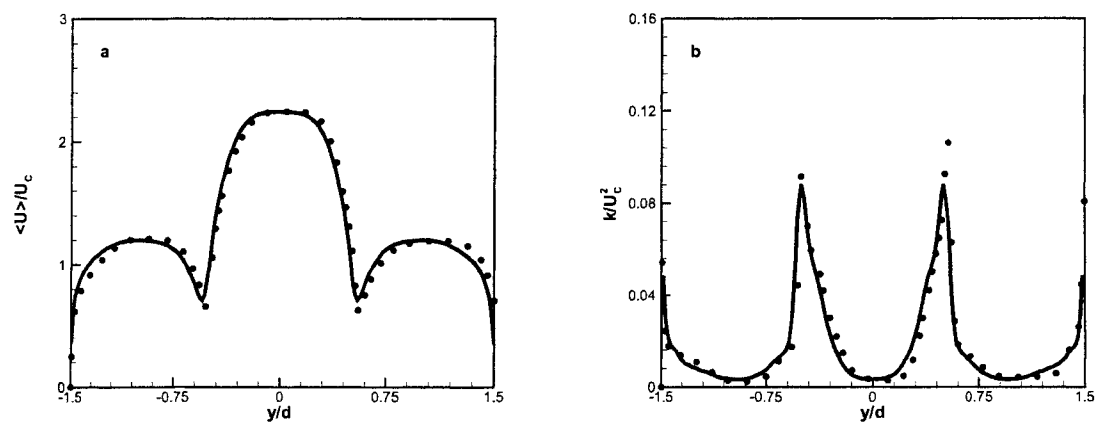


Figure 2.4 (a) Mean streamwise velocity and (b) turbulent kinetic energy at the entrance plane of the confined planar jet. —, Simulations; •, PIV data.

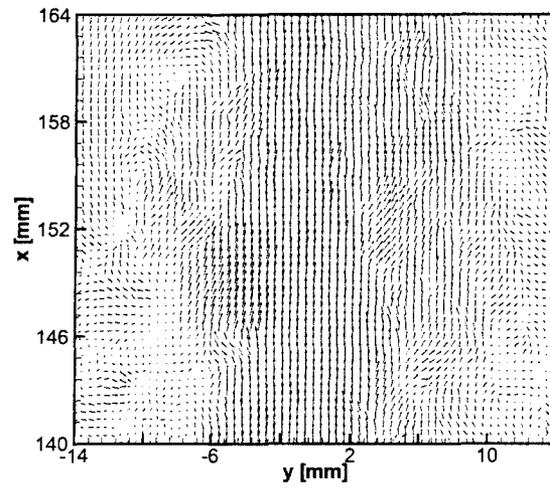


Figure 2.5 Sample instantaneous velocity field.

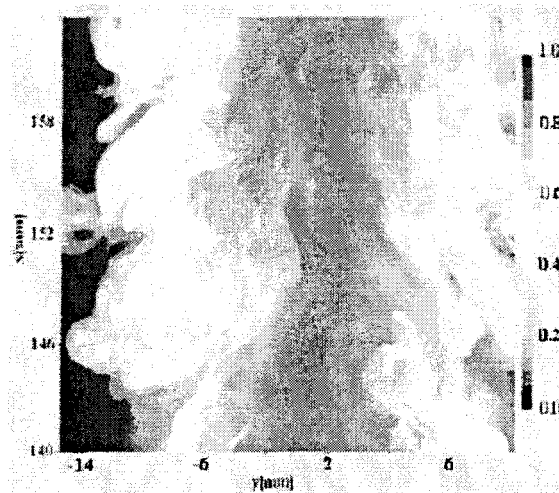


Figure 2.6 Sample instantaneous concentration field.

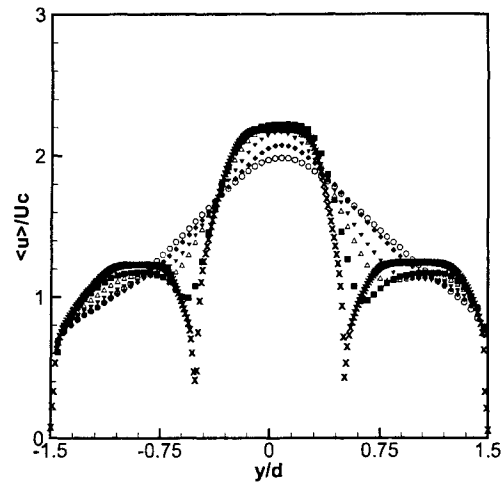


Figure 2.7 Normalized mean streamwise velocity at various downstream locations as measured by PIV. \times , $x/d = 0$; \blacksquare , $x/d = 1$; Δ , $x/d = 4.5$; \blacktriangledown , $x/d = 7.5$; \blacklozenge , $x/d = 12$; \circ , $x/d = 15$.

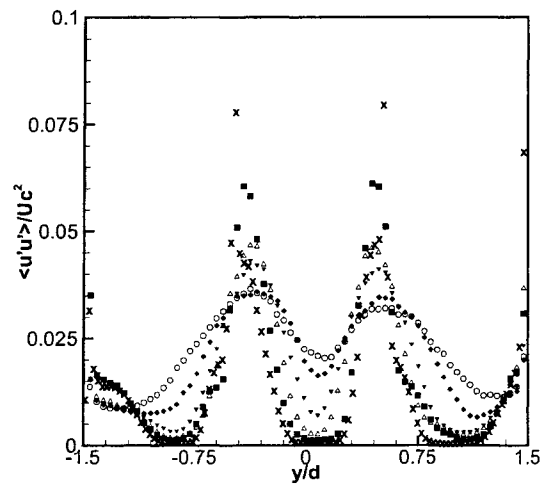


Figure 2.8 Streamwise Reynolds normal stress at various downstream locations as measured by PIV. \times , $x/d = 0$; \blacksquare , $x/d = 1$; Δ , $x/d = 4.5$; \blacktriangledown , $x/d = 7.5$; \blacklozenge , $x/d = 12$; \circ , $x/d = 15$.

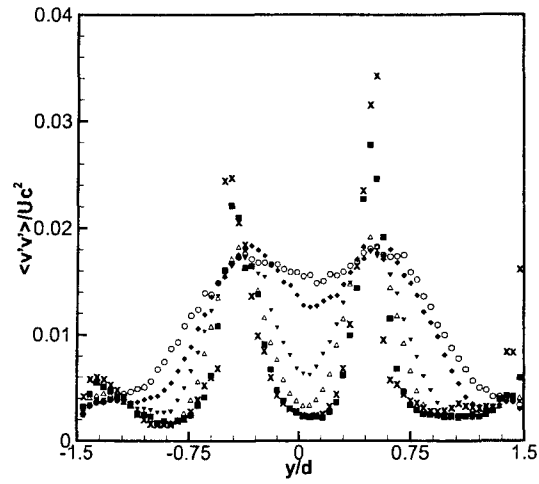


Figure 2.9 Cross-stream Reynolds normal stress at various downstream locations as measured by PIV. \times , $x/d = 0$; \blacksquare , $x/d = 1$; Δ , $x/d = 4.5$; \blacktriangledown , $x/d = 7.5$; \blacklozenge , $x/d = 12$; \circ , $x/d = 15$.

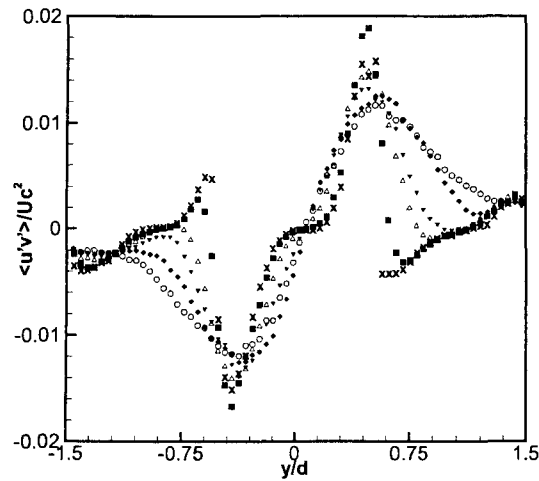


Figure 2.10 Reynolds shear stress at various downstream locations as measured by PIV. \times , $x/d = 0$; \blacksquare , $x/d = 1$; Δ , $x/d = 4.5$; \blacktriangledown , $x/d = 7.5$; \blacklozenge , $x/d = 12$; \circ , $x/d = 15$.

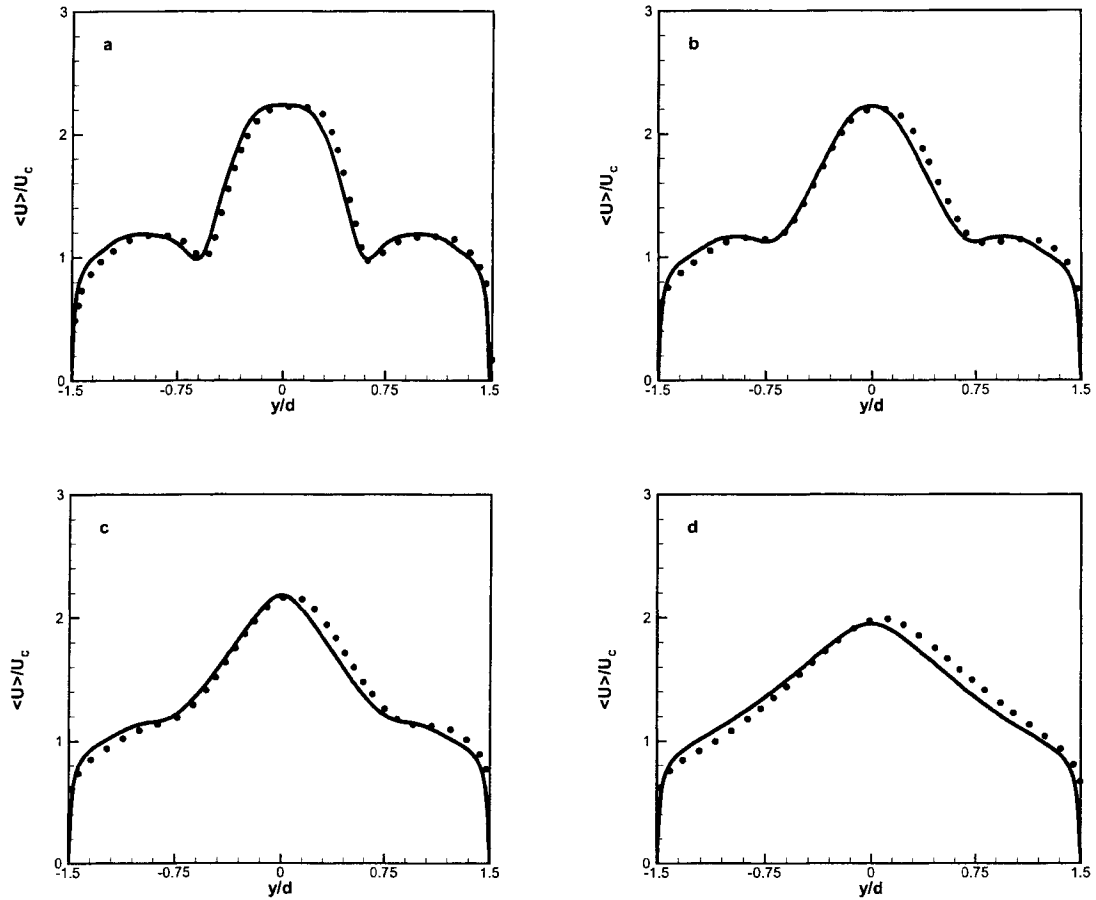


Figure 2.11 Comparison of the mean streamwise velocity profiles measured by PIV (symbols) and calculated from the RANS code (solid line) for (a) $x/d = 1$, (b) $x/d = 4.5$, (c) $x/d = 7.5$, (d) $x/d = 15$.

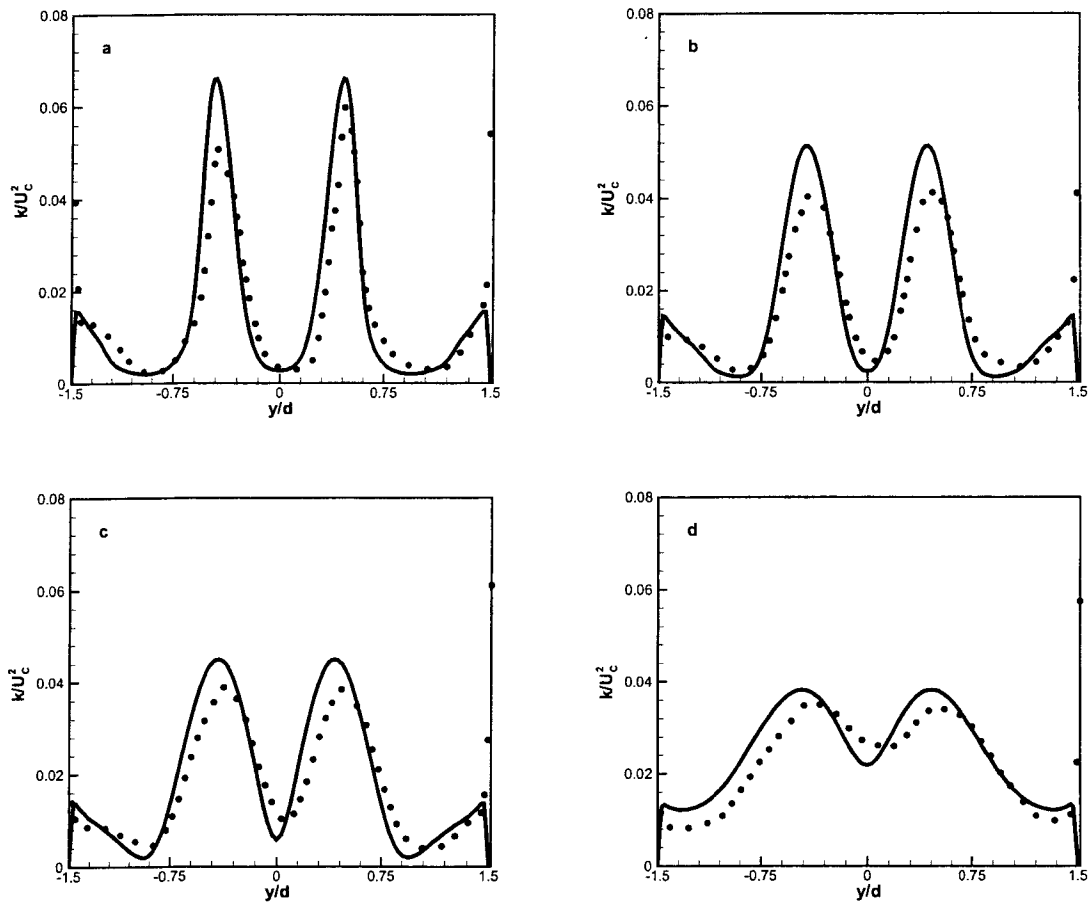


Figure 2.12 Comparison of the turbulent kinetic energy profiles measured by PIV (\bullet) and calculated from RANS code ($—$) for (a) $x/d = 1$, (b) $x/d = 4.5$, (c) $x/d = 7.5$, (d) $x/d = 15$.

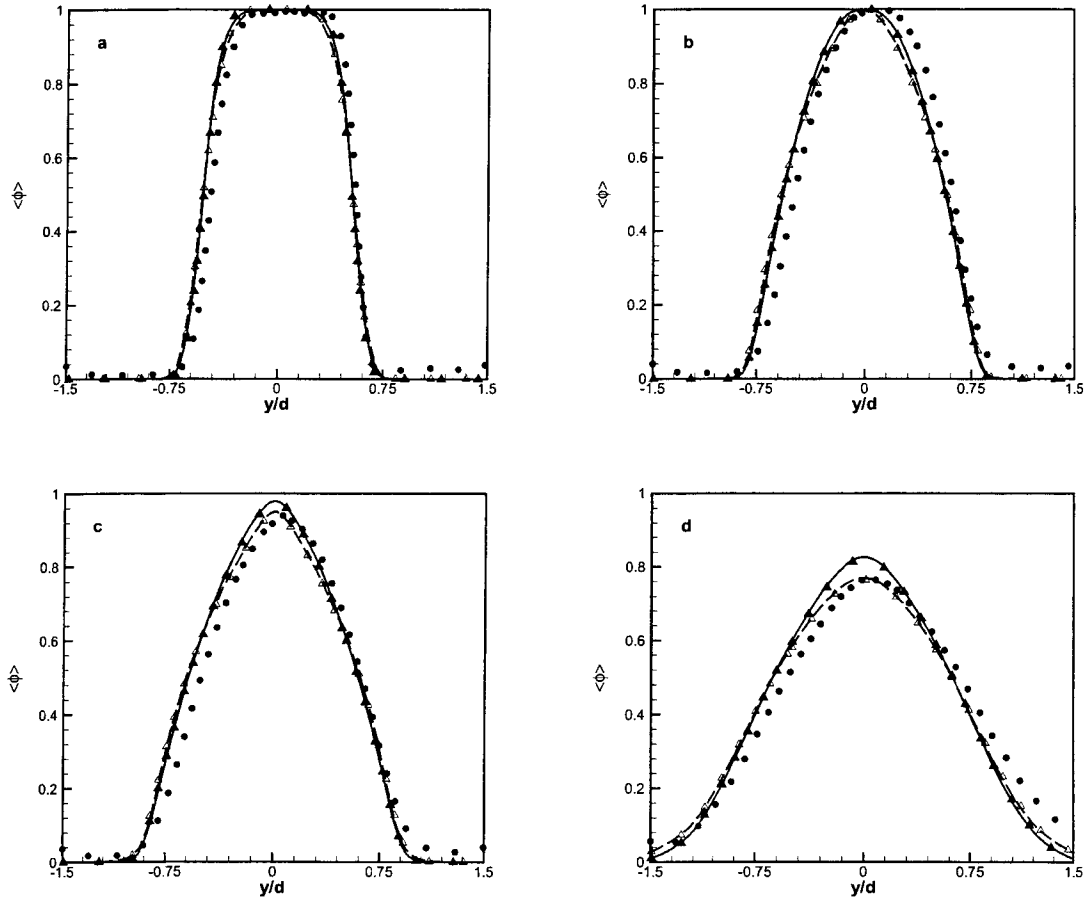


Figure 2.13 Comparison of mean mixture fraction profiles for (a) $x/d = 1$, (b) $x/d = 4.5$, (c) $x/d = 7.5$, (d) $x/d = 15$. \bullet , PLIF; —, RANS, $Sc_T = 0.7$; ---, RANS, $Sc_T = 0.5$; \blacktriangle , PDF, $Sc_T = 0.7$; \triangle , PDF, $Sc_T = 0.5$.

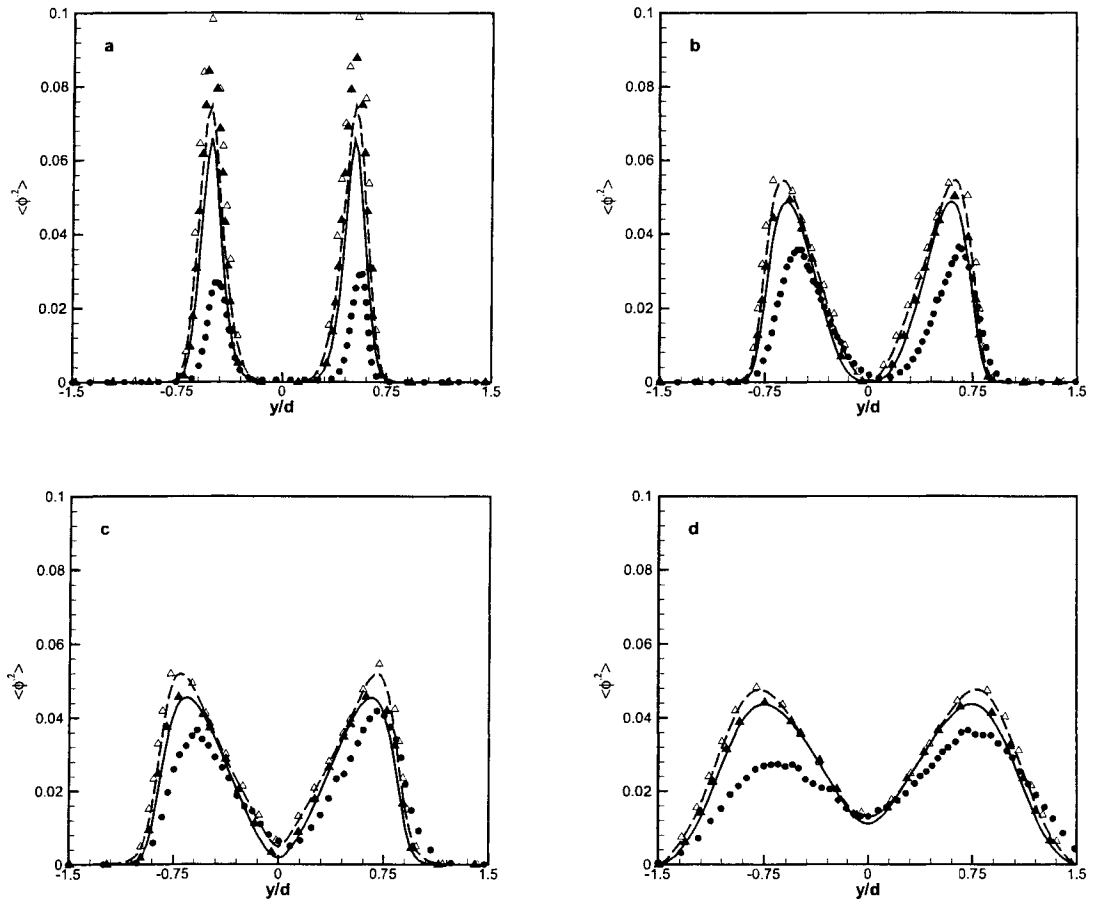


Figure 2.14 Comparison of mixture-fraction variance profiles (a) $x/d = 1$, (b) $x/d = 4.5$, (c) $x/d = 7.5$, (d) $x/d = 15$. \bullet , PLIF; —, RANS, $Sc_T = 0.7$; ---, RANS, $Sc_T = 0.5$; \blacktriangle , PDF, $Sc_T = 0.7$; \triangle , PDF, $Sc_T = 0.5$.

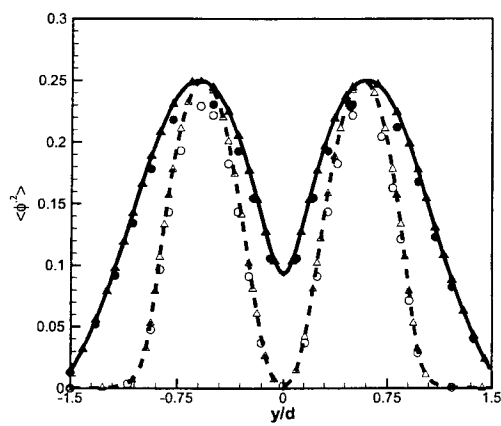


Figure 2.15 Comparison of analytical solution to mixture-fraction variance and calculated mixture-fraction variance. - - -, Analytical solution; \circ , RNAS; \triangle , PDF at $x/d = 7.5$; $-\bullet-$, analytical solution; \bullet , RANS; \blacktriangle , PDF at $x/d = 15$.

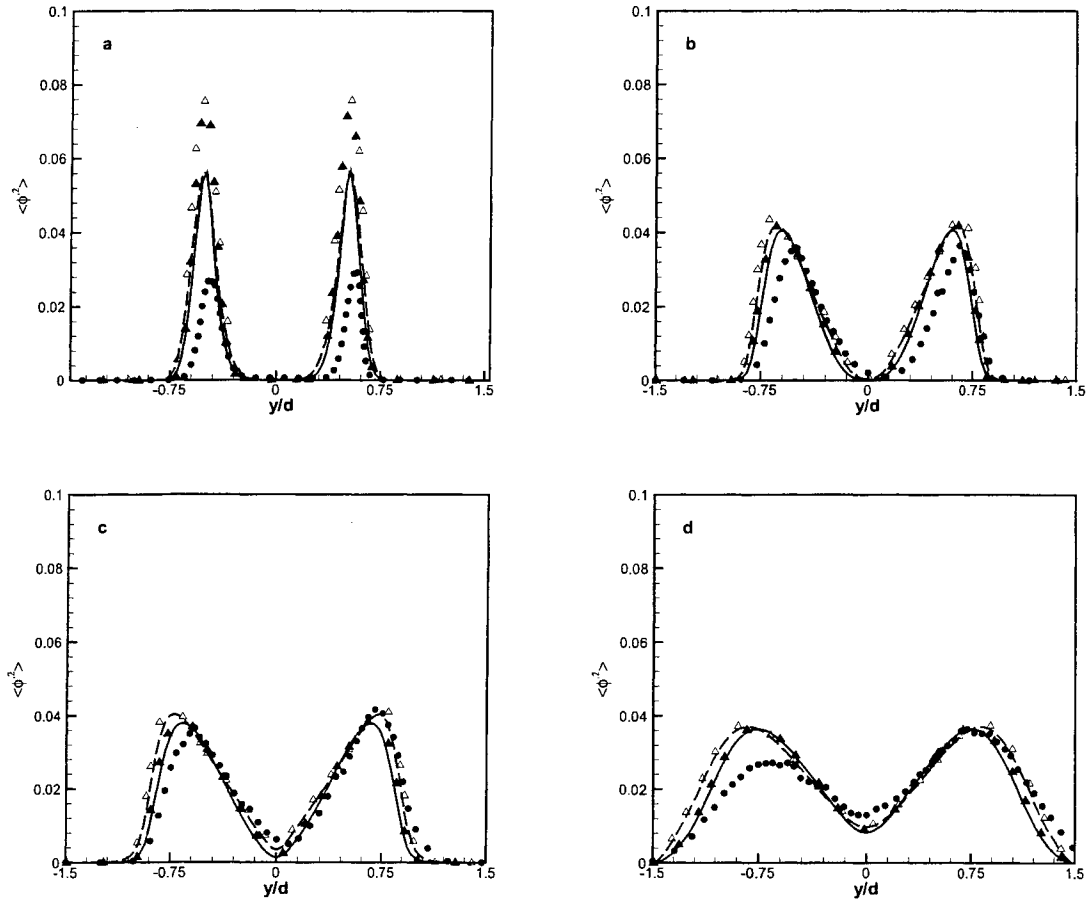


Figure 2.16 Effect of C_ϕ ($C_\phi = 2.5$) on the prediction of mixture-fraction variance profiles at (a) $x/d = 1$, (b) $x/d = 4.5$, (c) $x/d = 7.5$, (d) $x/d = 15$. \bullet , PLIF; —, RANS, $Sc_T = 0.7$; - - -, RANS, $Sc_T = 0.5$; \blacktriangle , PDF, $Sc_T = 0.7$; \triangle , PDF, $Sc_T = 0.5$.

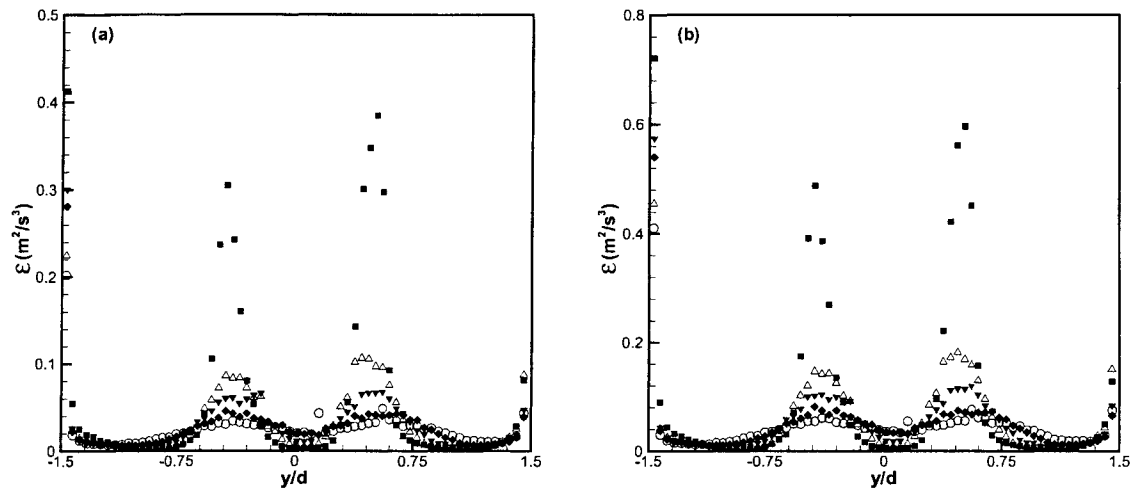


Figure 2.17 Turbulence dissipation rate at various downstream locations measured by PIV: (a) estimated by Sheng's method; (b) estimated with nine terms. \blacksquare , $x/d = 1$; \triangle , $x/d = 4.5$; \blacktriangledown , $x/d = 7.5$; \blacklozenge , $x/d = 12$; \circ , $x/d = 15$.

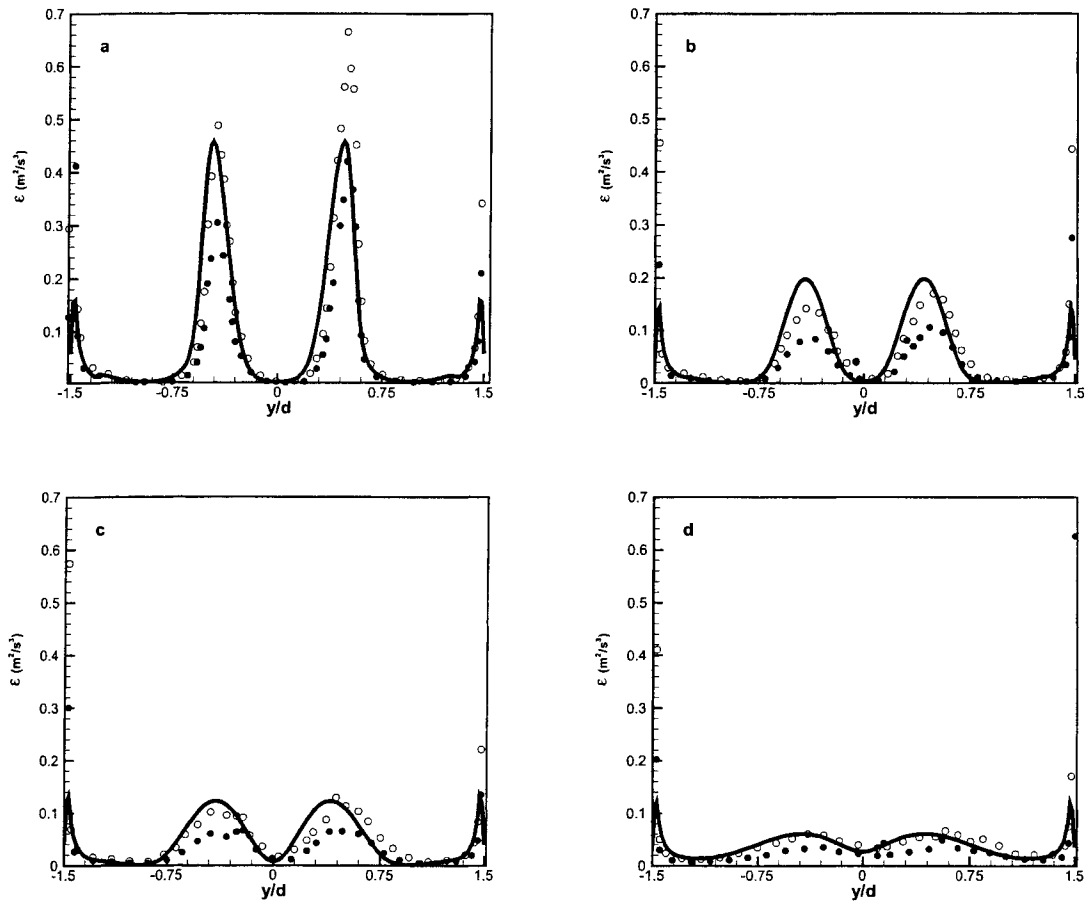


Figure 2.18 Comparison of dissipation profiles measured Sheng's method (\bullet), method 2 (\circ), and calculated from the RANS code ($—$) for (a) $x/d = 1$, (b) $x/d = 4.5$, (c) $x/d = 7.5$, (d) $x/d = 15$.

CHAPTER 3 TURBULENT MIXING IN A CONFINED RECTANGULAR WAKE

A paper submitted to *Chemical Engineering Science*

Ying Liu, Hua Feng, Michael G. Olsen, Rodney O. Fox and James C. Hill

(Ying Liu is responsible for the simulation work in this paper)

Abstract

Liquid-phase turbulent transport in a confined rectangular wake was investigated for a Reynolds number of 37,500 based on bulk velocity and the hydraulic diameter of the test section and a Schmidt number of 1,250 using particle image velocimetry (PIV) and planar laser-induced fluorescence (PLIF). The velocity and concentration field data were analyzed for flow statistics such as the mean velocity, Reynolds stresses, turbulent kinetic energy, turbulent dissipation rate, mixture-fraction mean, mixture-fraction variance and one-point composition PDF. Computational fluid dynamics (CFD) models, including a two-layer $k - \varepsilon$ turbulence model, a scalar gradient-diffusion model and a scalar dissipation rate model were validated against PIV and PLIF data collected at six downstream locations. Low-Reynolds-number effects on turbulent transport were taken into consideration through the mechanical-to-scalar time-scale ratio. The experimental and computational results were found to be in satisfactory agreement.

Introduction

Turbulent mixing is crucial in processes in the chemical process industry that require rapid mixing and transport of species, momentum and energy. Thus, it is imperative to have a

detailed understanding of turbulent mixing for the design and optimization of chemical reactors. Although computational fluid dynamics (CFD) models have great potential for studying turbulent flows and designing reactors, these models need to be validated against experimental data to avoid costly design mistakes on scale up. Therefore, experimental studies of mixing in turbulent shear flows (*e.g.*, wakes, jets and mixing layers) are of great importance not only in advancing turbulence theory, but also in the development and validation of CFD models. The primary objective of the work presented here is to obtain detailed experimental data for both the velocity field and concentration field in a liquid-phase turbulent confined, rectangular wake and to use these data to validate CFD models.

A wake is formed when a uniform stream flows over an obstacle, resulting in the formation of a region downstream with a velocity deficit. The flow in a wake may be divided into three regions: a near-wake, an intermediate wake and a far wake [Kiyama and Matsumura (1985); Tritton (1988)], although it is difficult to quantify the boundaries between these regions since they depend on many parameters [Mi et al. (2004)]. The near wake is a critical region as it determines the dominant instability in the flow [Triantafyllou et al. (1986); Unal and Rockwell (1988); Ma et al. (2000)]. Due to the difficulty of obtaining accurate experimental data in the near wake, only a few measurements have been reported for this region. Cantwell and Coles [Cantwell and Coles (1983)] investigated transport processes in the near wake of a circular cylinder using an X-array of hot wire probes for a Reynolds number of 140,000. Ong and Wallace [Ong and Wallace (1996)] also conducted hot-wire measurements in the very near wake of a circular cylinder at a Reynolds number of 3900. They noticed that measurements of the streamwise velocity component were inaccurate for such flow fields and the very near wake region was pre-dominantly 2-dimensional. Using laser Doppler velocimetry (LDV), Nakagawa et al. [Nakagawa et al. (1999)] measured the unsteady turbulent near wake of a rectangular cylinder in channel flow and found that the turbulent intensities on the centerline of the channel reached their maxima near the rear stagnation point of the recirculation region. More recently, in their numerical study on the dynamics of a turbulent near wake behind a circular cylinder, Ma et al. [Ma et al. (2000)] argued that the very near wake (characterized by downstream

distances of less than three diameters) was dominated by shear layer dynamics and was very sensitive to disturbances and cylinder aspect ratio, whereas farther downstream the flow was dominated by the vortex shedding dynamics and was not as sensitive to the aforementioned factors.

As the wake evolves, the profile of the mean streamwise velocity becomes asymptotically self-similar in the far wake [Wynanski et al. (1986)]. Self-similarity essentially indicates that the wake has reached a dynamical equilibrium. The local centerline velocity defect, $U_s(x)$, is defined as

$$U_s(x) \equiv U_0 - \langle U(x, 0, 0) \rangle, \quad (3.1)$$

where U_0 is the free-stream velocity. The half-width, $y_{1/2}(x)$, is defined such that

$$\langle U(x, \pm y_{1/2}(x), 0) \rangle = U_0 - \frac{1}{2}U_s(x). \quad (3.2)$$

Then with $\xi \equiv y/y_{1/2}(x)$ being the scaled cross-stream variable, the self-similar velocity defect $f(\xi)$ in a plane wake is defined by

$$f(\xi) = [U_0 - \langle U(x, y, 0) \rangle] / U_s(x). \quad (3.3)$$

However, it has been found that the wakes from the different generators do not reach the same self-similar state [Pope (2000)]. Instead, the self-similar state retains information about how the wake was generated [George (1989)].

The magnitude of the turbulent kinetic energy determines the quality and the efficiency of many industrial mixing processes. Therefore, the local turbulent dissipation rate, ε , is one of the fundamental parameters for the process designer. With the data collected from PIV measurements, it is possible to study the distribution of the dissipation rate over a large flow region. Based on the classical turbulence theory [Kolmogorov (1941)], the characteristic scale of the smallest turbulent motions is the Kolmogorov scale, which is defined by $\eta = (\nu^3/\varepsilon)^{1/4}$ where ν is the molecular kinematic viscosity. However, Tennekes and Lumley [Tennekes and Lumley (1972)] suggested that the spatial resolution of the velocity measurement could be as

large as 5η and still resolve the turbulent dissipation rate. Tsurikov and Clemens [Tsurikov and Clemens (2002)] also argued that kinetic energy dissipative structures have thickness ranging from approximately 1η to 10η and a mean thickness of 4η . In terms of the gradients of the instantaneous velocity, the turbulent dissipation rate can be evaluated by Eq. 3.4, provided that such gradients are measured with sufficient resolution [Sharp and Adrian (2001)]:

$$\begin{aligned} \varepsilon = \nu \left\{ \overline{2 \left[\left(\frac{\partial u}{\partial x} \right)^2 + \left(\frac{\partial v}{\partial y} \right)^2 + \left(\frac{\partial w}{\partial z} \right)^2 \right]} \right. \\ \left. + \overline{\left(\frac{\partial v}{\partial x} \right)^2 + \left(\frac{\partial w}{\partial x} \right)^2 + \left(\frac{\partial u}{\partial y} \right)^2 + \left(\frac{\partial w}{\partial y} \right)^2 + \left(\frac{\partial u}{\partial z} \right)^2 + \left(\frac{\partial v}{\partial z} \right)^2} \right. \\ \left. + 2 \overline{\left(\frac{\partial u}{\partial y} \frac{\partial v}{\partial x} + \frac{\partial u}{\partial z} \frac{\partial w}{\partial x} + \frac{\partial w}{\partial y} \frac{\partial v}{\partial z} \right)} \right\} \end{aligned} \quad (3.4)$$

where u, v and w are the three components of instantaneous velocity and ν is the kinematic viscosity. The overline denotes an ensemble-averaged quantity.

The study of turbulent mixing has benefited greatly from developments in laser-based flow diagnostic techniques. In the present study, velocity and concentration fields have been measured using two such techniques, particle image velocimetry (PIV) and planar laser induced fluorescence (PLIF). As non-intrusive techniques, both PIV and PLIF have distinct advantages over intrusive techniques and have been proven capable of providing high-quality measurements on turbulent flows [Aanen et al. (1999); Fukushima et al. (2000); Meyer et al. (2000)]. Moreover, because of their planar, rather than pointwise, nature, they are becoming the methods of choice for many experimental fluid mechanics investigations requiring velocity vector field or scalar field data.

Although numerous studies have been reported on turbulent planar wakes, experimental data for both the turbulent velocity field and concentration field in a liquid-phase, confined rectangular wake are scarce. To address this deficiency, in the present study turbulent mixing in a confined rectangular wake is investigated using both PIV and PLIF. Although the traditional method to form the wake is to place a circular cylinder in a freestream, in the present study the wake is produced by a plate (a characteristic of using a plate is the absence of a wake producing blunt body with the inevitable local separation and large pressure gradients [Ali

and Ibrahim (1996)). The velocity and concentration fields in the wake are analyzed to provide insight into the characteristics of turbulent mixing and to validate the predictions of CFD models.

Experimental Apparatus and Methodology

Flow Facility

The experimental flow system, shown in Fig. 3.1, is designed to provide a shear flow with a Reynolds number of up to 100,000, based on the channel hydraulic diameter. The reactor is mounted in an adjustable cage that can be raised or lowered in order to change the measurement location without moving the optics of the measurement system. As Fig. 3.2 shows, the reactor consists of a vertical Plexiglas test section and a flow conditioning section. The test section is 60 mm by 100 mm and 1 m in length. The width of each of the inlet channels is 20 mm. The slope of the surface of the splitter plates is 3 degrees along the side channels and 1 degree along the center channel. Three Fisher control valves and feedback control systems with flow accuracy of 0.5% are used to supply constant flow rates to the three inlet channels.

A flow-conditioning section consisting of a packed bed of 1 cm diameter spheres, turbulence reducing screens, and a pair of 4:1 contractions creates a uniform flow with reduced free-stream turbulence intensities. For the present study, the volumetric flow rate of each of the inlet channels was 1.0 liters/s, corresponding to a free-stream velocity (U_0) of 0.5 m/s. The Reynolds number based on the hydraulic diameter of the test section and the bulk velocity was 37,500.

In the coordinate system used in this study, x represents the streamwise direction and y represents the transverse direction. All planar images are acquired in the center plane between the front and back walls of the test section. More details of the experimental apparatus and methodology can be found in [Feng et al. (2005)].

Velocity Measurements

The optical setup for the PIV measurements is shown schematically in Fig. 3.1. The flow tracer particles were hollow glass spheres (Sphercel, Potters Industries, Inc.) with a nominal diameter of $11.7 \mu\text{m}$ and a density of 1.1 g/cm^3 . Before performing the measurements, approximately 24 grams of seed particles were added to the total reservoir volume of 3500 liters and mixed until the particles were distributed homogeneously.

A double-pulsed Nd:YAG laser (New Wave Research Gemini PIV laser) was used as the light source, providing two independent 532 nm light pulses with a maximum pulse energy of 120 mJ and a pulse duration of approximately 5 ns. The time delay between the two laser pulses was set to $700 \mu\text{s}$ for the present experiments. The laser beam was formed into a sheet and focused along the center line (in the y direction) of the test section. The minimum sheet thickness was approximately 0.5 mm in the measured flow field region.

10,000 PIV image pairs were collected at each observation location at a frame rate of 8 images/s using a 12-bit LaVision Flowmaster 3S CCD camera with a resolution of 1280×1024 pixels. A multi-pass interrogation scheme with decreasingly smaller window sizes was used with a final interrogation spot size measuring 16×16 pixels, corresponding to 0.9 mm on a side. With 50% overlap between adjacent interrogation spots, the velocity vector spacing was 0.45 mm in both the x and y directions. The image magnification was about 0.12, and the numerical aperture was 8. The experimental uncertainty for velocity was $\pm 3\%$ [Prasad et al. (1992)]. Peak locking [Christensen (2004)] is a potential problem in PIV experiments in which measured particle displacements can become biased towards integer pixel displacements. The peaking-locking effect can be quantified by determining the *peak-locking coefficient* [Stanislas et al. (2005)]. For the results presented here, this coefficient was found to be 0.04, indicating an acceptable low degree of peak locking.

Table 3.1 shows the Kolmogorov scales and the spatial resolution of the PIV measurements in terms of these Kolmogorov scales at the five observation locations in this work. To estimate the Kolmogorov scale, the following equation [Tennekes and Lumley (1972)] was used to approximate ε :

$$\varepsilon \approx A \frac{u'_0{}^3}{l} \quad (3.5)$$

where A is a constant of order 1. u'_0 denotes the characteristic fluctuating velocity, which was assumed to be the square root of $2/3$ of the maximum turbulent kinetic energy at each downstream location. The width of the wake was used as the integral length scale, l . As Table 3.1 shows, the spatial resolution of PIV measurements in terms of the Kolmogorov scale was 8.7η at $x/d = 1.0$ and continuously improved with downstream distance. At $x/d = 15$, the spatial resolution was 4.1η .

Concentration Measurements

The instantaneous concentration field was measured with PLIF using the same optical setup as in the PIV measurements. The fluorescent dye Rhodamine 6G was used as a passive scalar. Rhodamine 6G has $Sc \approx 1,250$ in water [Crimaldi and Koseff (2001)], and emits broadband fluorescence with a peak emission around 555 nm when excited by the light from an Nd:YAG laser [Penzkofer and Leupacher (1987)]. A long-pass (low pass for frequency) optical filter that blocked light with wavelengths shorter than 555 nm was attached on the camera lens so that reflected or scattered laser light did not interfere with the fluorescence measurements. In the center stream, the source concentration of Rhodamine 6G was $45 \mu\text{g/liter}$, while the outer two streams were pure water.

Preliminary PLIF experiments were performed to calculate the fluorescent dye and to determine if the shot-to-shot variability of the laser was a concern. This was done by performing PLIF measurements on fixed concentrations of dye in a small Plexiglas tank with identical cross-sectional area to the test section. Since the dye concentration in each measurement was constant, any measured concentration fluctuations could only be due to a combination of shot-to-shot laser variation and camera noise. In these experiments, the measured variation in dye concentration was approximately 2%, indicating that the shot-to-shot laser power was remarkably steady. Thus, it was deemed unnecessary to monitor the shot-to-shot laser power variations during the PLIF experiments.

The image magnification of the PLIF measurements was about 0.12, and the numerical aperture was 5.6. The diffraction-limited spot size for the PLIF optical system was $8.1 \mu\text{m}$. However, the spatial resolution was limited instead by the area viewed per pixel, which was $56 \mu\text{m}$. The smallest length scale of turbulent mixing is known as the Batchelor scale [Batchelor (1953)], which is defined by $\eta_B = \eta/\sqrt{Sc}$. As Table 3.2 shows, the resolution of PLIF measurements is much larger than the Batchelor scale in all directions, therefore the smallest concentration scale can not be resolved in the presented study.

At each observation location, 10,000 PLIF images were captured at a frame rate of 8 images/s. The local intensity of the fluorescent light is proportional to the local intensity of the excitation source and the local concentration of the fluorescent dye [Crimaldi and Koseff (2001)]. In the present study, we found that this relationship was valid for dye concentrations up to $100 \mu\text{g/liter}$ with our experimental setup. Each PLIF image was individually calibrated for the non-uniform energy distribution throughout the entire laser sheet and laser absorption across the illuminated field. The procedure to calibrate the concentration measurements is described by [Feng et al. (2005)].

Overview of CFD Models

Turbulent transport is described mathematically by the Reynolds-averaged Navier-Stokes (RANS) equations which need closures. Alternatively, one could use direct numerical simulation (DNS) [Rogallo and Moin (1984); Moin and Mahesh (1998)] or large-eddy simulation (LES) [Akselvoll and Moin (1996); Hughes et al. (2001)]. Though DNS can provide extremely detailed information (beyond what is possible in experimental measurements), its application is limited by its prohibitive computational costs. Similarly, LES, although it attempts to reduce computational costs by resolving only the largest turbulent scales, is also computational expensive. RANS simulations are more cost-effective, and thus these were adopted in this work. Here, a two-layer $k - \varepsilon$ model is employed to close the Reynolds stresses. This model was proposed by [Chen and Patel (1988)] and solves the near-wall effect [Wilcox (1998); Durbin and Petterson Relif (2001)] satisfactorily at reasonable cost even for complex flows.

More details of the RANS code used in this study can be found elsewhere [Liu et al. (2004)]. The performance of this model is evaluated by comparing predicted single-point turbulence statistics with ensemble-averaged PIV data (which is equivalent to time-averaged data for this stationary flow).

Inert Scalar Moment Transport Model

Closure problems are also frequently encountered when solving the Reynolds-averaged scalar (which is the mixture fraction in this study) transport equations. In these models, an inert scalar ϕ can be successfully described by a small set of statistical moments, the scalar mean $\langle\phi\rangle$ and the scalar variance $\langle\phi'^2\rangle$, for example. Denoting the mean velocity and fluctuation velocity by $\langle U_j\rangle$ and u_j , respectively, the RANS transport equation of an inert scalar mean can be written as (repeated indices imply summation)

$$\frac{\partial\langle\phi\rangle}{\partial t} + \langle U_j\rangle \frac{\partial\langle\phi\rangle}{\partial x_j} = \Gamma \nabla^2 \langle\phi\rangle - \frac{\partial\langle u'_j \phi\rangle}{\partial x_j}, \quad (3.6)$$

where Γ is the molecular diffusivity, and repeated indices imply summation. The only unclosed term in Eq. 3.6 is the scalar flux $\langle u'_j \phi\rangle$ representing turbulent transport. In order to be consistent with the Reynolds stress closure, a two-layer $k - \varepsilon$ model is used in this work where $\langle u'_j \phi\rangle$ is modeled by invoking the gradient-diffusion hypothesis [Taylor (1921)]:

$$\langle u'_j \phi\rangle = -\Gamma_T \frac{\partial\langle\phi\rangle}{\partial x_j}, \quad (3.7)$$

where Γ_T , the turbulent diffusivity, is related to the turbulent viscosity ν_T by $\Gamma_T = \nu_T / Sc_T$. Sc_T is the turbulent Schmidt number and has a typical value of 0.7 in this study.

The transport of an inert scalar variance is governed by

$$\frac{\partial\langle\phi'^2\rangle}{\partial t} + \langle U_j\rangle \frac{\partial\langle\phi'^2\rangle}{\partial x_j} = \Gamma \nabla^2 \langle\phi'^2\rangle - \frac{\partial\langle u'_j \phi'^2\rangle}{\partial x_j} + \mathcal{P}_\phi - \varepsilon_\phi. \quad (3.8)$$

Here \mathcal{P}_ϕ , the scalar-variance production term, is defined by

$$\mathcal{P}_\phi \equiv -2\langle u'_j \phi\rangle \frac{\partial\langle\phi\rangle}{\partial x_j}, \quad (3.9)$$

and represents the rate at which scalar energy is transferred from mean flow to turbulent fluctuations. The last term on the right-hand side ε_ϕ is the scalar dissipation rate defined by

$$\varepsilon_\phi = 2\Gamma \left\langle \frac{\partial \phi'}{\partial x_j} \frac{\partial \phi'}{\partial x_j} \right\rangle. \quad (3.10)$$

This term is responsible for dissipation of scalar variance due to molecular diffusion.

Since Eq. 3.9 is closed by Eq. 3.7, the remaining unclosed terms in Eq. 3.8 are the scalar-variance flux $\langle u'_j \phi'^2 \rangle$ and the scalar dissipation. Again, by invoking the gradient-diffusion hypothesis, the scalar-variance flux is modeled by

$$\langle u'_j \phi'^2 \rangle = -\Gamma_T \frac{\partial \langle \phi'^2 \rangle}{\partial x_j}. \quad (3.11)$$

By assuming proportionality between the scalar time scales and the turbulent time scales, [Spalding (1971); Beguier (1978)] the scalar dissipation can be related to the turbulent frequency ε/k by

$$\varepsilon_\phi = C_\phi \frac{\varepsilon}{k} \langle \phi'^2 \rangle, \quad (3.12)$$

with the mechanical-to-scalar time-scale ratio C_ϕ taking a Reynolds-number-dependent value determined by [Liu and Fox (2006)]

$$C_\phi = \sum_{n=0}^6 a_n (\log_{10} Re_T)^n \quad (3.13)$$

where, for $Sc = 1250$, $a_0 = 0.4093$, $a_1 = 0.6015$, $a_2 = 0.5851$, $a_3 = 0.09472$, $a_4 = -0.3903$, $a_5 = 0.1461$, $a_6 = -0.01604$, and the turbulent Reynolds number is defined by

$$Re_T = \frac{k}{\sqrt{\nu \varepsilon}}. \quad (3.14)$$

The RANS code solves Eqs. 3.6 and 3.8 closed by Eqs. 3.7, 3.11 and 3.12. These models are then validated against the inert scalar mean and variance measured by PLIF.

Transported PDF Model

The transport equation of the composition PDF, denoted by f_ϕ , for an incompressible fluid is

$$\frac{\partial f_\phi}{\partial t} + \frac{\partial}{\partial x_j} (\langle U_j \rangle f_\phi) + \frac{\partial}{\partial x_j} [\langle u'_j | \psi \rangle f_\phi] = - \frac{\partial}{\partial \psi} [\langle \Gamma \nabla^2 \phi | \psi \rangle f_\phi] \quad (3.15)$$

where ϕ and ψ represent the composition and the composition state space, respectively, and $\langle \cdot | \psi \rangle$ denotes the Reynolds average conditioned on $\phi = \psi$. The scalar-flux term $\langle u'_j | \psi \rangle f_\phi$, which denotes the scalar-conditioned velocity fluctuations (i.e., mesomixing), is closed by the gradient-diffusion model as

$$\langle u'_j | \psi \rangle f_\phi = -\Gamma_T \frac{\partial f_\phi}{\partial x_j}. \quad (3.16)$$

The term on the right-hand side of Eq. 3.15, representing transport in composition space due to molecular diffusion, is approximated in this study by a micromixing model - the interaction-by-exchange-with-the-mean (IEM) model and the Euclidean minimum spanning tree (EMST) model [Subramaniam and Pope (1998)], which are described later in this section.

The numerical discretization of Eq. 3.15 is intractable due to its high dimensionality. In our Lagrangian PDF code [Raman et al. (2001, 2003, 2004)], Eq. 3.15 is expressed in terms of stochastic differential equations for so-called “notional” particles. [Pope (1976, 1985)]. Denoting the position of a notional particle by $\mathbf{X}^{(n)}$, transport in physical space with Eq. 3.16 is governed by the following equation:

$$d\mathbf{X}^{(n)} = \left[\langle \mathbf{U} \rangle (\mathbf{X}^{(n)}, t) + \nabla \Gamma_T (\mathbf{X}^{(n)}, t) \right] dt + \sqrt{2\Gamma_T (\mathbf{X}^{(n)}, t)} d\mathbf{W}(t), \quad (3.17)$$

where $d\mathbf{W}(t)$ is a multi-variate Wiener process with a mean of zero and $\langle \mathbf{U} \rangle (\mathbf{X}^{(n)}, t)$ is the mean velocity vector at the particle location. The evolution equation for the particle composition $\phi^{(n)}$ can be written as

$$\frac{d\phi^{(n)}}{dt} = \Theta^{(n)}, \quad (3.18)$$

where Θ represents the micromixing model. For the IEM model, Eq. 3.18 is characterized by

$$d\phi^{(n)} = \frac{C_{\phi}\varepsilon}{2k} \left(\langle \phi \rangle \left(\mathbf{X}^{(n)}, t \right) - \phi^{(n)} \right) dt, \quad (3.19)$$

where $\langle \phi \rangle \left(\mathbf{X}^{(n)}, t \right)$ is the estimated scalar mean at the particle location. In the EMST model, which is local in composition space, composition interactions only occur between neighbor pairs of particles, m_e and n_e , connected by the edge e :

$$d\phi^{(n)} = \alpha \sum_{e=1}^{N_T-1} B_e \left\{ \left(\phi^{(m_e)} - \phi^{(n)} \right) \delta_{nm_e} + \left(\phi^{(n_e)} - \phi^{(n)} \right) \delta_{nn_e} \right\} dt, \quad (3.20)$$

where N_T denotes the number of particles chosen for mixing from the ensemble of N particles within a grid cell and B_e is the edge-weight. δ represents the Kronecker delta function. The parameter α is determined by requiring that the scalar variance decays exponentially with $C_{\phi}\varepsilon/k$. More details can be found in [Subramaniam and Pope (1998, 1999)].

The flow statistics appearing in Eqs. 3.17, 3.19 and 3.20 are known from the RANS code [Fox (2003); Raman et al. (2001)]. Given the composition of the notional particles, the scalar mean and variance, which are assumed to be independent of the particle locations within a grid cell, are estimated as

$$\langle \phi \rangle = \frac{\sum_{n=1}^N W^{(n)} \phi^{(n)}}{\sum_{n=1}^N W^{(n)}}, \quad (3.21)$$

$$\langle \phi'^2 \rangle = \frac{\sum_{n=1}^N W^{(n)} \left(\phi^{(n)} - \langle \phi \rangle \right)^2}{\sum_{n=1}^N W^{(n)}}, \quad (3.22)$$

where $W^{(n)}$ is the weight of the n th particle. Equation 3.15 is validated by comparing the inert scalar statistics predicted by the transported PDF method with PLIF data.

Simulation Conditions

The wake flow was simulated using the RANS and PDF models described above. All simulations were performed on a two-dimensional (2-D) grid by assuming that gradients in the spanwise direction are negligible. The computational grid consists of 80×120 Cartesian cells with denser grid cells near stream interfaces and walls to resolve sharp gradients. This methodology ensures a grid-independent solution.

The inlet boundary conditions of the streamwise mean velocity $\langle U \rangle$, the turbulent kinetic energy k and the turbulent dissipation rate ε for the RANS simulations were extracted from the experimental data measured at the entrance plane of the reactor. The distribution of the experimental data was found to be slightly asymmetric with respect to the centerline (Fig. 3.3). By averaging the experimental data with respect to $y/d = 0$ and then interpolating linearly between data points, the symmetric inlet boundary conditions for $\langle U \rangle$, k and ε were obtained (Fig 3.3). Due to the difference in resolution mentioned above, the inlet boundary conditions effectively cut off the large gradients appearing in the interfaces of streams. However this was found to have no impact on the calculated flow statistics. Note that the PIV data are 2-D measurements, containing no information on the out-of-plane velocity component. The PIV data for the turbulent kinetic energy were estimated from the streamwise and transverse velocity fluctuations, u' and v' , as

$$k = \frac{\langle u'^2 \rangle + 2\langle v'^2 \rangle}{2}. \quad (3.23)$$

The spanwise velocity fluctuation was assumed to be equal in magnitude to the cross-stream velocity fluctuation. By further assuming $\partial/\partial z = \partial/\partial y$, the turbulent dissipation rate was derived from the 2-D PIV data. More details can be found in Sec. 3.

Results and Discussion

Figure 3.4 displays a sample instantaneous velocity field from PIV measurements with a convective velocity subtracted from each vector. A system of double roller-like counter-rotating large eddies are observed in the wake region just downstream of the tips of the splitter plates. An instantaneous concentration field at this same location as measured by PLIF is illustrated in Fig. 3.5. The contour levels represent the concentration normalized by the source concentration, or mixture fraction. Note that the velocity and concentration fields shown in Figs. 3.4 and 3.5 are uncorrelated with each other, as the PIV and PLIF measurements in this study were not performed simultaneously. By themselves, instantaneous velocity and concentration fields such as those shown in Figs. 3.4 and 3.5 provide only anecdotal data

concerning the flow field. In order to be useful in validating the computational results, the PIV and PLIF data sets must be analyzed statistically.

Mean Velocities and Reynolds Stresses

The ensemble-averaged streamwise velocity profiles measured by PIV for six representative downstream locations are shown in Fig. 3.6, where the y -axis has been normalized by the inlet channel width, $d = 20$ mm. This normalization of the transverse coordinate is used throughout the present work. The mean velocity has been normalized by the bulk velocity, $U_0 = 0.5$ m/s, *i.e.*, the mean velocity as determined from the volumetric flow rate. As Fig. 3.6 shows, two wake regions appear just downstream of the tips of the splitter plates as the boundary layers on the splitter plate surfaces merge downstream of the tips. Also note that the velocity profiles are nearly symmetric about the centerline of the reactor at each downstream location. The wake velocity defect diminishes quickly at the lower downstream locations. The two wake regions meet at $x/d = 4.5$ near the channel centerline, as seen by the potential core in the center stream disappearing at this position. At $x/d = 30$ the velocity profile begins to look like a fully developed turbulent channel flow, with the wakes no longer observed.

The mean streamwise velocity predicted by the RANS code with the two-layer $k-\varepsilon$ model is compared with PIV measurements in Fig. 3.6. The spreading rate of the wake predicted by the RANS code is slightly lower than that measured by PIV, and this characteristic becomes more obvious further downstream. However, the agreement in Fig. 3.6(f) is good, and at $x/d = 30$ the RANS code also predicts the complete decay of the wakes. The smaller spreading rate in the RANS calculation is most likely caused by a lower diffusion rate of the turbulent kinetic energy, as discussed later.

The PIV measured Reynolds stresses, normalized by U_0^2 , for seven streamwise locations are plotted in Fig. 3.7. Just downstream of the splitter plate tips, the longitudinal Reynolds stress, $\langle u'u' \rangle$, in each wake displays two peaks. This is due to the two boundary layers along the splitter plates coming together to form the wakes. Each of these boundary layers has its own peak in Reynolds stress, and these peaks remain distinct for some distance downstream

of the splitter plate tip. However, at further downstream locations these two peaks become indistinct, and only a single peak is observed in each wake.

The disparate boundary layer development along the surfaces of the splitter plate gives rise to a slight asymmetry in the wakes such that $\langle u'u' \rangle$ is higher in the left wake. Also, at the first downstream location $\langle u'u' \rangle$ is 8 times larger than the lateral Reynolds stress, $\langle v'v' \rangle$. However, $\langle u'u' \rangle$ decays much more rapidly at lower downstream locations than $\langle v'v' \rangle$, and both normal stresses become almost identical in magnitude at $x/d = 7.5$ and further downstream. After the initial convergence of the two boundary layers forming each wake, both $\langle u'u' \rangle$ and $\langle v'v' \rangle$ initially increase near the centerline at $x/d = 1.0$, but then show a marked decrease at $x/d = 4.5$. Thereafter, the Reynolds normal stresses continually decrease to very small values as the results at $x/d = 30$ show.

The Reynolds shear stress, $\langle u'v' \rangle$, is antisymmetric around the center line of the channel: positive where the mean shear is negative, and negative where the mean shear is positive. The Reynolds shear stress also changes sign at the center of each wake, and along the center line of the channel the Reynolds shear stress is zero. Due to the boundary layers along the side walls, the Reynolds shear stress near the side walls is nonzero. At $x/d = 30$, after the wakes have completely disappeared, the Reynolds shear stress decreases to zero in the region near the center line of the channel.

Self-Similarity of the Rectangular Wake

Using Eqs. 3.1, 3.2, and 3.3, the self-similar velocity defect $f(\xi)$ in the wake downstream of the left splitter plate was calculated. It should be noted that the free-stream velocity U_c used in these calculations is taken to be 0.56 m/s which is the maximum local inlet velocity. The profiles at five downstream locations are shown in Fig. 3.8 for both the PIV and RANS simulation data. These results indicate that the mean velocity profile in the wake tends to reach an equilibrium state. However, unlike in a free wake, the distribution of the velocity defect at the edges of the wake is very different due to the interaction of the two wakes and the effect of boundary layers growing along the side walls. Moreover, since the potential core in the

center stream disappears faster than that in the side stream, the velocity defect corresponding to the positive scaled cross-stream variable (ξ) departs from the self-similar profile faster than that for negative ξ . Additionally, due to the different slopes of both surfaces of the splitter plate, the pressure gradients on both sides are slightly different. As a result, the profile of the self-similar velocity is not perfectly symmetric about the center line of the wake.

Turbulent Kinetic Energy

The turbulent kinetic energy predicted by the RANS code is compared with PIV data for downstream locations $x/d = 1, 4.5, 7.5, 12, 15$ and 30 in Fig. 3.9. The RANS code captures all the essential behavior of the turbulent kinetic energy, though the diffusivity in the central channel is slightly lower than expected based on comparisons with the PIV results. Figure 3.9 also indicates that the PIV measurements missed sharp gradients of the turbulent kinetic energy, especially near the walls where the mean and variance of the velocity are changing quickly. This is not surprising if we recall that PIV measures a filtered velocity field, given that the measurement resolution is lower than the Kolmogorov scale. The spatial resolution of PIV is limited by the interrogation spot size, l_{PIV}^* ($l_{PIV}^* = 9 \times 10^{-4}$ m in this study). In the boundary layers formed near the walls and at the stream interfaces, the size of the largest energy-containing eddies, which scales with the thickness of the boundary layers, is much smaller than l^* . Therefore, portions of the turbulent kinetic energy is cut off by the measurements at those regions. On the other hand, the RANS computation involves a grid the resolution of which is higher than the spatial resolution in the PIV measurements near stream interfaces and walls, capturing more local details of the turbulent kinetic energy.

Turbulent Dissipation Rate

Notice the spatial resolution of the PIV measurements in the present work was good enough to resolve the turbulent dissipation rate [Tennekes and Lumley (1972); Tsurikov and Clemens (2002)], Eq. 3.4 was therefore used to compute the turbulent dissipation rate. However the out-of-plane component of velocity (w) is not available in 2-D PIV measurements,

only four terms of the velocity gradient, i.e., $\partial u/\partial x$, $\partial u/\partial y$, $\partial v/\partial x$ and $\partial v/\partial y$, can be computed directly using PIV data. By using the incompressible continuity equation, $\partial w/\partial z$ can also be determined. To estimate the dissipation rate, the following assumptions were made to obtain the four unknown terms in Eq. 3.4: (1) $w = v$; and (2) $\partial/\partial z = \partial/\partial y$.

The results of the turbulent dissipation rate at six downstream locations computed by Eq. 3.4 are shown in Fig. 3.10 and compared with those predicted by the two-layer $k-\varepsilon$ model. The dissipation rate in the flow is highly inhomogeneous. Initially, the profile of dissipation rate has two distinct peaks in each wake (due once again to the two boundary layers along each splitter plate coming together at the splitter plate tip). However, the dissipation rate decreases very quickly with increasing downstream distance, and the two peaks are indistinct at farther downstream locations. The dissipation rate at the center of the channel starts to increase after the two mixing layers meet and the potential core disappears. At $x/d = 30$, the wakes have collapsed, and the dissipation rate decreases to small values. Comparing the profiles of the dissipation rate and turbulent kinetic energy, it is noticed that there exists strong correlation between these two properties.

The dissipation rate predicted by the two-layer $k-\varepsilon$ model agrees well with that estimated from the PIV data (Fig. 3.10), even in the near-wall regions, indicating that the performance of the turbulence model is satisfactory.

Mixture-Fraction Mean and Variance

The profiles of ensemble-averaged mixture-fraction mean and variance at the six streamwise locations as measured by PLIF are presented in Figs. 3.11 and 3.12, respectively, and compared with those predicted by the RANS and the micromixing models. The profile of mixture-fraction mean is symmetric about the center line of the channel. At $x/d = 1$, the mixture-fraction mean resembles a top-hat shape. As x increases, the mixture-fraction mean in the center stream decreases and the mixture-fraction mean in the side streams increases due to mass transport of the dye. After the two wakes meet at $x/d = 4.5$ (i.e., after the potential core in the center stream disappears), the profile of mixture-fraction mean becomes bell-shaped. At the farthest

observed downstream location, $x/d = 30$, the profile still remains bell shaped, indicating that even at this far downstream location, the fluid is not fully mixed. As Fig. 3.12 shows, the mixture-fraction variance profiles are also nearly symmetric. The magnitudes of the peaks of variance increase with x initially but then remain almost unchanged at $x/d = 4.5, 7.5$ and 12 , before decreasing slowly at $x/d = 15$ and beyond. After the potential core between the two wakes disappears, the mixture-fraction variance in the center of the channel becomes nonzero and increases with increasing downstream distance. At the farthest location investigated in this work, the two peaks in mixture-fraction variance are still distinct. Note also that at $x/d = 1.0$, the measured mixture-fraction variance at $y/d = 0$ is nearly zero. Since the measured variance at this location is primarily due to shot-to-shot variations in laser intensity, this demonstrates the consistency of the lasers used in these experiments.

The RANS code and the micromixing models yield similar profiles for the mixture-fraction mean at all locations. This is expected since the mean conservation property of the IEM model and the EMST model guarantees a mixture-fraction mean that is exclusively determined by the flow statistics given the inlet boundary condition of the mixture-fraction mean. In general, the predicted mixture-fraction mean agrees well with the PLIF data, though the former shows a lower spreading rate, which is consistent with observations in Figs. 3.6 and 3.9. It was also found that the spreading rate was insensitive to the value of the turbulent Schmidt number, indicating that it is the mean velocity rather than the gradient-diffusion model (Eqs. 3.7 and 3.16) that most likely causes the discrepancy in the spreading rate. The mixture-fraction mean near the wall becomes non-zero by $x/d = 30$.

The mixture-fraction variances predicted by the micromixing models are similar and agree closely with the results given by the RANS code except at $x/d = 1$, where the models predict a higher variance in the stream interfaces than the RANS code. The time step for the PDF calculations, which is 0.002 s in this study, is the key factor that initiates the overpredicted variance [Feng et al. (2005)]. Both codes predict a higher peak value for the variance, and the agreement cannot be improved by reducing the value of the turbulent Schmidt number. This is consistent with discussion concerning the mixture-fraction mean, which reveals that

the slower diffusion predicted by the two-layer $k - \varepsilon$ model leads to the smaller spreading rate. Meanwhile, the gradient of the mixture-fraction mean overpredicted by the RANS code and the micromixing models (Figs. 3.11e and f) results in a higher mixture-fraction variance production term. A overpredicted mixture-fraction variance is consequently expected. It should be noted that the variance decays at an identical rate in the IEM and EMST models, although how the particles interact is distinct.

The performance of the closure for the scalar dissipation rate is worth further investigation. Equation 3.12 is a model for the rate at which the scalar spectral energy transfers through the inertial-convective subrange in homogeneous turbulence. In the stream interfaces near the reactor entrance ($x/d = 1$), where the turbulence is highly inhomogeneous, the energy transfer rate from large to small scales cannot be represented completely by the closure. Therefore the scalar dissipation rate is underestimated, leading to a higher variance (Fig. 3.12a). The model can be expected to be more accurate as the flow develops except in the near-wall regions where the inhomogeneity persists (Fig. 3.9) [Feng et al. (2005)]. Figure 3.6 shows that the turbulence is still developing up to $x/d = 30$. The same tendency is indicated by Figs. 3.12a-d: the agreement of the predicted variance and PLIF data improves gradually from $x/d = 1$ to $x/d = 15$. The insufficient spreading rate and sharper mixture-fraction mean gradient affect the variance prediction more significantly after $x/d = 15$ (Figs. 3.12e and f).

Meanwhile, the PLIF measurements tend to underestimate the mixture-fraction variance since the spatial resolution of the PLIF measurements is insufficient to resolve the smallest mixing scales. The scalar variance can be found directly from the scalar energy spectrum $E_\phi(\kappa)$ by integrating over the space of the wavenumber κ :

$$\langle \phi'^2 \rangle = \int_0^\infty E_\phi(\kappa) d\kappa. \quad (3.24)$$

The thickness of the laser sheet used in the PLIF experiments, l_{PLIF}^* , determines a cut-off wavenumber

$$\kappa^* = \frac{1}{l_{PLIF}^*}, \quad (3.25)$$

where $l_{PLIF}^* = 5 \times 10^{-4}$ m. Consequently, the mixture-fraction variance that can be measured

by PLIF is limited to

$$\langle \phi'^2 \rangle^* = \int_0^{\kappa^*} E_\phi(\kappa) d\kappa. \quad (3.26)$$

By using a model scalar spectrum [Fox (2003)], the percentage of mixture-fraction variance “missed” by the PLIF measurements, represented by $1 - \langle \phi'^2 \rangle^* / \langle \phi'^2 \rangle$, is estimated at points where the predicted variance peaks in value for each downstream location (Table 3.3). This “missing” variance decreases from 24.44% at $x/d = 1$ to 8.3% at $x/d = 30$. This tendency is expected since more of the scalar energy spectrum is resolved as the Kolmogorov length scale increases in the streamwise direction.

One-Point Composition PDF

The evolution of the probability density function (PDF) of mixture fraction was studied using the PLIF data. Designating the midpoint of the peaks in mixture-fraction variance at each downstream location as position “0” and the left peak of mixture-fraction variance as “ δ ”, eight points along the transverse direction were chosen as positions of interest. In the transported PDF code, the N particles within the grid cells centered on the selected points were sorted into 20 equal-spaced bins between 0 to 1 by their composition. Denoting the number of particles in each bin by N_i , the PDF of the mixture fraction was approximated by $20N_i/N$. Figures 3.13 - 3.18 show the one-point composition PDF extracted from the PLIF data, the beta-PDF characterized by the measured mixture-fraction mean and variance, as well as the one-point composition PDF predicted by the IEM model and the EMST model at the points of interest for selected downstream locations.

The experimentally observed mixture-fraction PDF is well approximated by the beta PDF. This is partly because that the experimental values of the mixture-fraction mean and variance were used to define the beta PDF. At the lowest observed downstream location ($x/d = 1$), the PDF approximates a delta function at positions “0” and “ $3/2\delta$ ” (Figs. 3.13a and h) since very little mixing has occurred at regions far from the stream interface. When the observation position moves towards the point “ δ ” (*i.e.*, towards the peak in mixture-fraction variance), the PDF extracted from the PLIF data shows a tendency towards becoming bell-shaped while

the IEM model and the EMST model predict a saddle-shaped curve and a relatively flat line, respectively (Fig. 3.13d). The discrepancy can be well understood if we recall that the PLIF measures a mixture-fraction field averaged over a finite measurement volume. As a result, the experimentally observed PDF reaches its maximum value at $\phi = 0.5$ at the point “ δ ”. The spatial resolution of the PLIF measurements is much lower than the Batchelor scale (i.e., the PLIF measurement volume is much larger than the Batchelor scale), especially at near-entrance areas where the Batchelor scale is small. Therefore, scalar eddies smaller than the spatial resolution are filtered by averaging.

Unlike the mixture-fraction mean which was not affected by the spatial resolution, the PDF of the mixture fraction is expected to be more uniform than reality in the neighborhood of the point “ δ ”. On the other hand, two peaks near $\langle\phi\rangle = 0.2$ and $\langle\phi\rangle = 0.8$ (Fig. 3.13d) are predicted by the IEM model, revealing one of the properties of that model: two peaks initially formed by the delta functions at $\phi = 0$ and $\phi = 1$ persist until they merge at $\phi = \langle\phi\rangle$. In contrast, the EMST model predicts a relatively flat PDF (Fig. 3.13d) as a result of localness: a stochastic particle mixes preferentially with particles that are close to it in composition.

As the downstream distance increases, mixing does begin to take place at points far from point “ $3/2\delta$ ” since more interface stream fluid has been entrained into the channel streams, and the PDF curves become flatter but remain skewed (Figs. 3.13 - 3.18), indicating the persistence of high concentrations of fluorescent dye at these positions. A Gaussian distribution can be expected at a position far downstream from the entrance. The discrepancy between the experimentally observed PDF and the calculated PDF decreases gradually (Figs. 3.13 - 3.16) mainly due to two reasons. First, the Batchelor scale increases, leading to an improved resolution of the PLIF measurements. Second, the modeled PDFs relaxed towards a Gaussian gradually along the streamwise direction. However, the agreement of the measured PDF and calculated PDF does not improve from $x/d = 15$ to $x/d = 30$ since the insufficient spreading rate and the higher mixture-fraction gradient begin to play an important role in the PDF prediction. The insufficient spreading rate can be clearly observed at the point “0” (Figs. 3.15h and 3.17h). We attribute the discrepancy shown in these two figures to the

insufficient spreading rate since the spatial resolution is comparable to the Batchelor scale and the scalar variance production is zero at the point “0”. At all locations, the PDF predicted by the EMST model agrees with the experimental observation much better than does that predicted by the IEM model.

Conclusions

In this study, PIV and PLIF were employed to investigate a rectangular wake flow in a confined reactor with a Schmidt number of 1,250 and a Reynolds number of 37,500 based on bulk velocity and hydraulic diameter. Measurements were carried out at various downstream locations from $x/d = 1$ to $x/d = 30$. Flow statistics such as the mean velocity, Reynolds stresses, turbulent kinetic energy, mixture-fraction mean and variance were calculated from the PIV and PLIF data. The PDF of the mixture fraction at some representative positions in the flow as well as the turbulent dissipation rate were estimated from the experimental data. It was observed that the two confined wakes formed by the two splitter plates had completely decayed by $x/d = 30$.

The PIV and PLIF data were used to validate RANS and transported PDF models. In general, the overall agreement between the CFD models and the experimental data for this moderately complex flow is satisfactory. The mean velocity field was accurately predicted, demonstrating that the two-layer $k-\varepsilon$ model represents the Reynolds stresses successfully, even in near-wall regions. However this turbulence model predicted a lower spreading rate of the turbulent kinetic energy, which consequently slows down the diffusion of the mixture-fraction mean and variance. The predicted mixture-fraction mean and variance indicate that the scalar fluxes were reasonably approximated by the gradient-diffusion models. The scalar dissipation rate was closed by the “equilibrium” model which functioned better for a flow with weak inhomogeneity. Due to the limited spatial resolution, the PLIF measurement could not resolve the scalar variance completely. Nevertheless, the measurement accuracy improved gradually at farther downstream locations. The one-point PDF of the mixture fraction extracted from the PLIF data was compared with the PDFs predicted by the IEM model and the EMST model at

eight points in the transverse direction for selected downstream locations. The experimentally observed PDF tends to be more uniform than that predicted by the micromixing models, partially due to the limited spatial resolution. At the positions where the mixture-fraction variance peaks in value and points nearby, the measured PDF tends to approximate a unimodal distribution more quickly while the predicted PDF shows model characteristics: the IEM model introduced two peaks bounded on the high mixture-fraction and low mixture-fraction sides, respectively; the EMST model features localness.

Table 3.1 Kolmogorov Length Scale and Spatial Resolution of PIV Measurements.

x/d	$\eta[\mu\text{m}]$	Resolution
1.0	104	8.7η
4.5	139	6.5η
7.5	153	5.9η
12	183	4.9η
15	222	4.1η

Table 3.2 Batchelor Length Scale and Spatial Resolution of PLIF Measurements.

x/d	$\eta_B[\mu\text{m}]$	Resolution in x-/y-	Resolution in z-
1.0	2.93	$19.1\eta_B$	$171\eta_B$
4.5	3.93	$14.2\eta_B$	$127\eta_B$
7.5	4.33	$12.9\eta_B$	$115\eta_B$
12	5.17	$10.8\eta_B$	$97\eta_B$
15	6.27	$8.9\eta_B$	$80\eta_B$

Table 3.3 Estimated Variance Unresolved by PLIF at the Peak of the Variance Profile.

x/d	1	4.5	7.5	12	15	30
Unresolved(%)	24.44	15.36	13.09	11.43	10.64	8.3

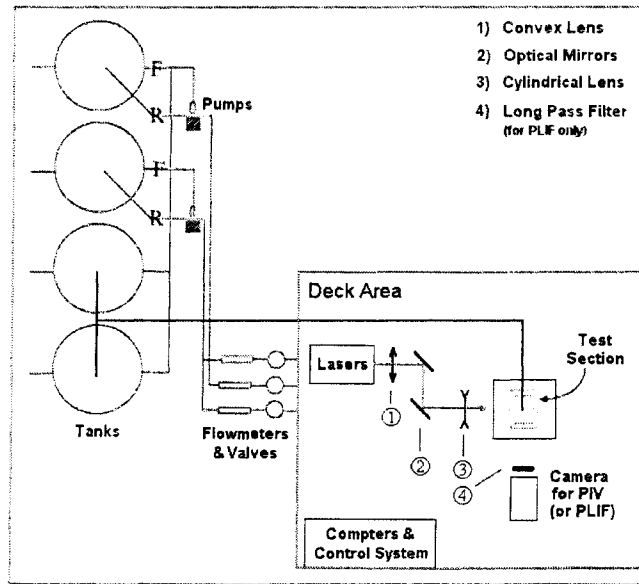


Figure 3.1 Schematic of the flow facility and the optical setup used in the PIV and PLIF experiments.

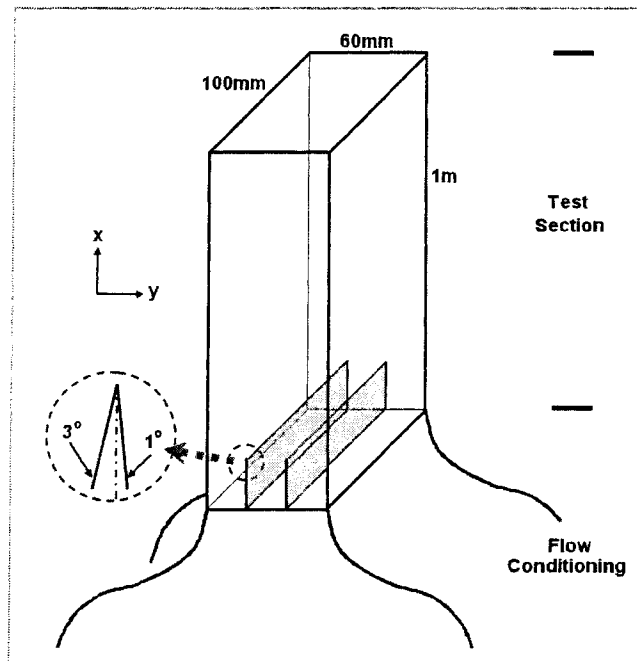


Figure 3.2 Schematic of the confined rectangular-wake reactor.

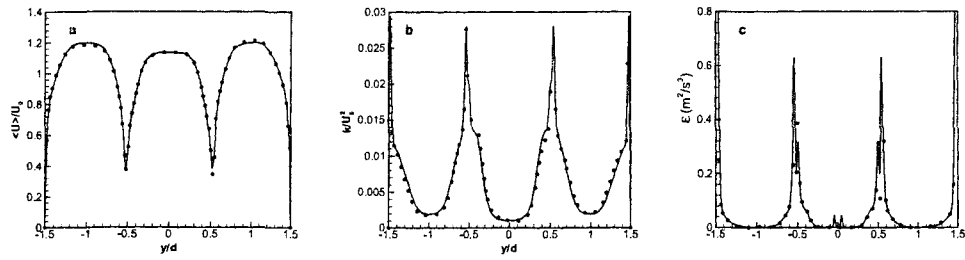


Figure 3.3 (a) Mean streamwise velocity, (b) turbulent kinetic energy and (c) dissipation at the entrance plane of the wake. —, inlet boundary conditions for simulations; •, PIV data.

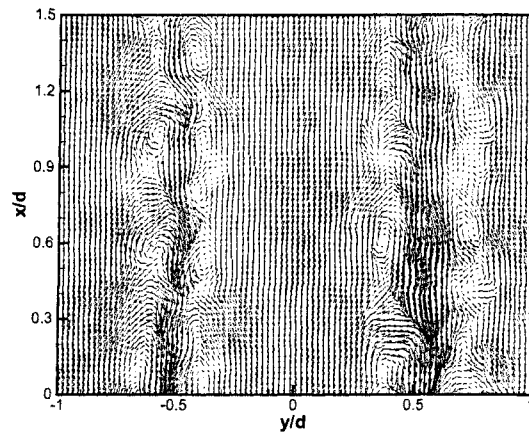


Figure 3.4 An instantaneous velocity field as measured by PIV.

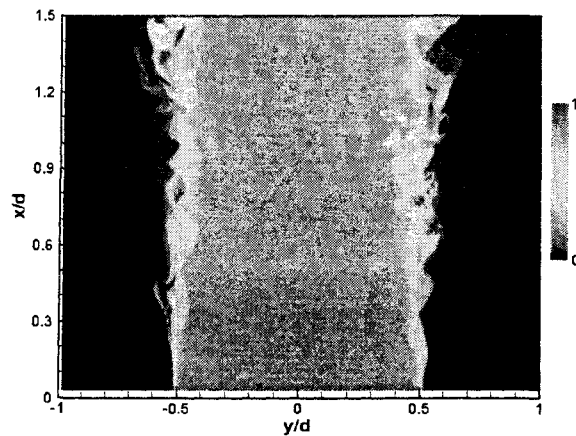


Figure 3.5 An instantaneous concentration field as measured by PLIF.

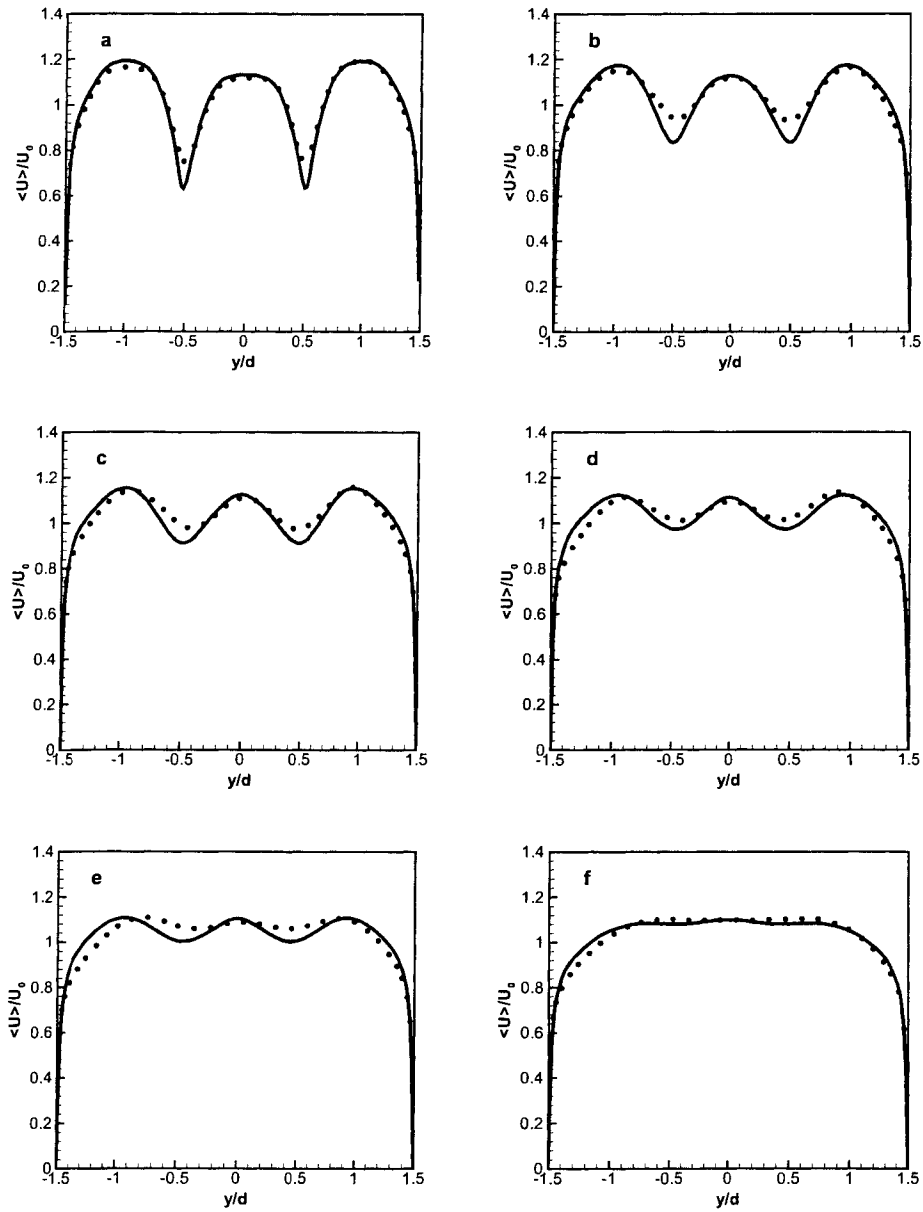


Figure 3.6 Comparison of the mean streamwise velocity profiles measured by PIV (\bullet) and calculated from RANS code ($—$) for (a) $x/d = 1$, (b) $x/d = 4.5$, (c) $x/d = 7.5$, (d) $x/d = 12$, (e) $x/d = 15$ and (f) $x/d = 30$.

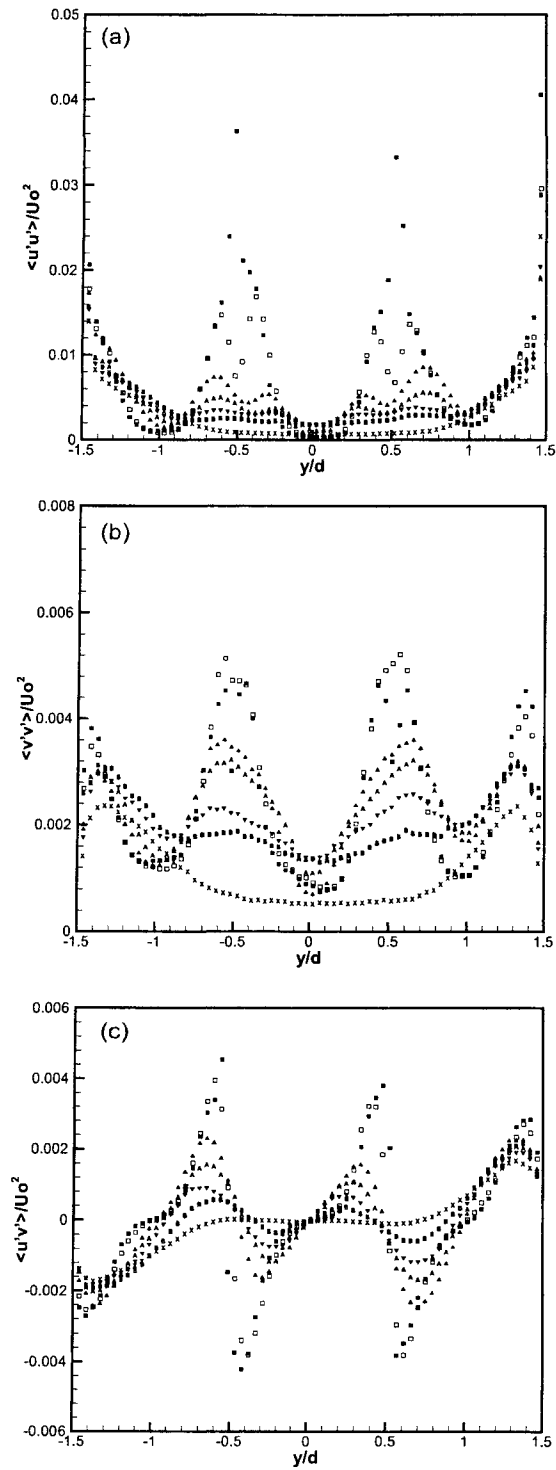


Figure 3.7 Normalized Reynolds stresses measured by PIV. ■, $x/d = 0$; □, $x/d = 1.0$; ▲, $x/d = 4.5$; △, $x/d = 7.5$; ▼, $x/d = 12$; ▽, $x/d = 15$; ×, $x/d = 30$.

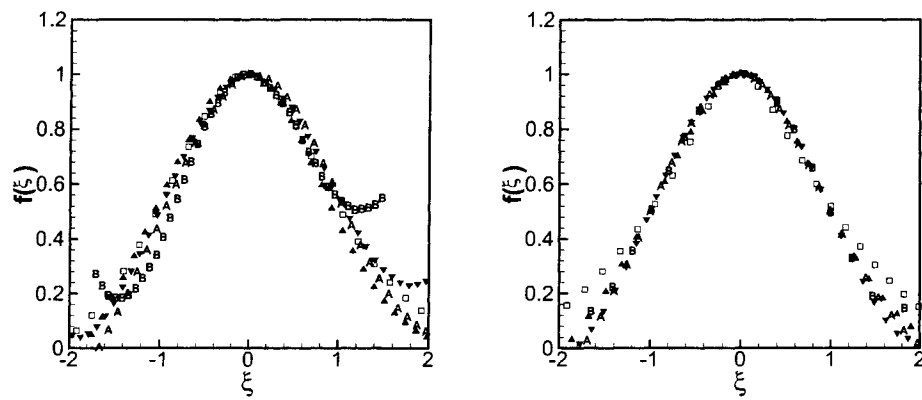


Figure 3.8 Normalized velocity defect measured by PIV (left) and predicted by RANS (right). \square , $x/d = 1.0$; \blacktriangle , $x/d = 4.5$; \triangle , $x/d = 7.5$; \blacktriangledown , $x/d = 12$; \circ , $x/d = 15$.

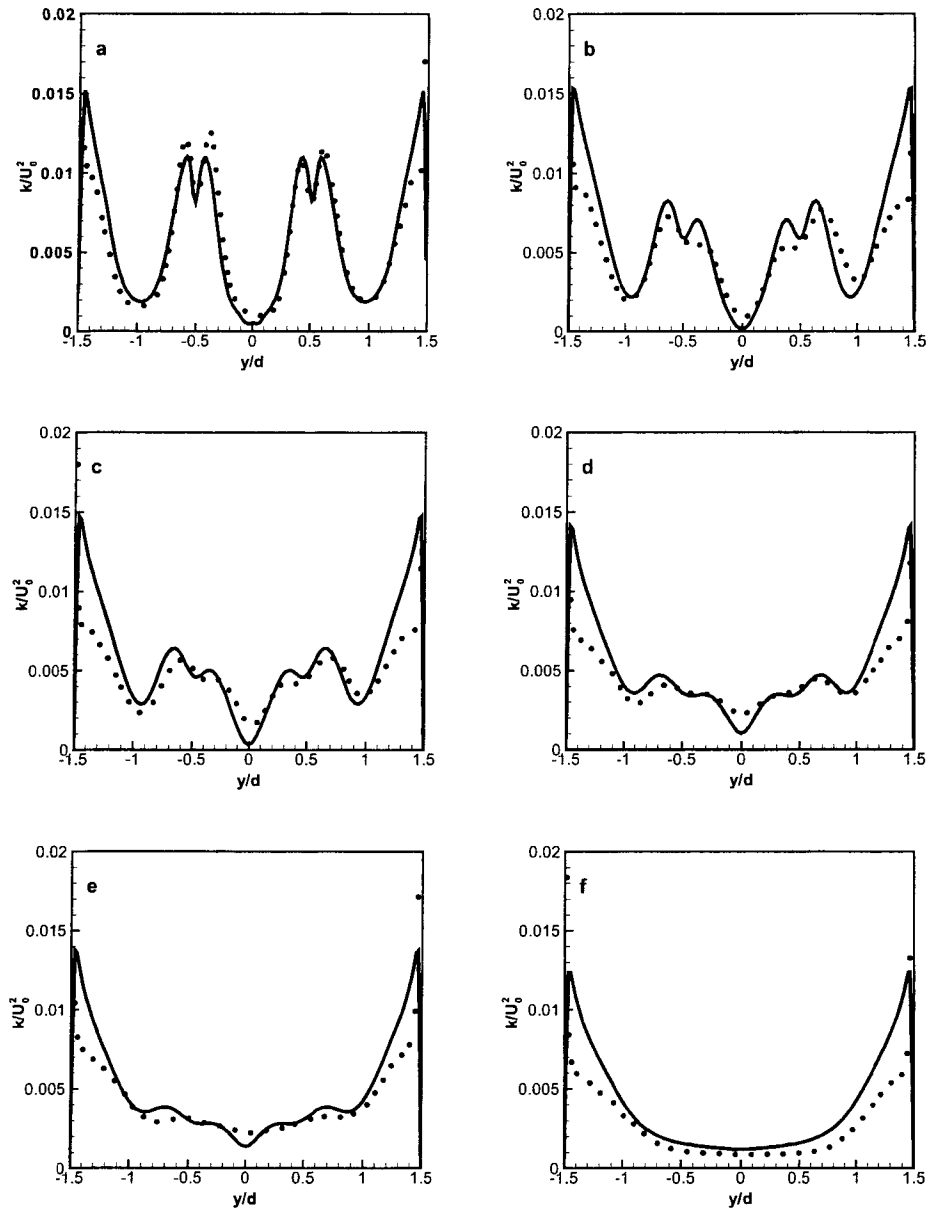


Figure 3.9 Comparison of the turbulent kinetic energy profiles measured by PIV (\bullet) and calculated from RANS code ($—$) for (a) $x/d = 1$, (b) $x/d = 4.5$, (c) $x/d = 7.5$, (d) $x/d = 12$, (e) $x/d = 15$ and (f) $x/d = 30$.

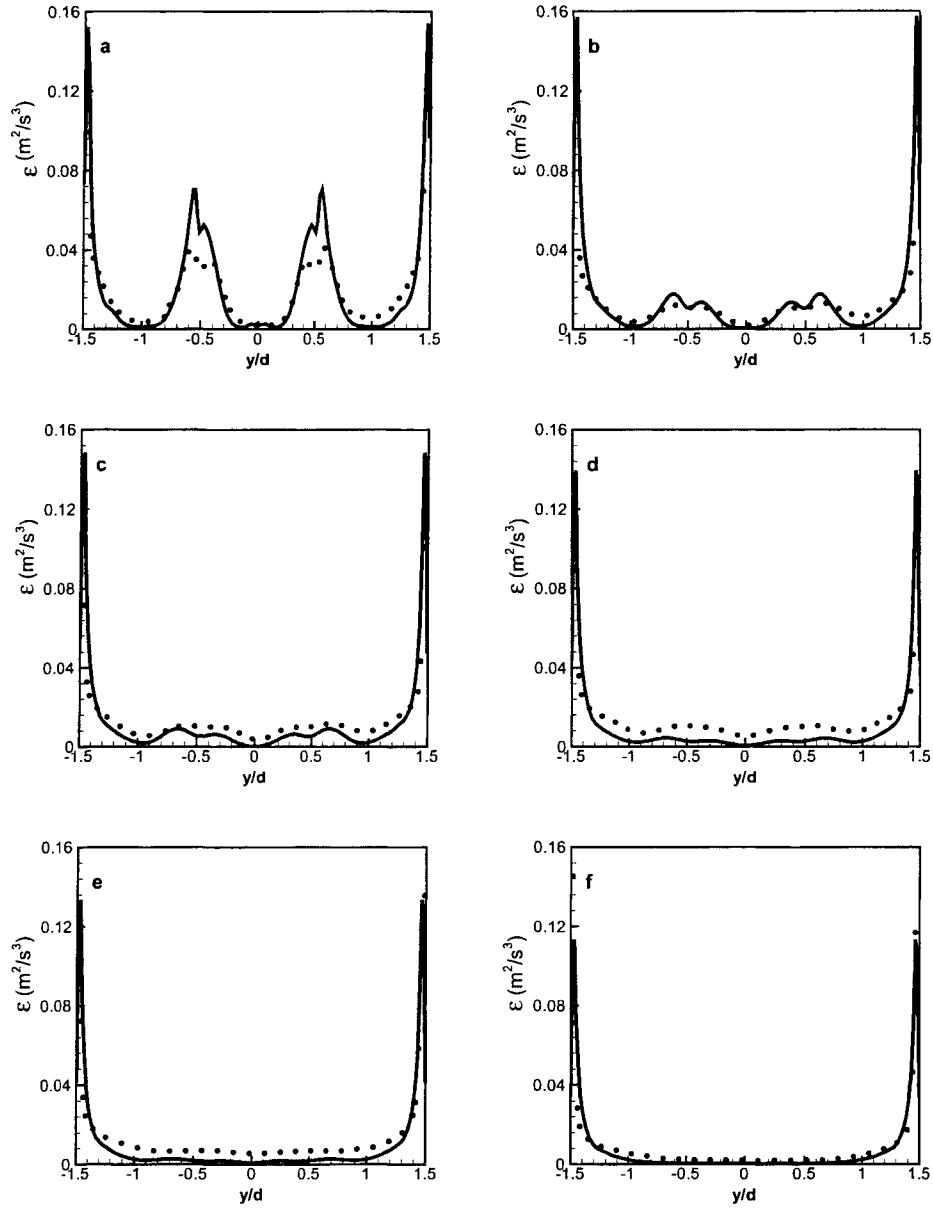


Figure 3.10 Comparison of dissipation rate profiles as measured by PIV (●) and as calculated from RANS code (—) for (a) $x/d = 1$, (b) $x/d = 4.5$, (c) $x/d = 7.5$, (d) $x/d = 12$, (e) $x/d = 15$ and (f) $x/d = 30$.

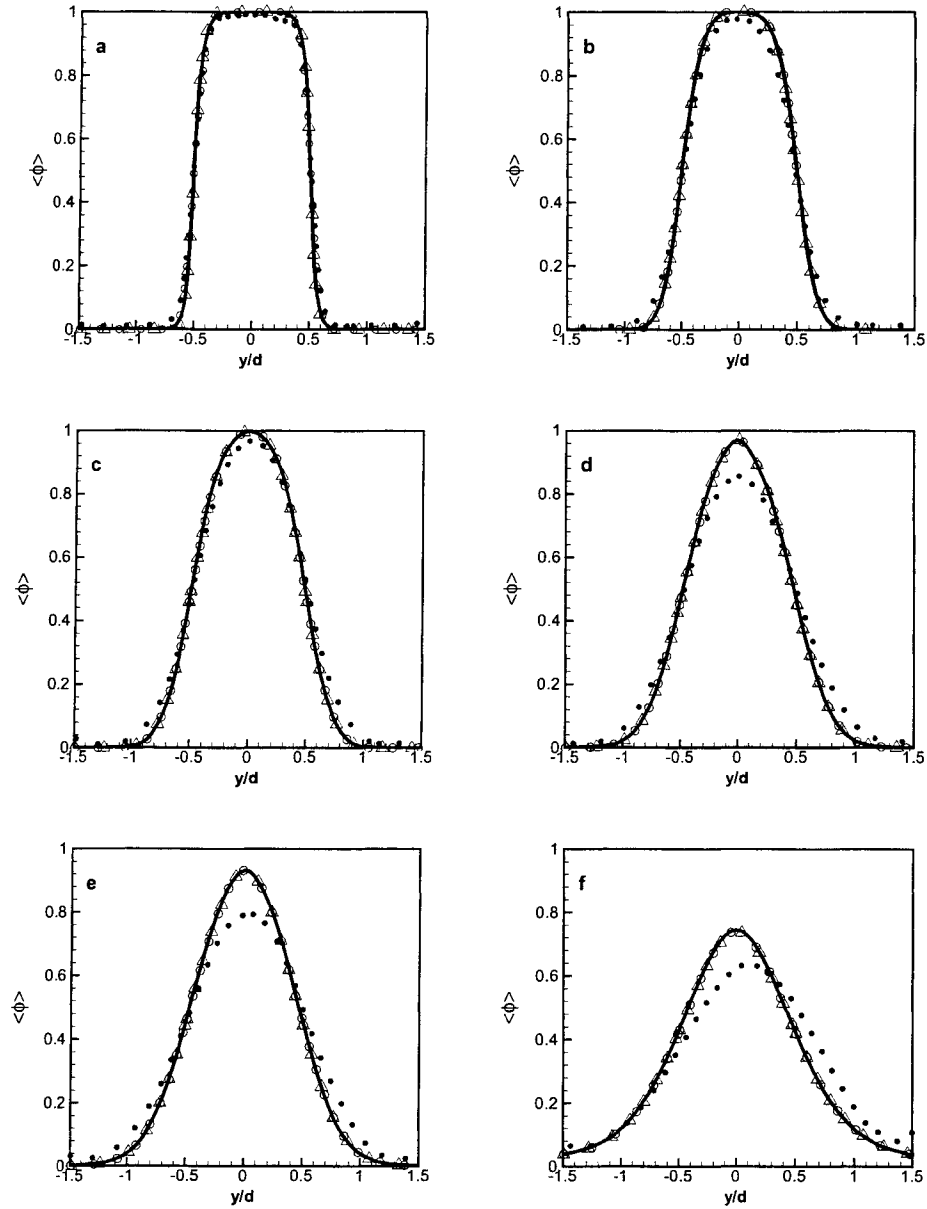


Figure 3.11 Comparison of mixture-fraction mean profiles measured by PLIF (\bullet) and calculated from RANS code ($—$), IEM model (Δ) and EMST model (\circ) for (a) $x/d = 1$, (b) $x/d = 4.5$, (c) $x/d = 7.5$, (d) $x/d = 12$, (e) $x/d = 15$ and (f) $x/d = 30$.

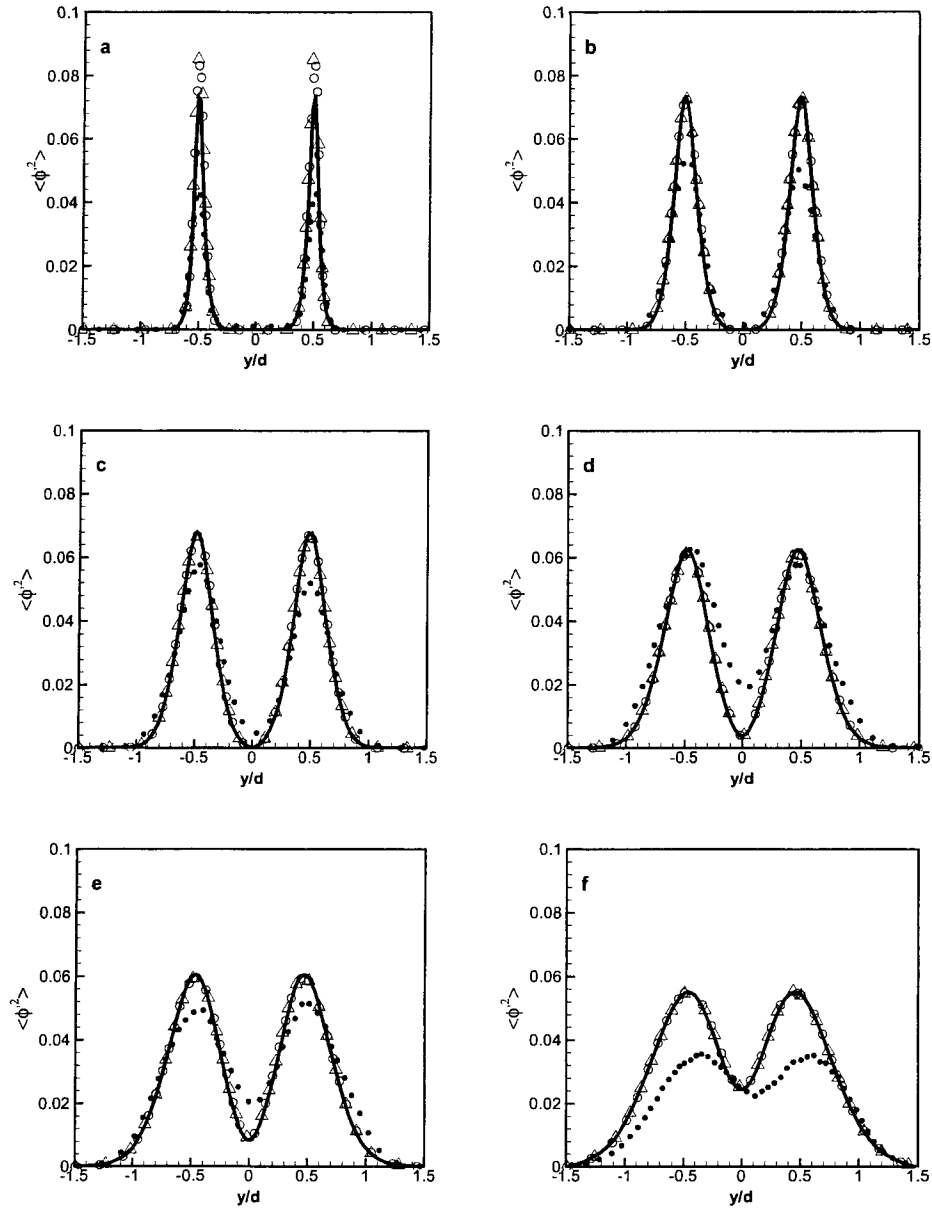


Figure 3.12 Comparison of mixture-fraction variance profiles measured by PLIF (\bullet) and calculated from RANS code ($—$), IEM model (Δ) and EMST model (\circ) for (a) $x/d = 1$, (b) $x/d = 4.5$, (c) $x/d = 7.5$, (d) $x/d = 12$, (e) $x/d = 15$ and (f) $x/d = 30$.

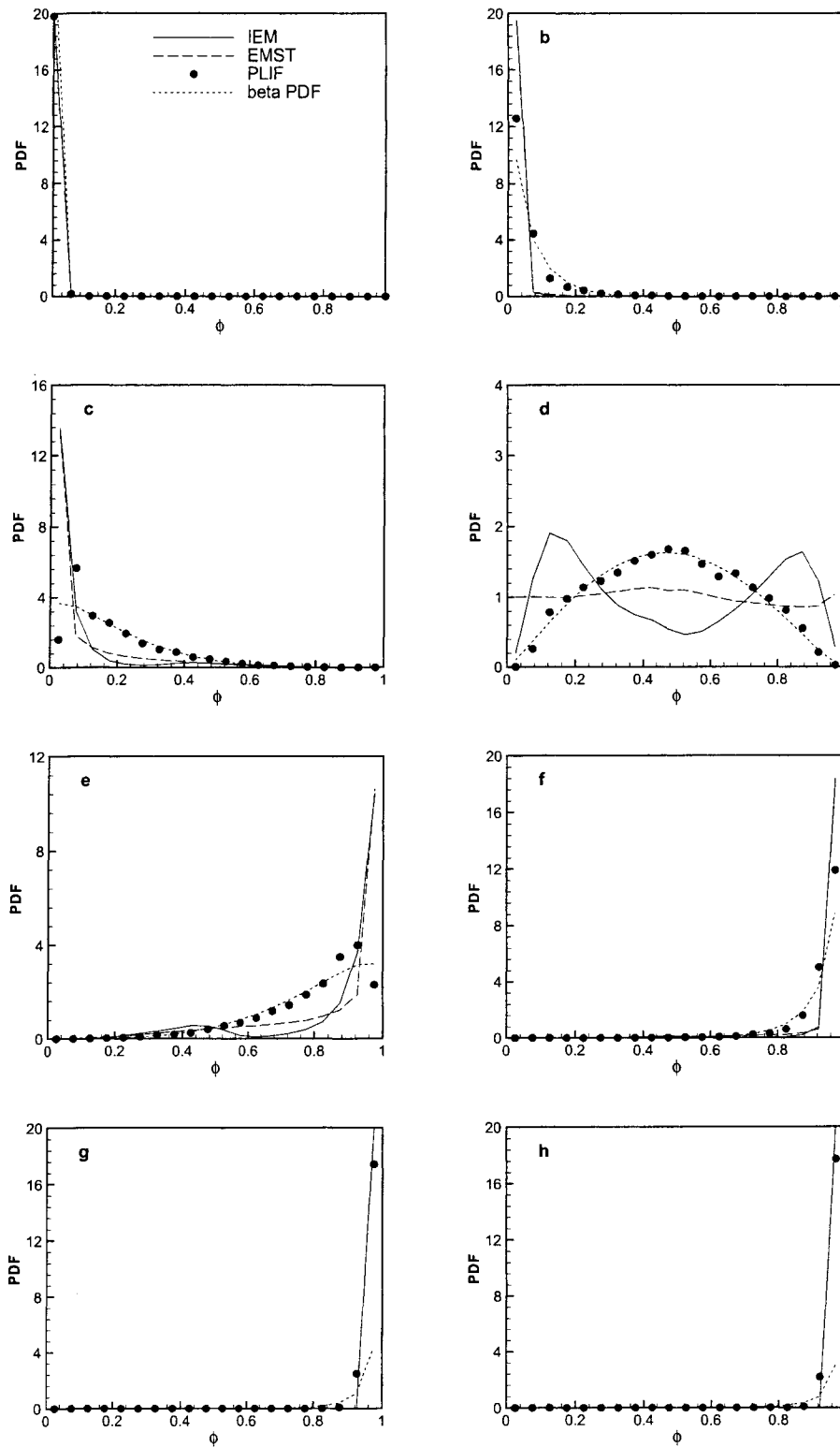


Figure 3.13 Comparison of one-point composition PDF measured by PLIF and calculated from PDF code for $x/d = 1$ at transverse distances from the centerline by (a) $3\delta/2$, (b) $5\delta/4$, (c) $9\delta/8$, (d) δ , (e) $7\delta/8$, (f) $3\delta/4$, (g) $\delta/2$ and (h) 0.

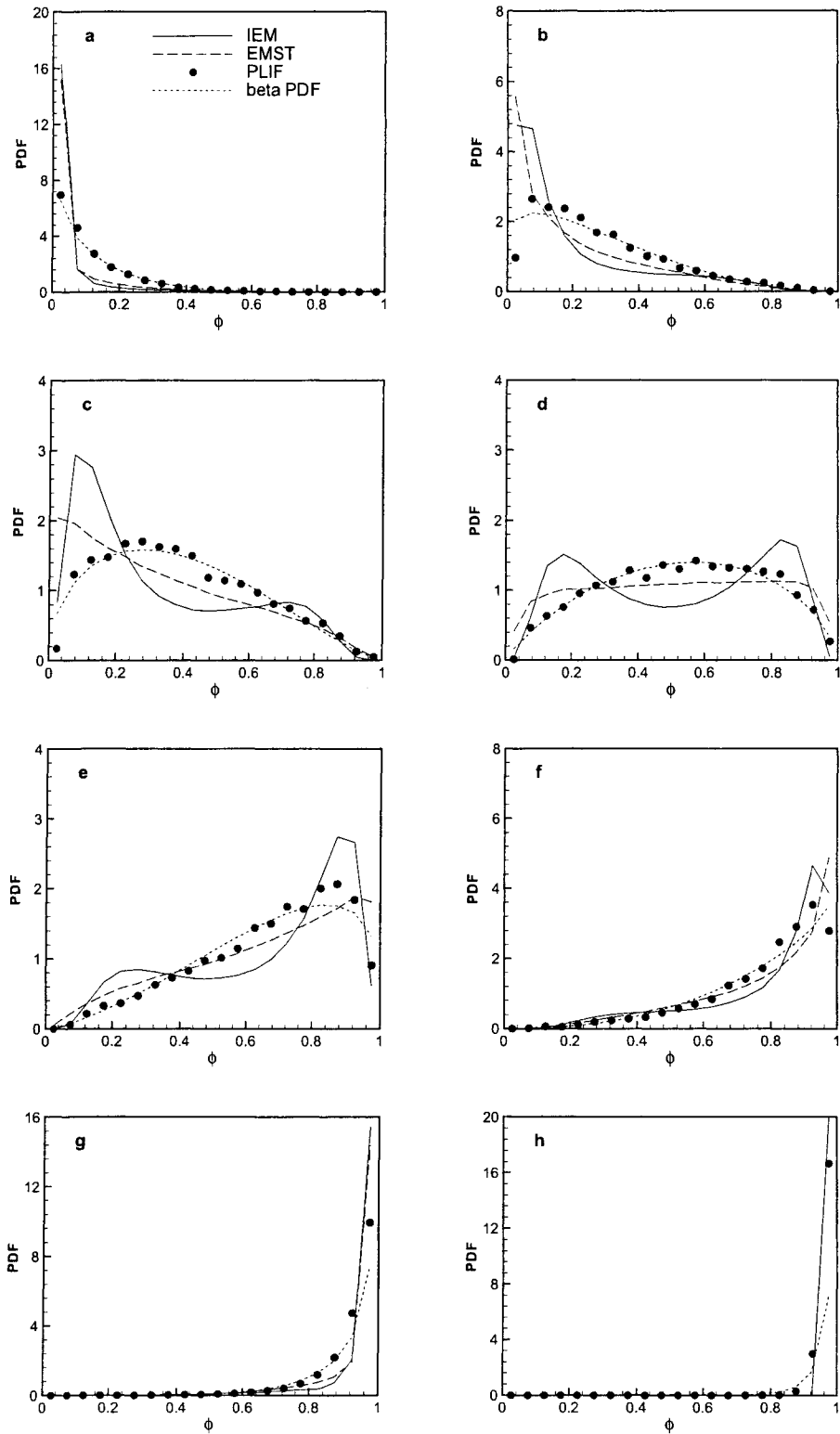


Figure 3.14 Comparison of one-point composition PDF measured by PLIF and calculated from PDF code for $x/d = 4.5$ at transverse distances from the centerline by (a) $3\delta/2$, (b) $5\delta/4$, (c) $9\delta/8$, (d) δ , (e) $7\delta/8$, (f) $3\delta/4$, (g) $\delta/2$ and (h) 0.

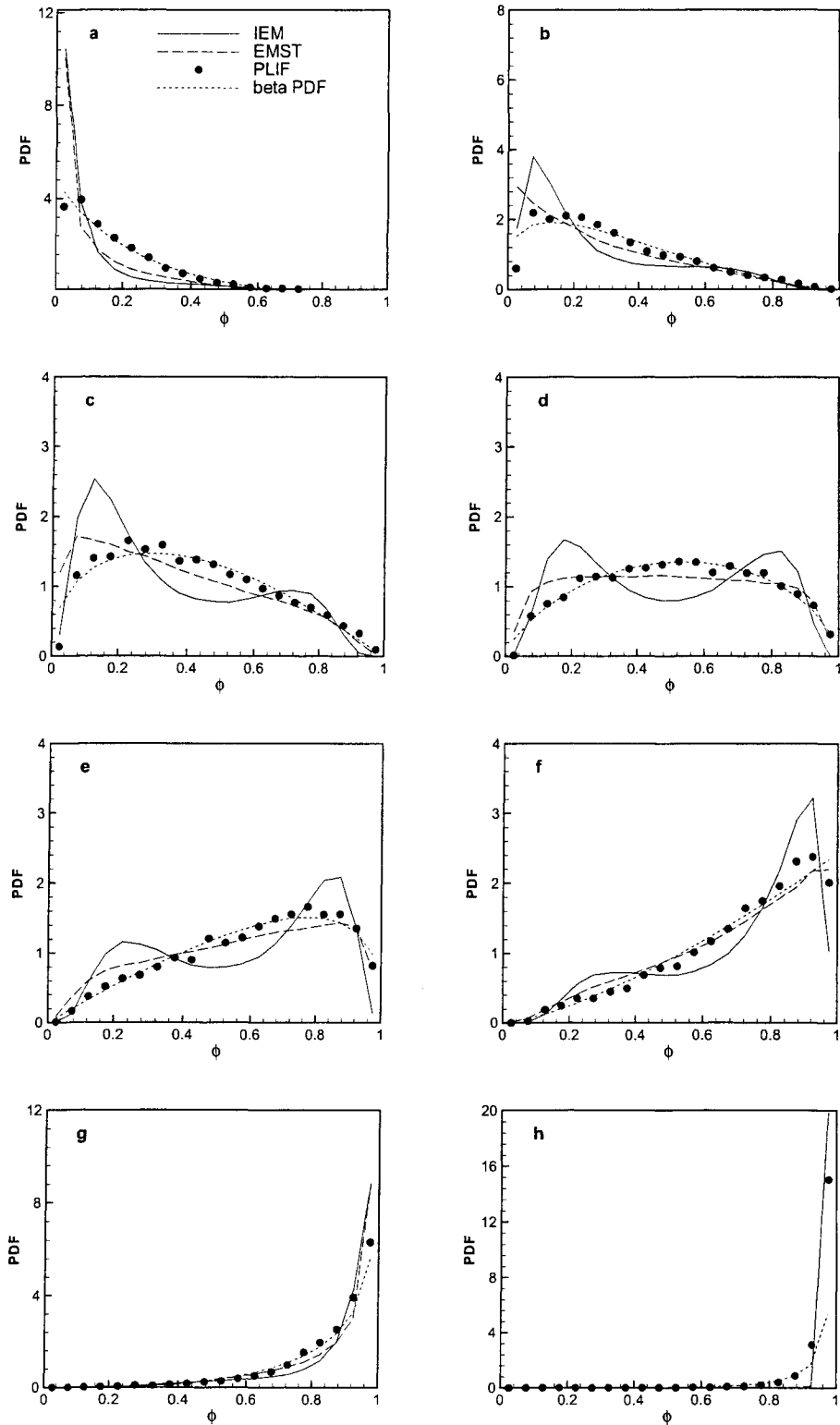


Figure 3.15 Comparison of one-point composition PDF measured by PLIF and calculated from PDF code for $x/d = 7.5$ at transverse distances from the centerline by (a) $3\delta/2$, (b) $5\delta/4$, (c) $9\delta/8$, (d) δ , (e) $7\delta/8$, (f) $3\delta/4$, (g) $\delta/2$ and (h) 0.

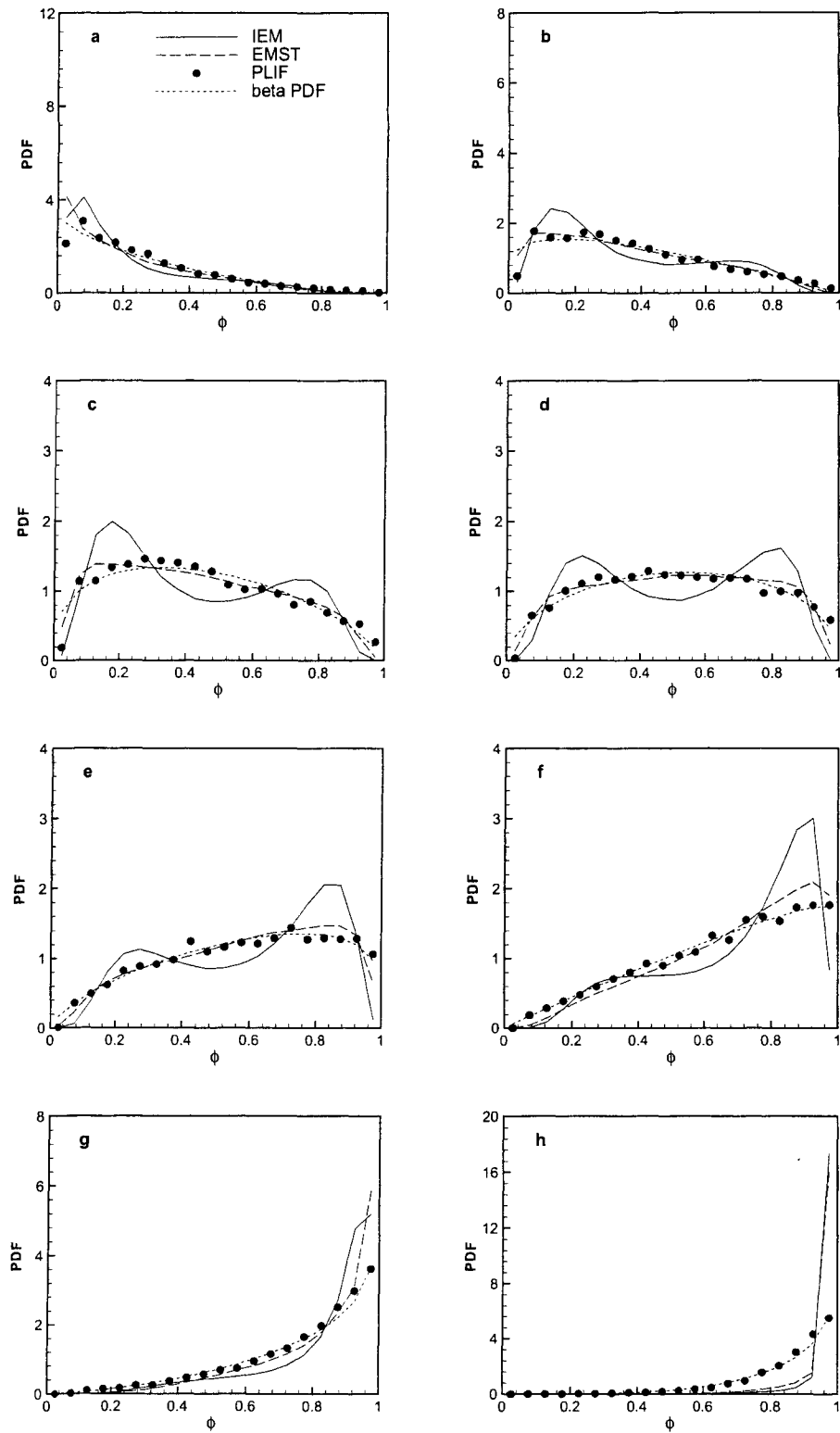


Figure 3.16 Comparison of one-point composition PDF measured by PLIF and calculated from PDF code for $x/d = 12$ at transverse distances from the centerline by (a) $3\delta/2$, (b) $5\delta/4$, (c) $9\delta/8$, (d) δ , (e) $7\delta/8$, (f) $3\delta/4$, (g) $\delta/2$ and (h) 0.

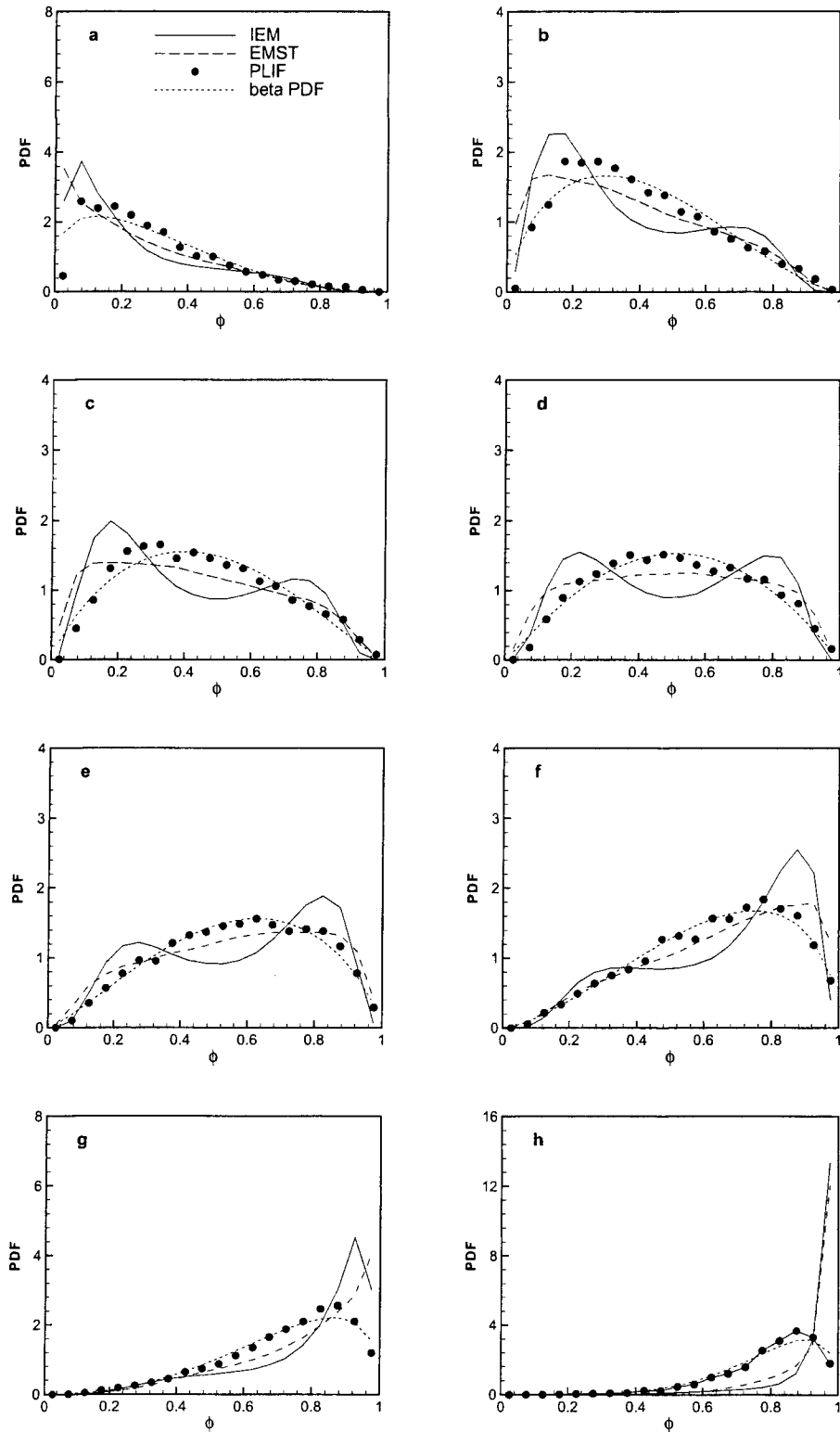


Figure 3.17 Comparison of one-point composition PDF measured by PLIF and calculated from PDF code for $x/d = 15$ at transverse distances from the centerline by (a) $3\delta/2$, (b) $5\delta/4$, (c) $9\delta/8$, (d) δ , (e) $7\delta/8$, (f) $3\delta/4$, (g) $\delta/2$ and (h) 0.

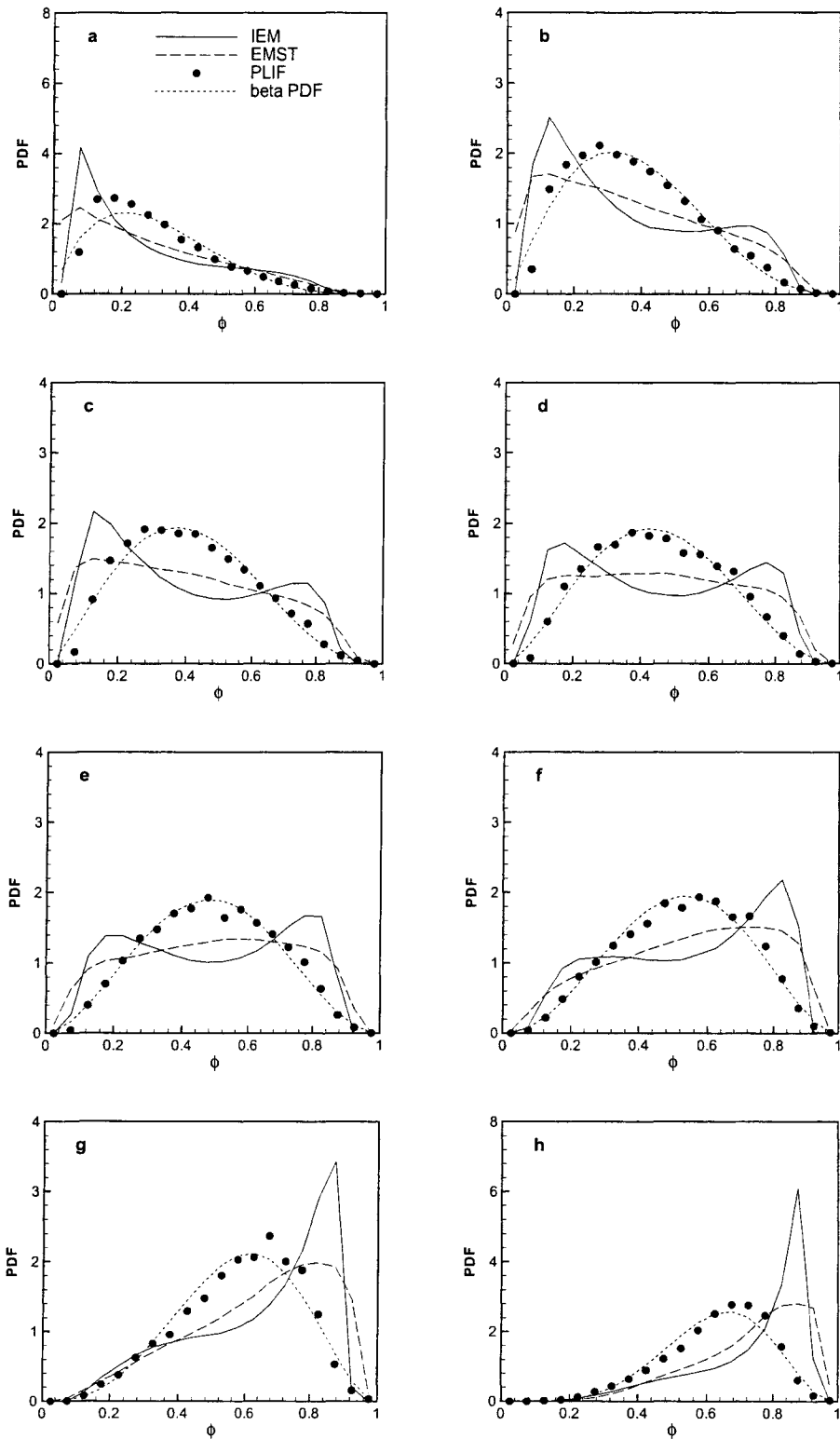


Figure 3.18 Comparison of one-point composition PDF measured by PLIF and calculated from PDF code for $x/d = 30$ at transverse distances from the centerline by (a) $3\delta/2$, (b) $5\delta/4$, (c) $9\delta/8$, (d) δ , (e) $7\delta/8$, (f) $3\delta/4$, (g) $\delta/2$ and (h) 0.

CHAPTER 4 SIMULTANEOUS VELOCITY AND CONCENTRATION FIELD MEASUREMENTS OF PASSIVE-SCALAR MIXING IN A CONFINED RECTANGULAR JET

A paper submitted to *Experiments in Fluids*

Hua Feng, Michael G. Olsen, James C. Hill and Rodney O. Fox

Abstract

Simultaneous velocity and concentration fields in a confined liquid-phase rectangular jet with a Reynolds number based on the hydraulic diameter of 50,000 (or 10,000 based on the velocity difference between streams and the jet exit dimension) and a Schmidt number of 1,250 were obtained by means of a combined particle image velocimetry (PIV) and planar laser-induced fluorescence (PLIF) system. Data were collected at the jet exit and six further downstream locations. The velocity and concentration field data were analyzed for flow statistics such as mean velocity, Reynolds stresses, turbulent kinetic energy, concentration mean and variance, turbulent fluxes, turbulent viscosity and diffusivity, and turbulent Schmidt number (Sc_T). The streamwise turbulent flux was found to be larger than the transverse turbulent flux, and the mean concentration gradient was not aligned with the turbulent flux vector. The average Sc_T was found to vary both in streamwise and in cross stream directions and had a mean value around 0.8, a value consistent with the literature. The self-similarity of the jet was also examined, showing that the mean transverse velocity achieves self-similarity but the Reynolds stresses do not, behavior different than that for free rectangular jets.

Spatial correlation fields of turbulent fluxes and concentration were then determined. The $R_{u'\phi'}$ correlation was elliptical in shape with a major axis tilted downward with respect to the

streamwise axis, whereas the $R_{v'\phi'}$ correlation was a horizontally oriented ellipse. Negative regions of $R_{u'\phi'}$ were observed in the outer streams, and these negatively correlated regions decayed with downstream distance and finally disappeared altogether. The $R_{\phi'\phi'}$ correlation field was found to be an ellipse with the major axis inclined at about 45-degrees with respect to the streamwise direction.

Linear stochastic estimation was used to interpret spatial correlation data and to determine conditional flow structures. It is believed that a vortex street formed near the splitter plate is responsible for the negatively correlated region observed in the $R_{u'\phi'}$ spatial correlations of turbulent fluxes. A positive concentration fluctuation event was observed to correspond to a finger of nearly uniform concentration fluid reaching out into the free stream, whereas a negative event corresponds to a pocket of nearly uniform fluid being entrained from the outer stream into the center jet region. Large-scale vortical structures were observed in the conditional velocity fields with an elliptical shape and a streamwise major axis. The growth of the structure size increased linearly initially but then grew more slowly as the flow transitioned towards channel flow.

Introduction

The study of turbulent jet flows is of importance due to the presence of turbulent jets in a very wide variety of engineering applications. One application where turbulent jets prominently appear is in industrial chemical reactors. Since the product distribution of chemical processes is significantly affected by turbulent transport, a detailed understanding of the mixing properties in turbulent jet flows is a critical step towards the development of environmentally benign, commercially efficient chemical technologies.

By virtue of its ability to quickly generate flow field predictions in complex geometries at a relatively low cost, computational fluid dynamics (CFD) has become a promising tool in recent years for chemical process engineers for flow field analysis and reactor design [Fox (2003)]. However, in order to avoid costly mistakes on scale up, it is vital that CFD models be validated against experimental data. Thus, experimental studies are still of great importance

in both advancing turbulence theory and in the development and validation of CFD models. The primary purpose of this work is to implement state-of-the-art experiment techniques to study the behavior and characteristics of turbulent mixing in a confined rectangular jet.

Because of their great importance, turbulent shear flows have been the subject of extensive study throughout the years. One of the most important studies was the seminal work on incompressible mixing layers of Brown and Roshko (1974), who observed large-scale organized motions in their visualization studies on turbulent planar mixing layers. Since then, a number of investigations have demonstrated the importance of these coherent structures in both momentum transport and chemical mixing in turbulent flows. The presence of coherent structures in turbulent jets has also been realized in previous investigations (for example, see Antonia et al. (1983); Thomas and Goldschmidt (1986); Tso and Hussain (1989); Gordeyev and Thomas (2000)). Unlike in mixing layers, however, the nature of coherent structures in turbulent jets is not fully established. This is partly because the energy content of coherent motion in jets is lower than mixing layers (about 10%, compared to 20%), making recognition of structures more difficult in jets [Fiedler (1987); Agrawal and Prasad (2002)].

A number of researchers have employed non-simultaneous PIV and PLIF in the studies on turbulent jets. For example, Agrawal and Prasad (2002) investigated the large-scale vortices in an axisymmetric free turbulent jet. They argued that large vortices tend to organize themselves in preferred modes. Ring and helical modes seem to occur prominently in jets, with the helical mode being the more frequent. The overall diameter of both ring and helical modes is comparable with the local jet width. Dahm and Dimotakis (1987) applied laser-induced fluorescence (LIF) to study an axisymmetric free turbulent jet in water. Their results indicate that the entrainment and mixing processes in the jet display a roughly periodic organization characterized by temporal and spatial scales approximately equal to the local large scales of the flow. The instantaneous profiles show that unmixed ambient fluid is transported deep into the jet, and that the mixed fluid composition can be fairly uniform within large regions. By means of PLIF, Guillard et al. (2000) measured the concentration field in a confined turbulent impinging jet. The mean concentration structure in the center plane of the jet was determined

and compared with both large eddy simulations (LES) and data from the literature. The agreement between the results was good.

The steady-state Reynolds-averaged equation for the conservation of the mean concentration of a passive scalar is given by

$$\langle u_i \rangle \frac{\partial \langle \phi \rangle}{\partial x_i} - \frac{1}{ReSc} \frac{\partial^2 \langle \phi \rangle}{\partial x_i \partial x_i} = - \frac{\partial \langle u_i \phi' \rangle}{\partial x_i} \quad (4.1)$$

where Re is the Reynolds number, Sc is the Schmidt number, and u_i and ϕ denote the instantaneous velocity and instantaneous concentration, respectively. Note that the correlations of the velocity fluctuation and the concentration fluctuation (i.e., turbulent fluxes), such as $\langle u' \phi' \rangle$ and $\langle v' \phi' \rangle$, are modeled in a RANS simulation. Therefore, the development and validation of CFD models for these terms require the simultaneous measurement of velocity and concentration.

Law and Wang (2000) performed measurements of turbulent-mixing processes in a turbulent round jet discharging into a stagnant environment. Their study demonstrated that PIV and PLIF can be combined successfully to capture both the time-averaged mean and turbulent mass-transport characteristics. They also investigated the potential interference effect between these two techniques and found that the interference of the fluorescent tracer on PIV is negligible, whereas the effect of the seeding particles on PLIF can be attributed to three factors: the attenuation of the laser light that can be described by the Beer-Lambert law, the interaction with the dye tracer leading to a small increase of local fluorescence, and the residual Mie scattering light that passes the PLIF filter. Fukushima et al. (2000) made detailed measurements for the mixing of a passive scalar in an axisymmetric turbulent free jet utilizing a combined PIV and LIF method. In order to examine the reliability of their data set, they compared these results with not only the results from DNS, but also with pointwise velocity measurements, and combined PIV, particle tracking velocimetry (PTV), and laser Doppler velocimetry (LDV) and LIF measurements. The agreement between the various techniques was found to be satisfactory.

In the work of Kothnur and Clemens (2001), simultaneous PIV and PLIF were used to study the dissipative length scales in a near unity Schmidt number turbulent planar jet

flow. The results indicate that it is impossible to model the dissipation layers as an ensemble of 1-D steady, strained laminar diffusion layers, and the alignment of the principal strain rate is orthogonal to the dissipation-layer normal vector in most of the cases. Tsurikov and Clemens (2002) also investigated the structure and dynamics of the dissipative scales using PIV and PLIF of a conserved scalar with $Sc = 1.5$ in an axisymmetric turbulent jet. They claimed that scalar dissipation layers have thickness ranging from approximately 1η to 6η . Kinetic energy dissipative structures are thicker, with thickness ranging from approximately 1η to 10η (η denotes the Kolmogorov scale).

Although a large body of experimental data exists for turbulent shear flows, detailed simultaneous measurement of velocity and concentration fields inside a confined jet is less common in the literature. The objective of the present study was to develop a combined PIV and PLIF system and obtain a comprehensive view of the velocity and concentration fields in a liquid-phase confined turbulent rectangular jet. In the present work, detailed simultaneous measurements were made along the center plane between the front and back walls of the test section, and turbulent statistics, such as the mean and fluctuating velocity, mean concentration, concentration fluctuating intensity, turbulent fluxes, *etc.*, were determined from the data. Also, the velocity and concentration fields were analyzed to provide insight into the characteristics and behavior of large-scale structures found in the turbulent jet.

The remainder of the paper is organized as follows. Section 2 is devoted to describing the rectangular-jet flow facility and the experimental methodology. In Sec. 3, we introduce the methodology used to determine stochastic estimates of velocity and concentration fields. Results from the experimental study and the properties of large-scale structures are presented and discussed in Sec. 4. Finally, the major conclusions of this work are given in Sec. 5.

Experimental Apparatus and Methodology

Flow Facility

The experimental flow system and test section used in the experiments presented here are shown in Figs. 4.1 and 4.2, respectively. The flow system is designed to provide a shear flow

with a Reynolds number based on the channel hydraulic diameter between 5,000 and 100,000. The measurements are carried out in a Plexiglas test section with a rectangular cross-section measuring 60 mm by 100 mm and with an overall length of 1 m. The width of each of the inlet channels is 20 mm and the aspect ratio of the rectangular jet is 5. The test section is mounted in an adjustable cage so that it can be moved up and down to change the measurement location without moving the optics of the measurement system. Three Fisher feedback control systems with flow accuracy of $\pm 0.5\%$ are used to supply constant flow rates to the three inlet channels.

Four 1750 liter tanks are incorporated into the flow facility. Two of these tanks serve as reservoirs for the incoming streams and supply the flow into the test section. The other two tanks are used to collect the mixed fluid as it exits the test section and temporarily store it. The purpose of these storage tanks is to store potentially harmful products so that they can be neutralized before being drained into the environment.

Flow conditioning consisting of a packed bed of 1 cm diameter spheres, turbulence reducing screens, and a pair of 4:1 contractions (resulting in an overall contraction ratio of 16:1) creates uniform flow and reduces free-stream turbulence intensities in the incoming free streams before they enter the test section (more details on the experimental apparatus can be found in Feng et al. (2005)). For the present study, the volumetric flow rates of each of the inlet channels were 1.0, 2.0 and 1.0 liters/s, corresponding to free stream velocities of 0.5 m/s, 1.0 m/s, and 0.5 m/s. The Reynolds number based on the hydraulic diameter of the test section and the bulk velocity was 50,000 (or 10,000 based on the velocity difference between streams and the jet exit dimension).

Velocity Measurements

PIV was used to measure instantaneous velocity fields in a planar cross section of the flow field. The flow was seeded with hollow glass spheres (Spherical, Potters Industries, Inc.) with a nominal diameter of 11.7 μm and a density of 1.1 g/cm^3 . The particles were added to the reservoir tanks before performing the measurements and mixed by running the pumping system in recycle mode until the particles were distributed homogeneously. About 24 grams of seed

particles were added to the total reservoir volume of 3500 liters.

Illumination was provided by a New Wave Research Gemini PIV laser. The Gemini is a double-pulsed Nd:YAG laser that emits two independent 532 nm light pulses. The maximum pulse energy is 120 mJ and the pulse duration is about 5 ns. A time delay between the two laser pulses of 600 μ s was used in the present study. Using a combination of mirrors and cylindrical and spherical lenses, the laser beam is directed towards the test section and formed into a thin light sheet with a minimum thickness of about 0.5 mm passing through the test section at the centerline in the z -direction. The waist of the light sheet was located near the test section centerline in the y -direction.

Images of the seeded flow were obtained using a 12-bit LaVision Flowmaster 3S CCD camera with a resolution of 1280×1024 pixels. The laser and cameras were connected to a host computer that controlled the timing of the laser illumination and image acquisition. For the PIV measurements, the image magnification was 0.12, and the numerical aperture was 8. Two images were captured per realization, and the corresponding velocity field was computed using a cross-correlation technique. A multi-pass interrogation scheme with decreasingly smaller window sizes was used with a final interrogation spot size measuring 16 pixels by 16 pixels, corresponding to 0.9 mm on a side. With 50% overlap between adjacent interrogation spots, the velocity vector spacing was 0.45 mm in both the x - and y -directions.

The Kolmogorov scale is the characteristic scale of the smallest turbulent motions [Kolmogorov (1941)] and is defined by $\eta = (\nu^3/\epsilon)^{1/4}$ where ν is the molecular kinematic viscosity and ϵ is the dissipation rate of turbulent kinetic energy. Table 4.1 presents the Kolmogorov scales and the spatial resolution of the PIV measurements in terms of the Kolmogorov scales in this work. In order to estimate the Kolmogorov scales, the following equation [Tennekes and Lumley (1972)] was used to approximate ϵ :

$$\epsilon \approx A \frac{u_0'^3}{l} \quad (4.2)$$

where A is a constant of order 1 [Antonia et al. (1980)]. We assumed the characteristic fluctuating velocity, $u_0'^3$, equals the square root of 2/3 of the maximum turbulent kinetic energy at each downstream location, and used the jet width to approximate the integral length scale,

l. As Table 4.1 shows, the spatial resolution of the PIV measurements is between 7.8η and 11.3η .

The accuracy of PIV measurements is affected by errors introduced during the recording of the images and bias introduced by large velocity gradients [Keane and Adrian (1992)]. The maximum uncertainty in determining the displacement of seed particles between laser pulses (and hence, the uncertainty of the PIV measurements) can be conservatively estimated as one-tenth of the particle image diameter [Prasad et al. (1992)]. The center free-stream velocity corresponds to a displacement of $600\ \mu\text{m}$ and the outer-free stream velocities correspond to a displacement of $300\ \mu\text{m}$, resulting in an experimental uncertainty of $\pm 1.6\%$ for the center stream and $\pm 3.2\%$ for the outer streams.

Peak locking [Christensen (2004)] is a potential problem in PIV experiments in which measured particle displacements can become biased towards integer pixel displacements. The peaking-locking effect in any given PIV experiment can be quantified by determining the *peak-locking coefficient* [Stanislas et al. (2005)]. For the results presented here, this coefficient was found to be 0.08, indicating an acceptably low degree of peak locking.

Concentration Measurements

The instantaneous concentration field was measured with PLIF using the same laser illumination system as in the PIV measurements but with a separate Flowmaster 3S CCD camera. The fluorescent dye Rhodamine 6G was used as a passive scalar. The Schmidt number of Rhodamine 6G in water is 1,250 [Crimaldi and Koseff (2001)]. Rhodamine 6G emits broadband fluorescence with a peak emission around a wavelength of 555 nm when excited by the 532 nm light emitted by a frequency-doubled Nd:YAG laser [Penzkofer and Leupacher (1987)]. In the center stream, the source concentration of Rhodamine 6G was $45\ \mu\text{g}/\text{liter}$, while the other two streams were pure water.

The image magnification of the PLIF measurements was 0.12, and the numerical aperture was 5.6. For the lens and aperture used in the PLIF experiments, the diffraction-limited spot size of the imaging system corresponded to $8.1\ \mu\text{m}$ [Adrian and Yao (1983)]. However, the

in-plane spatial resolution of the PLIF measurements in the present study was actually limited by the flow area imaged per pixel, which was approximately $56 \mu\text{m}$. The smallest length scale of turbulent mixing is known as the Batchelor scale [Batchelor (1959)], which is defined by $\eta_B = \eta/\sqrt{Sc}$. As Table 4.2 shows, the resolution of PLIF measurements is much larger than the Batchelor scale in all directions, therefore the smallest concentration scale can not be resolved in the present study.

Preliminary PLIF experiments were performed to calibrate the fluorescent dye and to determine if the shot-to-shot variability of the laser was a concern. This was done by performing PLIF measurements on fixed concentrations of dye in a small Plexiglas tank with identical cross-sectional area to the test section. Since the dye concentration in each measurement was constant, any measured concentration fluctuations could only be due to a combination of shot-to-shot laser variation and camera noise. In these experiments, the measured variation in dye concentration was approximately 2%, indicating that the shot-to-shot laser power was remarkably steady. Thus, it was deemed unnecessary to monitor the shot-to-shot laser power variations during the PLIF experiments.

Nd:YAG lasers have a Gaussian energy distribution, so it is impossible to obtain a uniform energy distribution throughout the entire light sheet. This drawback can be significant for PLIF that is based on light intensity [Law and Wang (2000)]. Moreover, the intensity of a laser beam decays as it passes through a dye solution due to absorption. Crimaldi and Koseff (2001) claimed that under appropriate experimental conditions, the local intensity of fluoresced light is proportional to the local intensity of the excitation source and the local concentration of the fluorescent dye. In the present study, we found that this relationship was valid for dye concentrations up to $100 \mu\text{g/liter}$ with our experimental setup.

To eliminate the variation of the local intensity due to the Gaussian nature of the beam, the following procedure was used to calibrate the concentration measurements. First, a series of 1000 dark images was taken and averaged at each pixel to determine the gray offset value distribution in the image field, and this was used to remove the dark field component from each PLIF image. Then, variations in illumination intensity were normalized for by filling the

test section with the dye solution and recording a series of 200 *in situ* calibration images at each measurement location. The instantaneous PLIF images at each measurement location were then normalized for illumination variations using the mean of the calibration images.

Combined PIV and PLIF System

A schematic depicting the combined PIV and PLIF measurement system is also shown in Fig. 4.1. The PLIF camera was aligned perpendicular to the laser sheet, whereas the PIV camera was placed parallel to the laser sheet. The positions of the two cameras were carefully adjusted so that the areas viewed by each camera overlapped, and the separate images formed by the two cameras were then registered so the coordinates describing space in both images were matched. Note that the light exiting from the test section consists of both laser light scattered by the seed particles and light emitted by the fluorescent dye, and thus the optical system had to be designed to separate these two image components. This was accomplished by first using a dichroic mirror placed at an angle of 45° to the laser sheet to separate the scattered and emitted components of the light and direct these separated components to either the PIV or the PLIF camera. In accordance with the proposed coordinate system, all mirror images captured by the PIV camera were inverted horizontally before being analyzed.

To ensure the cleanest possible PIV and PLIF images, filters were attached to both the PIV and the PLIF camera lenses. The PLIF camera lens was fitted with a long-pass (i.e., low pass for frequency) optical filter that blocked light below 555 nm. The purpose of this filter was to both clean up any laser light that may have passed through the dichroic mirror and also to remove any background laser light from diffuse reflections off surfaces. Likewise, a narrow-band-pass optical filter centered at 532 nm was attached to the PIV camera lens to filter out any stray light emitted by the fluorescent dye.

The PLIF camera was set in single-exposure mode with an exposure time of 500 μs . Kolmogorov time scales at the investigated locations, defined by $\tau = (\nu/\epsilon)^{\frac{1}{2}}$, are given in Table 4.1. Since the duration of the combined PIV/PLIF measurement was very small in comparison to the Kolmogorov time scale in the present study, the PIV and PLIF measurements could

be considered to be simultaneous. The simultaneous PIV and PLIF images were captured at a frame rate of 1 image/sec. Due to the limited volume of holding tanks, 650 sets of images (consisting of two PIV frames and one PLIF frame) were captured in one run. To obtain more realizations, 5 runs of measurements were carried out at each observed location under the same experimental conditions. Therefore, 3250 sets of simultaneous images in total were acquired and analyzed at each observation location.

Stochastic Estimation of Velocity and Concentration Fields

Linear stochastic estimation (LSE) has proven to be a useful tool to reduce the large-scale structure in turbulent flows [Adrian (1994)]. Linear stochastic estimation is a method for determining conditional averages based on some defining event and offers several distinct advantages compared to calculating conditional averages directly from a collected data set. One such advantage is that, using linear stochastic estimation, conditional averages can often be determined using far smaller data sets than would be necessary to determine the conditional averages directly from the measured data. This is because linear stochastic estimation reconstructs a conditional average in terms of unconditional spatial correlations, thus making use of the entire dataset, and not only the subset of data which contains the specified event. Once the estimation coefficients have been determined, it is a trivial matter to evaluate many different events since the coefficients are independent of the conditional event data [Adrian et al. (1989)].

Any number of criteria can be used for the defining event. In studies consisting only of velocity-field measurements, the conditional event upon which the estimation of velocity fields is based is generally a velocity fluctuation at some location [Prasad and Gonuguntla (1996), Agrawal and Prasad (2002)] or a characteristic value of the deformation tensor [Olsen and Dutton (2002), Olsen and Dutton (2003)]. In the present work, the simultaneous nature of the PIV and PLIF measurements enabled the measurement of spatial correlations of turbulent fluxes and therefore motivated an attempt to predict conditional velocity fields and concentration fields based on an event of the concentration fluctuation.

Stochastic Estimation of Concentration Fields

Suppose that the concentration field is decomposed into a mean and a fluctuating part, such that

$$\phi(\mathbf{x}, t) = \Phi(\mathbf{x}) + \phi'(\mathbf{x}, t) \quad (4.3)$$

where ϕ is the instantaneous concentration, Φ is the ensemble-averaged concentration, and ϕ' is the fluctuation component of concentration. Assuming the mean concentration is known, one can then calculate conditional velocity and concentration fields over the entire field based upon a defining event at some location \mathbf{x}_o (the basis point), and thus determine the corresponding large-scale structure. In the work presented here, a concentration fluctuation event is chosen as the defining event.

Let $\phi'(\mathbf{x}_o)$ be the concentration fluctuation at location \mathbf{x}_o . The stochastic estimate of the concentration fluctuation over the entire field given the condition $\phi'(\mathbf{x}_o)$ is

$$\langle \phi'(\mathbf{x}) | \phi'(\mathbf{x}_o) \rangle = A(\mathbf{x}) + B(\mathbf{x})\phi'(\mathbf{x}_o) + C(\mathbf{x})\phi'^2(\mathbf{x}_o) + \dots \quad (4.4)$$

For a linear estimate, only the first two terms are used, i.e.,

$$\langle \phi'(\mathbf{x}) | \phi'(\mathbf{x}_o) \rangle = A(\mathbf{x}) + B(\mathbf{x})\phi'(\mathbf{x}_o). \quad (4.5)$$

The coefficients A and B must now be determined. The best choice of coefficients would be ones that minimize the mean square error of the estimated concentration field compared to the actual concentration field. Minimizing the mean-square error results in

$$\langle \phi'(\mathbf{x}_o)\phi'(\mathbf{x}) \rangle = B(\mathbf{x})\langle \phi'(\mathbf{x}_o)\phi'(\mathbf{x}_o) \rangle. \quad (4.6)$$

However, $\langle \phi'(\mathbf{x}_o)\phi'(\mathbf{x}) \rangle$ is the (unnormalized) spatial correlation (two-point correlation function) of ϕ' , which we will denote as $\hat{R}_{\phi'\phi'}$. Thus

$$B(\mathbf{x}) = \frac{\hat{R}_{\phi'\phi'}}{\langle \phi'(\mathbf{x}_o)\phi'(\mathbf{x}_o) \rangle}. \quad (4.7)$$

The stochastic estimate of concentration for a given event is then determined by first finding $B(\mathbf{x})$ using the experimentally measured spatial correlation of concentration fluctuation, and then using Eqn 4.5 to estimate the conditional concentration field given the event $\phi'(\mathbf{x}_o)$.

Stochastic Estimation of Velocity Fields

Following a similar derivation to that above for concentration, suppose that the velocity can be decomposed into a mean and fluctuating part, such that

$$u_i = U_i + u'_i \quad (4.8)$$

where u_i is the instantaneous velocity, U_i is the mean velocity, and u'_i is the fluctuating velocity component. Assuming that the mean velocity is known, one can calculate the velocity fluctuations over the entire field based upon the defining event at \mathbf{x}_o to determine the corresponding conditional large-scale structure.

Once again letting $\phi'(\mathbf{x}_o)$ be the concentration at location \mathbf{x}_o , the linear stochastic estimate of the velocity fluctuation over the entire field given the condition $\phi'(\mathbf{x}_o)$ is

$$\langle u'_i(\mathbf{x}) | \phi'(\mathbf{x}_o) \rangle = A_i(\mathbf{x}) + B_i(\mathbf{x})\phi'(\mathbf{x}_o). \quad (4.9)$$

Following a similar manner as before in determining the coefficients results in

$$\langle \phi'(\mathbf{x}_o) u'_i(\mathbf{x}) \rangle = B_i(\mathbf{x}) \langle \phi'(\mathbf{x}_o) \phi'(\mathbf{x}_o) \rangle. \quad (4.10)$$

However, $\langle \phi'(\mathbf{x}_o) u'_i(\mathbf{x}) \rangle$ is the (unnormalized) spatial correlation of ϕ' and u'_i , which we will denote as $\hat{R}_{\phi' u'_i}$, thus

$$B_i(\mathbf{x}) = \frac{\hat{R}_{\phi' u'_i}}{\langle \phi'(\mathbf{x}_o) \phi'(\mathbf{x}_o) \rangle}. \quad (4.11)$$

After solving for $B_i(\mathbf{x})$ Eqn 4.9 can be used to estimate $u'_i(\mathbf{x})$ given the event $\phi'(\mathbf{x}_o)$.

Results and Discussion

The coordinate system used in the work presented here is such that x is in the streamwise direction and y is in the transverse direction. The origin is designated at the center point between the tips of the splitter plates. Figure 4.3(a) shows a typical velocity field from PIV measurements, with a convective velocity of 0.75 m/s subtracted from each vector to aid in the visualization of turbulent structures in this figure. The corresponding concentration field as measured by PLIF is presented in Fig. 4.3(b). In Fig. 4.3(b), the contour levels represent the

concentration normalized by the input source concentration Φ_0 . Turbulent vortices are readily observed in both figures.

Mean Velocities, Reynolds Stresses and Turbulent Kinetic Energy

Profiles of the normalized ensemble-averaged streamwise velocity and Reynolds stresses at the exit of the jet and 6 downstream locations in flow are presented in Fig. 4.4. The mean velocity is normalized by the difference between inlet free-stream velocities of the center stream and side streams, $\Delta U = 0.5$ m/s, and the Reynolds stresses are normalized by $(\Delta U)^2$. The inlet jet width, $d = 20$ mm, is used to normalize the transverse coordinate in plots throughout the presented work. Mean velocity and Reynolds stress profiles are presented for locations: $x/d = 0, 1, 4.5, 7.5, 12, 15,$ and 30 . Note that data at $x/d = 0$ are the initial conditions.

The data in Fig. 4.4(a) demonstrate that the mean velocity profile is nearly symmetric for all 7 downstream measurement locations. The incoming boundary layers that form along the surfaces of the splitter plates result in two wake regions with lower velocity just downstream of the tips of the splitter plates. These wakes quickly disappear and are replaced by two mixing layers at the boundaries of free streams. These mixing layers are short lived, however, as they grow together so quickly that the potential core in the center jet has completely disappeared at $x/d = 4.5$. Thereafter, the flow continues its development towards channel flow.

The distributions of Reynolds normal stresses in Figs. 4.4(b) and (c) are nearly symmetric about the centerline of the jet and the maximum normal stresses appear in regions just downstream of the tips of the splitter plates. Initially, the peaks of the cross-sectional profile decrease quickly while the stresses in the potential core increase appreciably. After the two mixing layers have grown together, the stresses along the centerline of the channel begin to increase from their near zero values in the potential core region. At the farthest downstream location in this study, $x/d = 30$, the $\langle v'v' \rangle$ normal stress becomes nearly constant over a large region in the center of the channel, with smaller values near the channel walls. However, the two peaks in the distribution for the $\langle u'u' \rangle$ normal stress are still distinct. Moreover, unlike in free jets, in which the outer stream flow is unbounded, in the confined jet the boundary layers

that develop along the test-section sidewalls play important roles, and both Reynolds normal stresses continually increase in the near-wall regions.

The Reynolds shear stress, $\langle u'v' \rangle$, shown in Fig. 4.4(d), is antisymmetric and is zero along the centerline of the test section. Consistent with the eddy-viscosity hypothesis, the stress is positive where the mean shear is negative, and negative where the mean shear is positive. The peak Reynolds shear stress decreases slowly with increasing downstream distance. In the wake regions near the tips of the splitter plates, there is a sign change in the Reynolds shear stress due to the sign change of the gradient of mean streamwise velocity in the wakes.

Since PIV is a 2-D measurement, only streamwise and transverse velocity components are available in the present work. In order to estimate the turbulent kinetic energy, the spanwise velocity fluctuation (w') was assumed to be equal in magnitude to v' so that

$$TKE = \frac{\langle u'^2 \rangle + 2\langle v'^2 \rangle}{2}. \quad (4.12)$$

Figure 4.5 shows the profile of turbulent kinetic energy at each investigated location. As expected, the turbulent kinetic energy is symmetric about the centerline of the test section. As x increases, the peak of the turbulent kinetic energy decreases. However, the two peaks remain distinct even at the farthest downstream location in this study.

Self-similarity of the Rectangular Jet

For turbulent jets, it has been observed that the flow may reach a self-similar state [Gutmark and Wygnanski (1976); Pope (2000)]. The flow field of a rectangular free jet can be characterized by three regions: the potential core region, a two-dimensional-type region, and an axisymmetric-type region [Krothapalli et al. (1981)]. The latter two regions originate at the location where the two shear layers in the $X - Y$ plane meet, and at the location where the two shear layers in the $X - Z$ plane meet. However, it is found that the onsets of these two regions are strongly related to the nozzle aspect ratio, especially when the ratio is less than 10 [Krothapalli et al. (1981); Tsuchiya et al. (1986)]. In their study of an incompressible free rectangular jet issuing into quiescent surroundings, Krothapalli et al. (1981) found that the mean velocity and Reynolds shear stress profiles exhibit self-similarity in both the second

and the third regions; however, profiles of Reynolds normal stresses only show similarity in the second region.

To calculate the self-similar mean velocity, define the centerline velocity in the jet, $U_m(x)$, and half-width, $y_{1/2}(x)$, as following:

$$U_m(x) \equiv \langle U(x, 0, 0) \rangle, \quad (4.13)$$

$$\langle U(x, \pm y_{1/2}(x), 0) \rangle = \frac{1}{2} (U_m(x) - U_0) + U_0, \quad (4.14)$$

where U_0 is the free-stream velocity in the outer streams. In this work, $U_0 = 0.55 \text{ m/s}$. Then with $\xi \equiv y/y_{1/2}(x)$ being the scaled cross-stream variable, the self-similar mean streamwise velocity, $f(\xi)$, is defined by

$$f(\xi) = [\langle U(x, y, 0) \rangle - U_0] / [U_m(x) - U_0]. \quad (4.15)$$

With the assumption that the turbulent viscosity is uniform across the flow, Pope (2000) derived another expression of $f(\xi)$ for planar jets exhausting into quiescent surroundings,

$$f(\xi) = \text{sech}^2(\alpha\xi), \quad (4.16)$$

where $\alpha = \frac{1}{2} \ln(1 + \sqrt{2})^2$.

Using Eqns. 4.13, 4.14 and 4.15, the self-similar mean streamwise velocity in the rectangular jet was calculated. Figure 4.6(a) shows the profiles for 6 downstream locations as measured with PIV and the profile as evaluated from Eqn. 4.16. Although the confined jet in this study is not expected to display behavior identical to a rectangular free jet, it is clear from the overlap in the data at the downstream measurement locations that the mean streamwise velocity profile in the jet reaches a self-similar state. However, at the two measurement locations ($x/d = 1$ and $x/d = 4.5$) where the potential core has not disappeared (i.e., potential core region), the mean velocity has not yet achieved this self-similar state. The similarity persists up to $x/d = 30$, indicating the constraint of the jet flow does not affect the self-similar mean streamwise velocity profile between $\pm 1.6\xi$. The jet spreading rate was found to be about 0.1, in good agreement with that of the free planar jet [Gutmark and Wygnanski (1976); Pope (2000)].

The agreement between the self-similar mean streamwise velocity as measured by PIV and the profile as calculated from Eqn. 4.16 is good in the center region of the jet. One possible reason causing the discrepancies at the edges could be that the turbulent viscosity is not uniform in the jet flow; another reason could be the nature of the coflowing jet in this study. For example, Gutmark and Wignanski (1976) found that a jet exhausting into a slow-moving coflow stream is narrower than a comparable one exhausting into quiescent surroundings.

The profiles of normalized $\langle u'u' \rangle$, $\langle v'v' \rangle$ and $\langle u'v' \rangle$ are displayed in Figs. 4.6(b), (c) and (d), respectively. As these plots show, the Reynolds stresses are not self-similar. This is not surprising because the constraint of the jet gives rise to a much shorter two-dimensional region than in a free rectangular jet and the axisymmetric region does not exist in a confined jet, such that the Reynolds stresses can not achieve the self-similar states. The $\langle u'u' \rangle$ and $\langle v'v' \rangle$ stresses appear to approach somewhat self-similar states at $x/d = 7.5, 12$ and 15 , and the maximum values of the self-similar states agree well with the corresponding results in Krothapalli et al. (1981).

Concentration Mean and Variance

The transverse profiles of the ensemble-averaged concentration and the concentration variance at the six downstream locations previously described are summarized in Fig. 4.7. Both the mean concentration and concentration variance profiles are approximately symmetric around the centerline of the channel. Just downstream of the splitter plate tips at $x/d = 1$ the mean concentration very closely resembles a top-hat function. The shape of this profile rapidly changes with downstream distance, however, due to turbulent mixing. As the flow convects downstream, the mean concentration decreases in the center stream and increases in the outer streams as fluorescent dye is transported from the inner to the outer streams. However, even at the farthest downstream location investigated ($x/d = 30$), the mixing is not yet complete as the the mean concentration has not yet reached a uniform value.

Two peaks of the concentration variance for each downstream location are observed in Fig. 4.7(b). The peak values of concentration variance decay with increasing downstream

distance. Moreover, due to the growth of the jet-like region in the center of the channel, the peaks move towards the sidewalls as downstream distance increases. The non-zero variance in concentration at $x/d = 30$ is further evidence that the flow has not been completely mixed at this downstream location.

Figure 4.8 exhibits the orientation of the gradient vector of the mean concentration at each downstream location. As described before (or refer to Fig. 4.2), the coordinate system in this work is such that 0° is in the streamwise direction and $+90^\circ$ is in the y -direction. Since the component of the mean concentration gradient in x -direction is very small, the orientation of the vector is approximately $+90^\circ$ in the left-half channel or -90° in the right half, indicating that the mean concentration gradient is perpendicular to the streamwise direction. At the lower downstream locations, the result of the vector orientation is noisy in the potential core of each free stream due to the near-zero value of the cross-stream gradient in these regions.

Turbulent Fluxes and Velocity-Concentration Correlation Coefficients

In the Reynolds-averaged scalar transport equation, the turbulent fluxes play an analogous role to that of the Reynolds stresses in the Reynolds-averaged Navier-Stokes equations. The turbulent flux terms describe both the direction and the magnitude of the mass transported by turbulence and therefore are very important in the understanding of the turbulent scalar transport.

The measured turbulent flux profiles at six downstream locations, normalized by ΔU and Φ_0 , are presented in Fig. 4.9. The profiles of the streamwise turbulent flux, $\langle u'\phi' \rangle$, are symmetric about the centerline. In Fig. 4.9(a) two peaks develop from the tips of the splitter plates. Initially, the $\langle u'\phi' \rangle$ flux is zero in both the center region of the channel and in the outer streams. This is to be expected since these regions correspond to the unmixed potential cores. As the flow convects downstream, the two peaks increase both in magnitude and width, eventually growing together. After the peaks have grown together, nonzero $\langle u'\phi' \rangle$ is measured between the two peaks and increases as the observation location moves downstream. At $x/d = 30$, the $\langle u'\phi' \rangle$ flux becomes small due to the decrease of the concentration variance. However,

even at this far downstream location, the two peaks are still distinct.

The profiles of the cross-stream turbulent flux, $\langle v'\phi' \rangle$, are shown in Fig. 4.9(b). The profiles of $\langle v'\phi' \rangle$ are antisymmetric about the centerline. The cross-stream turbulent flux is negative where the gradient of concentration mean is positive and positive where the gradient is negative. Like $\langle u'\phi' \rangle$, $\langle v'\phi' \rangle$ is zero in potential core regions just downstream of the splitter-plate tips. As the mixing layers develop, the nonzero region of $\langle v'\phi' \rangle$ grows and spreads. Also notice that the streamwise turbulent flux is larger than the transverse turbulent flux, which is consistent with the previously observed relationship between the normal Reynolds stresses $\langle u'u' \rangle$ and $\langle v'v' \rangle$.

Normalizing the turbulent fluxes by the *rms* of the local velocity fluctuation and local concentration fluctuation yields the velocity-concentration correlation coefficients. As Fig. 4.10 shows, the longitudinal correlation coefficient is symmetric about the center plane, whereas the lateral coefficient is antisymmetric. Both correlation coefficients are zero in the unmixed potential cores, indicating the uncorrelated relationship between the fluctuations of velocity and concentration. The longitudinal correlation coefficient changes sign (becomes negative) in the wakes near the tips of the splitter plate because of the velocity deficit. At the farthest downstream location observed in the present experiments ($x/d = 30$), the longitudinal correlation coefficient was found to be nearly uniform around the value of 0.55, which is in good agreement with the results of Tavoularis and Corrsin (1981). The profiles of the orientation of the turbulent flux vector at the observed locations are presented in Fig. 4.11. As expected, the orientation of the vector is antisymmetric about the centerline of the channel, positive where the $\langle v'\phi' \rangle$ flux is positive, and negative where the $\langle v'\phi' \rangle$ flux is negative. Tavoularis and Corrsin (1981) and Rogers et al. (1989) found that the streamwise scalar flux is much larger than in the transverse direction in homogeneous turbulent shear flows. In the present study, the orientation of the turbulent flux vector is nearly uniform around -30° in the left half channel and around $+30^\circ$ in the right half channel, which is close to the value of 20° reported by Rogers et al. (1989) in a shear layer. Note that the angle between the mean scalar gradient and the turbulent flux vector is approximately 120° at all observed locations. Therefore, the simple gradient transport model using a scalar turbulent diffusivity cannot completely describe

the behavior of the turbulent flux in this flow.

Turbulent Viscosity and Turbulent Diffusivity

According to the turbulent-viscosity hypothesis, the scalar coefficient ν_T , called the *turbulent viscosity* (or *eddy viscosity*), can be evaluated from the experimental data using the below equation:

$$\nu_T = \frac{-\langle u'v' \rangle}{\partial U / \partial y}. \quad (4.17)$$

Profiles of turbulent viscosity at six downstream locations are presented in Fig. 4.12. This coefficient shows wide variation in both the streamwise and transverse directions. At each downstream location, the maximum turbulent viscosity appears in the shear-layer regions between the center-jet region and the outer free streams. In regions near the sidewalls, the coefficient becomes small. These observed trends are consistent with the results reported by Lemoine et al. (1999).

Batchelor (1949) proposed a generalization to the gradient-transport hypothesis which defines the turbulent diffusivity tensor (Γ_{ij}). Since the mean concentration gradient is not aligned with the turbulent flux vector for this flow, Γ_{ij} is not a diagonal tensor. In the present study, only two components of the tensor are measureable:

$$\Gamma_{12} = \frac{-\langle u'\phi' \rangle}{\partial \Phi / \partial y}, \quad (4.18)$$

$$\Gamma_{22} = \frac{-\langle v'\phi' \rangle}{\partial \Phi / \partial y} \quad (4.19)$$

where Γ_{22} is the so-called *turbulent diffusivity*, Γ_T [Tavoularis and Corrsin (1981)].

Figures 4.13 and 4.14 show the profiles of Γ_{12} and Γ_{22} at six downstream locations, respectively. As expected, the profiles of Γ_{12} are antisymmetric about the centerline, negative where the mean concentration gradient is positive and positive where the gradient is negative. Also, the magnitude of Γ_{12} is small initially but increases as the flow convects downstreams. The non-zero value of Γ_{12} in the present study indicates that the gradient-transport models with scalar turbulent diffusivity are inadequate because the mean concentration gradient is

not aligned with the turbulent flux, i.e., a simple scalar diffusivity coefficient is inadequate to represent the behavior of the turbulent flux.

The profiles of Γ_{22} (or turbulent diffusivity, Γ_T) are symmetric about the the centerline with the maximum appearing in the shear layer regions at each downstream location. The turbulent diffusivity becomes small in regions near the sidewalls. These trends agree with the results reported by Lemoine et al. (1999) as well.

Tavoularis and Corrsin (1981) found that the magnitude of the ratio of Γ_{12}/Γ_{22} is a constant about 2.1. The ratio computed from the experimental data in this work is displayed in Fig. 4.15. The ratio remains nearly constant in the cross-stream direction, although its magnitude increases sharply in regions around the centerline or near the sidewalls. Moreover, the magnitude of the ratio increases slightly as the flow convects downstreams. At the farthest downstream location, Γ_{12}/Γ_{22} is approximately 2 in the high shear regions of the flow, in good agreement with Tavoularis and Corrsin (1981).

The turbulent Schmidt number, $Sc_T \equiv \nu_T/\Gamma_T$, is an important modelling parameter for numerical simulations on turbulent flows, as it may impact the prediction of scalar fields significantly. Although results from previous experiments have led to questions about the assumption of using a constant Sc_T for the whole flow field (see for example, He and Hsu (1999)), it was found that Sc_T , which spatially varying, is everywhere of order one for non-rotating shear flows with transverse mean scalar gradient[Brethouwer (2005)]. Therefore, to simply modelling, the average turbulent Schmidt number across the jet is still frequently used in scalar transport closures. The empirical value of the average Sc_T reported varies from experiment to experiment, but reported values typically are around 0.7. For instance, Panchapakesan and Lumley (1993) estimated an average Sc_T of 0.7 in their study on axisymmetric jets; whereas Lubbers et al. (2001) suggested to use 0.74 as an average value of Sc_T . Figure 4.16 shows the cross-sectional profiles of the turbulent Schmidt number at various downstream locations obtained in the present study. Since $\langle u'v' \rangle$, $\langle v'\phi' \rangle$, $\partial U/\partial y$ and $\partial \Phi/\partial y$ all are close to zero at the jet centerline, the result of the computed Sc_T is very noisy in regions near the jet centerline. At $x/d = 7.5$, the turbulent Schmidt number reaches a maximum in the shear layers and

decreases in the center region of the flow, which agrees with the trend for the turbulent Prandtl number reported by Lemoine et al. (1999). At further downstream locations, although some spatial variation in Sc_T is observed (most notably, the value of Sc_T in the high shear regions is still a little higher than in the center stream region), Sc_T is fairly constant around a value of 0.8. Hence, the present results for the turbulent Schmidt number are consistent with the existing body of experimental data, showing spatial variation in Sc_T and an average value in agreement with previous studies.

Two-Point Spatial Correlations

The simultaneous nature of the combined PIV and PLIF measurements allows for the determination of the two-point spatial correlations of turbulent fluxes. Normalized by the *rms* of velocity and concentration fluctuations, these spatial correlations are defined as

$$R_{u'_i\phi'}(x, y; X, Y) = \frac{\langle u'_i(x, y)\phi'(X, Y) \rangle}{\sqrt{\langle u'^2_i(x, y) \rangle \langle \phi'^2(X, Y) \rangle}} \quad (4.20)$$

where (X, Y) and (x, y) are the coordinates of a basis point (*i.e.*, the point about which the spatial correlation is measured) and an arbitrary point in the flow field, respectively. In the present study, the location of the left peak of concentration variance was chosen as the basis point. The area over which the spatial correlations were calculated is a square grid corresponding to 89×89 vectors centered about the basis point.

The spatial correlations $R_{u'_i\phi'}$ for basis points located at the six downstream locations examined in this study are presented in Fig. 4.17. The bold dashed lines in some plots represent the left sidewall of the test section (beyond which no data exist). The streamwise flow direction in all the presented correlation fields is from the bottom to the top of the figure. The $R_{u'_i\phi'}$ correlation field is elliptical in shape with the major axis oriented in the streamwise direction. This is similar to the shapes of the correlation field for streamwise velocity fluctuations ($R_{u'u'}$) found in incompressible mixing layers [Oakley et al. (1996); Olsen and Dutton (2002)]. These elliptical correlation fields suggest that the correlation distance in the streamwise direction is relatively longer than in the transverse direction.

As the basis point moves downstream, the peak value of $R_{u'\phi'}$ at the origin increases slightly, whereas the overall size of the positively correlated region grows, suggesting an increase in the size of the turbulent structures. Notice also that a negatively correlated region appears to the left of the basis point in the free-stream region at $x/d = 1$. This negative region grows larger and moves towards the sidewall as x increases. However, this region also becomes weaker (i.e., the value of the correlation coefficient becomes smaller) with downstream distance and finally disappears at $x/d = 30$. Notice also that these plots cover such a large area in the flow that the other shear layer in the channel is partly captured. The negatively correlated region near the right border of each plot is due to the existence of a large structure developing in the other shear layer, where the rotation of the vortex is expected to be in the opposite direction.

Figure 4.18 shows the spatial correlations $R_{v'\phi'}$. This correlation field is a horizontally oriented ellipse with negative values of the correlation coefficient. This is expected because $R_{v'\phi'}$ at the basis point is indeed the velocity-concentration correlation coefficient as shown in Fig. 4.10. The short correlation distance in the x direction implies the rapid variation in the corresponding v velocity fluctuations. Once again, the shape of the correlation field is found to be very similar to those of transverse velocity fluctuations ($R_{v'v'}$) as reported by previous researchers [Olsen and Dutton (2002)].

By replacing u'_i by ϕ' , Eqn 4.20 describes the spatial correlation of concentration fluctuations. The area over which these spatial correlations were calculated was a grid of 323×323 camera pixels centered around the basis point. Figure 4.19 shows the spatial correlation $R_{\phi'\phi'}$ at different downstream locations. The correlation field is an ellipse with the major axis inclined at approximately 45-degree with respect to the x direction. This inclination is due to the mean shear of the flow field [Tavoularis and Corrsin (1981)] and occurs because a finger of unmixed fluid reaches out from the center jet to the outer stream it is stretched obliquely due to the decrease in mean velocity moving from the center region to the outer stream. The shape of the correlated field indicates that the concentration fluctuations follow the stream-wise velocity more closely than the cross-stream velocity. Like the other spatial correlations presented, the highly correlated region in the $R_{\phi'\phi'}$ correlation field grows larger with increas-

ing distance downstream of the splitter plate suggesting an increase in the size of large-scale turbulent structures.

Linear Stochastic Estimation

Concentration Fields

It can be difficult to visualize what types of flow structures are responsible for the features observed in spatial correlations. Consequently, a useful tool for interpreting spatial correlation data is linear stochastic estimation. In linear stochastic estimation, conditional averages are calculated directly from measured correlation fields. As such, stochastic estimation has a couple of key features. First, it allows for conditional averages to be determined from a much smaller ensemble size than would be required from a direct calculation. Perhaps more importantly, because stochastic estimates are derived directly from spatial correlations, *LSE is a useful tool in determining what types of underlying flow structures are responsible for the observed spatial correlations.* Finally, LSE is useful for investigating the behavior and characteristics of large-scale turbulent structures, as the technique acts as a form of spatial filter removing small turbulent scales so the underlying large turbulent structures can be more readily observed.

Estimated concentration fields given the events of $\phi'(\mathbf{x}_o) = \pm 2\phi'_{rms}(\mathbf{x}_o)$, respectively, are shown in Figs. 4.20 and 4.21, where \mathbf{x}_o represents the basis point located at the left peak in the variance. These events were chosen because they are characteristic of a mixing event that transports higher concentration fluid from the center stream to the outer stream ($\phi'(\mathbf{x}_o) = 2\phi'_{rms}(\mathbf{x}_o)$) or a mixing event that transports low dye concentration outer stream fluid to the center stream ($\phi'(\mathbf{x}_o) = -2\phi'_{rms}(\mathbf{x}_o)$). As seen in these plots, a positive concentration fluctuation event corresponds to a finger of nearly uniform concentration fluid reaching out into the free stream. This finger is inclined at an approximately 45 degree angle due to the deformation caused by the mean shear in the flow. Conversely, for an event defined by a negative fluctuation in concentration, the event corresponds to a finger of nearly uniform fluid being entrained from the outer stream into the center jet region. This finger, too, is inclined at a 45 degree angle due to stretching caused by the mean shear of the flow. The sequence of

stochastic estimates for basis point locations from $x/d = 1$ to $x/d = 30$ reveals that the length scales of the fingers of entrained fluid grow with increasing downstream distance.

Velocity Fields

The estimated velocity fields around the basis point given the events of $\phi'(\mathbf{x}_o) = \pm 2\phi'_{rms}(\mathbf{x}_o)$ are shown in Figs. 4.22 and 4.23, respectively. As Fig. 4.22 illustrates, for a positive concentration fluctuation event, the estimated velocity fields at each downstream location are dominated by the presence of a large-scale roller structure, and it is this roller structure that is responsible for the transport of unmixed fluid from the center stream to the outer streams (and *vice versa*). At each downstream location, the basis point is located just downstream of the center of a roller structure in a region where the local velocity vectors indicate that fluid is being transported from the center stream (where concentration is high) to the outer stream (where concentration is low). This behavior is consistent with a positive concentration fluctuation event. The roller structures increase in size with increasing downstream distance.

Evidence of a counter-rotating vortex towards the outer stream and just upstream of the large roller structure can be observed at $x/d = 1$. This phenomenon can be observed upstream of both the roller structure centered just upstream of the basis point and also upstream of the roller structure farther downstream (of which only the very tail end is visible in Fig. 4.22). These counter-rotating vortices become weaker with increasing downstream distance and eventually disappear altogether. This vortex street formed in the wake region near the tip of the splitter plate is responsible for the negatively correlated region observed in the $R_{w'\phi'}$ spatial correlations of turbulent fluxes discussed earlier.

Similarly, Fig. 4.23 shows the estimated velocity field around the basis point for the negative concentration event, $\phi'(\mathbf{x}_o) = -2\phi'_{rms}(\mathbf{x}_o)$. Figure 4.23 shows that a negative concentration fluctuation event is also dominated by the presence of a large-scale roller structure, the only difference being the location of the basis point relative to the roller structure center. For the negative concentration event, the basis point is located just upstream of the center of a roller structure in a region where the local velocity vectors indicate that fluid is being transported

from the outer stream to the center stream, behavior consistent with a negative-concentration fluctuation event. The large-scale roller structures are also seen to increase in size with increasing downstream distance for the negative concentration event. Evidence of the counter-rotating vortices in the outer stream at small x/d is also observed in Fig. 4.23.

The evolution of the size of the large-scale structures observed in the stochastic estimates of the velocity fields are shown in Fig. 4.24. The structure size is defined as twice the distance from the center of a roller structure to the braid region between roller structures. Initially the structure size is about 13 mm and then grows nearly linearly at a rate of about 2.2 mm in size per cm of streamwise movement. This linear growth is observed from $x/d = 1$ through $x/d = 15$. For a free jet, this linear growth would be expected to continue; however, this is not the case in the confined jet. The structure size at the farthest downstream location investigated is smaller than would be expected for continued linear growth. This is to be expected as the confined jet flow transitions from a jet-like flow to a channel-like flow, which would have large-scale structures whose size is independent of downstream location.

Conclusions

A combined PIV and PLIF system was developed to conduct simultaneous velocity and concentration measurements of turbulent mixing in a confined rectangular jet. 3,250 sets of instantaneous PIV velocity field and PLIF concentration field were collected at each of the seven representative downstream regions for a $Sc = 1,250$ and a Reynolds number based on hydraulic diameter of 50,000 (or 10,000 based on the velocity difference between streams and the jet exit dimension). The profiles of mean velocity, Reynolds stresses, turbulent kinetic energy, concentration mean and variance reveal that there are two mixing layers growing symmetrically about the centerline of the test section from the tips of the splitter plates. The potential core in the center stream disappears very quickly and the flow continues its development towards channel flow. At the farthest observed location, $x/d = 30$, the fluid has not been fully mixed. The finite nature of the outer streams in the confined jet results in some different characteristics of the profiles of the above flow properties from those in a free jet, indicating

that the sidewalls affect the evolution of the jet significantly.

In the potential-core region of flow, the profile of the normalized streamwise mean velocity is very different from the profile of the self-similar velocity. However the self-similarity persists up to $x/d = 30$ in the center region of the jet. The spreading rate is around 0.1, in good agreement with that of the planar jet [Gutmark and Wygnanski (1976); Pope (2000)]. However, unlike in free rectangular jets, the Reynolds stresses do not reach self-similarity. Although at some downstream locations, the $\langle u'u' \rangle$ and $\langle u'v' \rangle$ stresses appear to approach somewhat self-similar states with comparable maximum values found for free jets [Krothapalli et al. (1981)], the stresses never actually reach self-similar states due to the constraint of the jet. Moreover, the Reynolds stresses exhibit significant anisotropy, as revealed both by the shear stress and by the differences in the normal stresses.

The streamwise turbulent flux was found to be symmetric about the centerline, whereas the cross-stream turbulent flux was antisymmetric. Similar to the relationship between normal Reynolds stresses $\langle u'u' \rangle$ and $\langle v'v' \rangle$, the streamwise turbulent flux was larger than the transverse turbulent flux, and the orientation of the turbulent flux vector was nearly uniform around 30° with respect to the streamwise direction. Since the mean concentration gradient was in the transverse direction, the angle between the mean gradient and the turbulent flux was about 120-degrees. Therefore, the simple gradient transport model using a scalar turbulent diffusivity cannot represent the behavior of the turbulent flux in this flow, and the non-diagonal components should be nonzero. Velocity-concentration correlation coefficients were also determined. In the potential core of each stream, the fluctuating velocity and concentration were uncorrelated. At the farthest observed location, the measured coefficients appeared to converge to a constant value of approximately 0.55.

Based on the turbulent-viscosity hypothesis and the gradient-diffusion hypothesis, the turbulent viscosity and the turbulent diffusivity in the rectangular jet have been characterized. Consistent with the existing literature (Lemoine *et al.* 1999), both of these transport coefficients increased with downstream distance. The cross-sectional distributions show that these transport coefficients are larger in the shear-layer regions than in either the center region of

the jet or in the boundary layers near the sidewalls. The results for turbulent Schmidt number are consistent with the existing body of experimental data, showing spatial variation in Sc_T and an average around 0.8.

The simultaneous velocity and concentration data were also used to calculate the correlation fields of turbulent fluxes and concentration for the turbulent jet. The $R_{u'\phi'}$ correlation was elliptical in shape with a major axis tilted downward with respect to the streamwise axis, whereas the $R_{v'\phi'}$ correlation was a horizontally oriented ellipse. There were negative regions on the $R_{u'\phi'}$ correlation fields, some in the left free stream and others in the other shear layer. The negatively correlated regions in the free stream decayed as x increased and finally disappeared altogether. The $R_{\phi'\phi'}$ correlation field was found to be an ellipse with the major axis inclined at about 45-degrees with respect to the streamwise direction. This inclination is due to the mean shear of the flow field. The shape of the correlated field indicates that the concentration fluctuations follow the streamwise velocity more closely than the cross-stream velocity.

Finally, linear stochastic estimation was used to interpret spatial correlation data and to determine conditional structures in both the concentration field and velocity field. A vortex street is responsible for the negatively correlated region observed in the $R_{u'\phi'}$ spatial correlations of turbulent fluxes. It was found that a positive concentration fluctuation event corresponds to a finger of nearly uniform concentration fluid reaching out into the free stream, whereas a negative event corresponds to a finger of nearly uniform fluid being entrained from the outer stream into the center jet region. The inclination in both cases is approximately at a 45 degree angle due to the mean shear of the flow. Large-scale vortical structures were observed in the conditional velocity fields with an elliptical shape and a streamwise major axis. The rotation of the vortex near the basis point at the left peak in concentration variance was always in the counterclockwise direction. The growth of the structure size increased linearly initially but then grew more slowly as the flow transitioned towards channel flow.

Table 4.1 Estimated Komolgorov time scale, length scale and spatial resolution of PIV measurements.

x/d	$\tau[ms]$	$\eta[\mu m]$	Resolution
1.0	6.3	80	11.3η
4.5	7.7	88	10.2η
7.5	8.2	91	9.9η
12	10.0	100	9.0η
15	10.7	103	8.7η
30	13.5	116	7.8η

Table 4.2 Estimated Batchelor length scale and spatial resolution of PLIF measurements.

x/d	$\eta_B[\mu m]$	Resolution in x-/y-	Resolution in z-
1.0	2.25	$25.0\eta_B$	$222\eta_B$
4.5	2.48	$22.7\eta_B$	$201\eta_B$
7.5	2.57	$21.9\eta_B$	$195\eta_B$
12	2.83	$19.9\eta_B$	$177\eta_B$
15	2.92	$19.3\eta_B$	$171\eta_B$
30	3.28	$17.1\eta_B$	$152\eta_B$

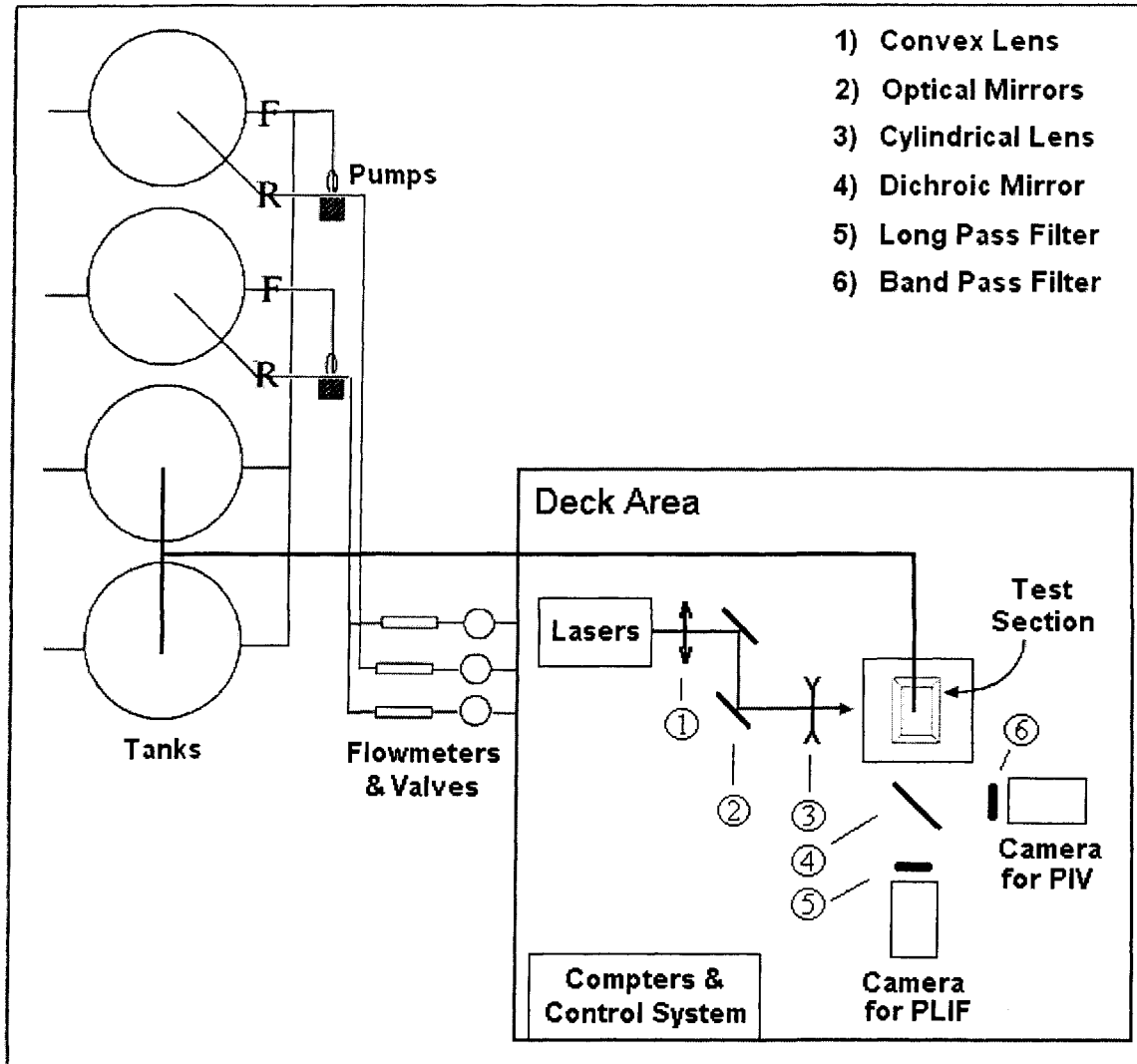


Figure 4.1 Schematic of the flow facility and the optical setup used in the combined PIV and PLIF experiments.

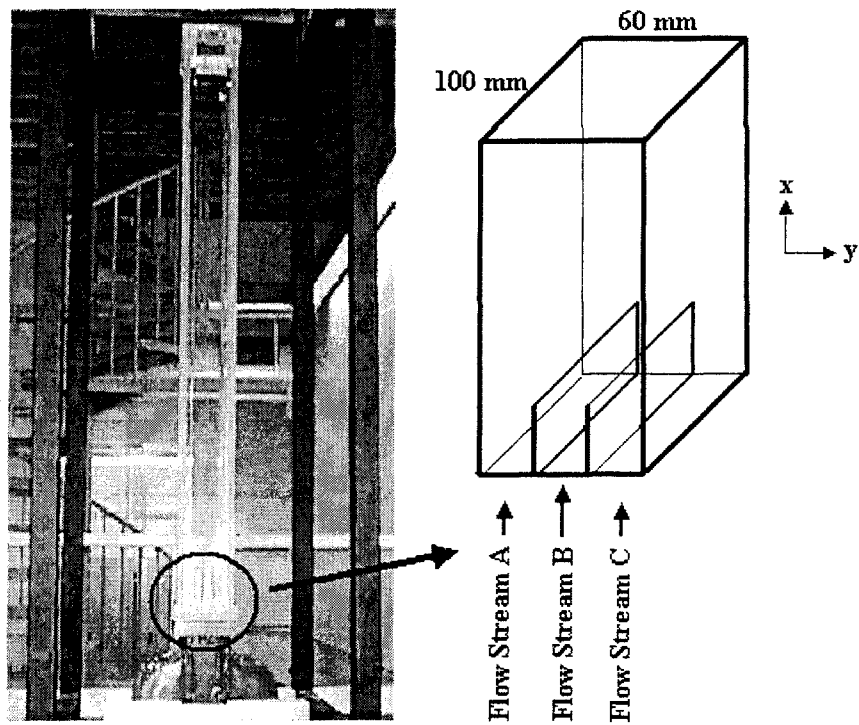


Figure 4.2 Photograph and schematic of the confined rectangular-jet test section.

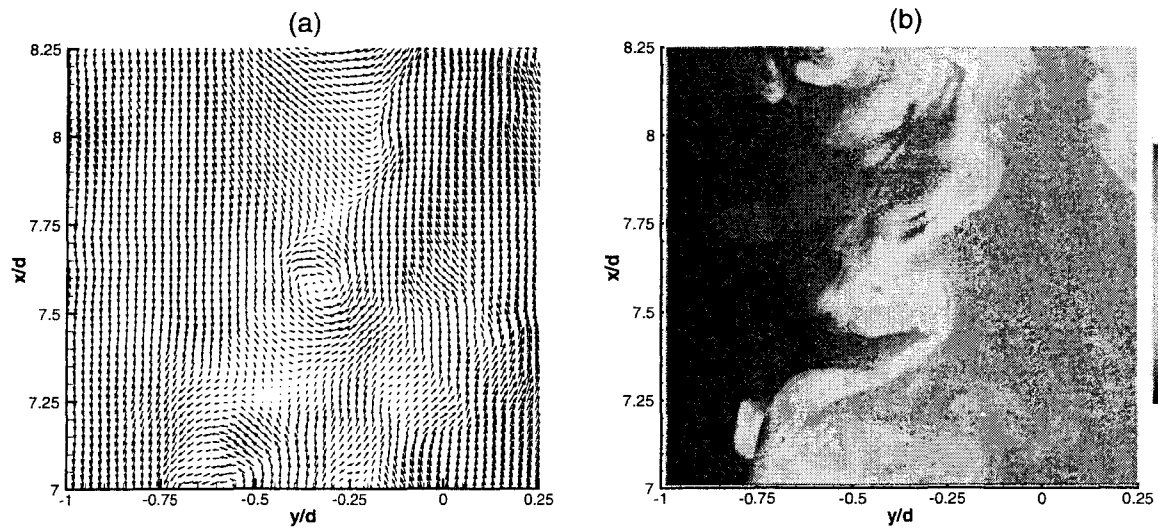


Figure 4.3 (a) An instantaneous velocity field as measured by PIV, and (b) the corresponding instantaneous concentration field as measured by PLIF.

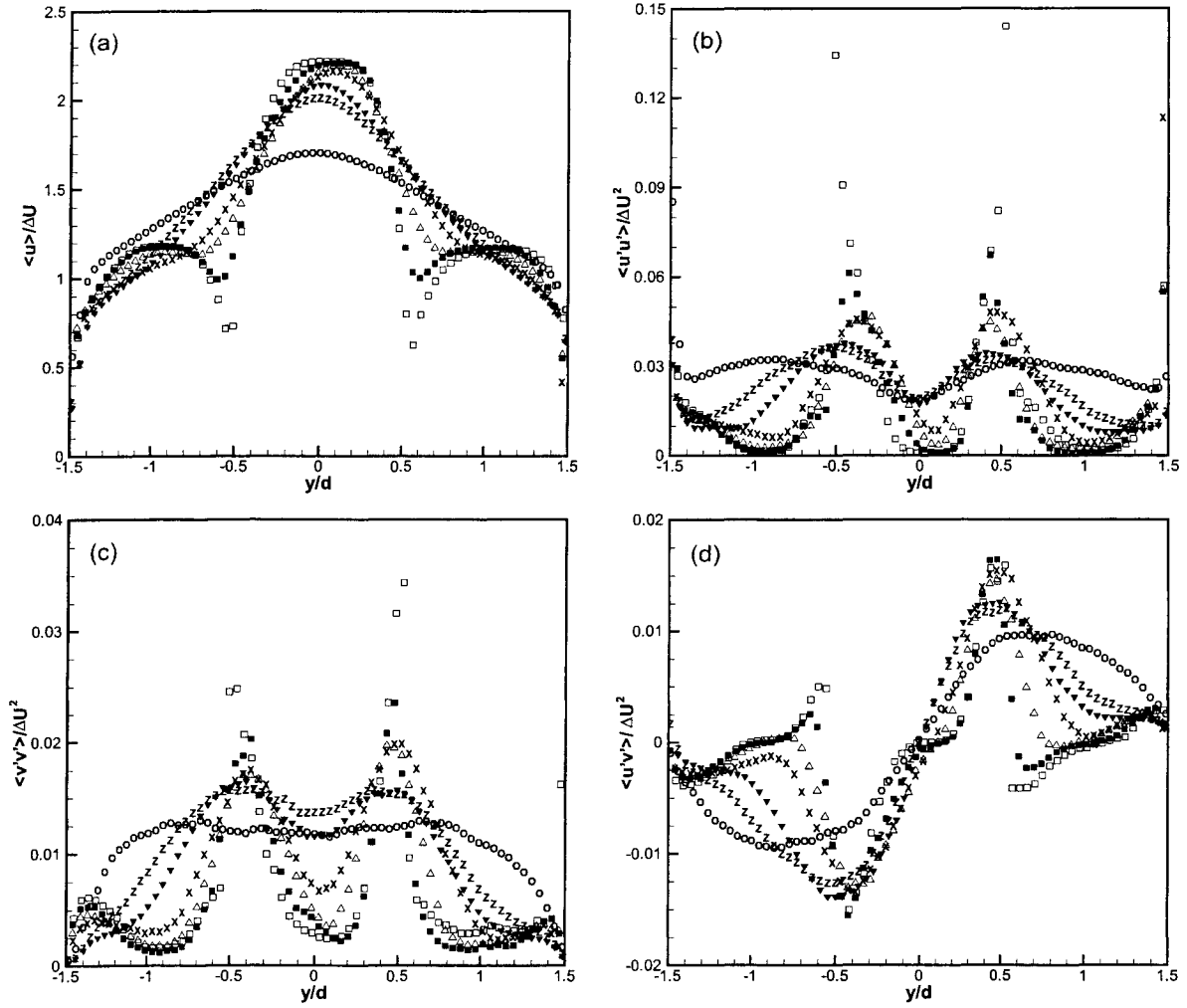


Figure 4.4 Normalized mean streamwise velocity and Reynolds stresses at different streamwise locations. (a) Mean velocity; (b) longitudinal stress; (c) lateral stress; (d) shear stress. \square , $x/d = 0$; \blacksquare , $x/d = 1.0$; \triangle , $x/d = 4.5$; \times , $x/d = 7.5$; \blacktriangledown , $x/d = 12$; \blacktriangle , $x/d = 15$; \circ , $x/d = 30$.

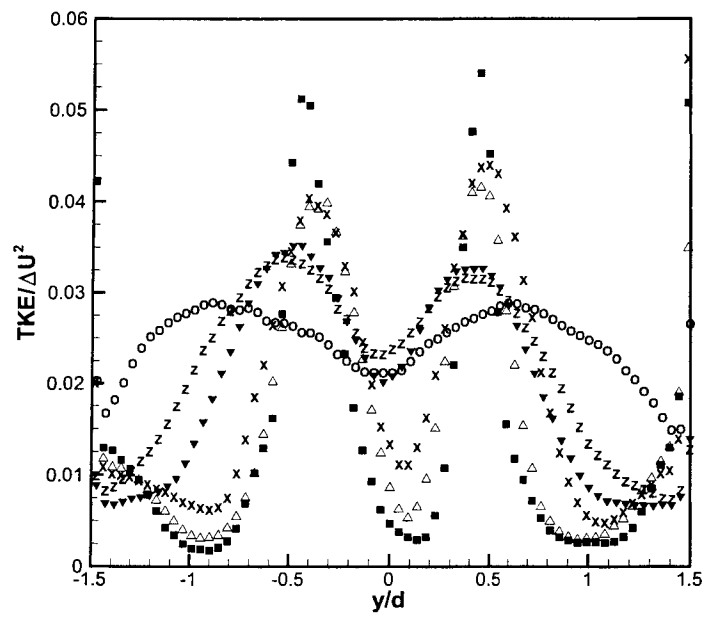


Figure 4.5 Normalized turbulent kinetic energy at different streamwise locations. ■, $x/d = 1.0$; △, $x/d = 4.5$; ×, $x/d = 7.5$; ▼, $x/d = 12$; z, $x/d = 15$; ○, $x/d = 30$.

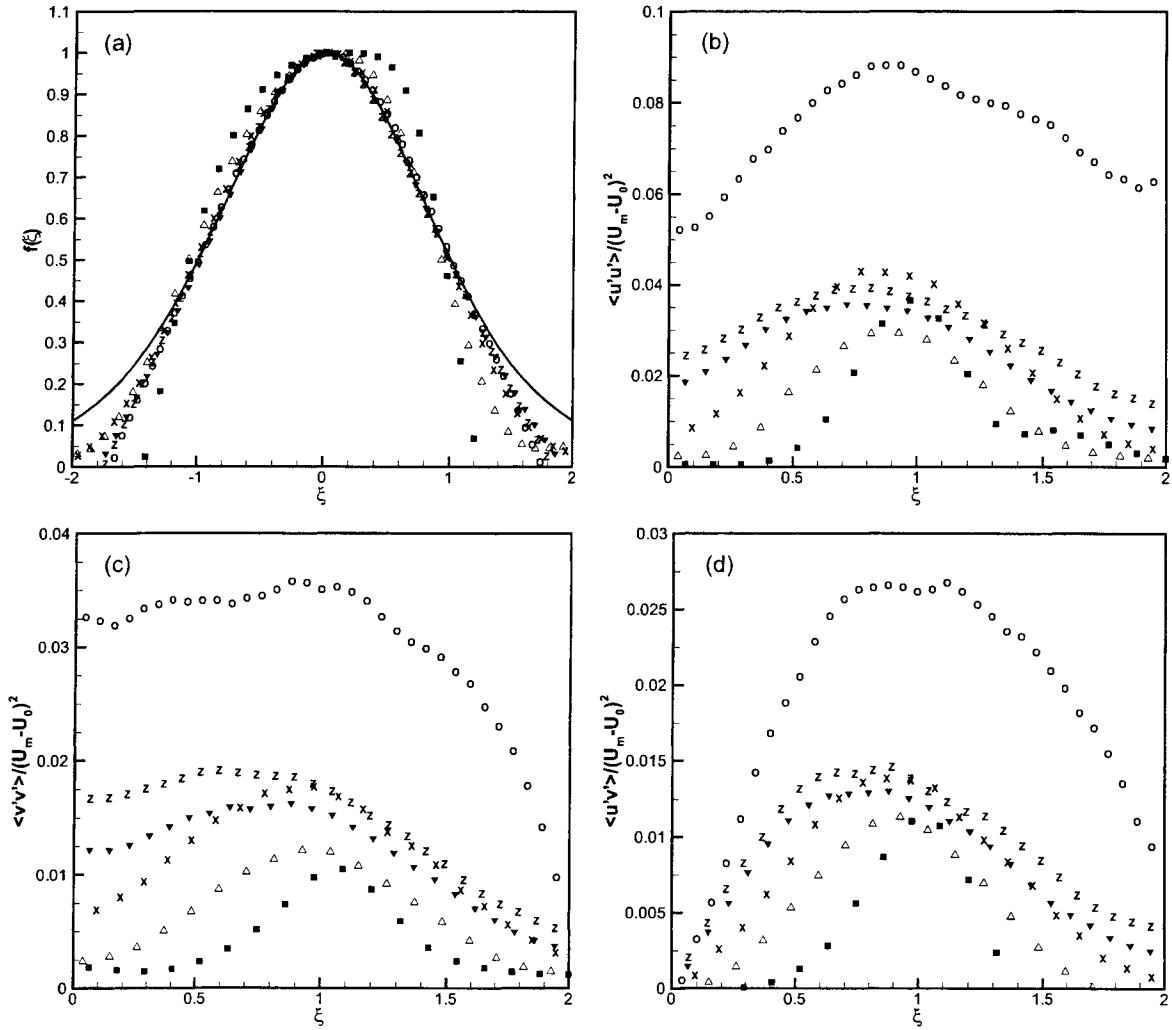


Figure 4.6 Self-similar of mean streamwise velocity and Reynolds stresses. (a) Mean velocity; (b) longitudinal stress; (c) lateral stress; (d) shear stress. Symbols, experimental data (■, $x/d = 1.0$; △, $x/d = 4.5$; ×, $x/d = 7.5$; ▼, $x/d = 12$; z, $x/d = 15$; ○, $x/d = 30$.); line, Eqn. 4.16.

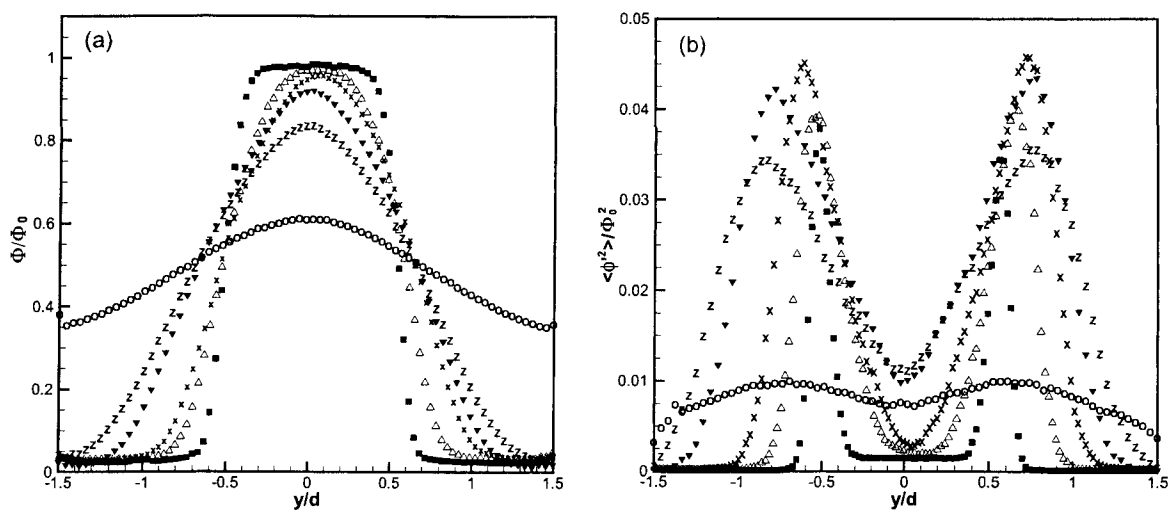


Figure 4.7 Normalized concentration mean and variance at different streamwise locations. (a) Mean concentration; (b) concentration variance. \blacksquare , $x/d = 1.0$; \triangle , $x/d = 4.5$; \times , $x/d = 7.5$; \blacktriangledown , $x/d = 12$; z , $x/d = 15$; \circ , $x/d = 30$.

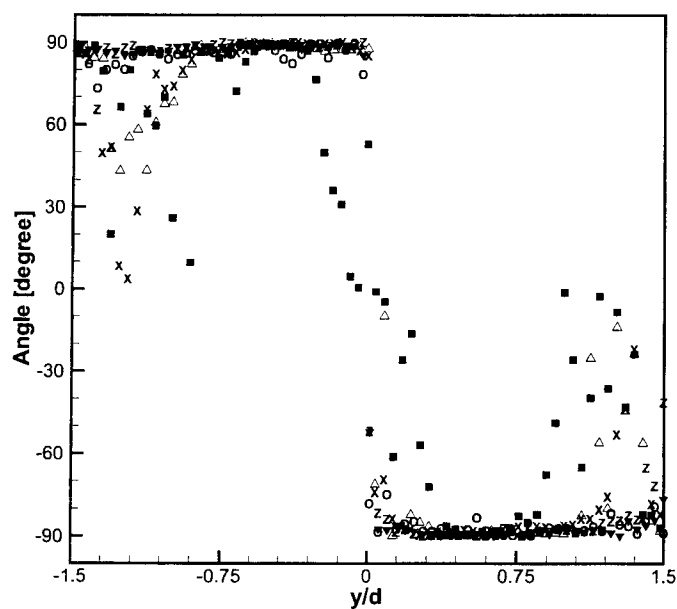


Figure 4.8 Orientation of the gradient vector of mean concentration at different streamwise locations. \blacksquare , $x/d = 1.0$; \triangle , $x/d = 4.5$; \times , $x/d = 7.5$; \blacktriangledown , $x/d = 12$; z , $x/d = 15$; \circ , $x/d = 30$.

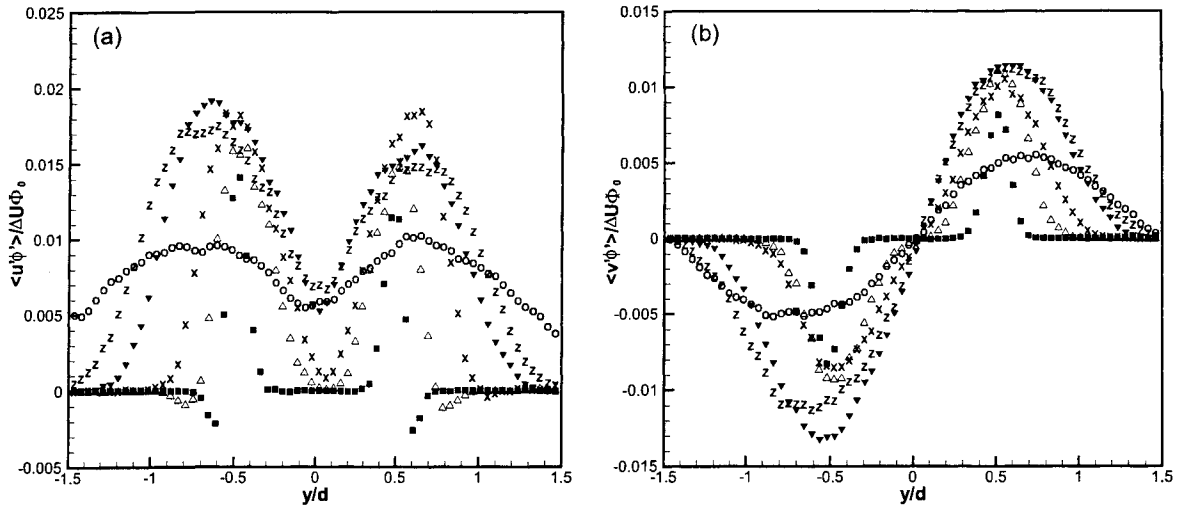


Figure 4.9 Turbulent fluxes at different streamwise locations. (a) Longitudinal flux; (b) lateral flux. \blacksquare , $x/d = 1.0$; \triangle , $x/d = 4.5$; \times , $x/d = 7.5$; \blacktriangledown , $x/d = 12$; z , $x/d = 15$; \circ , $x/d = 30$.

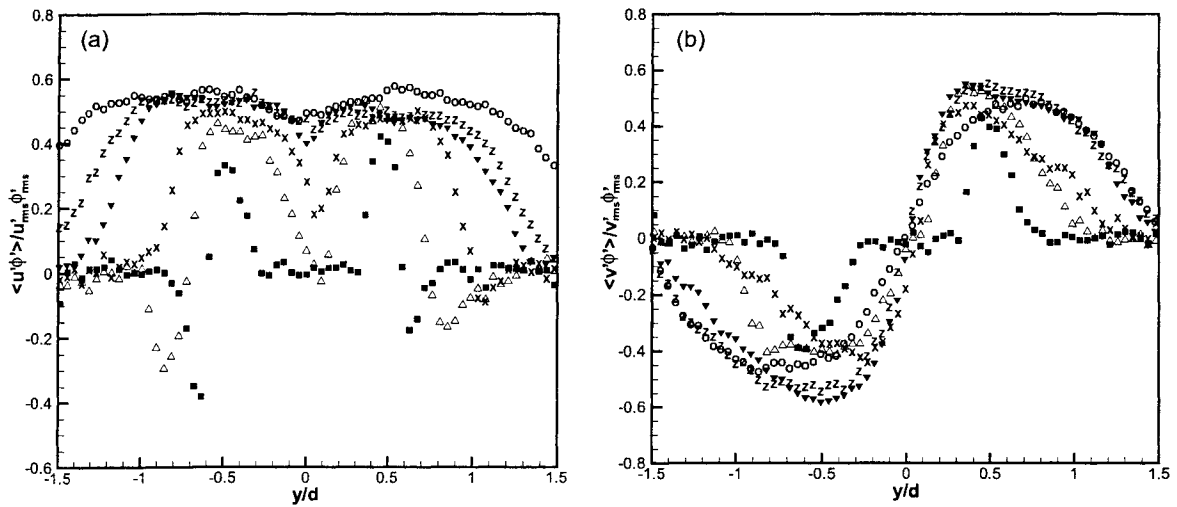


Figure 4.10 Velocity-concentration correlation coefficients at different streamwise locations. (a) Longitudinal coefficient; (b) lateral coefficient. \blacksquare , $x/d = 1.0$; \triangle , $x/d = 4.5$; \times , $x/d = 7.5$; \blacktriangledown , $x/d = 12$; z , $x/d = 15$; \circ , $x/d = 30$.

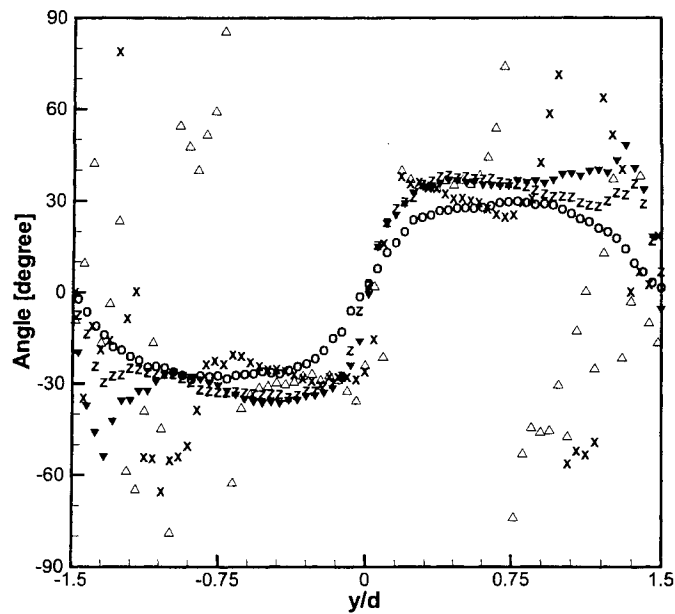


Figure 4.11 Orientation of the turbulent flux vector at different streamwise locations. \triangle , $x/d = 4.5$; \times , $x/d = 7.5$; ∇ , $x/d = 12$; z , $x/d = 15$; \circ , $x/d = 30$.

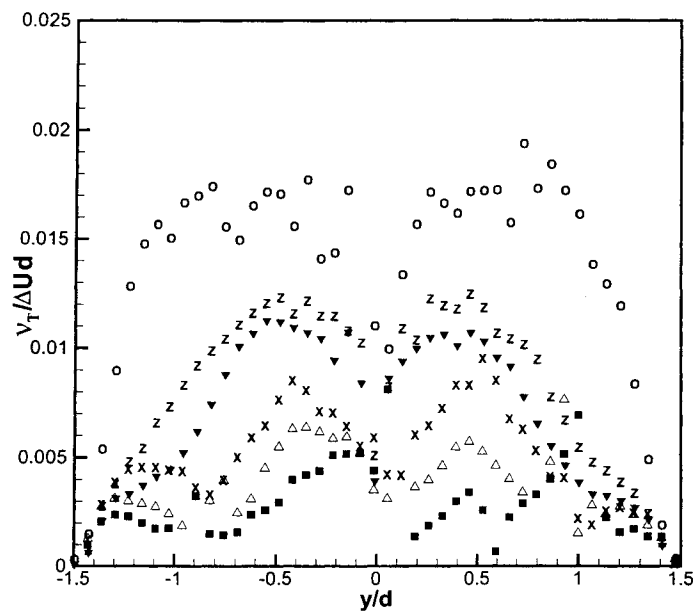


Figure 4.12 Dimensionless turbulent viscosity at different streamwise locations. \blacksquare , $x/d = 1.0$; \triangle , $x/d = 4.5$; \times , $x/d = 7.5$; ∇ , $x/d = 12$; z , $x/d = 15$; \circ , $x/d = 30$.

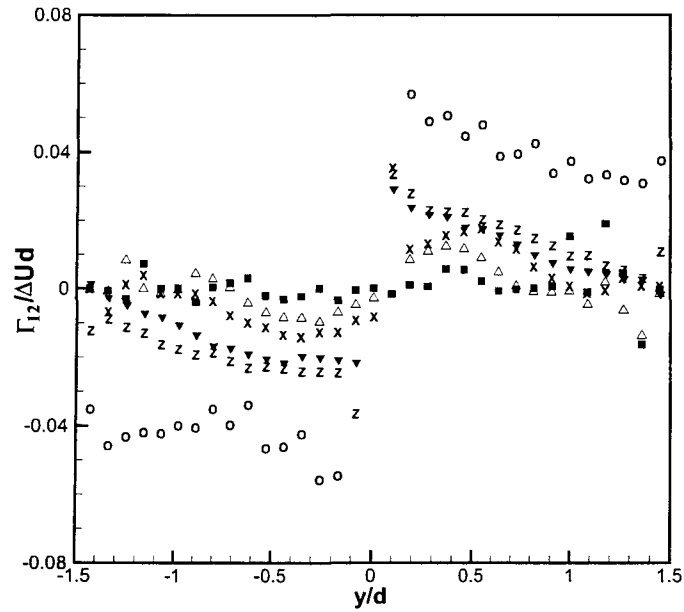


Figure 4.13 Dimensionless cross-component of the turbulent diffusivity tensor. ■, $x/d = 1.0$; \triangle , $x/d = 4.5$; \times , $x/d = 7.5$; ∇ , $x/d = 12$; z , $x/d = 15$; o , $x/d = 30$.

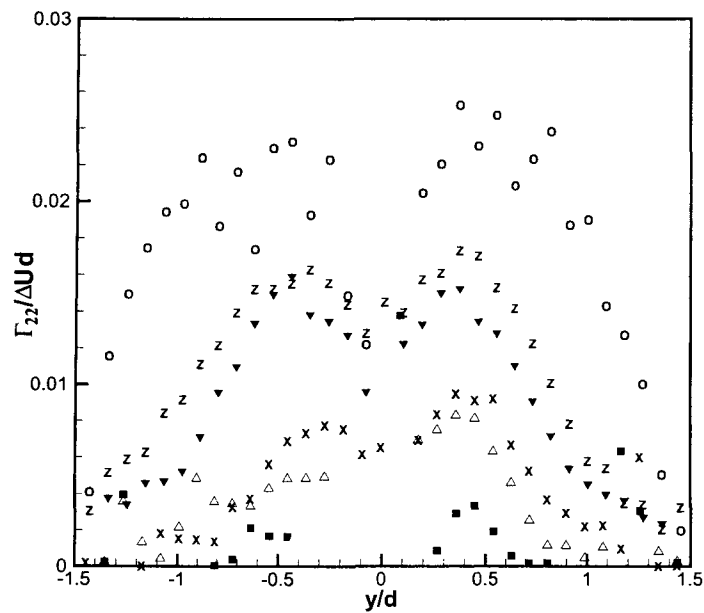


Figure 4.14 Dimensionless turbulent diffusivity. ■, $x/d = 1.0$; \triangle , $x/d = 4.5$; \times , $x/d = 7.5$; ∇ , $x/d = 12$; z , $x/d = 15$; o , $x/d = 30$.

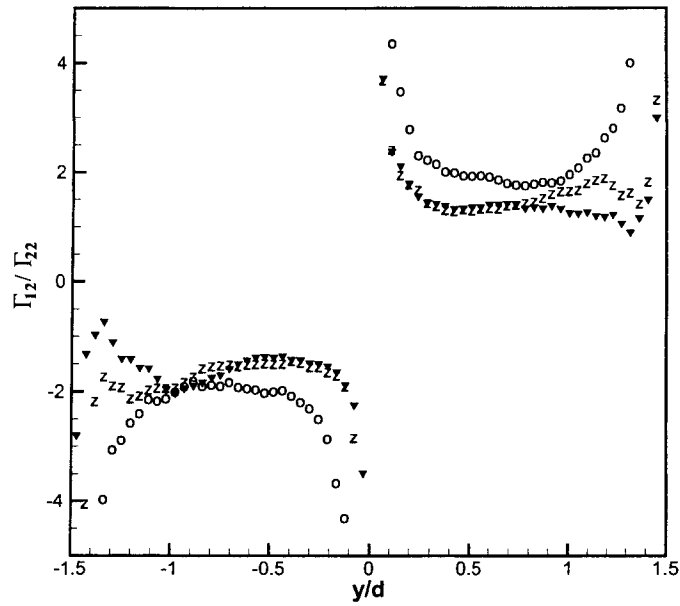


Figure 4.15 The ratio of the two components of turbulent diffusivity tensor.
 ■, $x/d = 1.0$; Δ , $x/d = 4.5$; \times , $x/d = 7.5$; \blacktriangledown , $x/d = 12$; z ,
 $x/d = 15$; \circ , $x/d = 30$.

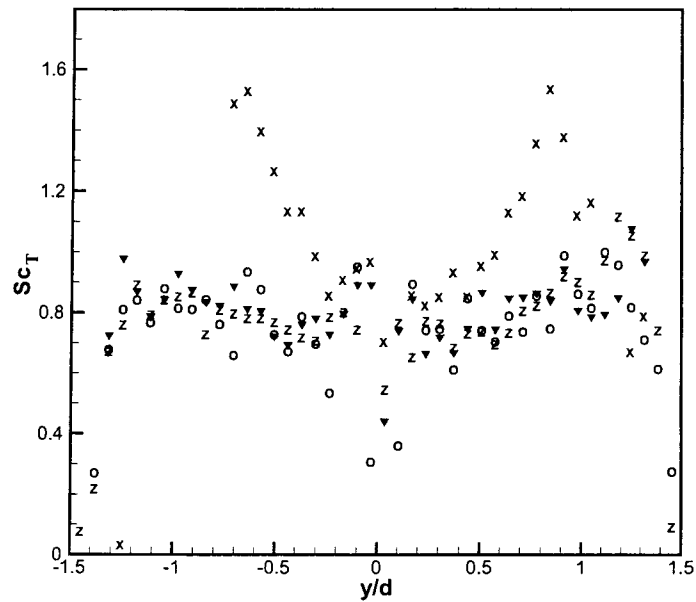


Figure 4.16 Turbulent Schmidt number at different streamwise locations.
 \times , $x/d = 7.5$; \blacktriangledown , $x/d = 12$; z , $x/d = 15$; \circ , $x/d = 30$.

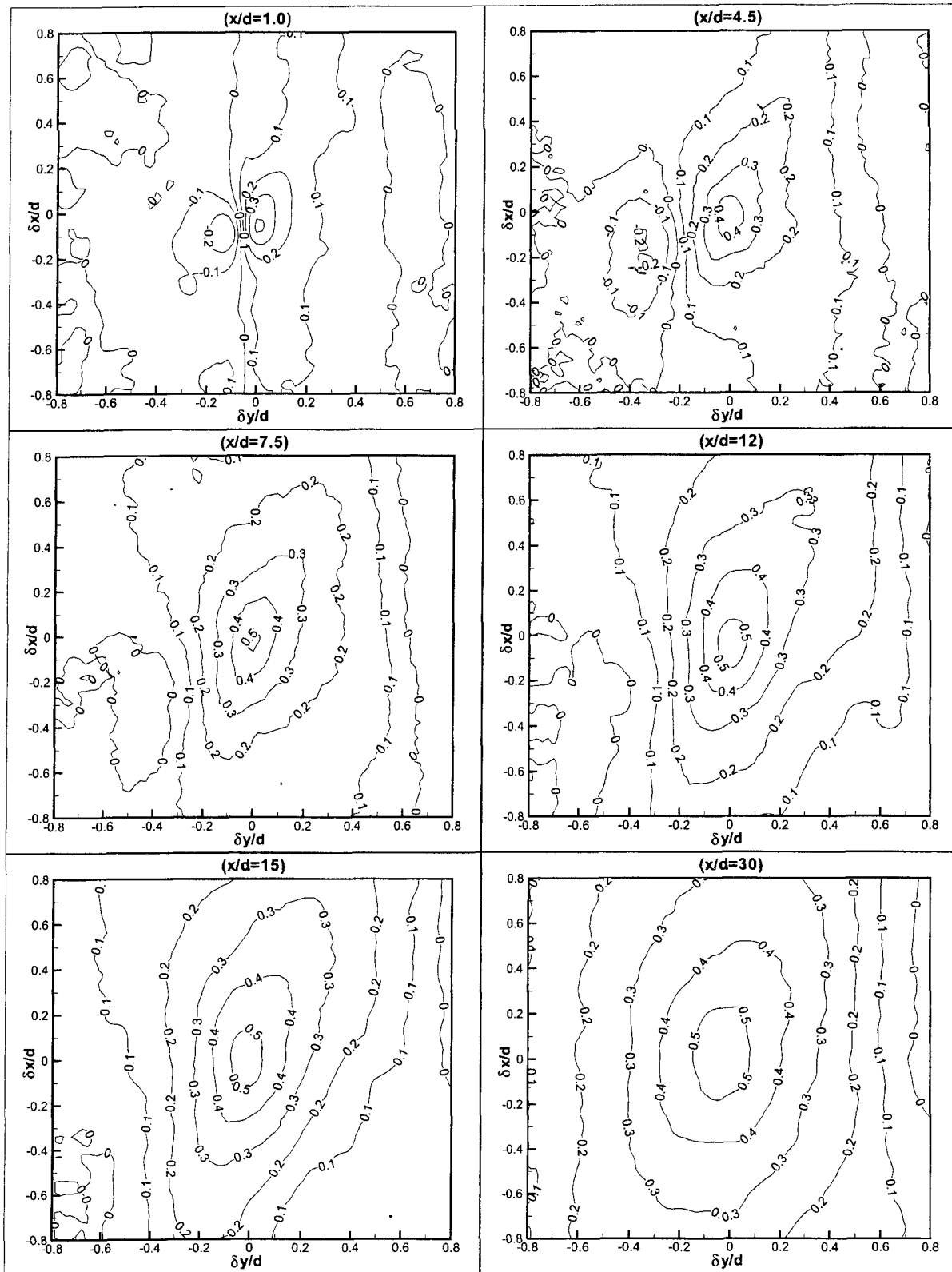


Figure 4.17 Contours of two-point spatial correlation $R_{u'\phi'}$.

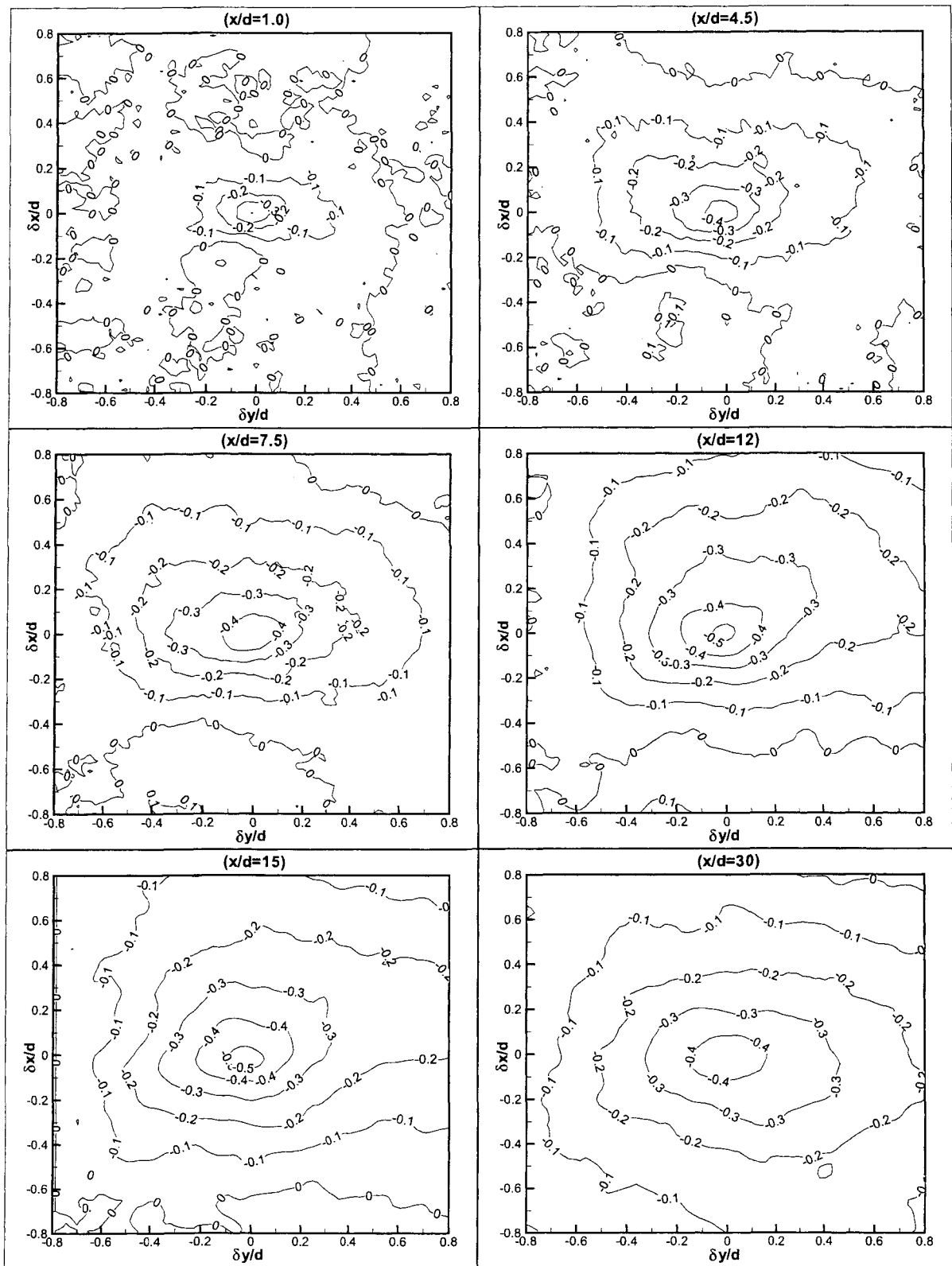


Figure 4.18 Contours of two-point spatial correlation $R_{\psi'\phi'}$.

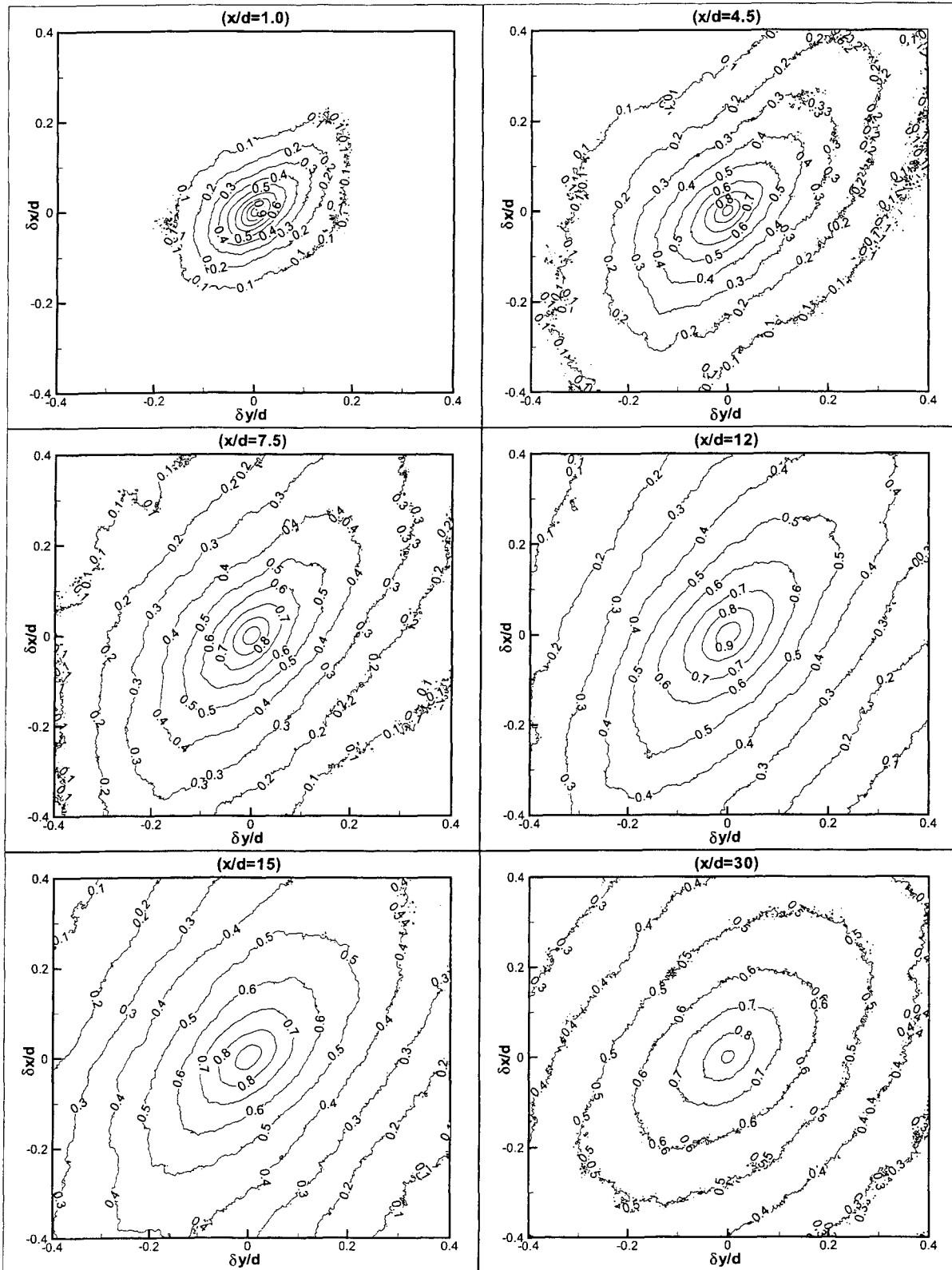


Figure 4.19 Contours of two-point spatial correlation $R_{\phi'\phi'}$.

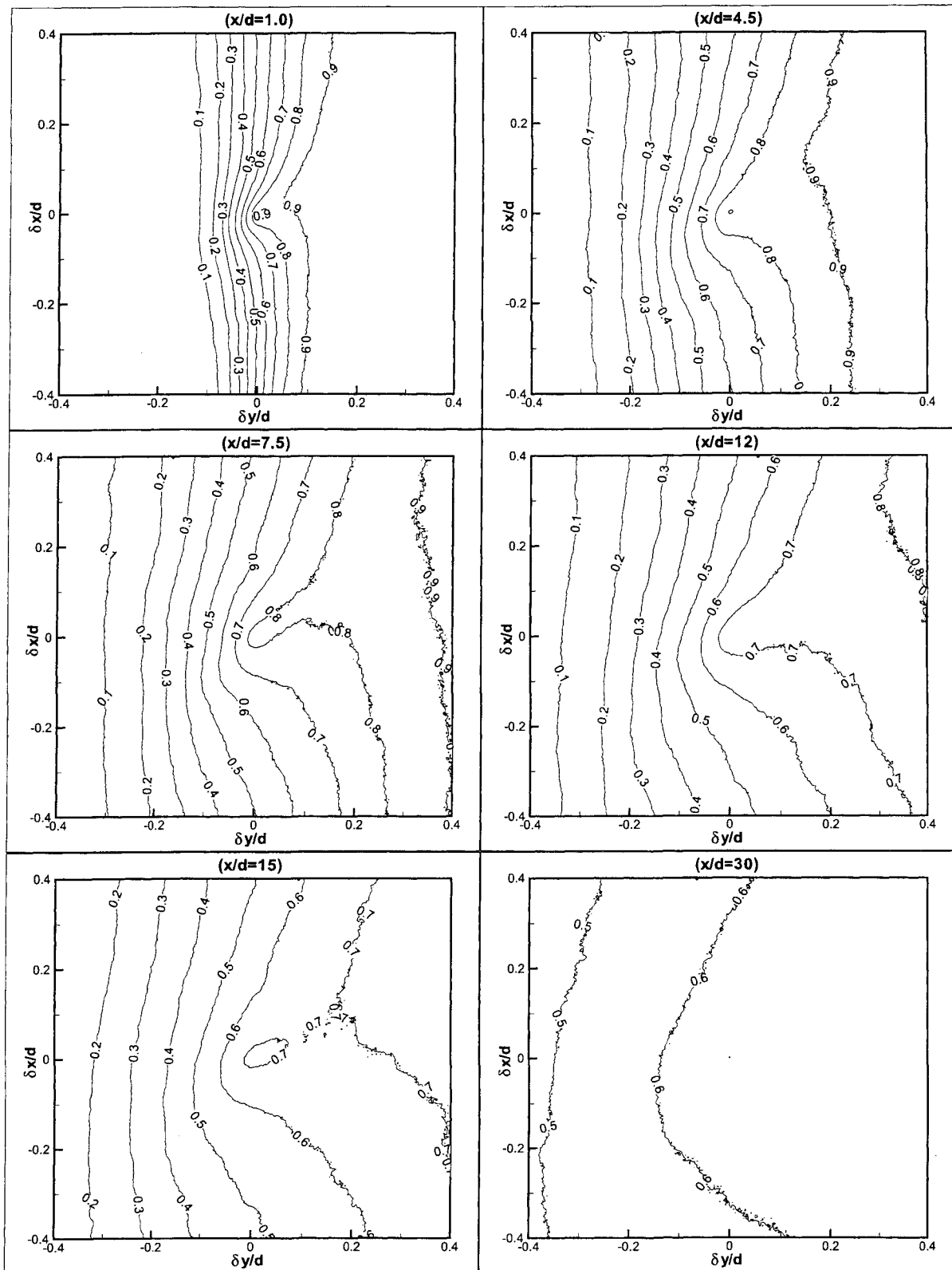


Figure 4.20 Linear stochastic estimate of a concentration field given an event of $\phi'(\mathbf{x}_0) = 2\phi'_{rms}(\mathbf{x}_0)$.

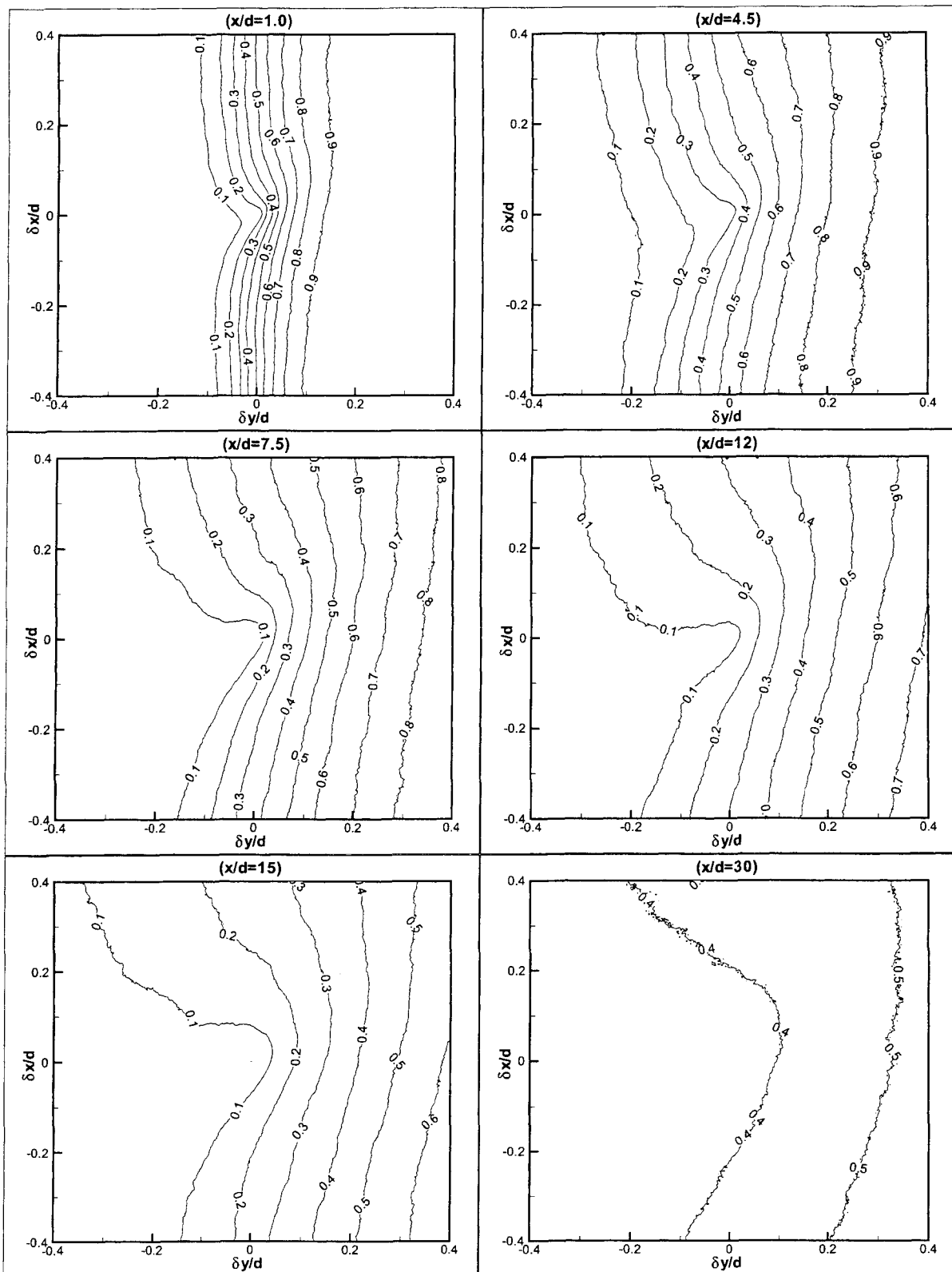


Figure 4.21 Linear stochastic estimate of a concentration field given an event of $\phi'(\mathbf{x}_0) = -2\phi'_{rms}(\mathbf{x}_0)$.

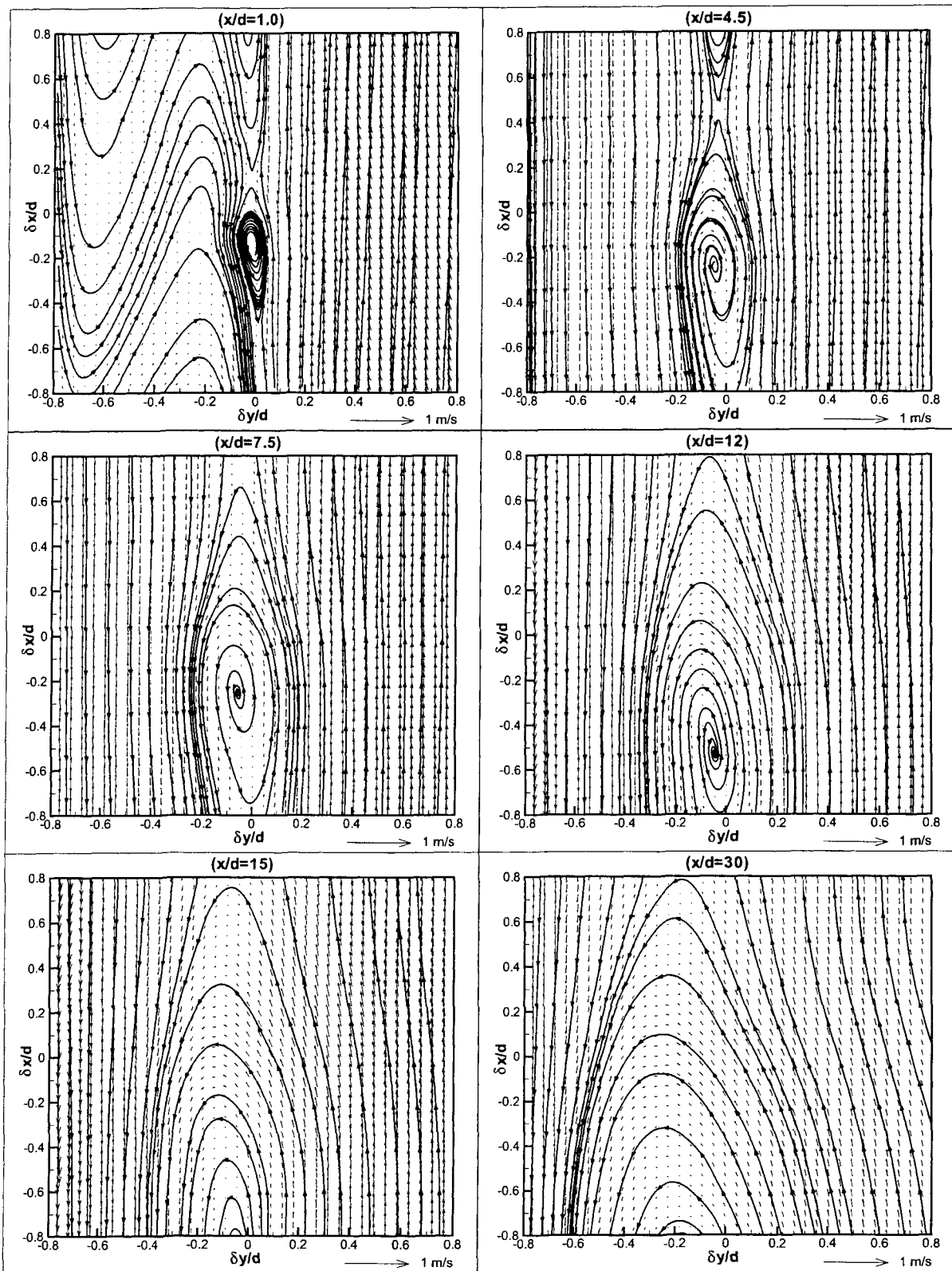


Figure 4.22 Estimated velocity fields given an event of $\phi'(\mathbf{x}_o) = 2\phi'_{rms}(\mathbf{x}_o)$, with $U(\mathbf{x}_o)$ subtracted from each vector.

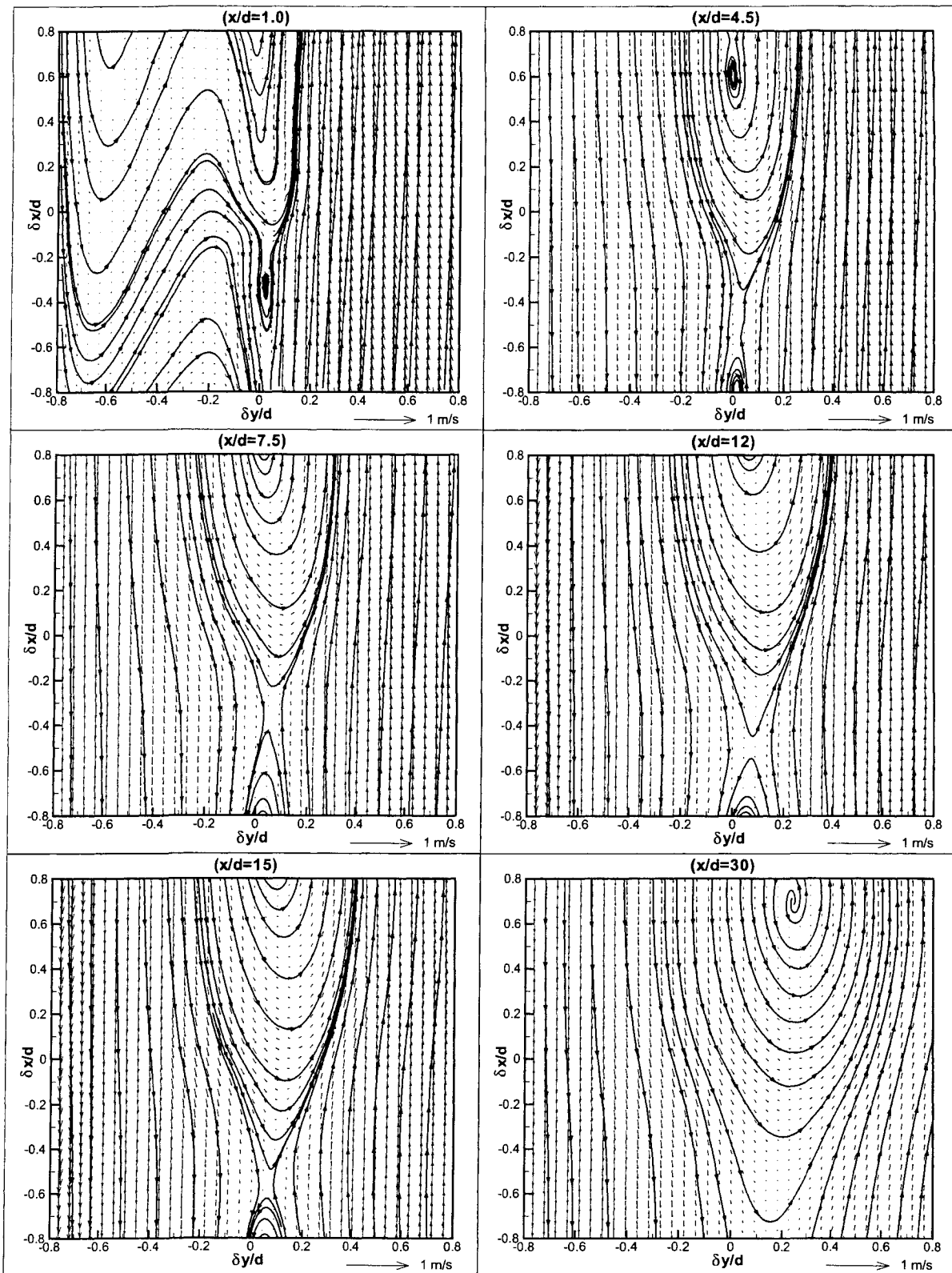


Figure 4.23 Estimated velocity fields given an event of $\phi'(\mathbf{x}_0) = -2\phi'_{rms}(\mathbf{x}_0)$, with $U(\mathbf{x}_0)$ subtracted from each vector.

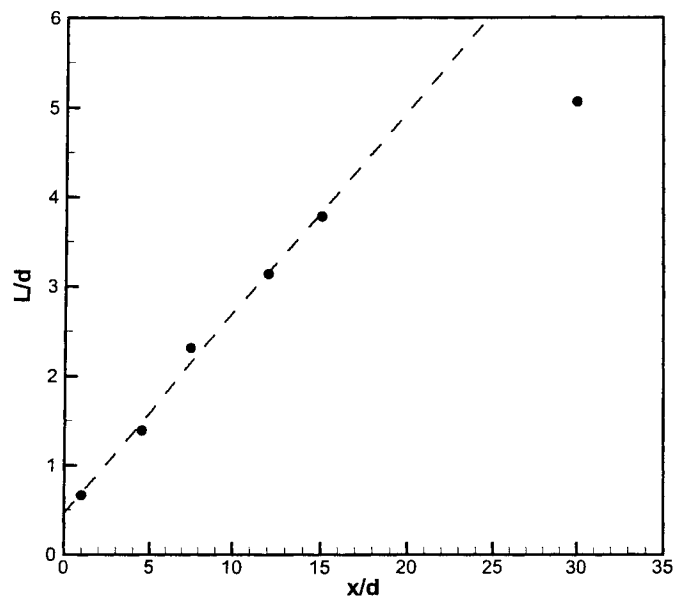


Figure 4.24 Large-structure size based on estimated velocity fields at the measured downstream locations in the flow. The dashed line represents the linear-fit trend line.

CHAPTER 5 SIMULTANEOUS VELOCITY AND CONCENTRATION FIELD MEASUREMENTS OF PASSIVE SCALAR MIXING IN A CONFINED PLANE WAKE

A paper in preparation

Abstract

A combined particle image velocimetry (PIV) and planar laser-induced fluorescence (PLIF) system was employed to investigate the turbulent mixing in a confined liquid-phase rectangular-wake flow with a Reynolds number based on hydraulic diameter of 37,500 and a Schmidt number of 1,250. The simultaneous velocity and concentration field data were analyzed for flow statistics such as mean velocity, Reynolds stresses, concentration mean and variance, turbulent fluxes, turbulent viscosity and diffusivity, and turbulent Schmidt number. The streamwise and transverse turbulent fluxes were found to be of the same magnitude. The turbulent flux vector was not aligned with the mean concentration gradient. The turbulent Schmidt number was about 0.8.

The spatial correlations of turbulent fluxes and concentration fluctuations were evaluated. In the $R_{u'\phi'}$ correlation field, there were a positive and a negative vertically-oriented-elliptical correlation region, which were symmetric around the basis point. The $R_{v'\phi'}$ correlation region was a horizontally oriented ellipse with negative values of the correlation coefficient. The correlation field of $R_{\phi'\phi'}$ was also an ellipse with a horizontal major axis. The behavior of large-scale structures in both the velocity and concentration field was studied using linear stochastic estimation with a defined event of concentration fluctuation. Vortex street was observed in the estimated velocity fields. The streamwise growth of the structure size increased linearly

initially but then grew more slowly.

Introduction

Turbulent mixing is of great importance in many engineering applications due to the outstanding ability to mix and transport species, momentum and energy. A detailed understanding of turbulent shear flows, such as turbulent wakes and jets, is crucial for the development of environmentally benign, commercially efficient chemical processing technologies. Therefore, the present work is devoted to implement state-of-the-art experimental techniques to study the characteristics of turbulent mixing in a confined rectangular wake.

Wakes are generated in the form of a velocity deficit profile when a uniform stream flows over an obstacle. A wake flow is usually distinguished between three regions: a near-wake, an intermediate wake and a far wake [Kiya and Matsumura (1985); Tritton (1988)]. It has been found that a turbulent wake approaches a dynamical equilibrium state in the far wake region and exhibits so called self-similarity [Townsend (1956); Tennekes and Lumley (1972)]. However, many experimental studies on turbulent wakes have reported that the self-similarity of wakes is non-universal, the wakes from different generators do not tend to precisely the same self-similar state [Wyganski et al. (1986); Zhou and Antonia (1995); Ghosal and Rogers (1997)]. Furthermore, studies have revealed that turbulent wakes relax to self-similar states that are dependent on their initial conditions as well [Wyganski et al. (1986); Ghosal and Rogers (1997)].

Another important feature of turbulent wakes is the existence of the large-scale coherent structures. One of the seminal work is the study of turbulent shear flows of Townsend [Townsend (1956)], who realized that the large eddies ought to have a quasi-deterministic form and analyzed the velocity spatial-correlation tensor to describe the large-eddy motion. Later on, Grant investigated a fully developed cylinder wake and suggested two possible types of structures, i.e. the “double-roller” eddies and the “mixing jets” [Grant (1958)]. Since then, extensive studies have been done on the large-scale structures in turbulent wakes. Although it has been found recently that the double roller and mixing jet structures are just different

aspects of a single structure, probably a horseshoe-shaped structure [Vernet et al. (1997)], the importance of the organized large-eddy motion in controlling turbulent transport has been well accepted [Cantwell (1981)].

With the advancement of flow visualization techniques, planar laser diagnostic techniques, such as particle image velocimetry (PIV) and planar laser-induced fluorescence (PLIF), have been developed for experimental investigations of turbulent flows. These whole field techniques are capable of giving instantaneous spatial information in turbulent flows and therefore have distinct advantages over pointwise measurements to visualize the large-scale coherent structures. Furthermore, the non-intrusive character enables both PIV and PLIF to provide high-quality measurements of the instantaneous velocity and concentration distribution in turbulent flows. For these reasons, both PIV and PLIF have become attractive to researchers and have been successfully employed to investigate turbulent wake flows (e.g. see Soria (1996) and Elavarasan and Meng (2000)).

The steady-state Reynolds-averaged equation for the conservation of the mean concentration of a passive scalar is given by

$$\langle u_i \rangle \frac{\partial \langle \phi \rangle}{\partial x_i} - \frac{1}{ReSc} \frac{\partial^2 \langle \phi \rangle}{\partial x_i \partial x_i} = - \frac{\partial \langle u'_i \phi' \rangle}{\partial x_i} \quad (5.1)$$

where Re is the Reynolds number, Sc is the Schmidt number, and u_i and ϕ denote the instantaneous velocity and instantaneous concentration, respectively. In this equation, the effects of turbulent transport appear in terms the correlations of the velocity and concentration fluctuations (i.e., turbulent fluxes, or $\langle u'_i \phi' \rangle$), which are usually modeled in a RANS simulation. Therefore, the simultaneous experimental studies of the velocity and concentration fields are needed for the development and validation of numerical models for these terms.

In recent years, many combined PIV and PLIF systems have been developed for the simultaneous measurements of velocity and concentration fields in turbulent flows. Simones and Ayrault (1994) were among the first researchers to combine PIV and PLIF techniques. They employed the combined PIV and PLIF system to measurement the velocity-concentration correlations in gas-phase turbulent flows and validated the technique by comparing their results with classical results. Aanen et al. (1999) performed simultaneous PIV and PLIF measure-

ments of the fully developed liquid-phase axisymmetric turbulent flow in a smooth pipe and found their experimental results consistent with reported numerical and analytical results. Law and Wang (2000) investigated the potential interference effect between PIV and PLIF techniques and claimed that the interference of the fluorescent tracer on PIV is negligible, whereas the effect of the seeding particles on PLIF can be attributed to three factors: the attenuation of the laser light as described by the Beer-Lambert law, the interaction with the dye tracer leading to a small increase of local fluorescence, and the residual Mie scattering light that passes the PLIF filter. For this reason, optical filters were employed in most reported combined PIV and PLIF systems to reject the PIV particle scattering on the PLIF images in the simultaneous PIV and PLIF measurements.

Although there is an extensive body of experimental data for turbulent wake flows, studies involving simultaneous velocity and concentration measurements in confined wake flows are far less common in the literature. The objective of the present study was to implement detailed simultaneous measurements of the velocity and concentration fields in a liquid-phase confined turbulent rectangular-wake flow using a combined PIV and PLIF diagnostic system. Also, the spatial correlations of turbulent fluxes and concentration fluctuations and linear stochastic estimates of large-scale structures were calculated to provide insight into the characteristics and behavior of large-scale structures found in the flow.

The remainder of the paper is organized as follows. In Sec. 5, the rectangular-wake flow facility and the experimental methodology are introduced. Section 5 describes the methodology used to determine stochastic estimates of velocity and concentration fields, and Sec. 5 discusses the results from the experiments and the properties of large-scale structures. A summary of results and conclusions is given in Sec. 5.

Experimental Apparatus and Methodology

Flow Facility

The experiments are conducted at the Experimental Fluid Mechanics Laboratory of the Iowa State University. Figure 5.1 shows the flow system, which is designed to provide a shear

flow with a Reynolds number based on channel hydraulic diameter between 5,000 and 10,000. Figure 5.2 is a schematic of the reactor. The reactor is mounted in an adjustable cage so that it is easy to change the interrogation location without moving the optics of the measurement system. The three inlet channels of the reactor are supplied with constant flow rates by three Fisher feedback control systems with flow accuracy of 0.5%. A combination of a packed bed of 1 cm diameter spheres, turbulence reducing screens, and a pair of 4:1 contractions reduces the free stream turbulence intensities and provides nearly uniform flow to each of the three streams. More details of the experimental apparatus can be found in Feng et al. (2005).

The test section is made from Plexiglass with a rectangular cross section of 60×100 mm and with an overall length of 1 m. At the inlet of the test section, there are two splitter plates with a machined angle on the side stream side of 3 degrees and on the center stream side of 1 degree. The width of each of the inlet channels is 20 mm at the tips of splitter plates. For the present study, the volumetric flow rate of each of the inlet channels was 1.0 liter/s, corresponding to a mean free-stream velocity (U_0) of 0.5 m/s. The Reynolds number based on the area-averaged velocity and the hydraulic diameter of the test section was 37,500. The three streams come together downstream of the splitter plate and form two rectangular wakes in the test section.

The seed particles for PIV measurements were hollow glass spheres (Sphericel, Potters Industries, Inc.) with a nominal diameter of $11.7 \mu\text{m}$ and a density of 1.1 g/cm^3 . Before performing the measurements, 24 grams of seed particles were added to 3,500 liters water and mixed until they were distributed homogeneously. Rhodamine 6G was used as the fluorescence dye for PLIF measurements. The Schmidt number of Rhodamine 6G is 1,250 [Crimaldi and Koseff (2001)]. In the center stream, the source concentration of Rhodamine 6G was $45 \mu\text{g/liter}$, while the other two streams were pure water.

In the present study, all planar images were acquired in the center plane between the front and back walls of the test section. The coordinate system is such that x is in the streamwise direction and y is in the transverse direction. The center point between the tips of the splitter plates is designated as the origin.

Combined PIV and PLIF system

A schematic depicting the combined PIV and PLIF measurement system is also shown in Fig. 5.1. Illumination of these experiments was provided by a double-pulsed New Wave Research Gemini Nd:YAG laser that emits two independent 532 nm light pulses. The maximum pulse energy is 120 mJ and the pulse duration is about 5 ns. The laser beam was formed into a thin light sheet and focused on the center line (in the y - direction) of the test section using a combination of mirrors and lenses. The thickness of the light sheet was about 0.5 mm in the measured flow field.

PIV and PLIF image pairs were captured using two 12-bit LaVision Flowmaster 3S CCD cameras with a resolution of 1280×1024 pixels. The PIV camera was placed parallel to the laser sheet, whereas the PLIF camera was aligned perpendicular to the laser sheet. The two cameras were positioned carefully so that they viewed the same regions in space and the image magnification of each camera was about 0.12. Since the light exiting from the test section consists of both laser light scattered by the seed particles and fluorescence emitted by the fluorescent dye (when excited by the Nd:YAG laser, Rhodamine 6G emits broadband fluorescence with a peak emission around 555 nm [Penzkofer and Leupacher (1987)]), a dichroic mirror placed at a 45-degree angle to the laser sheet was used to separate these components of the light and direct them to either the PIV or the PLIF camera. To ensure the cleanest possible PIV and PLIF images, optical filters were also attached to both the PIV and PLIF camera lenses. A narrow band pass filter centered at 532 nm was attached to the PIV camera lens. Likewise, the PLIF camera lens was fitted with a long pass filter blocking light below 555 nm to clean up any laser light that may have passed through the dichroic mirror and also to remove any background laser light from diffuse reflections off surfaces.

The PIV camera was set in the double-frame-double-exposure mode, thus two images were captured per realization, and the corresponding velocity field was computed using a cross-correlation technique. The time interval between two laser pulses was $700 \mu\text{s}$ in this study. The numerical aperture of the PIV camera was 8. A multi-pass interrogation scheme with decreasingly smaller window sizes was used with a final interrogation spot size measuring

16×16 pixels, corresponding to 0.9 mm on a side. With 50% overlap between adjacent interrogation spots, the velocity vector spacing was 0.45 mm in both the x- and y- directions. In our previous non-simultaneous PIV and PLIF study on this wake, the Kolmogorov scales and the spatial resolution in terms of the Kolmogorov scales at some observed locations were evaluated [Liu et al. (2006)]. As Table 5.1 shows, the spatial resolution of PIV measurements in terms of the Kolmogorov scale improves from 8.7η at $x/d = 1.0$ to 4.1η at $x/d = 15$. The experimental uncertainty of the the PIV measurements was $\pm 3\%$ [Liu et al. (2006)]. Peak locking [Christensen (2004)] is a potential problem in PIV experiments in which measured particle displacements can become biased towards integer pixel displacements. The peaking-locking effect in any given PIV experiment can be quantified by determining the *peak-locking coefficient* [Stanislas et al. (2005)]. For the results presented here, this coefficient was found to be 0.04, indicating an acceptably low degree of peak locking.

The signal processing and image calibration of PLIF measurements have been described in our previous study [Feng et al. (2005); Liu et al. (2006)]. In the present work, the PLIF camera was set in the single-frame-single-exposure mode with an exposure time of $500 \mu\text{s}$. The numerical aperture of the PLIF camera was 5.6. The diffraction-limited spot size for the PLIF optical system was $8.1 \mu\text{m}$, however the in-plane spatial resolution of the PLIF measurements was limited instead by the area viewed per pixel, which was $56 \mu\text{m}$. The smallest length scale of turbulent mixing is known as the Batchelor scale. As Table 5.2 shows, the resolution of PLIF measurements is much larger than the Batchelor scale in all directions, therefore the smallest concentration scale can not be resolved in the present study. The shot-to-shot variability of the laser power was tested in our previous study and was found to be remarkably steady in this diagnostic system [Liu et al. (2006)]. Thus, it was deemed unnecessary to monitor the shot-to-shot laser power variations during the PLIF experiments.

Using the method given by our previous work [Liu et al. (2006)], Kolmogorov time scales at the investigated locations were estimated and also given in Table 5.1. Notice that duration of the combined PIV/PLIF measurement ($600 \mu\text{s}$) was very small in comparison to the Kolmogorov time scale at each location. The PIV and PLIF measurements thus could be con-

sidered to be simultaneous in the present study. The laser and the two cameras were connected to a host computer that controlled the timing of the laser illumination and image acquisition. The simultaneous PIV and PLIF images were captured at a frame rate of 1 image/sec (note that each image consists of two PIV frames and one PLIF frame). Since the volume of water reservoirs is limited, 650 sets of images were captured in one run experiment. At each investigated location, 5 runs of measurements were performed under the same experimental conditions. This resulted in a realization of 3250 sets of simultaneous images in total at each location.

Stochastic Estimation of Concentration and Velocity Fields

Linear stochastic estimation (LSE) is a useful method to reduce the large-scale structure in turbulent flows [Adrian (1994)]. When the conditions corresponding to a specific large-scale structure are properly defined, the flow field representing that structure based on the spatial correlations can be directly calculated using linear stochastic estimation. Any number of criteria can be used for the defining event. Generally, the event upon which a linear stochastic estimate is based is a velocity fluctuation in studies consisting only of velocity-field measurements [Prasad and Gonuguntla (1996); Agrawal and Prasad (2002)]. A characteristic value of the deformation tensor has also been used as the defining event to find the linear stochastic estimate of velocity fields [Olsen and Dutton (2002, 2003)]. Taking advantage of the simultaneous PIV and PLIF measurements in the present work, a concentration fluctuation was used as the defining event for the linear stochastic estimation to predict concentration fields and velocity fields.

Linear Stochastic Estimation of Concentration Fields

Let $\phi'(\mathbf{x}_o)$ be the concentration fluctuation at location \mathbf{x}_o . Using $\phi'(\mathbf{x}_o)$ as the defining event, the linear stochastic estimate of the concentration fluctuation over the entire field is given by

$$\langle \phi'(\mathbf{x}) | \phi'(\mathbf{x}_o) \rangle = A(\mathbf{x}) + B(\mathbf{x})\phi'(\mathbf{x}_o). \quad (5.2)$$

The coefficients $A(\mathbf{x})$ and $B(\mathbf{x})$ are then determined by minimizing the mean square error of the estimated concentration field compared to the actual concentration field. This yields the results

$$A(\mathbf{x}) = 0, \quad (5.3)$$

$$\langle \phi'(\mathbf{x}_o)\phi'(\mathbf{x}) \rangle = B(\mathbf{x})\langle \phi'(\mathbf{x}_o)\phi'(\mathbf{x}_o) \rangle. \quad (5.4)$$

Notice that $\langle \phi'(\mathbf{x}_o)\phi'(\mathbf{x}) \rangle$ is the (unnormalized) two-point spatial correlation of ϕ' , which we will denote as $\hat{R}_{\phi'\phi'}$. Thus

$$B(\mathbf{x}) = \frac{\hat{R}_{\phi'\phi'}}{\langle \phi'(\mathbf{x}_o)\phi'(\mathbf{x}_o) \rangle}, \quad (5.5)$$

which can be evaluated using the experimentally measured spatial correlation of concentration fluctuation. Then, with a given event $\phi'(\mathbf{x}_o)$, Eq. 5.2 can be used to determine the linear stochastic estimate of the concentration field.

Linear Stochastic Estimation of Velocity Fields

Following a similar derivation to that above for concentration, the linear stochastic estimate of the velocity fluctuation over the entire field given the defining event $\phi'(\mathbf{x}_o)$ is

$$\langle u'_i(\mathbf{x})|\phi'(\mathbf{x}_o) \rangle = A_i(\mathbf{x}) + B_i(\mathbf{x})\phi'(\mathbf{x}_o). \quad (5.6)$$

The coefficients A_i and B_i can be determined in a similar manner as before, resulting in

$$A_i(\mathbf{x}) = 0, \quad (5.7)$$

$$\langle \phi'(\mathbf{x}_o)u'_i(\mathbf{x}) \rangle = B_i(\mathbf{x})\langle \phi'(\mathbf{x}_o)\phi'(\mathbf{x}_o) \rangle. \quad (5.8)$$

However, $\langle \phi'(\mathbf{x}_o)u'_i(\mathbf{x}) \rangle$ is the (unnormalized) two-point spatial correlation of ϕ' and u'_i , which we will denote as $\hat{R}_{\phi'u'_i}$, thus

$$B_i(\mathbf{x}) = \frac{\hat{R}_{\phi'u'_i}}{\langle \phi'(\mathbf{x}_o)\phi'(\mathbf{x}_o) \rangle}. \quad (5.9)$$

Then solving for $B_i(\mathbf{x})$ Eq. 5.6 can be used to estimate $u'_i(\mathbf{x})$ given the event $\phi'(\mathbf{x}_o)$.

Results and Discussion

Figure 5.3 exhibits a pair of instantaneous velocity and concentration fields captured by the combined PIV and PLIF system. The distance between the tips of the splitter plates, $d = 20$ mm, is used to normalized the coordinates in all plots. In Fig. 5.3(a), the free-stream velocity (U_0) of 0.5 m/s has been subtracted from each vector to aid in the visualization of turbulent structures. A system of double roller-like counter-rotating large eddies can be readily observed in each of the wakes. The contour levels in Fig. 5.3(b) represent the concentration normalized by the input source concentration Φ_0 .

Evolution of Wakes

Profiles of the ensemble-averaged streamwise velocity and Reynolds stresses (normalized by U_0 and U_0^2 respectively) are presented in Fig. 5.4 for seven representative downstream locations: $x/d = 0, 1, 4.5, 7.5, 12, 15,$ and 30 . Note that data at $x/d = 0$ are the initial conditions. Figure 5.5 shows the transverse profiles of ensemble-averaged concentration and variance at six streamwise locations. All these results are nearly identical as those obtained by the non-simultaneous PIV and PLIF measurements in our previous work [Liu et al. (2006)], indicating that the combined PIV and PLIF system developed in the present study is capable of providing high-quality measurements.

It is seen that two wakes regions form just downstream of the tips of the splitter plates as the boundary layers on the splitter plate surfaces merge downstream of the tips. The potential core in the center stream disappears at $x/d = 4.5$, indicating that the two wakes meet at this location. At the lower downstream locations the wake velocity defect diminishes quickly, so that the wakes already decay at $x/d = 30$ and the velocity profile begins to look like a fully developed channel flow. Also note that due to the two boundary layers along the splitter plates, the longitudinal Reynolds stress, $\langle u'u' \rangle$, in each wake displays two peaks at lower downstream locations. These peaks remain distinct until the wake decays. As an impact of the boundary layers along side walls, all Reynolds stresses are non-zero in regions near side walls.

The mean concentration profile is a top-hat shape initially but becomes bell-shaped after

the potential core in the center stream disappears. This bell-shaped profile persists through $x/d = 30$, indicating that the fluid is not fully mixed at the farthest observed downstream location in this study. Consequently, the profile of concentration variance still has two pronounced peaks at $x/d = 30$. Figure 5.6 shows the orientation of the mean concentration gradient in the flow. As a reminder, the coordinate system in this work is such that 0° is in the streamwise direction and $+90^\circ$ is in the y - direction. Except in the potential core of each stream, the orientation of the mean concentration gradient is $+90^\circ$ in the left part of the test section but -90° in the right part, indicating that the mean gradient in the streamwise direction is much smaller than that in the cross-stream direction.

Our previous study [Liu et al. (2006)] examined the self-similarity in this wake flow, showing that the mean velocity profile of the wake tends to reach an equilibrium state, but unlike in a free wake the distribution of the velocity defect near the edges of the wake is very different due the interaction of the two wakes and the effect of the boundary layers growing along the side walls.

Turbulent Fluxes

The turbulent fluxes are very important in the understanding of the turbulent scalar transport since these terms describe both the direction and the magnitude of the mass transported by the turbulence. The profiles of the measured turbulent flux at six downstream locations are exhibited in Fig. 5.7.

As Fig. 5.7(a) shows, the profiles of the streamwise turbulent flux, $\langle u'\phi' \rangle$, are approximately symmetric about the centerline of the test section. Before the potential cores disappear, $\langle u'\phi' \rangle$ is zero in each of the free streams. However, $\langle u'\phi' \rangle$ is nonzero in the wakes and in the boundary layers near the side walls. Due to the velocity deficit, $\langle u'\phi' \rangle$ changes sign in each of the wakes. The magnitude of the peaks for $\langle u'\phi' \rangle$ in the wakes decreases as the wakes evolve. At the farthest downstream location, $x/d = 30$, although the concentration variance is still significant, $\langle u'\phi' \rangle$ becomes nearly zero in the center region of the test section due to the collapse of the wakes.

The profiles of the cross-stream turbulent flux, $\langle v'\phi' \rangle$, are antisymmetric about the centerline of the test section, as shown in Fig. 5.7(b). Consistent with the gradient-diffusion hypothesis, $\langle v'\phi' \rangle$ is negative where the gradient of concentration mean is positive and positive where the gradient is negative. Like $\langle u'\phi' \rangle$, $\langle v'\phi' \rangle$ is zero in potential core regions. As the wakes evolve, the peak in each of the profiles of $\langle v'\phi' \rangle$ increases first and reaches a maximum at $x/d = 4.5$, and then decreases gradually but still remains distinct after the wakes collapse. Also notice that $\langle v'\phi' \rangle$ has the same magnitude as $\langle u'\phi' \rangle$.

The mass transport correlation coefficients are given by normalizing the turbulent fluxes with the *rms* of the local velocity fluctuation and local concentration fluctuation. The cross-stream turbulent flux has been found to be self-similar in free turbulent flows [Ma and Warhaft (1986); de Bruyn Kops and Mortensen (2005)]. As Fig. 5.8 shows, the profile of the cross-stream mass transport correlation coefficient shows somewhat self-similarity at some locations after the potential core in free stream disappears. The peak value of the cross-stream coefficient is about 0.6, approximately the same as the coefficient observed in grid turbulence, mixing layer and rectangular jet [Ma and Warhaft (1986); de Bruyn Kops and Mortensen (2005); Feng et al. (2006)].

Figure 5.9 shows the profiles of the orientation of the turbulent flux vector at the measurement locations. Obviously the orientation of the turbulent flux vector is positive where the $\langle v'\phi' \rangle$ flux is positive, and negative where the $\langle v'\phi' \rangle$ flux is negative. Note that the angle is approximately a constant of -140° between $y/d = -1$ and $y/d = -0.5$ and about -40° between $y/d = -0.5$ and $y/d = 0$, implying symmetry about -90° . This is because $y/d = -0.5$ is the center line of the wake, where the $\langle u'\phi' \rangle$ flux changes sign and the $\langle v'\phi' \rangle$ flux reaches its maximum, such that the orientation of the flux vector is -90° at $y/d = -0.5$. Similar result is observed for the wake in the right half of the test section. Uniform orientation of the flux vector have been reported in turbulent shear flow and jet [Rogers et al. (1989); Feng et al. (2006)]. However, due to the effects of the constraint of the flow and the interaction of the two wakes, regions with uniform orientation of the flux vector disappear quickly in the present study. Moreover, since the the mean scalar gradient and the turbulent flux vector are

not aligned, the simple gradient transport model using a scalar diffusivity cannot completely describe the behavior of the turbulent flux in this flow.

Turbulent Viscosity and Turbulent Diffusivity

According to the turbulent-viscosity hypothesis, the scalar coefficient ν_T , called the *turbulent viscosity* (or *eddy viscosity*) can be evaluated from the experimental data using the below equation:

$$\nu_T = \frac{-\langle u'v' \rangle}{\partial U / \partial y}. \quad (5.10)$$

Figure 5.10 displays the profiles of the turbulent viscosity at six downstream locations. It is seen that the dimensionless turbulent viscosity is initially around 0.002 and increases in the streamwise direction. In regions near the sidewalls, the turbulent viscosity drops to zero. Since both the Reynolds shear stress and the gradient of the mean streamwise velocity are very close to zero at farther downstream locations, the results of the turbulent viscosity become noisy at these locations.

It has been noted that the turbulent diffusivity, Γ_T , has a different value for different orientations of the mean scalar gradient in some turbulent flows [Richardson (1920); Rogers et al. (1989)]. The turbulent diffusivity tensor (Γ_{ij}) is defined by the generalization to the gradient-transport hypothesis [Batchelor (1949)]. Since the mean concentration gradient is not aligned with the turbulent flux vector for this flow, Γ_{ij} is not a diagonal tensor. In the present study, only two components of the tensor are measurable:

$$\Gamma_{12} = \frac{-\langle u'\phi' \rangle}{\partial \Phi / \partial y}, \quad (5.11)$$

$$\Gamma_{22} = \frac{-\langle v'\phi' \rangle}{\partial \Phi / \partial y}. \quad (5.12)$$

The profiles of Γ_{12} at six downstream locations are displayed in Fig. 5.11. Like $\langle u'\phi' \rangle$, the profiles are antisymmetric about the centerline of the test section, but the sign of Γ_{12} is the opposite of $\langle u'\phi' \rangle$ as expected. The significantly non-zero value of Γ_{12} indicates that the mean concentration gradient is not aligned with the turbulent flux in the present study.

Figure 5.12 exhibits the profiles of Γ_{22} at six downstream locations. Γ_{22} is the so-called *turbulent diffusivity*, Γ_T [Tavoularis and Corrsin (1981)]. The profiles of Γ_{22} are symmetric about the centerline of the test section. At first, Γ_{22} increases rapidly as the wake evolves, then remains nearly constant until the wake collapses. In regions near the side walls, Γ_{22} becomes small as well.

As seen in Fig. 5.13, the profiles of the ratio of Γ_{12} and Γ_{22} are antisymmetric about the centerline of the test section. This ratio indeed reflects the ratio of the turbulent fluxes. Although it was reported that this ratio is a constant of 2 in turbulent shear layers [Feng et al. (2006); Tavoularis and Corrsin (1981)], the present result indicates that this ratio is not a constant in wakes but varies between ± 1 .

As an important modelling parameter for numerical simulations on turbulent flows, the turbulent Schmidt number, defined by $Sc_T \equiv \nu_T/\Gamma_T$, is usually assumed uniform throughout the flow in numerical studies. Although the assumption of using a constant Sc_T has been questioned, it has been reported that the turbulent Schmidt number, although spatially varying, is everywhere of order one with transverse mean scalar gradient [Brethouwer (2005); Feng et al. (2006)]. Figure 5.14 exhibits the cross-sectional profiles of the turbulent Schmidt number at various downstream locations obtained in the present study. Although some spatial variation in Sc_T is observed, the value of Sc_T is fairly constant around 0.8.

Two-point Spatial Correlations

The simultaneous nature of the combined PIV and PLIF measurements facilitates the computation of the two-point spatial correlations of turbulent fluxes. Normalized by the *rms* of velocity and concentration fluctuations, these spatial correlations are defined as

$$R_{u'_i\phi'}(x, y; X, Y) = \frac{\langle u'_i(x, y)\phi'(X, Y) \rangle}{\sqrt{\langle u'^2_i(x, y) \rangle \langle \phi'^2(X, Y) \rangle}} \quad (5.13)$$

where (X, Y) are the coordinates of a basis point (*i.e.*, *the point about which the spatial correlation is measured*) and (x, y) is an arbitrary point in the flow field. The area over which the spatial correlation is calculated is a square grid corresponding to 89×89 vectors centered

on the basis point. In the present study, the location of the left peak in the concentration variance was chosen as the basis point.

Figure 5.15 shows the spatial correlations $R_{u'\phi'}$ for basis points located at the six downstream locations. The streamwise flow direction in all the presented correlation fields is from the bottom to the top of the figure. The corresponding spatial correlation for a confined rectangular jet has been previously calculated and presented [Feng et al. (2006)]. In the rectangular jet, the correlation field is an ellipse centered on the basis point. However, in this study, both a positive-correlated region and a negative-correlated region are observed and symmetric around the basis point. This is expected because a pocket of fluid jumping from the left side stream into the wake yields a positive ϕ' but a negative u' , whereas a pocket of fluid jumping from the center stream into the wake yields both a negative ϕ' and a negative u' .

Both the positive and the negative correlated regions are elliptical in shape with the major axis oriented in the streamwise direction, implying that the correlation distance in the streamwise direction is relatively longer than in the transverse direction. The overall sizes of both the positive and the negative correlated regions grow as the basis point moves downstream, suggesting an increase in the size of the turbulent structures. The correlated region becomes weaker as the wakes evolve until they are uncorrelated at the farthest observed downstream location, $x/d = 30$.

The spatial correlations $R_{v'\phi'}$ are presented in Fig. 5.16. This correlation field is a horizontally oriented ellipse with negative values of the correlation coefficient. This is expected because $R_{v'\phi'}$ at the basis point is indeed the mass transport correlation coefficient as shown in Fig. 5.8. The short correlation distance in the x direction implies the rapid variation in the corresponding v velocity fluctuations.

When u'_i is replaced by ϕ' , Eq. 5.13 calculates the spatial correlation of concentration fluctuations. The basis point was still set on the location of the left peak in the concentration variance. The area over which these spatial correlations were calculated was a grid of 323×323 camera pixels centered around the basis point. In the previous rectangular jet study, the correlation field is an ellipse with the major axis inclined at approximately 45-degree due to

the mean shear of the flow field [Feng et al. (2006)]. As Fig. 5.17 shows, the correlation field in the present study is also elliptical in shape but with a horizontal major axis. Like the other spatial correlations presented, the highly correlated region in the $R_{\phi'\phi'}$ correlation field grows larger as the wake evolves, suggesting an increase in the size of large-scale turbulent structures.

Linear Stochastic Estimation

Concentration Fields

As introduced in previous sections, linear stochastic estimation allows for conditional averages to be determined from a much smaller ensemble size than would be required from a direct calculation. More importantly, stochastic estimates are derived directly from spatial correlations, LSE is therefore a useful tool to visualize what types of flow structures are responsible for the features observed in spatial correlations. Also note that as the technique acts as a form of spatial filter removing small turbulent scales, the underlying large turbulent structures can be more readily observed with LSE.

Figures 5.18 and 5.19 exhibit the estimated concentration fields given the events of $\phi'(\mathbf{x}_o) = \pm 2\phi'_{rms}(\mathbf{x}_o)$, respectively, where \mathbf{x}_o represents the basis point located at the left peak in the variance. The event as defined by $\phi'(\mathbf{x}_o) = 2\phi'_{rms}(\mathbf{x}_o)$ is representative of a finger of unmixed fluid reaching out from the center stream into the outer stream. Similarly, $\phi'(\mathbf{x}_o) = -2\phi'_{rms}(\mathbf{x}_o)$ is characteristic of a mixing event that transports fluid from the outer stream into the center stream. These plots reveal that, as expected, for a defining event of positive fluctuation in concentration, higher concentration fluid is expelled from the center stream to the outer stream; conversely, a negative concentration fluctuation event corresponds to a pocket of low dye concentration outer stream fluid being transported into the the center stream. In both cases, the finger advects fluid from one stream into the other stream horizontally. Moreover, the sequence of stochastic estimates for basis point locations from $x/d = 1$ to $x/d = 30$ reveals that the length scales of the fingers of entrained fluid grow with increasing downstream distance.

Velocity Fields

Figures 5.20 and 5.21 are samples of the estimated velocity fields around the basis point given the events of $\phi'(\mathbf{x}_o) = \pm 2\phi'_{rms}(\mathbf{x}_o)$, respectively. In observing these plots, one notices that a vortex street is formed in the wake, indicating that the estimated velocity field at each downstream location is dominated by the presence of a large-scale roller structure. The structures increase in size with increasing downstream distance.

For a positive concentration fluctuation event, the basis point at each downstream location is located just downstream of the center of a roller structure, and the counterclockwise roller structure is responsible for the transport of higher dye concentration fluid from the center stream to the outer streams. Similarly, for a negative concentration fluctuation event, the basis point at each downstream location is also located just downstream of the center of a roller structure, but the fluid is being transported from the lower dye concentration outer stream to the center stream by the clockwise roller structure.

The large-scale structure size may be defined as twice the distance from the center of a roller structure to the braid region. Figure 5.22 shows the evolution of the size of the large-scale structures based on the stochastic estimates of the velocity fields. It is seen that the structure size is initially about $0.36d$ and grows nearly linearly from $x/d = 1$ through $x/d = 15$ at a rate of about 0.075. Unlike in a free wake, this linear growth cannot continue in the confined wake flow. Therefore, at the farthest downstream location, the structure size is smaller than would be expected for continued linear growth.

Conclusions

The turbulent mixing in a confined liquid-phase rectangular-wake flow was investigated using a combined PIV and PLIF system. 3,250 sets of simultaneous velocity and concentration field were collected at each of the seven representative downstream regions. The Reynolds number based on the hydraulic diameter and the bulk velocity was 37,500. The Schmidt number of the fluorescent dye is 1,250. The measured flow statistics, such as the mean velocity, Reynolds stresses, and concentration mean and variance agreed remarkably well with those of

our previous non-simultaneous PIV and PLIF study on this flow. It was found that two wakes grew from the tips of the splitter plates such that the potential core in the center stream disappeared at $x/d = 4.5$ where the two wakes met. The wakes evolved quickly so that they already decayed at the farthest measurement location ($x/d = 30$).

The streamwise turbulent flux, $\langle u'\phi' \rangle$, was found to be symmetric about the centerline of the test section, whereas the transverse turbulent flux, $\langle v'\phi' \rangle$, was antisymmetric about the centerline with the same magnitude of the other turbulent flux. Both fluxes were zero in the potential core of each stream. The peak value for $\langle u'\phi' \rangle$ decreased as the wakes evolved. At $x/d = 30$, although the concentration variance was still significant, $\langle u'\phi' \rangle$ became nearly zero in the center region of the test section due to the decay of the wakes. The peak value for $\langle v'\phi' \rangle$ increased first and reached its maximum at $x/d = 4.5$, then decreased as the wake evolved. The orientation of the turbulent flux vector was found varying in the flow but remained uniform in some regions. For example, the angle was a constant of -140° between $y/d = -1$ and $y/d = -0.5$ and about -40° between $y/d = -0.5$ and $y/d = 0$, showing symmetry about -90° or the centerline of the wake in the left part of the test section.

Since the mean concentration gradient was found in the cross-stream direction, the turbulent flux vector was not aligned with the mean gradient. Therefore, the simple gradient transport model using a scalar diffusivity cannot completely describe the behavior of the turbulent flux in this flow. Two components of the turbulent diffusivity tensor were evaluated, as expected the non-diagonal component of the tensor was significantly non-zero. The diagonal component was nearly constant in streamwise direction. The dimensionless turbulent viscosity was initially around 0.002 and increased in the streamwise direction. The results for the turbulent Schmidt number were consistent with the existing body of experimental data [Brethouwer (2005); Feng et al. (2006)], showing spatial variation and an average around 0.8.

Spatial correlations of the turbulent fluxes and concentration fluctuations were evaluated with the simultaneous velocity and concentration data. In the $R_{u'\phi'}$ correlation field, there were a positive and a negative vertically-oriented-elliptical correlation region, which were symmetric around the basis point. The $R_{v'\phi'}$ correlation region was a horizontally oriented ellipse with

negative values of the correlation coefficient. The correlation field of $R_{\phi'\phi'}$ was also an ellipse with horizontal major axis.

Finally, linear stochastic estimation was used to interpret spatial correlation data and to determine conditional structures in both the velocity and concentration fields. The results showed that a positive concentration fluctuation event presented a finger of unmixed fluid reaching out from the center stream into the outer stream and vice versa. In both cases, the finger advected fluid from one stream into the other horizontally. Vortex street was observed in the estimated velocity fields. It was found that the rotation of the vortex was counterclockwise corresponding to a positive concentration fluctuation, whereas clockwise to a negative event. The growth of the structure size increased linearly initially at a rate of 0.075 but then grew more slowly as the flow transitioned towards channel flow.

Table 5.1 Komolgorov time scale, length scale and spatial resolution of PIV measurements.

x/d	τ [ms]	η [μm]	Resolution
1.0	10.7	104	8.7η
4.5	19.3	139	6.5η
7.5	23.4	153	5.9η
12	33.4	183	4.9η
15	49.1	222	4.1η

Table 5.2 Batchelor length scale and spatial resolution of PLIF measurements.

x/d	η_B [μm]	Resolution in x-/y-	Resolution in z-
1.0	2.93	$19.1\eta_B$	$171\eta_B$
4.5	3.93	$14.2\eta_B$	$127\eta_B$
7.5	4.33	$12.9\eta_B$	$115\eta_B$
12	5.17	$10.8\eta_B$	$97\eta_B$
15	6.27	$8.9\eta_B$	$80\eta_B$

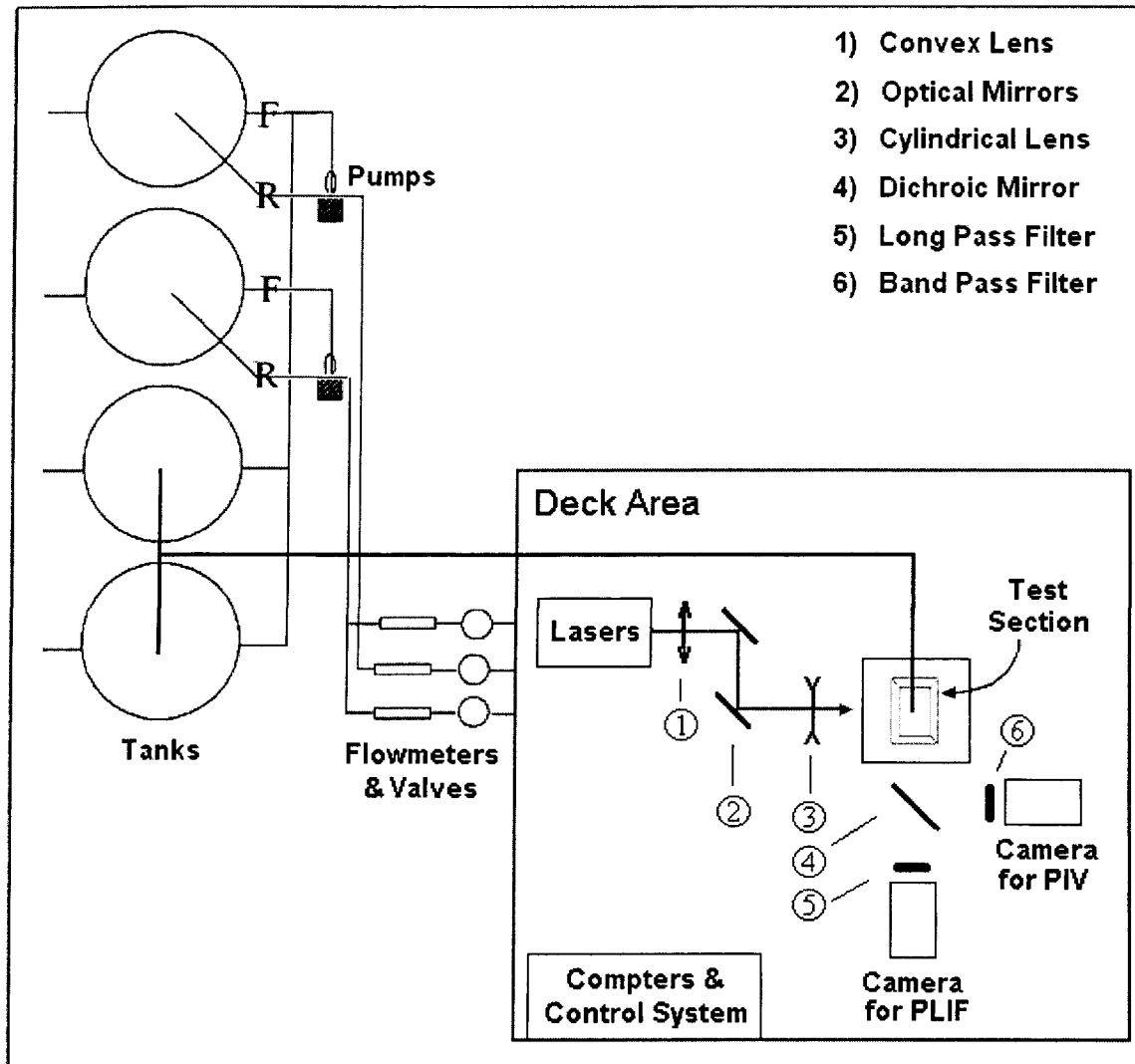


Figure 5.1 Schematic of the flow facility and the optical setup used in the combined PIV and PLIF experiments.

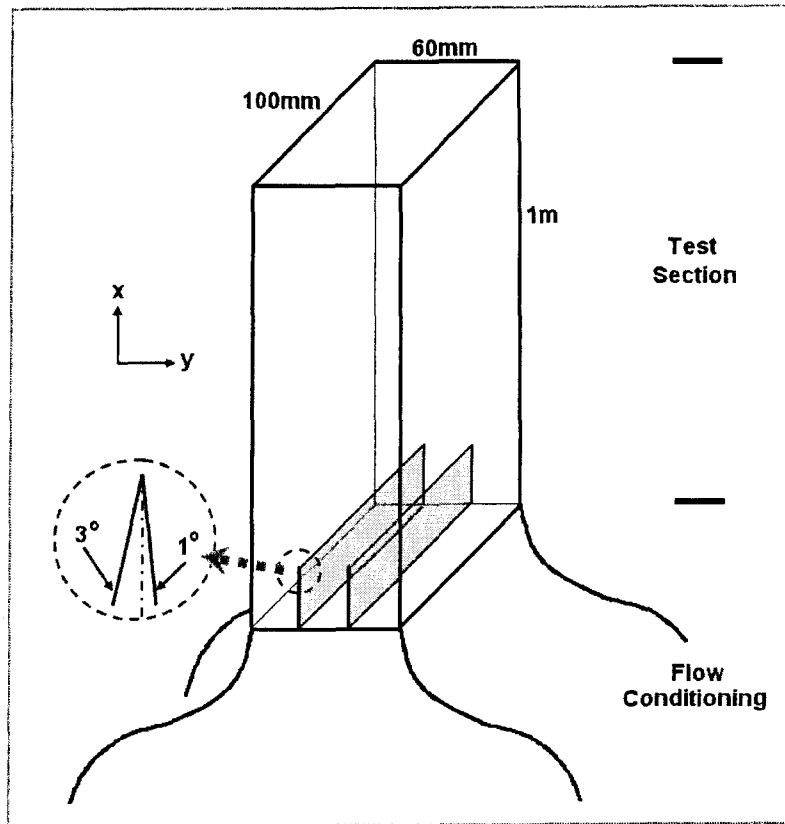


Figure 5.2 Schematic of the confined rectangular-wake reactor.

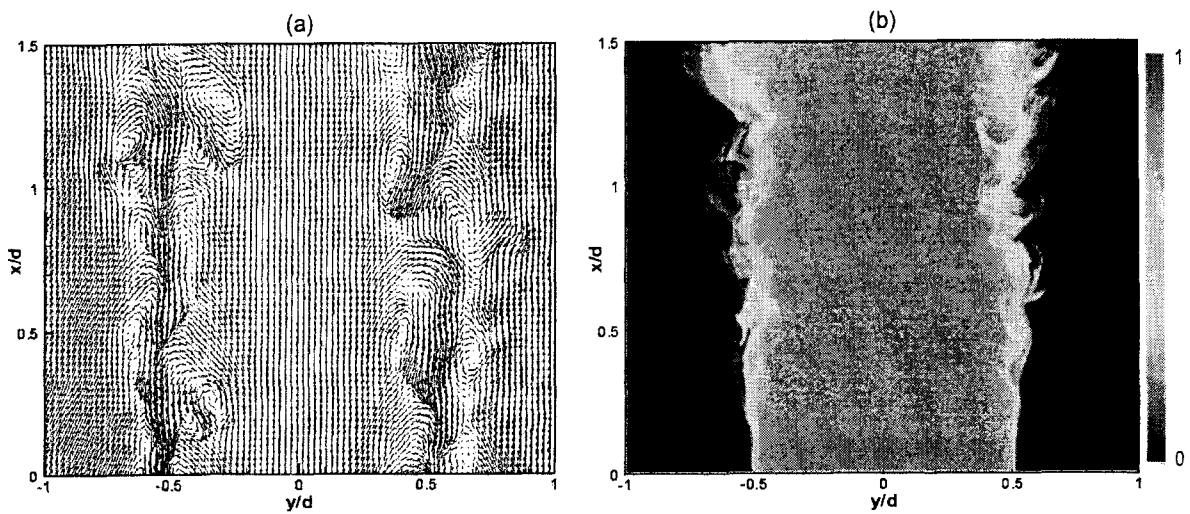


Figure 5.3 (a) An instantaneous velocity field as measured by PIV, and (b) the corresponding instantaneous concentration field as measured by PLIF.

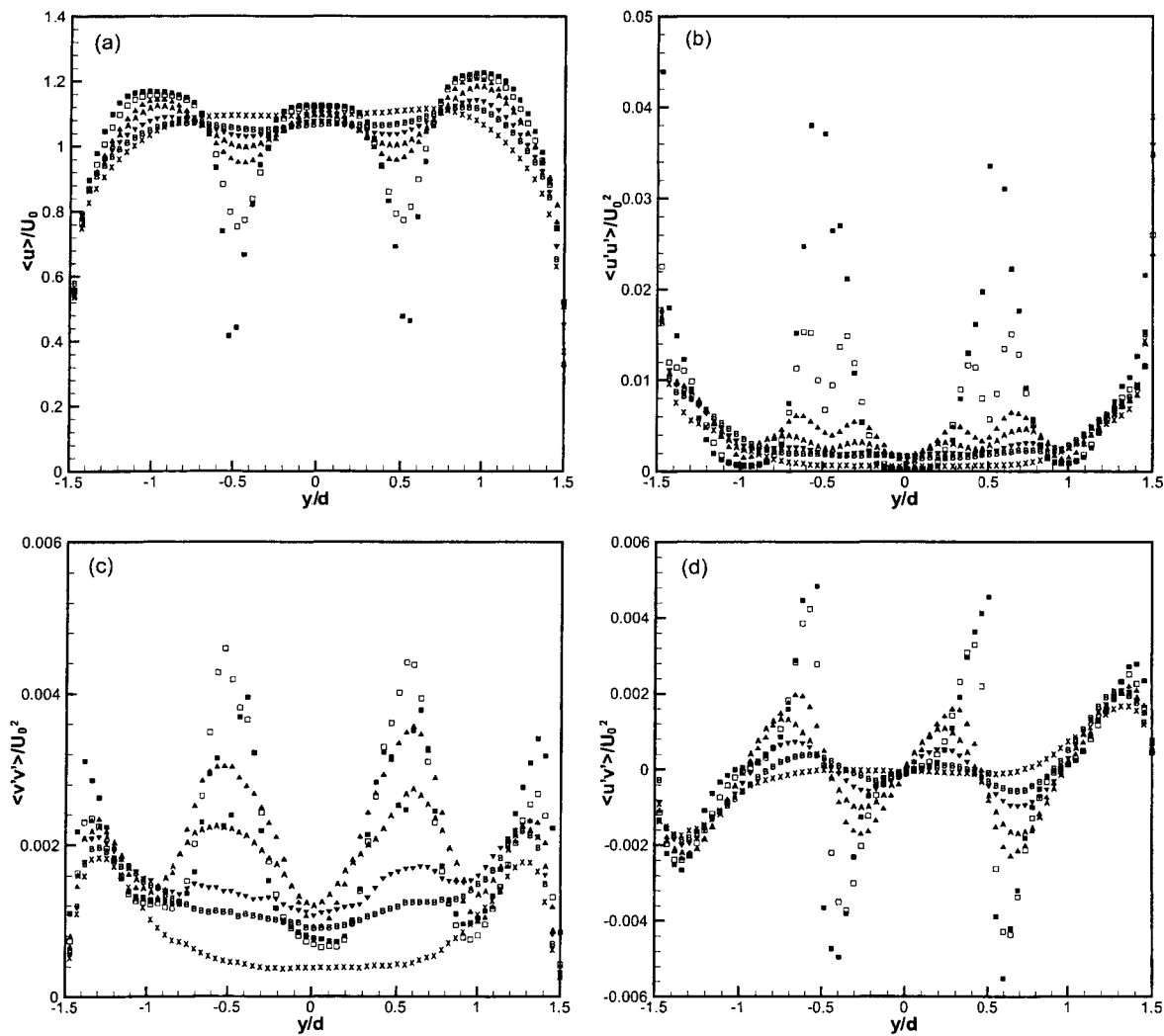


Figure 5.4 Normalized mean streamwise velocity and Reynolds stresses.

■, $x/d = 0$; □, $x/d = 1.0$; ▲, $x/d = 4.5$; A, $x/d = 7.5$; ▼, $x/d = 12$; B, $x/d = 15$; ×, $x/d = 30$.

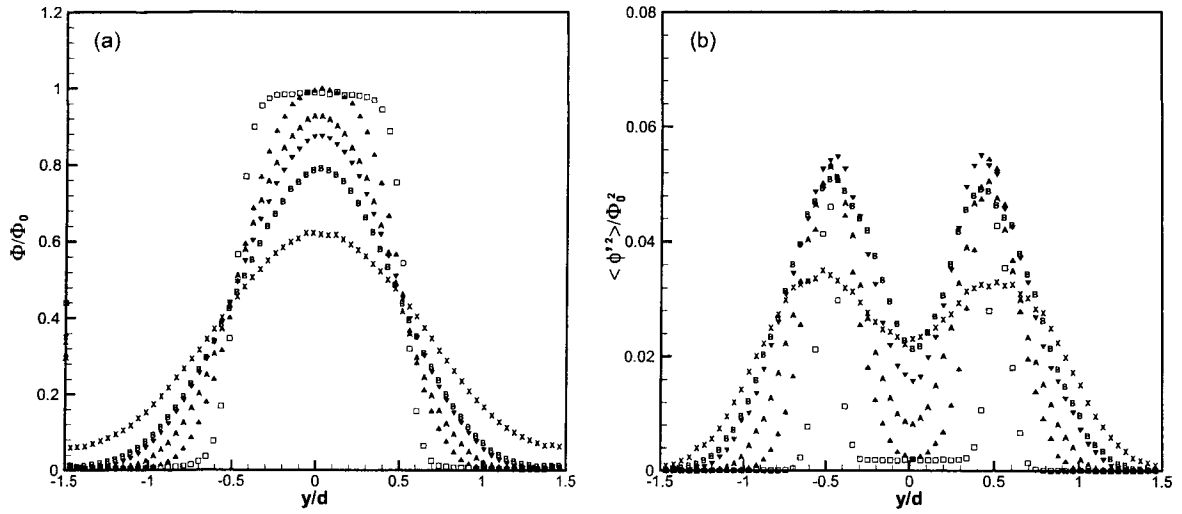


Figure 5.5 Concentration mean and variance. \square , $x/d = 1.0$; \blacktriangle , $x/d = 4.5$; A, $x/d = 7.5$; \blacktriangledown , $x/d = 12$; B, $x/d = 15$; \times , $x/d = 30$.

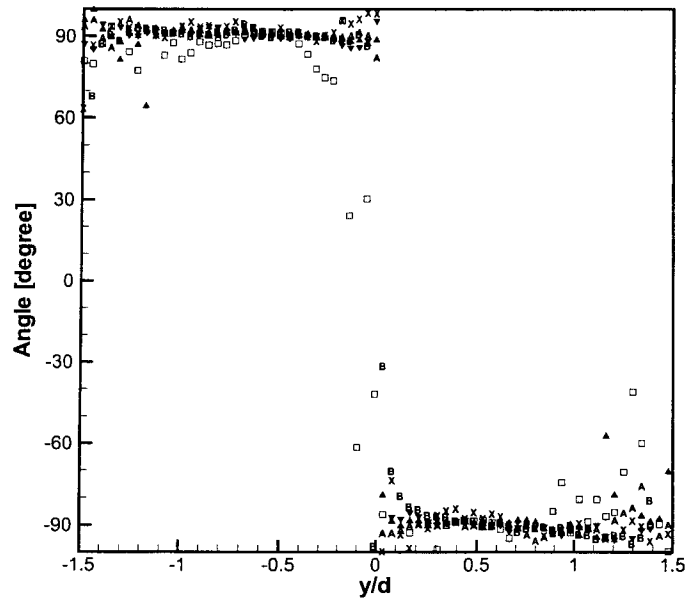


Figure 5.6 Orientation of the mean concentration gradient at different streamwise locations. \square , $x/d = 1.0$; \blacktriangle , $x/d = 4.5$; A, $x/d = 7.5$; \blacktriangledown , $x/d = 12$; B, $x/d = 15$; \times , $x/d = 30$.

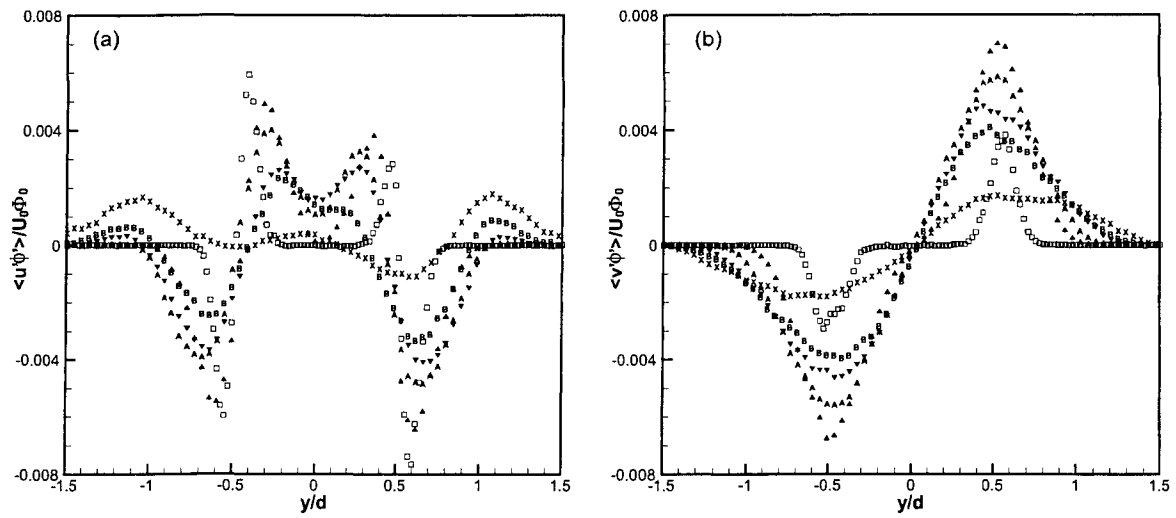


Figure 5.7 Turbulent fluxes. \square , $x/d = 1.0$; \blacktriangle , $x/d = 4.5$; \triangle , $x/d = 7.5$; \blacktriangledown , $x/d = 12$; \triangleright , $x/d = 15$; \times , $x/d = 30$.

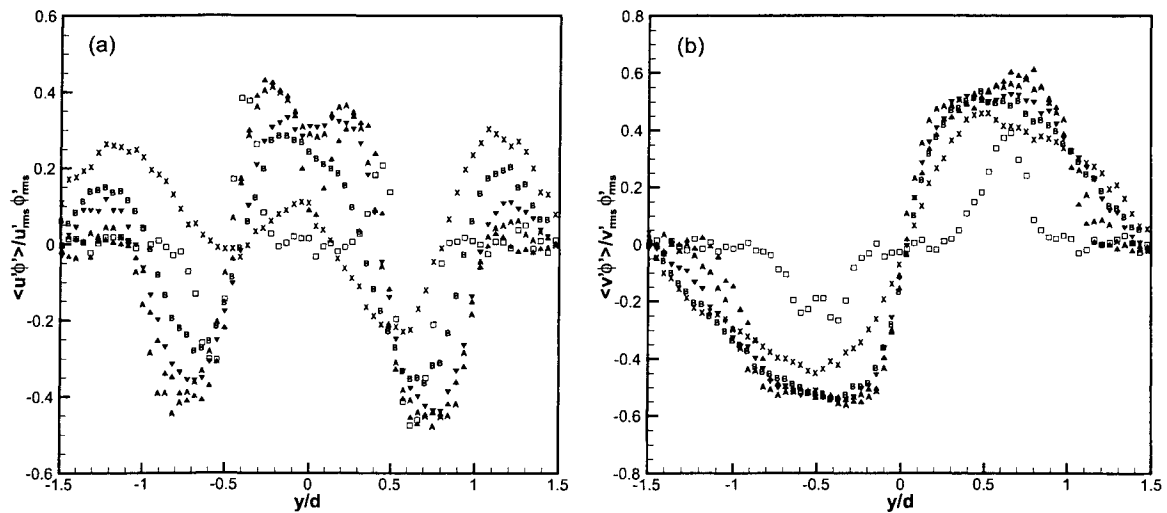


Figure 5.8 Mass transport correlation coefficients. \square , $x/d = 1.0$; \blacktriangle , $x/d = 4.5$; \triangle , $x/d = 7.5$; \blacktriangledown , $x/d = 12$; \triangleright , $x/d = 15$; \times , $x/d = 30$.

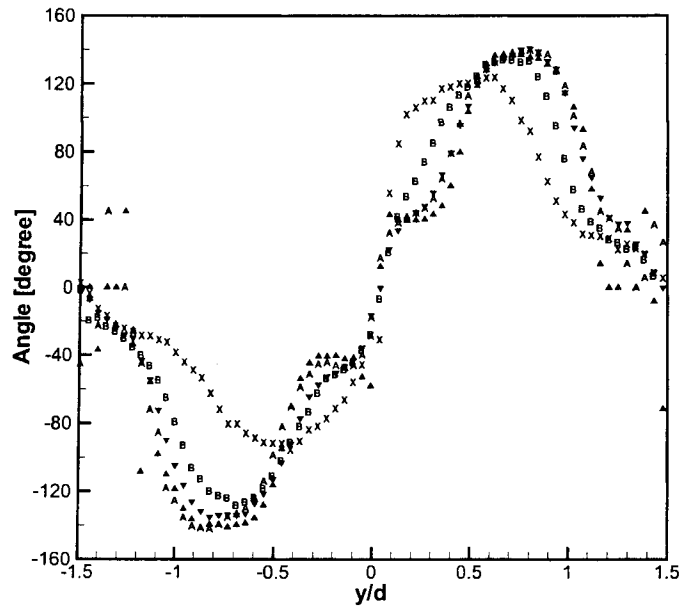


Figure 5.9 Orientation of the turbulent flux vector at different stream-wise locations. \blacktriangle , $x/d = 4.5$; \triangle , $x/d = 7.5$; \blacktriangledown , $x/d = 12$; \square , $x/d = 15$; \times , $x/d = 30$.

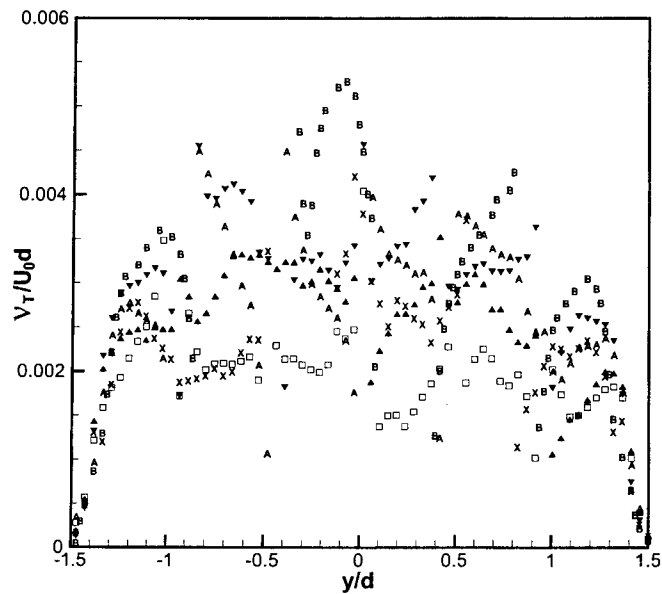


Figure 5.10 Dimensionless turbulent viscosity. \square , $x/d = 1.0$; \blacktriangle , $x/d = 4.5$; \triangle , $x/d = 7.5$; \blacktriangledown , $x/d = 12$; \square , $x/d = 15$; \times , $x/d = 30$.

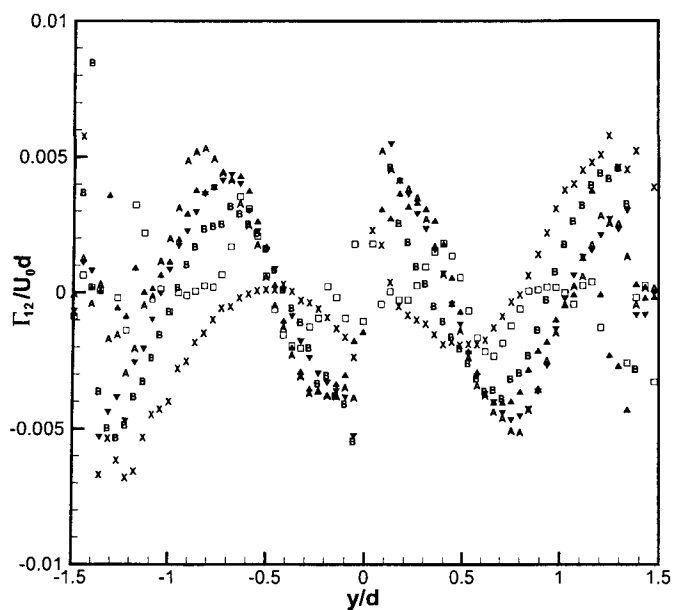


Figure 5.11 Cross-component of the turbulent diffusivity tensor. \square , $x/d = 1.0$; \blacktriangle , $x/d = 4.5$; \blacktriangle , $x/d = 7.5$; \blacktriangledown , $x/d = 12$; B , $x/d = 15$; \times , $x/d = 30$.

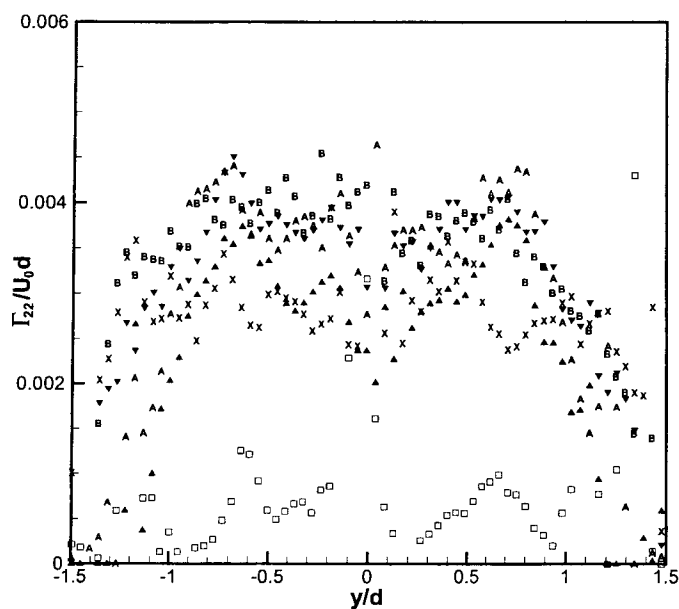


Figure 5.12 Dimensionless turbulent diffusivity. \square , $x/d = 1.0$; \blacktriangle , $x/d = 4.5$; \blacktriangle , $x/d = 7.5$; \blacktriangledown , $x/d = 12$; B , $x/d = 15$; \times , $x/d = 30$.

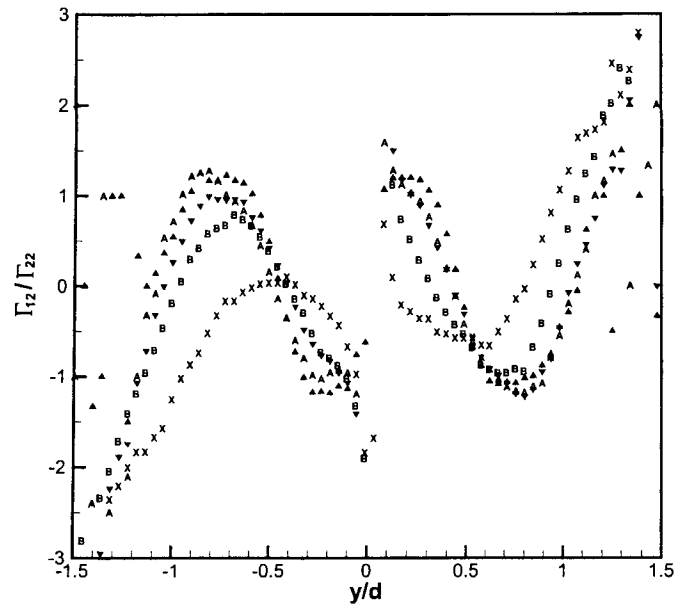


Figure 5.13 Ratio of Γ_{12} and Γ_{22} . \blacktriangle , $x/d = 4.5$; \triangle , $x/d = 7.5$; \blacktriangledown , $x/d = 12$; \triangleleft , $x/d = 15$; \times , $x/d = 30$.

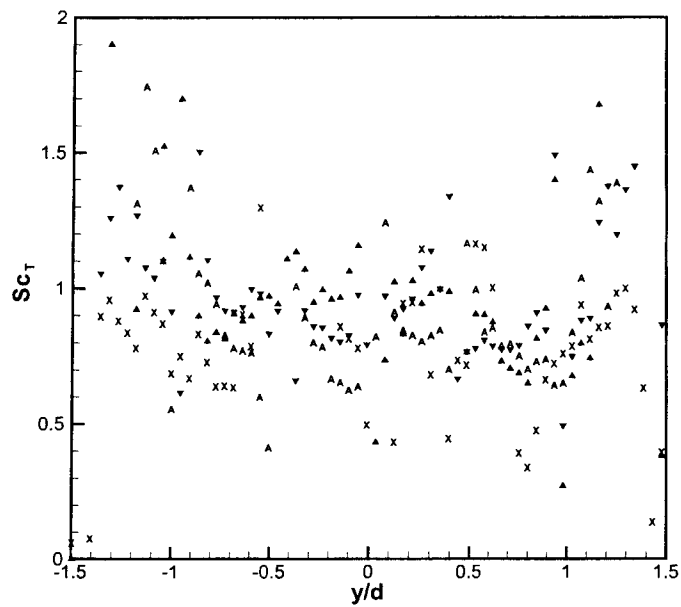


Figure 5.14 Turbulent Schmidt number. \blacktriangle , $x/d = 4.5$; \triangle , $x/d = 7.5$; \blacktriangledown , $x/d = 12$; \times , $x/d = 30$.

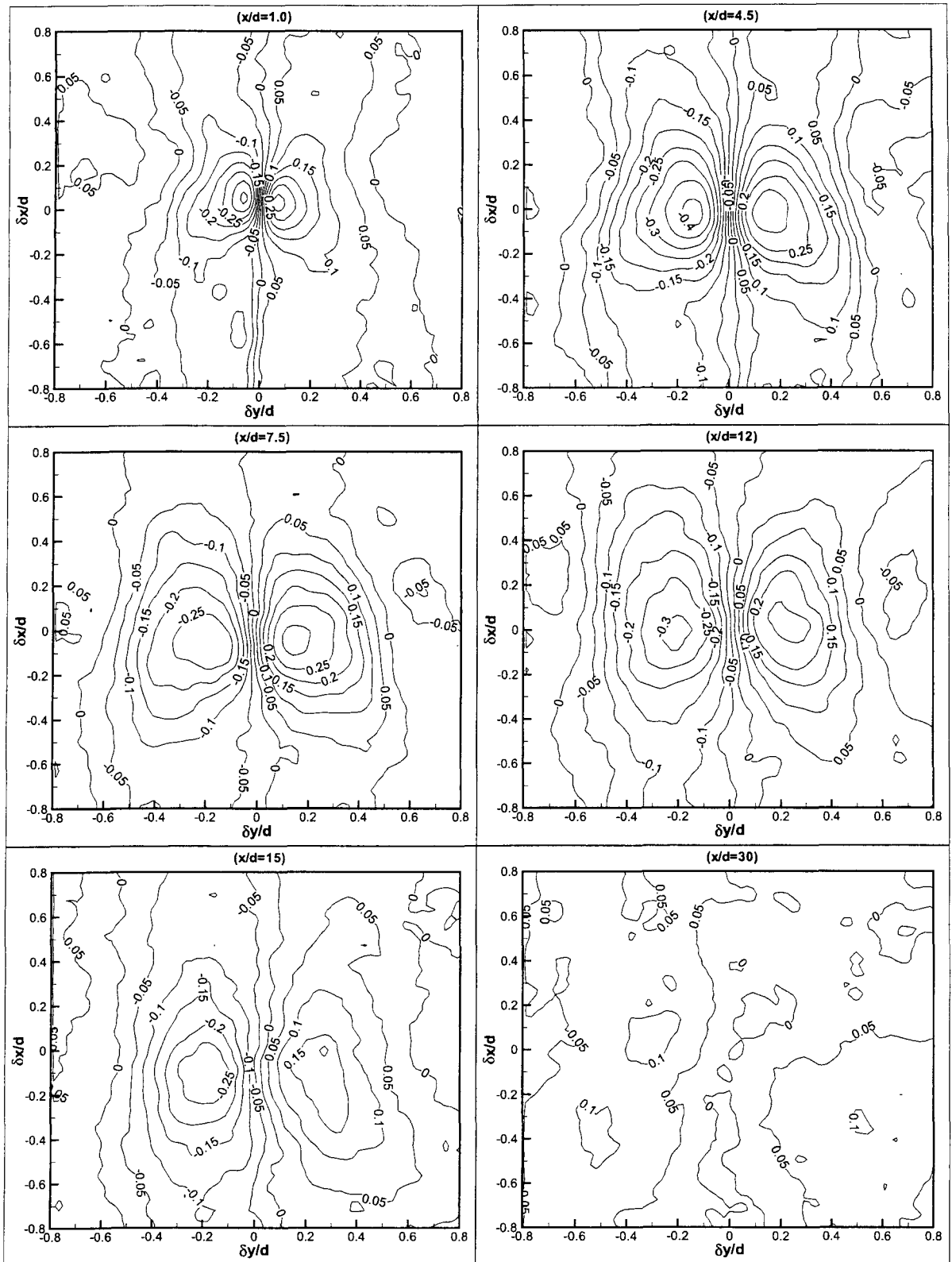


Figure 5.15 Contours of two-point spatial correlation $R_{u'\phi'}$.

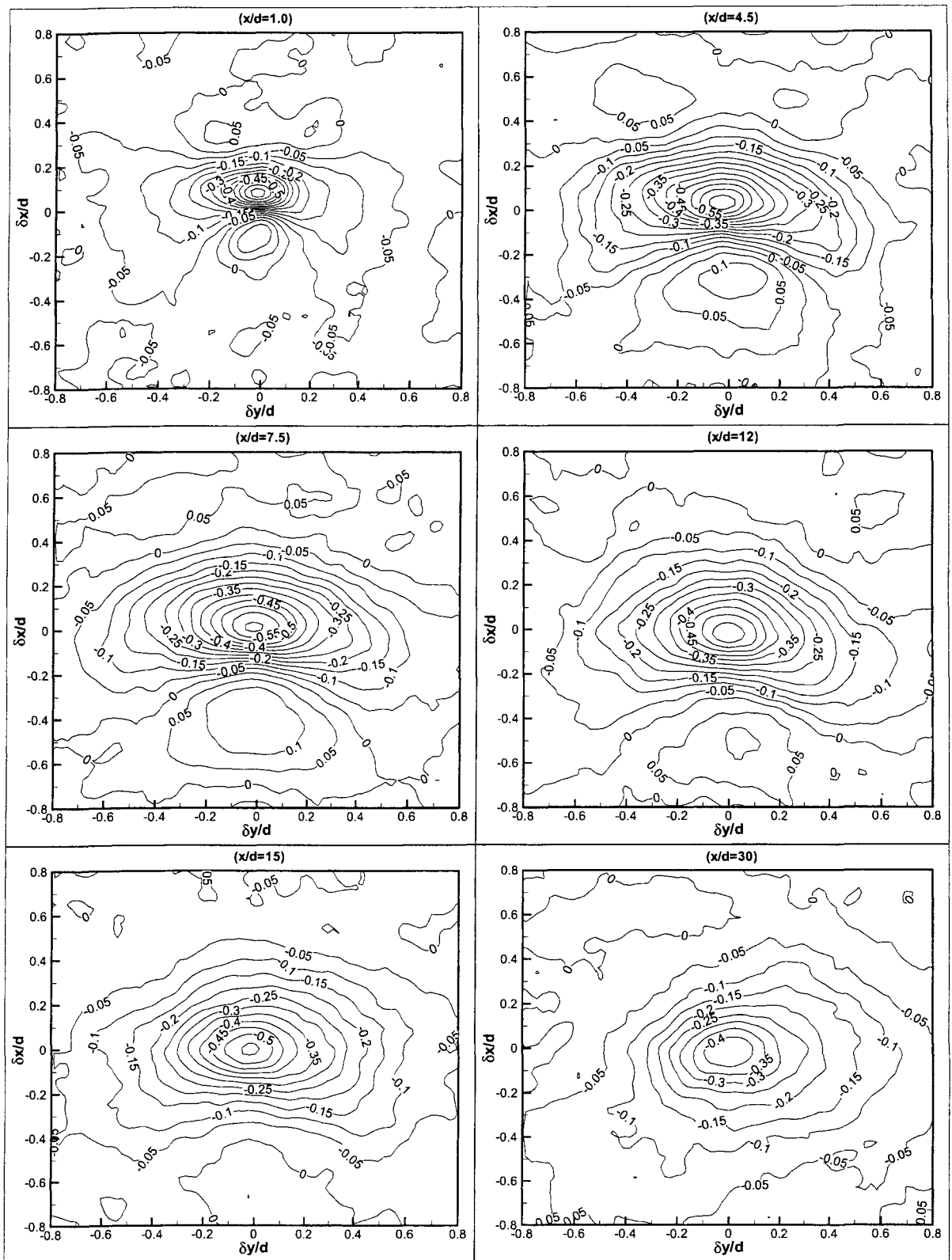


Figure 5.16 Contours of two-point spatial correlation $R_{v'\phi'}$.

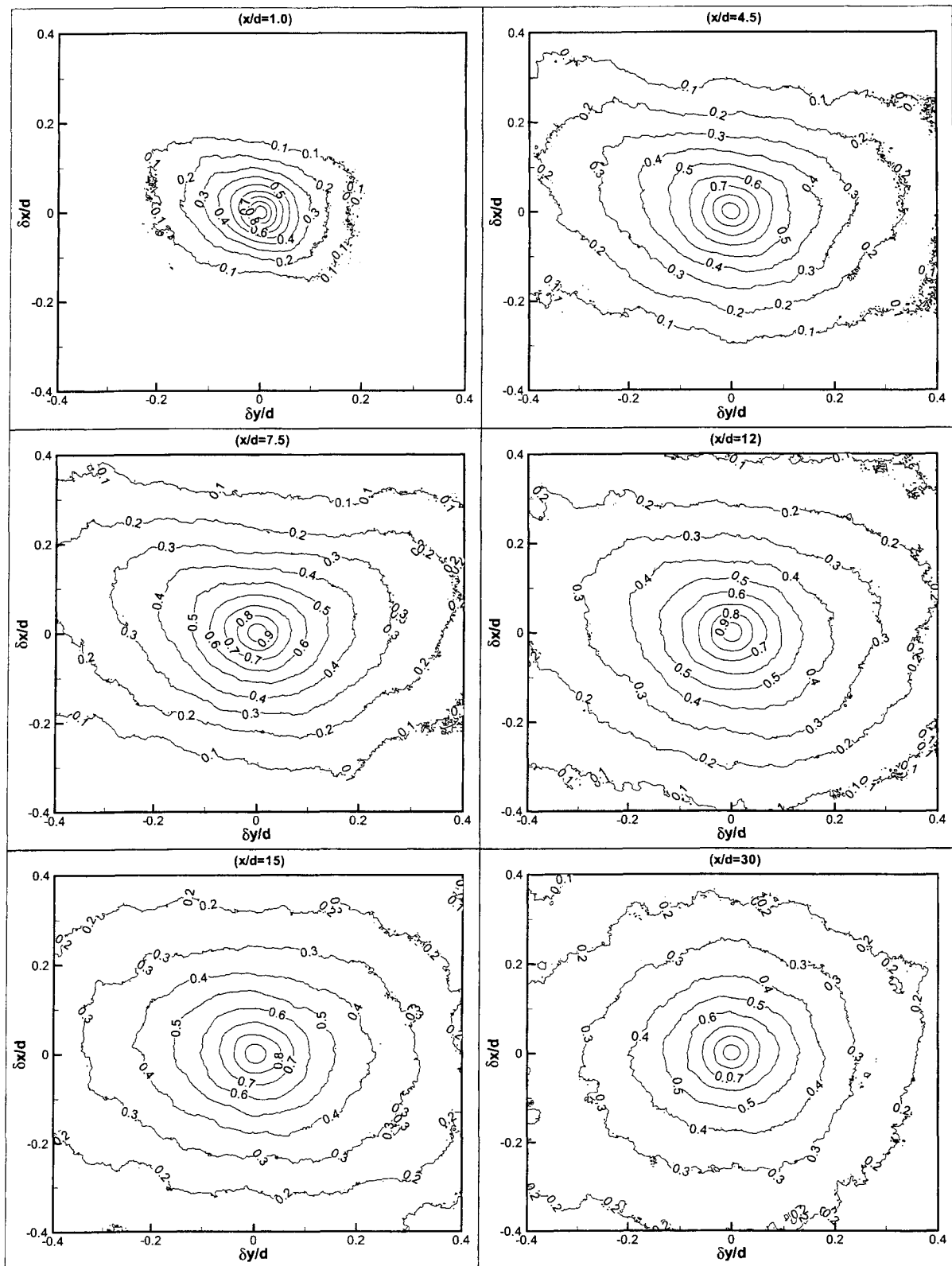


Figure 5.17 Contours of two-point spatial correlation $R_{\phi'\phi'}$.

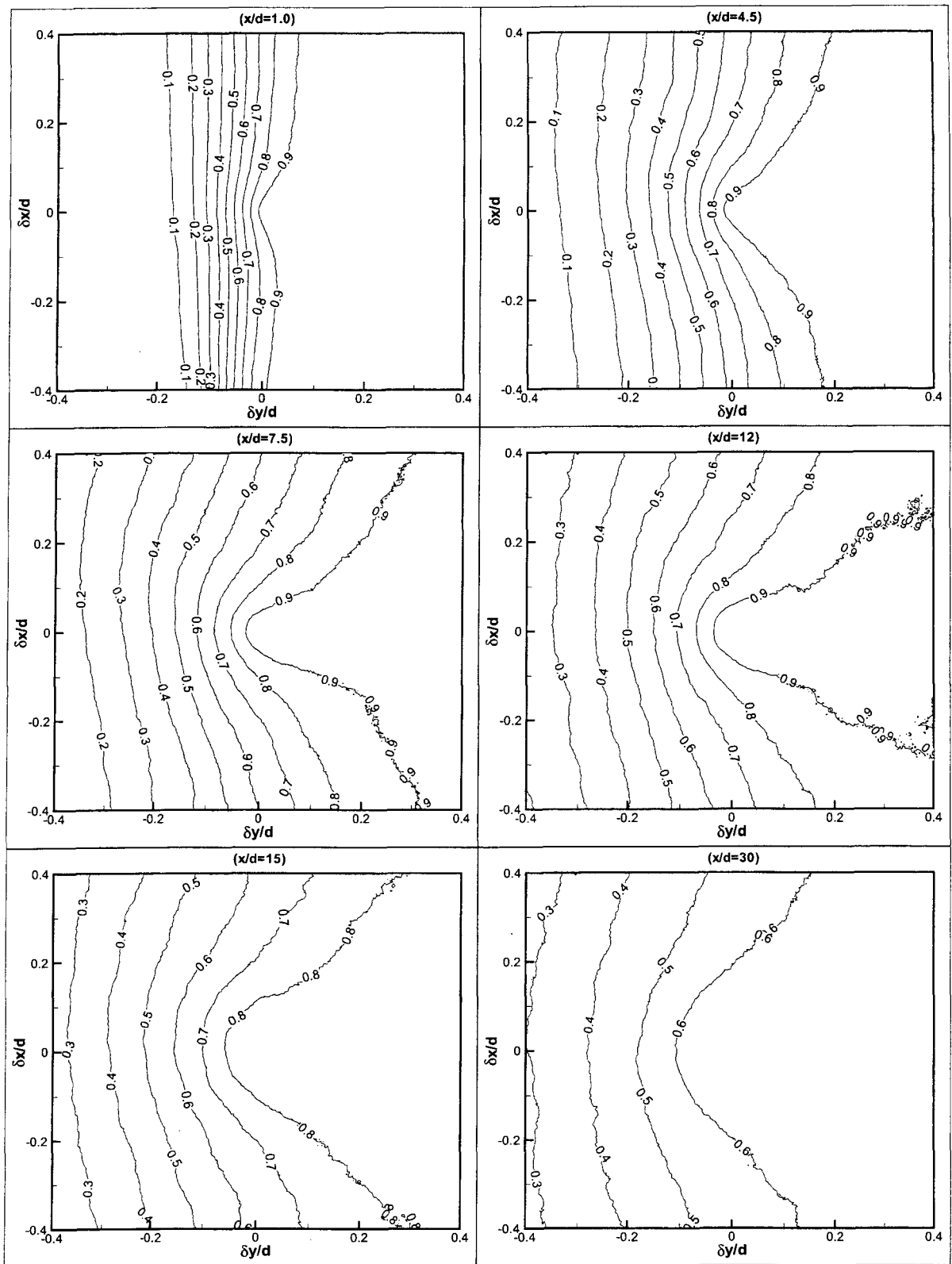


Figure 5.18 Linear stochastic estimation of a concentration field given an event of $\phi'(\mathbf{x}_0) = 2\phi'_{rms}(\mathbf{x}_0)$.

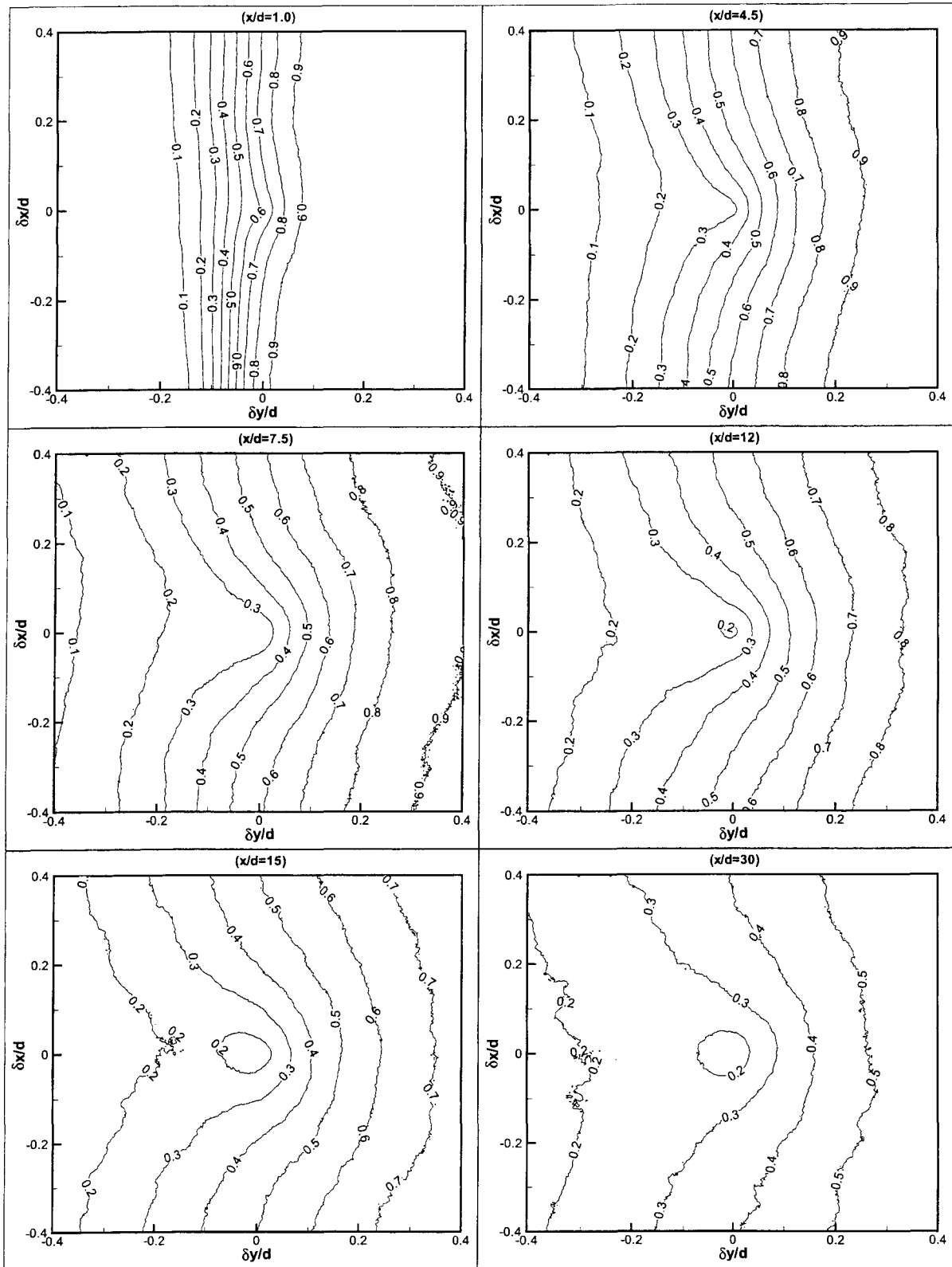


Figure 5.19 Linear stochastic estimation of a concentration field given an event of $\phi'(\mathbf{x}_0) = -2\phi'_{rms}(\mathbf{x}_0)$.

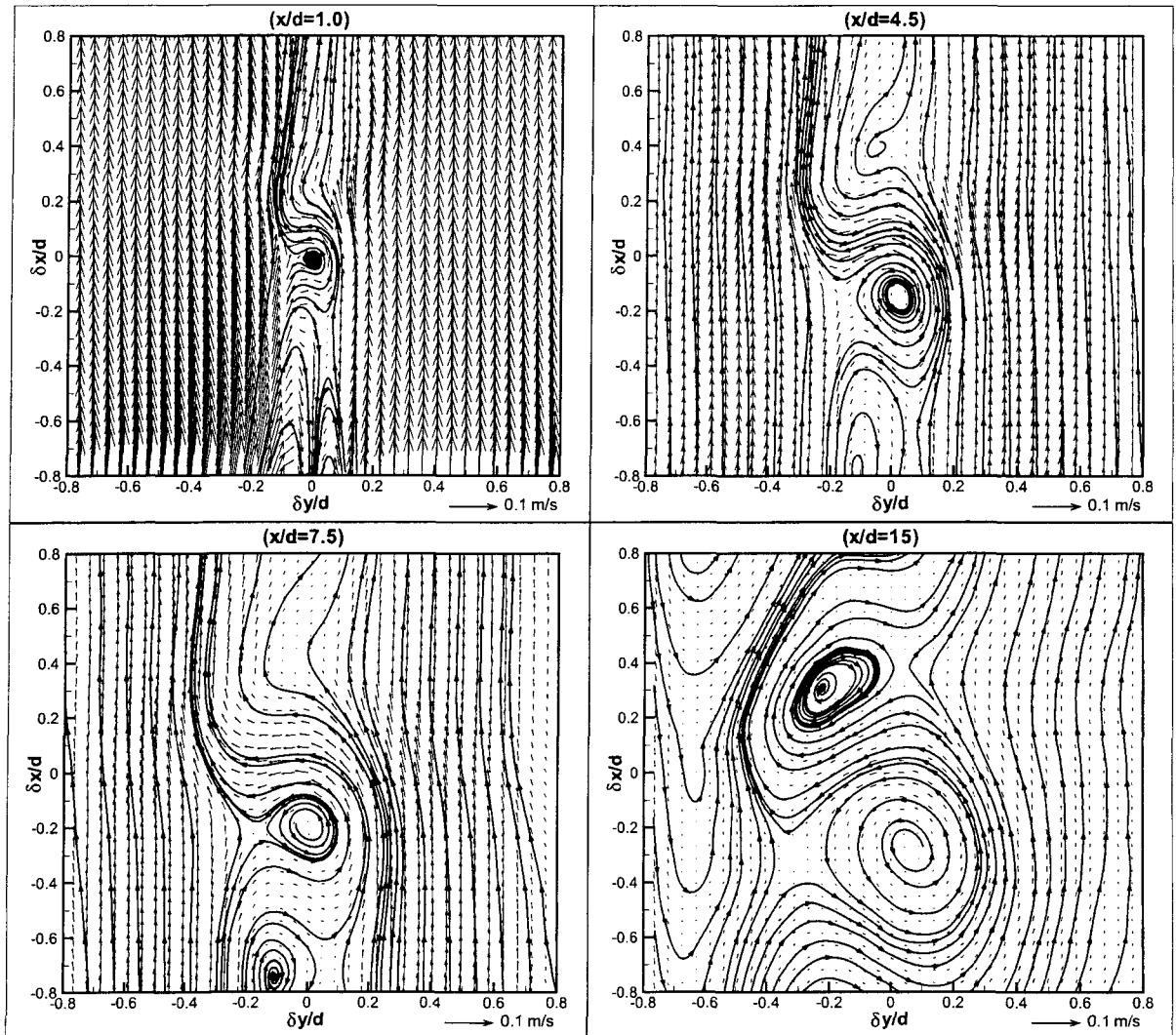


Figure 5.20 Estimated velocity fields given an event of $\phi'(\mathbf{x}_0) = 2\phi'_{rms}(\mathbf{x}_0)$, with $U(\mathbf{x}_0)$ subtracted from each vector.

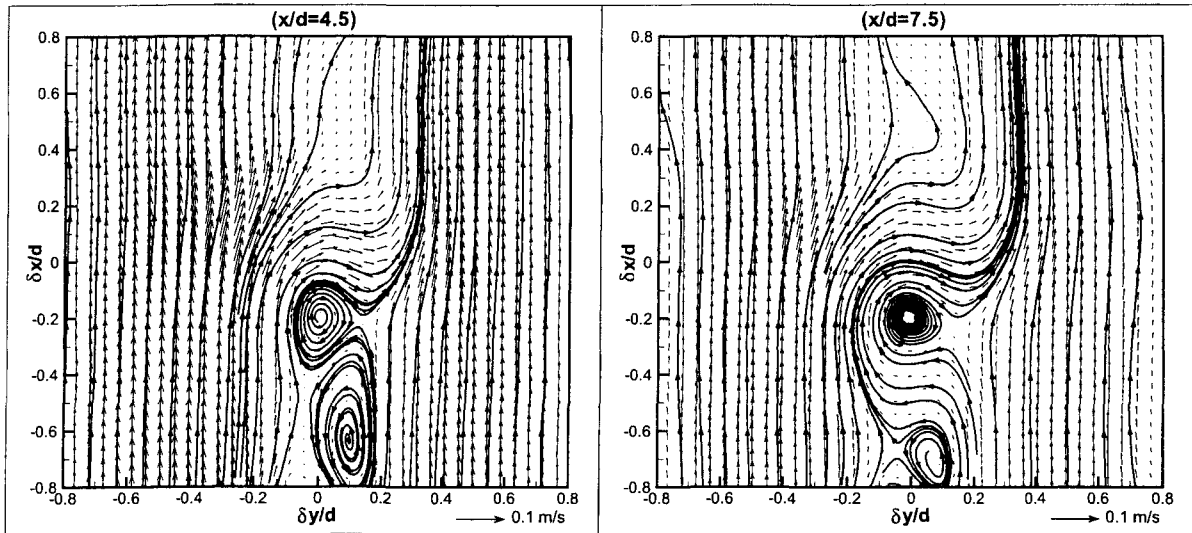


Figure 5.21 Estimated velocity fields given an event of $\phi'(\mathbf{x}_o) = -2\phi'_{rms}(\mathbf{x}_o)$, with $U(\mathbf{x}_o)$ subtracted from each vector.

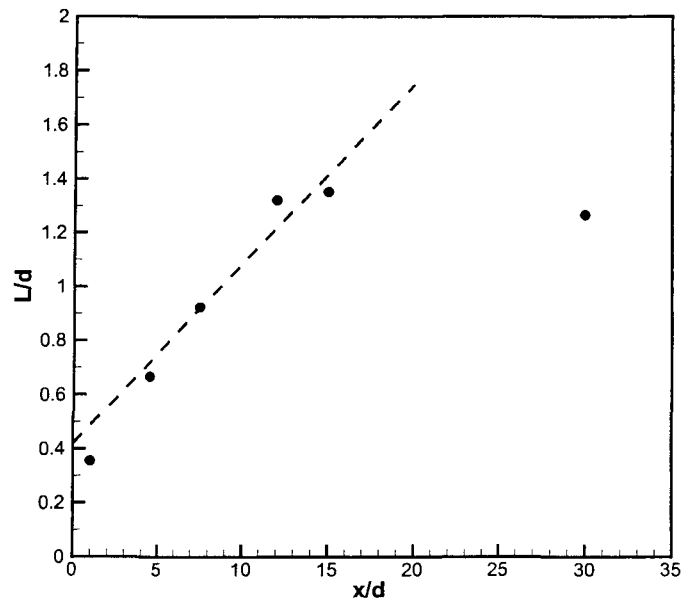


Figure 5.22 Dimensionless large-scale structure size based on estimated velocity fields at the measured downstream locations in the flow. The dashed line represents the linear-fit trend line.

CHAPTER 6 CONDITIONAL STATISTICS FOR PASSIVE-SCALAR MIXING IN A CONFINED RECTANGULAR TURBULENT JET

A paper in preparation

Abstract

Experimental results for the conditional statistics, such as the velocity conditioned on a conserved scalar and the scalar conditioned on velocity, in a confined liquid-phase rectangular jet are presented and analyzed for a data set collected using simultaneous particle image velocimetry (PIV) and planar laser-induced fluorescence (PLIF). The joint velocity-scalar probability density function (PDF) is not jointly Gaussian in this flow, as the PDF of the conserved scalar is accurately described by a beta-PDF. The conditional mean velocity is found to agree with a linear model when the scalar is close to its local mean value. A gradient PDF model is found to give poor predictions for the streamwise conditional velocity. However, the improved gradient PDF model predicts both the streamwise and transverse conditional velocities well. A linear model for the scalar fluctuation conditioned on velocity is also tested against the experimental data, showing that this model only obtains good approximations when the joint velocity-scalar PDF approaches a joint Gaussian at further downstream locations in this flow.

Introduction

Scalar mixing in turbulent non-premixed flows is one of the most active areas of research in fluid mechanics and is encountered in many processes in industry and the environment. In recent years, the conditional moment closure (CMC) introduced by Klimenko (1990) and Bilger (1993) has been a fundamental model for describing turbulent reactive flows. The

great advantages of the CMC method are that the dependence on Reynolds averages and fluctuations is severely reduced and the reaction can be more easily modeled than in the conventional Reynolds averaged moment methods [Mortensen (2005)]. However, the CMC method brings up a number of additional unknown terms such as the conditional mean velocity, the conditional scalar dissipation and the conditional scalar diffusion, and these conditionally averaged terms have to be modeled.

There are a few models [Sinai and Yakhot (1989); O'Brien and Jiang (1992); Overholt and Pope (1996)] available to predict the conditional scalar dissipation and the conditional scalar diffusion, and a large body of experimental data [Jayesh and Warhaft (1992); Kailasnath et al. (1993); Anselmet et al. (1994); Sardi et al. (1998)] exists for these quantities as well. However the conditional velocity has received little attention. One popular model for the mean velocity conditioned on the scalar in the CMC community has been the linear model, written as [Mortensen (2005); Li and Bilger (1994)]

$$\langle \mathbf{U} | \psi \rangle = \langle \mathbf{U} \rangle + \frac{\langle \mathbf{u} \phi' \rangle}{\langle \phi'^2 \rangle} (\psi - \langle \phi \rangle), \quad (6.1)$$

where ϕ is the conserved scalar, ψ the sample space variable for ϕ , \mathbf{U} the instantaneous velocity vector, \mathbf{u} the fluctuating velocity, $\langle \mathbf{U} \rangle$ the unconditional mean velocity, $\langle \mathbf{U} | \psi \rangle = \langle \mathbf{U} | \phi = \psi \rangle$ the mean velocity conditioned on $\phi = \psi$, $\langle \mathbf{u} \phi' \rangle$ the scalar fluxes, $\langle \phi'^2 \rangle$ the scalar variance, and $\langle \phi \rangle$ is the mean conserved scalar. This model uses the assumption that the joint probability density function (PDF) between the velocity and the conserved scalar is Gaussian [Li and Bilger (1994)]. Tavoularis and Corrsin (1981) confirmed this assumption in their experimental investigation of homogenous turbulent shear flow with a uniform mean scalar gradient. However, Sreenivasan and Antonia (1978) and Bilger et al. (1991) found that for inhomogeneous turbulent flows the joint PDF between the velocity and the conserved scalar is generally not Gaussian. Li and Bilger (1994) compared their experimental data with the conditional mean transverse velocity predicted by the linear model, and found that the linear model produces large errors when $|\psi - \langle \phi \rangle|$ is large.

Another existing model for the velocity conditioned on the scalar is the PDF gradient model

proposed by Pope (1985), written as

$$\langle \mathbf{U} | \psi \rangle = \langle \mathbf{U} \rangle - \frac{D_T}{P_\phi} \frac{\partial P_\phi}{\partial \mathbf{x}}, \quad (6.2)$$

where D_T is the turbulent diffusivity, \mathbf{x} the spatial coordinate vector, and P_ϕ is the PDF of the conserved scalar. Mortensen (2005) claimed that this model is the only model conserving the unconditional reactive scalar when used in moment methods. Obviously, both the accuracy of the PDF of the conserved scalar and the use of different presumed PDF shapes significantly affect the results from the PDF gradient model. Girimaji (1991) compared the beta-PDF with two-scalar mixing data from DNS and concluded that the beta-PDF captures all of the important features of the transition PDFs. Kim (2004) also found that the beta-PDF is more accurate than the clipped Gaussian PDF for both homogeneous and inhomogeneous cases. Moreover, Eswaran and Pope (1988) summarized their DNS results and claimed that the scalar PDF evolves towards the familiar bell-shaped curve, which is indeed Gaussian.

Although there is a large body of literature on turbulent shear flows, conditional statistics of experimental data are scarce, despite their necessity for understanding turbulent flows and validating numerical models. In this paper, we present the conditional statistics of the experimental data at various locations in a liquid-phase turbulent confined rectangular jet. The remainder of the paper is organized as follows. Section 6 describes the experimental details and conditions. In Sec.6, results of the conditional mean velocities and the conditional mean scalar in the flow are discussed. Models for the conditional velocity and the conditional scalar are also tested against the experimental data. A summary of results and conclusions is given in Sec.6.

Experimental Details and Conditions

The statistics for turbulent passive-scalar mixing are derived from measurements in a confined rectangular jet. Since a detailed description of the experimental apparatus [Feng et al. (2005)] and methodology [Feng et al. (2006)] has been given elsewhere, only a brief summary of the experimental details pertinent to the present investigation is given here. As

Fig. 6.1 shows, the Plexiglas test section is 1 m in length and has a rectangular cross-section measuring 60 mm by 100 mm. The width of each of the three inlet channels is 20 mm. The coordinate system used in the present study is such that x is the streamwise direction and y is the transverse direction. The origin is designated at the center point between the tips of the splitter plates. For the present study, the volumetric flow rates of each of the inlet channels were 1.0, 2.0 and 1.0 liters/s, corresponding to free stream velocities of 0.5 m/s, 1.0 m/s, and 0.5 m/s. The Reynolds number based on the hydraulic diameter of the test section and the bulk velocity was 50,000 (or 10,000 based on the velocity difference between streams and the jet exit dimension). The fluorescent dye Rhodamine 6G was used as a passive scalar. The Schmidt number of Rhodamine 6G in water is 1,250 [Crimaldi and Koseff (2001)]. In the center stream, the source concentration (ϕ_0) of Rhodamine 6G was 45 $\mu\text{g/liter}$, while the other two streams were tap water.

A combined particle image velocimetry (PIV) and planar laser-induced fluorescence (PLIF) system was employed to simultaneously measure the instantaneous velocity and concentration fields. Illumination was provided by a double-pulsed Nd:YAG laser that emits two independent 532 nm light pulses. A time delay between the two laser pulses of 600 μs was used for the PIV measurements. The laser light sheet passes through the test section at the centerline in the z -direction with a thickness of about 0.5 mm. The spatial resolution of the PIV measurements was 0.9 mm in both the x - and y -directions, or between 7.8η and 11.3η in terms of the Kolmogorov scale (η) at different downstream measurement locations. The experimental uncertainty of the PIV measurements [Prasad et al. (1992)] was $\pm 1.6\%$ for the center stream and $\pm 3.2\%$ for the outer streams. The in-plane spatial resolution of the PLIF measurements in the present study was limited by the flow area imaged per pixel, which was approximately 56 μm . At each downstream measurement location, 3,250 sets of simultaneous velocity and concentration images were acquired and analyzed.

Complete conventional statistics of this flow have been presented in Feng et al. (2006). For convenience, we present again those quantities needed for testing the conditional models. Profiles of the normalized ensemble-averaged streamwise velocity and Reynolds stresses at the

exit of the jet and 6 downstream locations in the flow are presented in Fig. 6.2. The mean velocity is normalized by the difference between inlet free-stream velocities of the center stream and side streams, $\Delta U = 0.5$ m/s, and the Reynolds stresses are normalized by $(\Delta U)^2$. In this paper, u and v denote the streamwise and transverse velocity fluctuations, respectively. The inlet jet width, $d = 20$ mm, is used to normalize the transverse coordinate. Mean velocity and Reynolds stress profiles are presented for seven locations: $x/d = 0, 1, 4.5, 7.5, 12, 15,$ and 30 . Note that data at $x/d = 0$ correspond to the inlet conditions. The transverse profiles of the ensemble-averaged scalar and the scalar variance at six downstream locations are summarized in Fig. 6.3. Here the conserved scalar is the concentration normalized by the source concentration ϕ_0 . Turbulent fluxes are shown in Fig. 6.4.

Results and Discussion

In this section, we present experimental data for various transverse positions at each observed downstream locations. These transverse positions are given in terms of “ δ ”, which is defined as the distance between the centerline of the confined jet and the left peak in the transverse profile of the scalar variance, such that the left peak in the scalar variance profile appears at $y = -\delta$.

Probability Densities

As introduced in Sec. 6, the probability density of the conserved scalar is an important quantity in CMC and PDF models. Figure 6.5 shows the experimental measured PDFs of the conserved scalar at 8 transverse positions for 6 downstream locations. The scalar data is divided into 20 bins between 0 and 1. The lines in the plots are the corresponding beta-PDFs given by Bilger (1980)

$$P_\phi(\psi) = \frac{\Gamma(a+b)}{\Gamma(a)\Gamma(b)} \psi^{a-1} (1-\psi)^{b-1}, \quad (6.3)$$

where the parameters a and b are determined from the mean and variance:

$$a = \langle \phi \rangle \left(\frac{\langle \phi \rangle (1 - \langle \phi \rangle)}{\langle \phi'^2 \rangle} - 1 \right), \quad b = a \frac{1 - \langle \phi \rangle}{\langle \phi \rangle} \quad (6.4)$$

and Γ is the gamma function. It is seen that for all locations, the beta-PDF predicts the experimental data remarkably well. Note the relationship between the joint velocity-scalar PDF and the marginal PDF of the scalar is

$$P_{u_i\phi}(u_i, \psi) = P_{u_i|\phi}(u_i|\psi)P_\phi(\psi), \quad (6.5)$$

therefore given that $P_\phi(\psi)$ is described with a beta-PDF, the joint velocity-scalar PDF $P_{u_i\phi}(u_i, \psi)$ cannot be joint Gaussian in the present study.

At $x/d = 1$, P_ϕ for $y = 0$ or $y = -3\delta/2$ approximates a delta function, indicating that the probability of a fluid parcel being transferred between streams without mixing is very low at this location. For transverse positions near $y = -\delta$, although still skewed, the shapes of the PDF are more bell-shaped than those of positions far from $y = -\delta$. At $x/d = 30$, the PDFs for all transverse positions become nearly bell-shaped and tend to collapse, showing that the beta-PDF evolves to a Gaussian distribution when the r.m.s. of conserved scalar is relatively small, which is consistent with the results from reported DNS studies [Kim (2004); Eswaran and Pope (1988)].

Conditional Mean Velocities

The scatter plots of normalized velocity fluctuations at various locations are shown in Fig. 6.6. The distribution of the scatter is not joint Gaussian at any of these locations. At locations for $y = 0$, $\langle u|v \rangle$ is symmetric about $v = 0$, and $\langle v|u \rangle$ is near zero, which is expected considering the symmetry of the flow. The result at $x/d = 1.0$ is an exception, which is probably because this location is in the potential core of the center stream where both the velocity fluctuations and the local velocity r.m.s. are close to zero, the profile of the velocity may look noisy after being normalized by the local velocity r.m.s. For locations at $y = -\delta$, both $\langle u|v \rangle$ and $\langle v|u \rangle$ are nonzero and not symmetric about $u = 0$ or $v = 0$. However, at the farthest observed location ($x/d = 30$), the conditional mean velocities approach linearity.

Figures 6.7 and 6.8 are scatter plots of scalar and velocity fluctuations (normalized by the local velocity r.m.s.) at $y = 0$ and $y = -\delta$ for three downstream locations, respectively. It is apparent that the distribution of the scatter is not joint Gaussian at any location (except,

perhaps $x/d = 30$). At $y = 0$, the data concentrate in a narrow range of the scalar around the local scalar mean, although this range becomes wider as the observed location moves downstream, consistent with the fact that the scalar PDF at the jet center evolves from a delta function towards a skewed Gaussian distribution. As expected, the data are scattered about the mean scalar at $y = -\delta$ where the maximum of the scalar variance appears. However, as the maximum of the variance at $x/d = 30$ is smaller than at upstream locations, the distribution of the data becomes relatively more concentrated around the local scalar mean.

The mean velocity fluctuations (normalized by the local velocity r.m.s.) conditioned on the conserved scalar and the mean scalar conditioned on velocity fluctuations are also displayed in Figs. 6.7 and 6.8. The scalar is divided into 20 bins between 0 and 1, whereas the velocity fluctuations are divided into 21 bins between $\pm 3r.m.s$ of velocity fluctuation. For positions within the potential core of the center stream (such as $x/d = 1.0$ and $y = 0$), both the streamwise and the transverse conditional velocity fluctuations are zero. Also, the mean transverse conditional velocity at $y = 0$ is always near zero due to the symmetry of the flow, although nonzero values are observed in some scalar ranges because of the small sample size. At other positions, the streamwise conditional velocity fluctuation increases as the scalar increases; whereas the transverse conditional velocity fluctuation decreases as the scalar increases. Moreover, note that the streamwise velocity fluctuation is positive where the scalar is greater than the local mean scalar, but negative where the scalar is less than the local mean scalar, such that the $\langle u\phi' \rangle$ flux is positive at all observed positions as shown in Fig. 6.4. Similarly, the transverse velocity fluctuation is positive for smaller scalar but negative for larger scalar, resulting in a negative $\langle v\phi' \rangle$ flux at all observed positions.

In observing Figs. 6.7 and 6.8, it is seen that for downstream locations at $y = 0$, the profile of the scalar conditioned on the transverse velocity is a concave curve such that the conditional scalar reaches its maximum when the velocity fluctuation is zero but decreases as the magnitude of the velocity fluctuation increases. This is expected because the scalar mean at the jet center is always the highest at each downstream location in this study, and fluid parcels being transferred from side streams to the jet center (thus with nonzero transverse

velocity fluctuation) bring smaller ψ . For other locations, the conditional scalar holds a nearly linear relationship with the velocity fluctuations. Apparently, $\langle\phi|u\rangle$ increases as u increases, but $\langle\phi|v\rangle$ decreases as v increases, also consistent with the signs of turbulent fluxes shown in Fig. 6.4. At $x/d = 30$, the data distribute nearly symmetric about the line representing the conditional mean scalar.

Figures 6.9 and 6.10 show the conditional mean velocity fluctuations from the experimental data normalized in accordance with Eq.6.1. In presenting the data, only results from bins that have at least 15 samples in them are shown in order to reduce the scatter. Since the turbulent fluxes are used to normalize the conditional velocities, to avoid dividing by a small number, only positions where the local turbulent fluxes have magnitude greater than 0.001 (refer to Fig. 6.4) are displayed in Figs. 6.9 and 6.10. Notice that the linear model gives reasonable approximations to the experimental data at most of the measurement locations. At each observed position, the agreement is good within a range of $\pm |\psi - \langle\phi\rangle| / \phi_{rms}$. However for some ψ far from the $\langle\phi\rangle$, the model poorly predicts the velocity, which is also reported in Li and Bilger (1994) and de Bruyn Kops and Mortensen (2005) (although only the transverse conditional mean velocity was tested in these studies). Also note that the range of $\pm |\psi - \langle\phi\rangle| / \phi_{rms}$ in which a linear relationship holds continuously increases and becomes large at $x/d = 30$, implying the nearly Gaussian distribution of the joint PDF at this location. Moreover, the data for some positions are not distributed symmetrically about the local mean scalar, as the profile of the scalar PDF is skewed at these positions.

The conditional mean streamwise velocity as predicted by the gradient PDF model is compared with the experimental data in Fig. 6.11. Since the beta-PDF accurately describes the scalar PDF in the present study, the results from Eq. 6.3 are used to compute the velocity with the gradient PDF model. The gradient of the PDF is evaluated with the slope given by the linear fit of the PDFs at 21 adjacent points (the step width is $56 \mu\text{m}$ as mentioned in Sec. 6). The turbulent diffusivity in this flow has been reported in our previous study [Feng et al. (2006)], and is evaluated using [Tavoularis and Corrsin (1981)]

$$D_T = \frac{-\langle v\phi' \rangle}{\partial \langle \phi \rangle / \partial y}. \quad (6.6)$$

As seen in Fig. 6.11, the results of the linear model agree well with the experimental data; however, it is apparent that the gradient PDF model leads to a very poor prediction of the streamwise conditional mean velocity fluctuation. The predicted velocity fluctuation is almost always zero for all transverse positions. The large discrepancy between the experimental data and the predicted streamwise velocity from the gradient model can be explained by recalling that the mean scalar gradient is in the transverse direction everywhere in this flow [Feng et al. (2006)], resulting a very small streamwise gradient of the PDF. In observing Eq. 6.2, a near-zero conditional velocity fluctuation is expected when given a small PDF gradient. Also, when the small PDF gradient is divided by small PDF values, the predicted velocity becomes non-zero.

On the other hand, the scalar turbulent diffusivity used in Eq. 6.2 may also cause errors. Tavoularis and Corrsin (1981) claimed that a simple scalar diffusivity coefficient is inadequate to represent the behavior of the turbulent flux. In our previous study [Feng et al. (2006)], it has been found that the turbulent diffusivity in this confined jet flow is not a diagonal tensor. Two components of the tensor have been evaluated in Ref. Feng et al. (2006) using the gradient-transport hypothesis proposed by Batchelor (1949),

$$D_{12} = \frac{-\langle u\phi' \rangle}{\partial \langle \phi \rangle / \partial y}, \quad (6.7)$$

$$D_{22} = \frac{-\langle v\phi' \rangle}{\partial \langle \phi \rangle / \partial y} \quad (6.8)$$

where D_{22} is the so-called *turbulent diffusivity* [Tavoularis and Corrsin (1981)], i.e. D_T . The ratio of D_{12}/D_{22} has been found to remain nearly constant in the transverse direction in this flow, although its magnitude increases sharply in regions around the centerline of the jet or near the sidewalls [Feng et al. (2006)]. In the high shear regions of the flow, the ratio is approximately -2 [Tavoularis and Corrsin (1981); Feng et al. (2006)].

Replacing the scalar D_T in Eq. 6.2 by a tensor \mathbf{D} , as

$$\langle \mathbf{U} | \psi \rangle = \langle \mathbf{U} \rangle - \frac{\mathbf{D}}{P_\phi} \cdot \nabla P_\phi. \quad (6.9)$$

then the conditional velocities are given by

$$\langle u|\psi \rangle = -\frac{D_{11}}{P_\phi} \frac{\partial P_\phi}{\partial x} - \frac{D_{12}}{P_\phi} \frac{\partial P_\phi}{\partial y}, \quad (6.10)$$

$$\langle v|\psi \rangle = -\frac{D_{21}}{P_\phi} \frac{\partial P_\phi}{\partial x} - \frac{D_{22}}{P_\phi} \frac{\partial P_\phi}{\partial y}. \quad (6.11)$$

Note that the streamwise gradient of PDF in this study is near zero, and the above two equations may be simplified such that

$$\langle u|\psi \rangle = -\frac{D_{12}}{P_\phi} \frac{\partial P_\phi}{\partial y}, \quad (6.12)$$

$$\langle v|\psi \rangle = -\frac{D_{22}}{P_\phi} \frac{\partial P_\phi}{\partial y}. \quad (6.13)$$

Using the results of D_{12} and D_{22} reported in our previous study [Feng et al. (2006)], the conditional mean velocity fluctuations as predicted by Eqs. 6.12 and 6.13 are compared with the experimental data in Figs. 6.12 and 6.13, respectively. As seen in Fig. 6.12, the results of the predicted streamwise velocity have been improved remarkably and agree well with the experimental data. As Fig. 6.13 shows, the gradient PDF model predicts the transverse conditional mean velocity very well except at low probability densities. The discrepancy for low probability densities has been previously reported in DNS studies and considered not important, since the events occurring at low probability densities have little effect on overall mixing [de Bruyn Kops and Mortensen (2005); Eswaran and Pope (1988)].

Scalar Mean Conditioned on Velocities

The scalar mean conditioned on velocity, $\langle \phi|U_i \rangle$, is often of interest when developing models based on the interaction by exchange with the conditional mean (IECM) micromixing approach. It has been found that the $\langle \phi|U_i \rangle$ is linearly related with U_i in turbulent flows that exhibit a nearly Gaussian composition PDF [Fox (1996)]. A few models [Eswaran and Pope (1988); Fox (1996); Pope (1998)] have been proposed for modeling the conditional mean scalar. However, since terms in some of these models cannot be directly evaluated with the current

set of experimental data, here we only test the linear model proposed by Pope (1998) for homogenous isotropic turbulence with an imposed uniform mean scalar gradient. Note that the model of Pope (1998) is only for predicting the mean scalar conditioned on the velocity component in the direction of the mean scalar gradient, here we use this model for the mean scalar conditioned on both the streamwise and transverse velocity components, such that

$$\langle \phi' | U_i \rangle = \frac{\langle u_i \phi' \rangle}{\langle u_i^2 \rangle} (U_i - \langle U_i \rangle), \quad (6.14)$$

where U_i is the component of the velocity \mathbf{U} .

Figures 6.14 and 6.15 show the conditional mean scalar from the experimental data normalized in accordance with Eq.6.14. Again, only data at positions where the local turbulent fluxes are greater than 0.001 (refer to Fig. 6.4) are presented in these plots. At lower downstream locations, a sizable difference is observed between the normalized experimental data and the linear relationship. This is not surprising, as the strong non-Gaussian scalar PDF may invalidate the linear form of $\langle \phi' | U_i \rangle$ according to the argument in Fox (1996). As the PDF evolves towards Gaussian at further downstream locations, the linear model results in better approximations of the experimental results within a range of velocity fluctuations. Apparently, the range in which the linear relationship holds becomes wider as the measurement location moves downstream.

Conclusions

The conditional statistics of the velocity and scalar fields have been calculated from experimental data taken in a confined liquid-phase rectangular jet using a combined PIV and PLIF system. It was noticed that the PDF of the conserved scalar was accurately described by the beta-PDF at each of the observed positions, and consequently, the joint velocity-scalar PDF was not jointly Gaussian. The conditional mean velocity was found to agree with a linear model when the scalar is close to the local mean value. As the PDF of the scalar becomes more Gaussian at the further downstream locations, this linearity holds for a larger range of $|\psi - \langle \phi \rangle| / \phi_{rms}$. It was found that the gradient PDF model gave poor predictions for the

streamwise conditional velocity, as the streamwise gradient of PDF was very small in this flow. By replacing the scalar turbulent diffusivity by a tensor, the gradient PDF model was improved so that both the predicted streamwise and transverse conditional velocities agreed well with the experimental data. Finally, the scalar fluctuations conditioned on velocity were presented and analyzed against a linear model, showing that the linear model only obtained good approximations of the experimental data when the joint velocity-scalar PDF approached nearly jointly Gaussian.

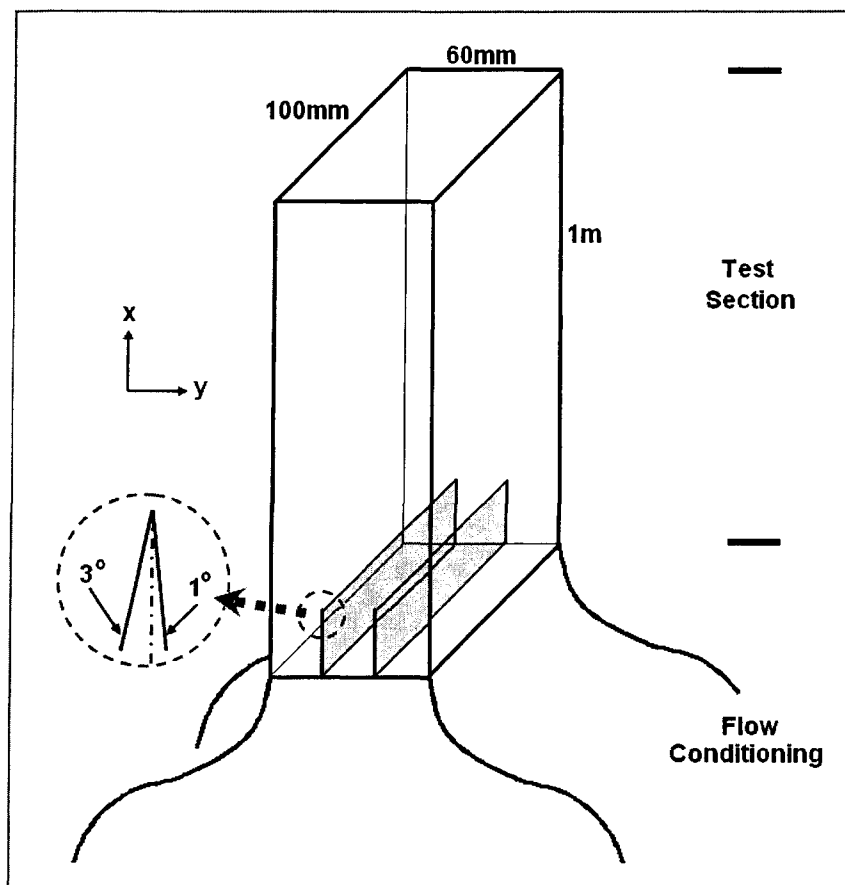


Figure 6.1 Schematic of the confined rectangular-jet test section.

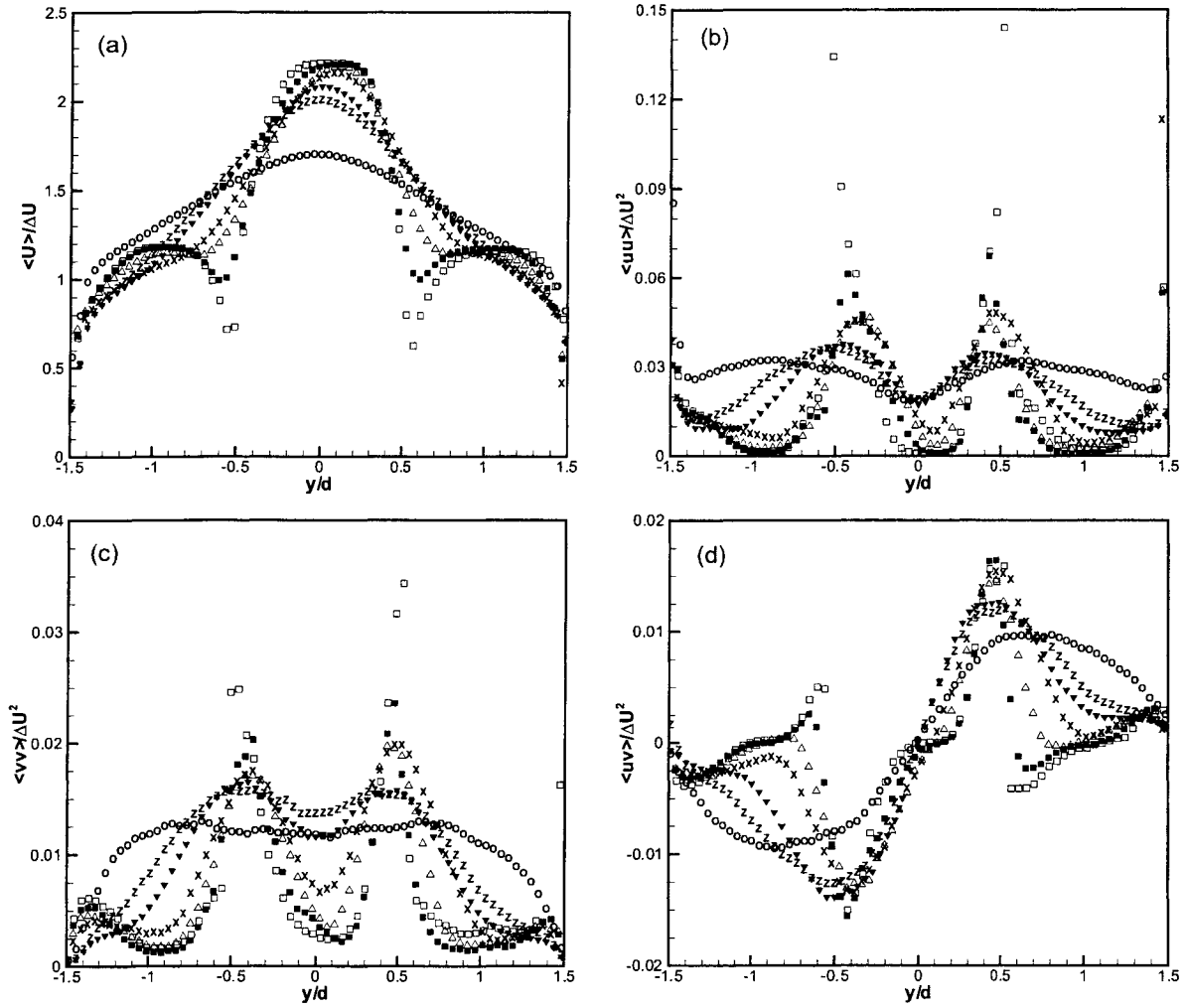


Figure 6.2 Normalized mean streamwise velocity and Reynolds stresses at different streamwise locations. \square , $x/d = 0$; \blacksquare , $x/d = 1.0$; \triangle , $x/d = 4.5$; \times , $x/d = 7.5$; \blacktriangledown , $x/d = 12$; z , $x/d = 15$; \circ , $x/d = 30$.

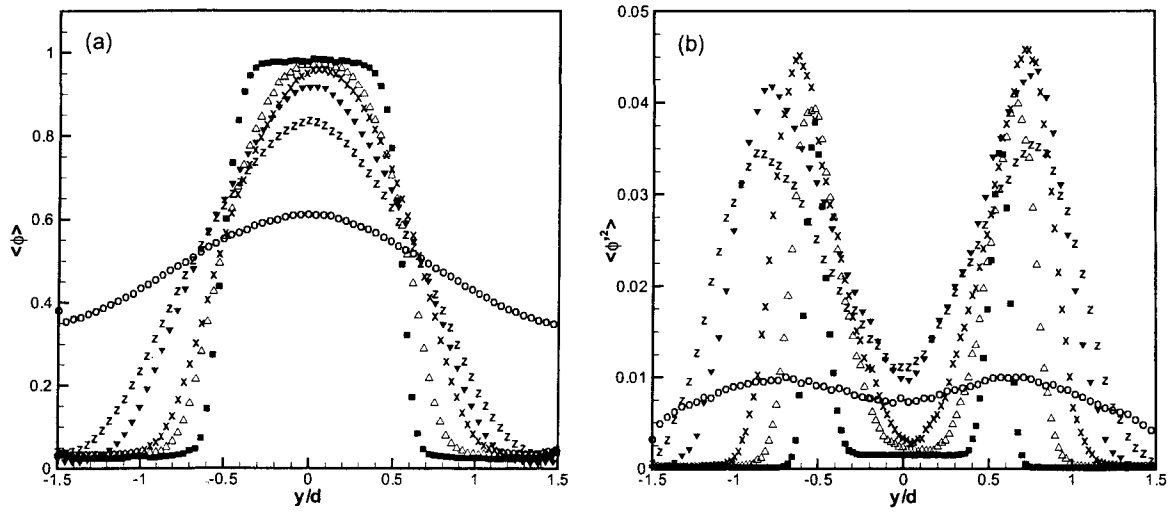


Figure 6.3 Normalized concentration mean and variance at different streamwise locations. ■, $x/d = 1.0$; △, $x/d = 4.5$; ×, $x/d = 7.5$; ▼, $x/d = 12$; z, $x/d = 15$; ○, $x/d = 30$.

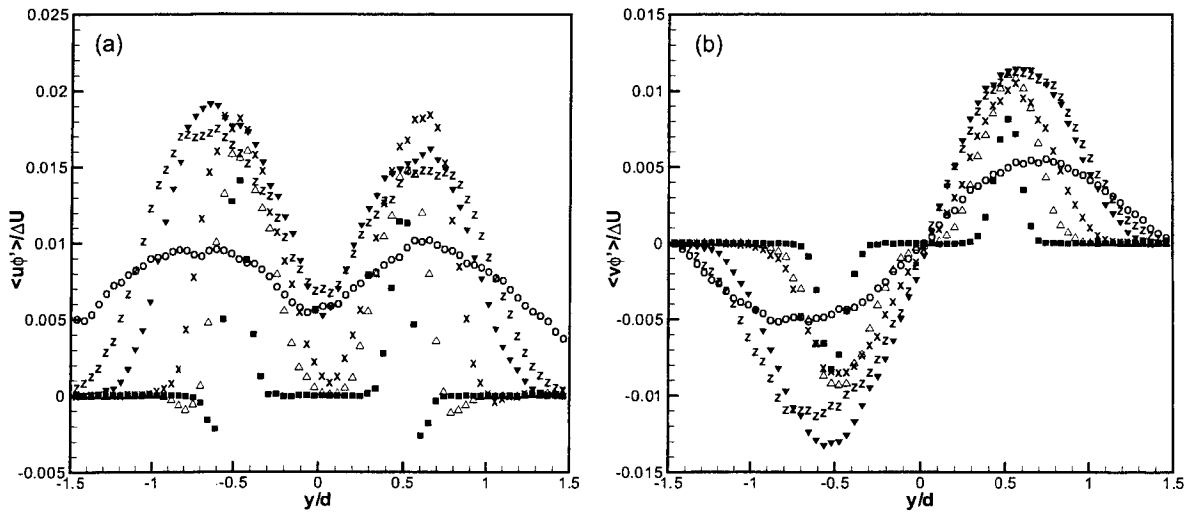


Figure 6.4 Turbulent fluxes at different streamwise locations. ■, $x/d = 1.0$; △, $x/d = 4.5$; ×, $x/d = 7.5$; ▼, $x/d = 12$; z, $x/d = 15$; ○, $x/d = 30$.

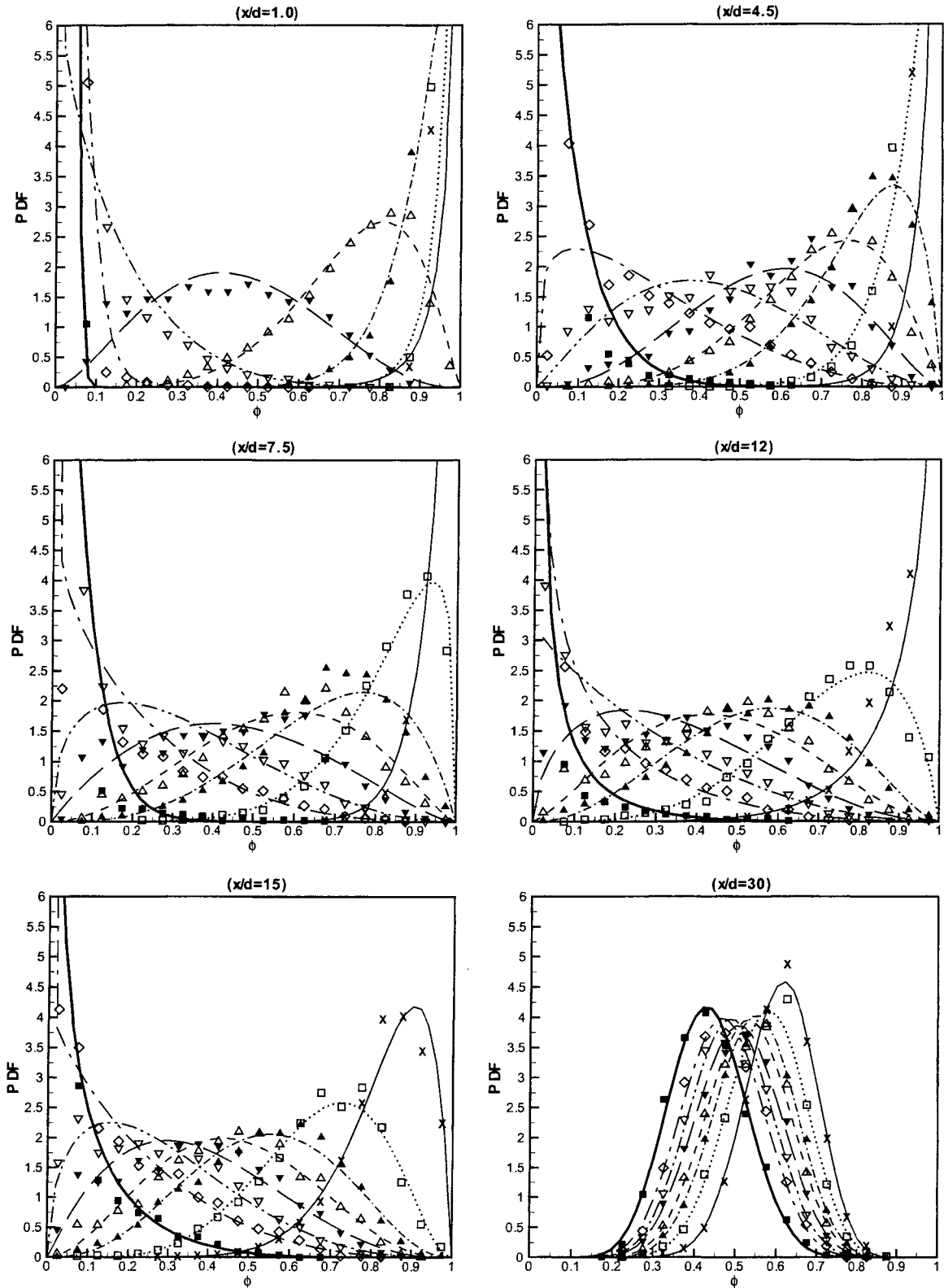


Figure 6.5 The comparison of the experimental probability densities (symbols) and beta-PDFs (lines) at various positions. $y = 0$, \times , thin line; $y = -\delta/2$, \square , dotted line; $y = -3\delta/4$, \blacktriangle , short-dash-dot line; $y = -7\delta/8$, \triangle , short-dash line; $y = -\delta$, \blacktriangledown , long-dash line; $y = -9\delta/8$, ∇ , dash-dot-dot line; $y = -5\delta/4$, \diamond , long-dash-dot line; $y = -\delta/4$, \blacksquare , bold solid line.

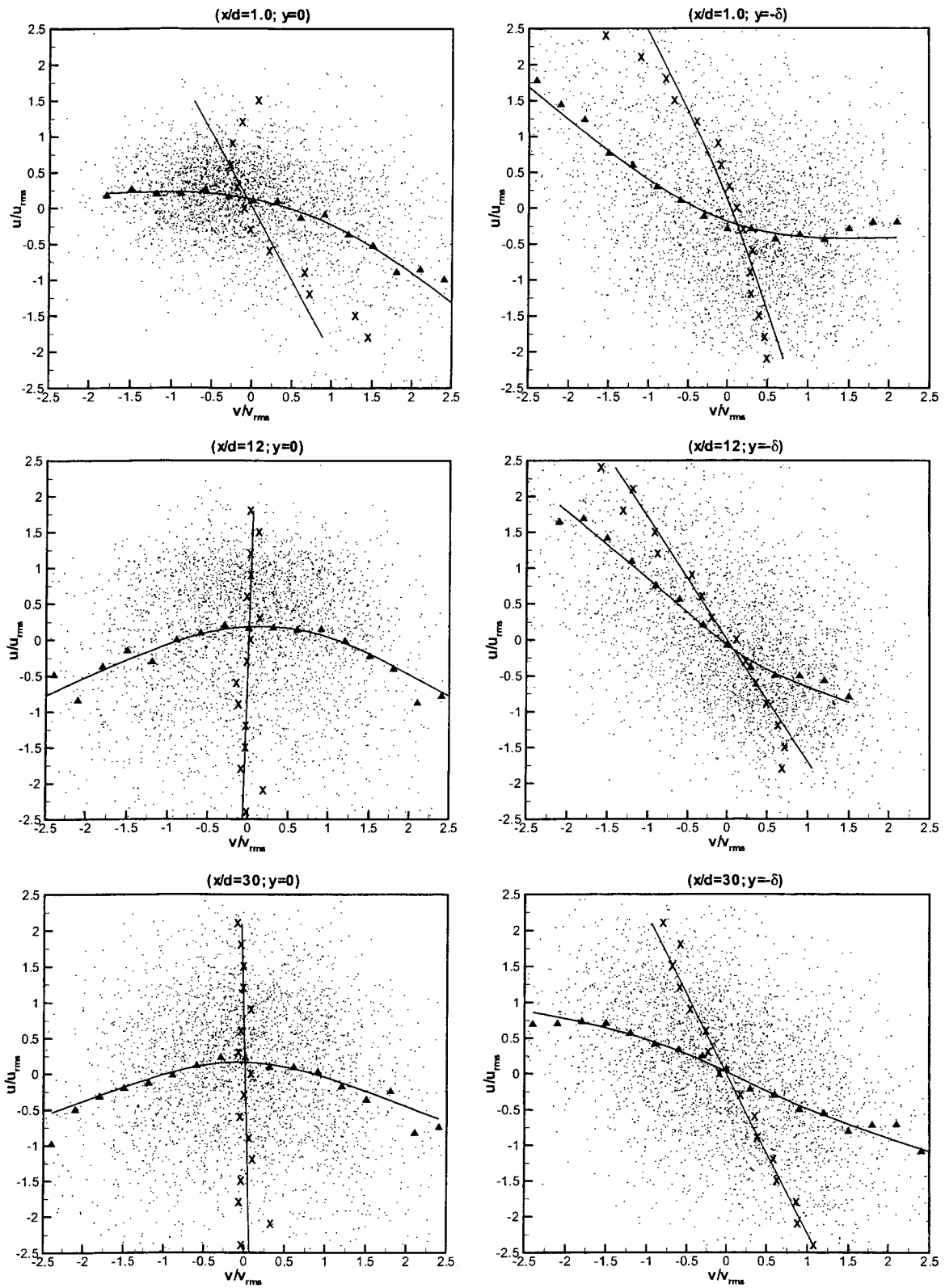


Figure 6.6 Scatter plots of velocity fluctuations for various downstream locations at $y = 0$ and $y = -\delta$. Line with triangle, $\langle u|v \rangle$; line with cross, $\langle v|u \rangle$. The lines represent the weighted smoothing splines to the data points.

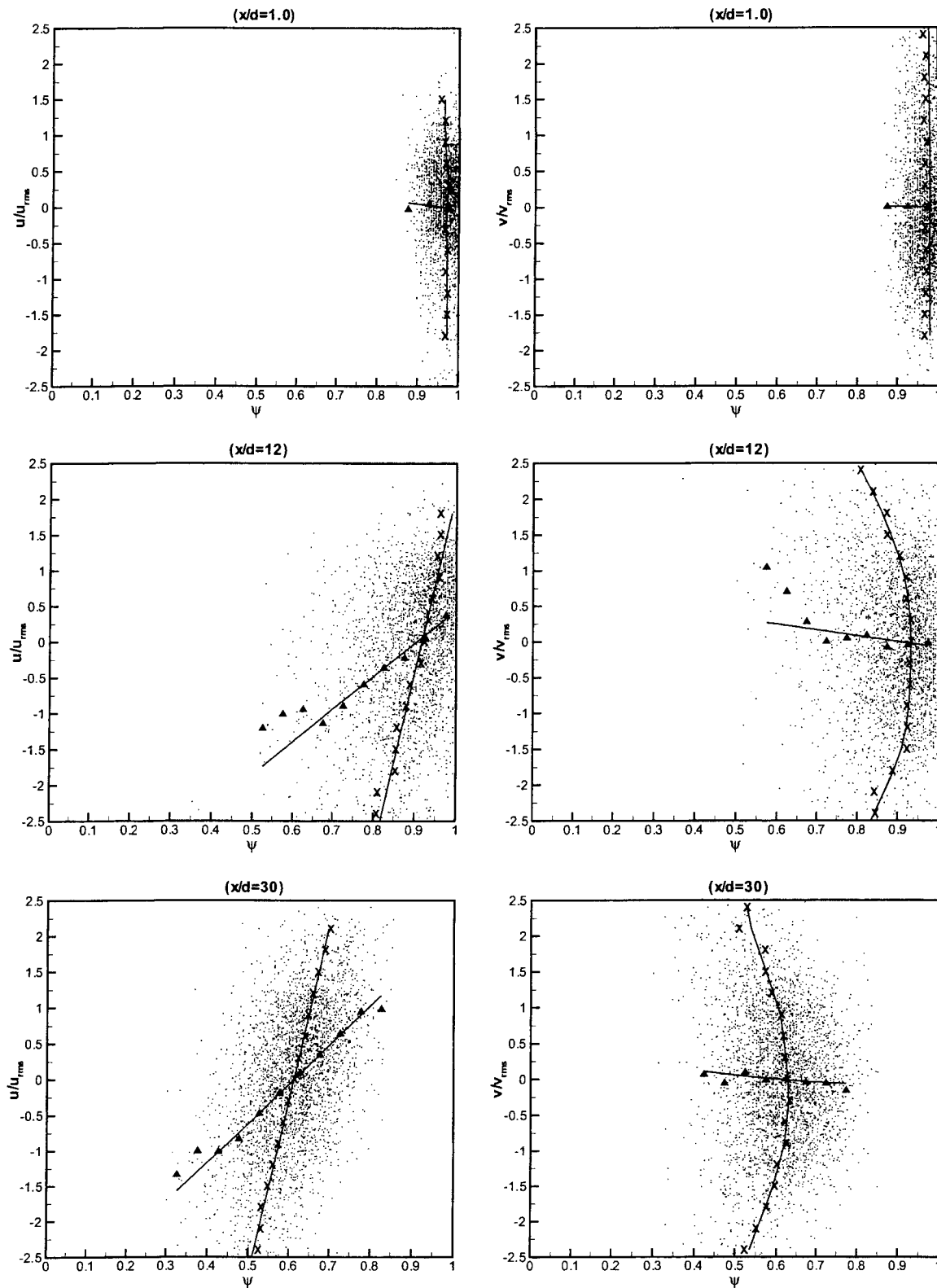


Figure 6.7 Scatter plots for various downstream locations at $y = 0$. Line with triangle, $\langle \mathbf{u} | \psi \rangle$; line with cross, $\langle \phi | \mathbf{u} \rangle$. The lines represent the weighted smoothing splines to the data points.

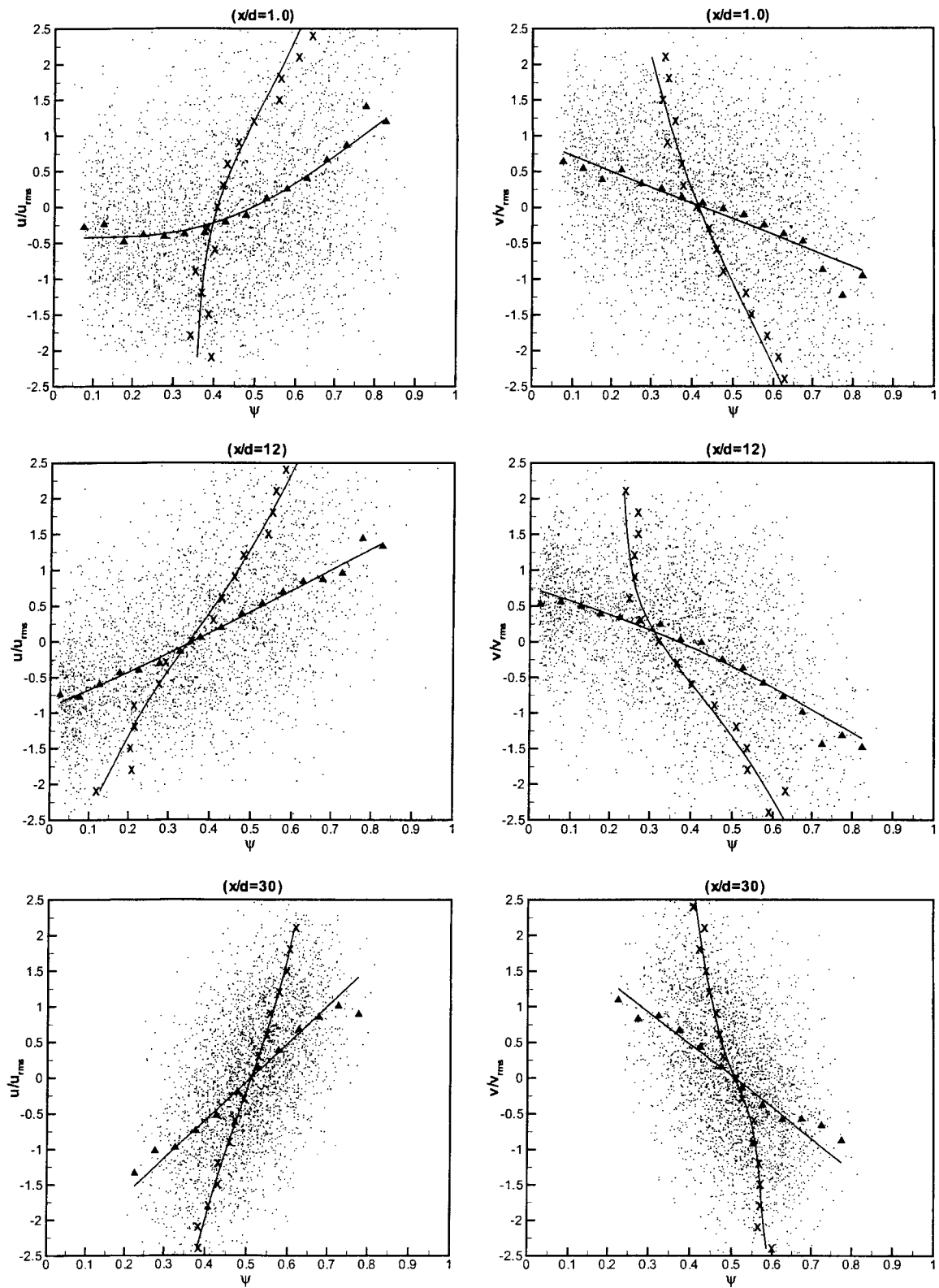


Figure 6.8 Scatter plots for various downstream locations at $y = -\delta$. Line with triangle, $\langle \mathbf{u} | \psi \rangle$; line with cross, $\langle \phi | \mathbf{u} \rangle$. The lines represent the weighted smoothing splines to the data points.

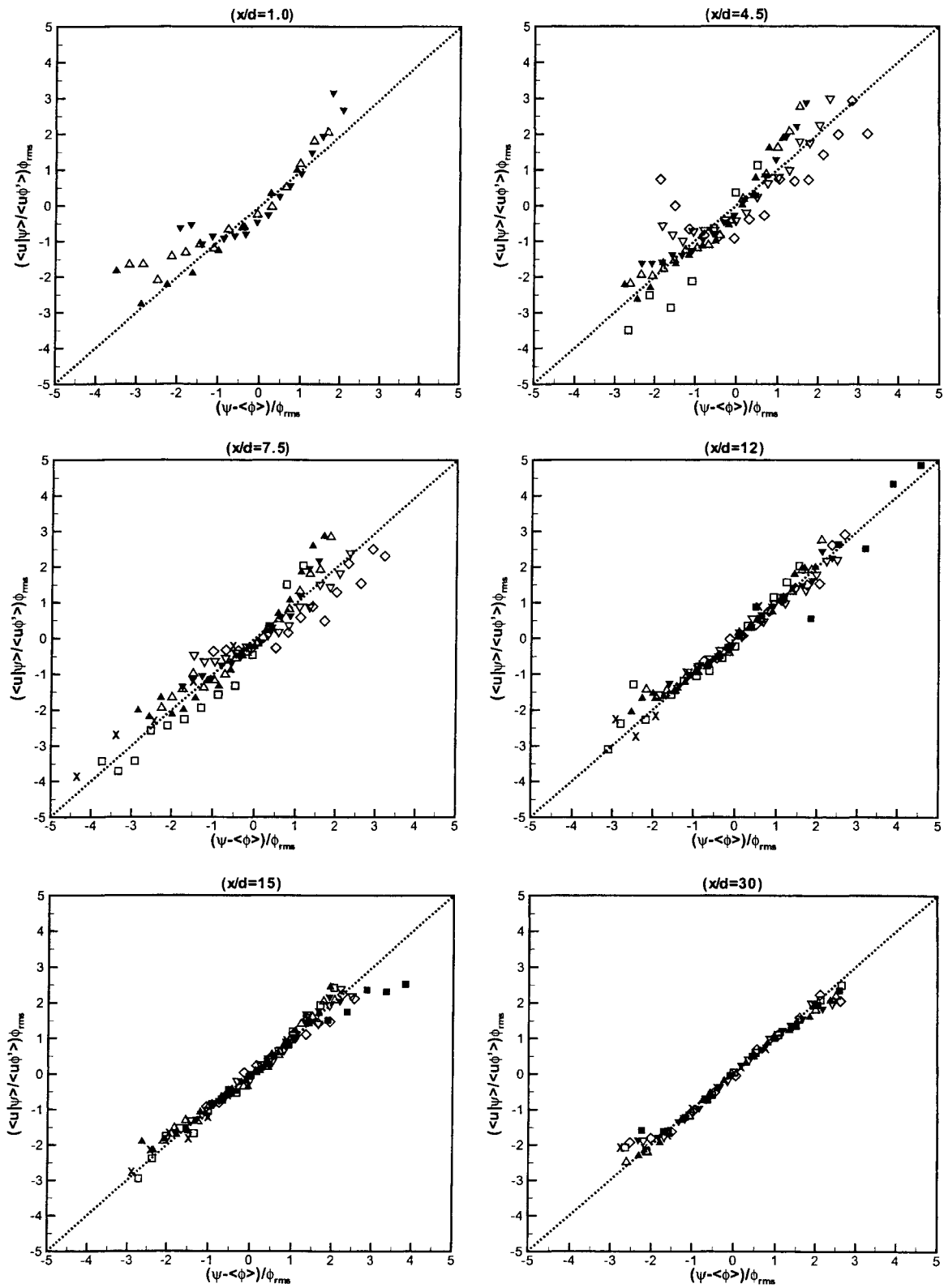


Figure 6.9 The conditional mean streamwise velocity from the experimental data at various positions normalized according to Eq.6.1. Symbols are the same as in Fig. 6.5.

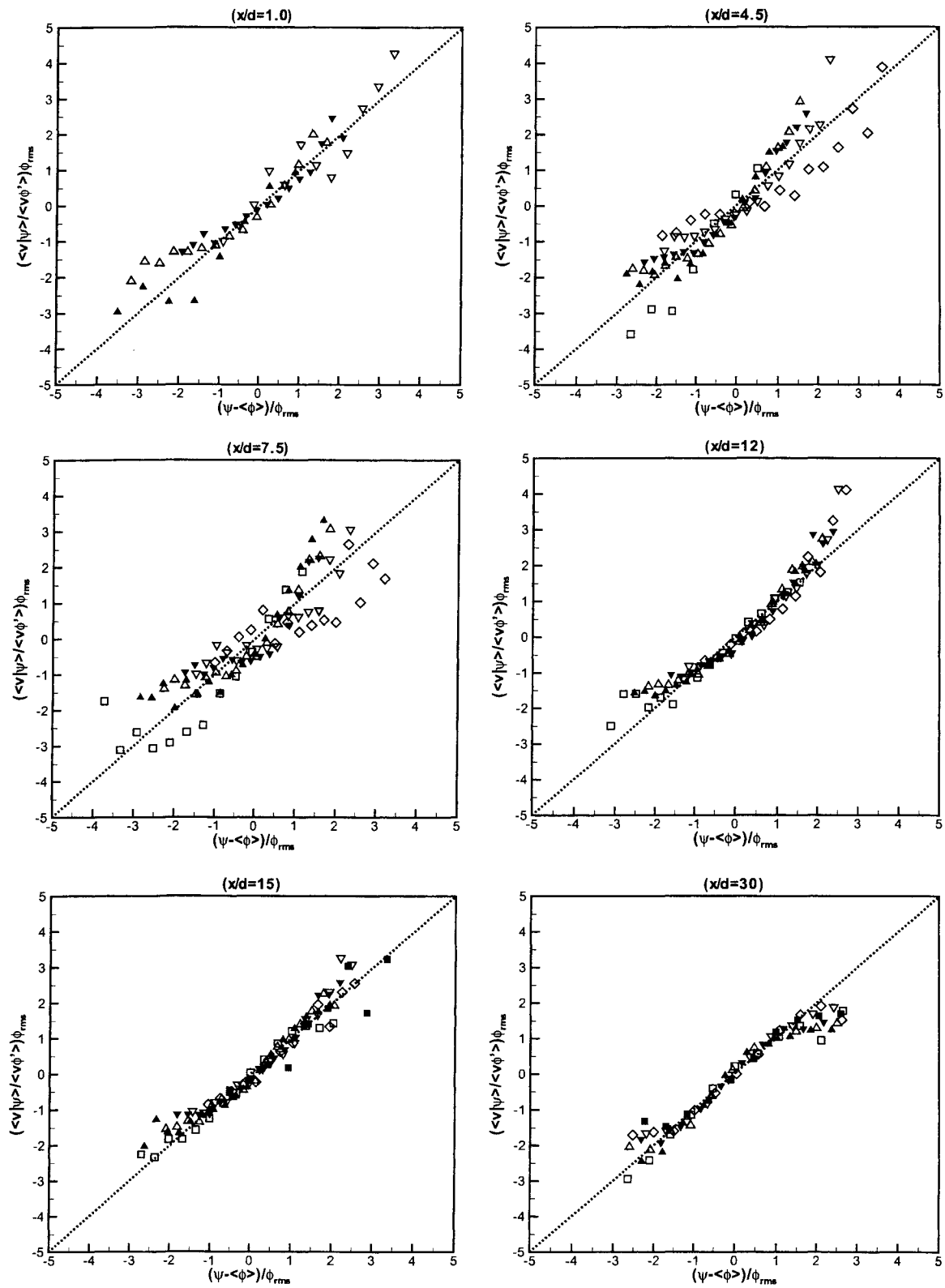


Figure 6.10 The conditional mean transverse velocity from the experimental data at various positions normalized according to Eq.6.1. Symbols are the same as in Fig. 6.5.

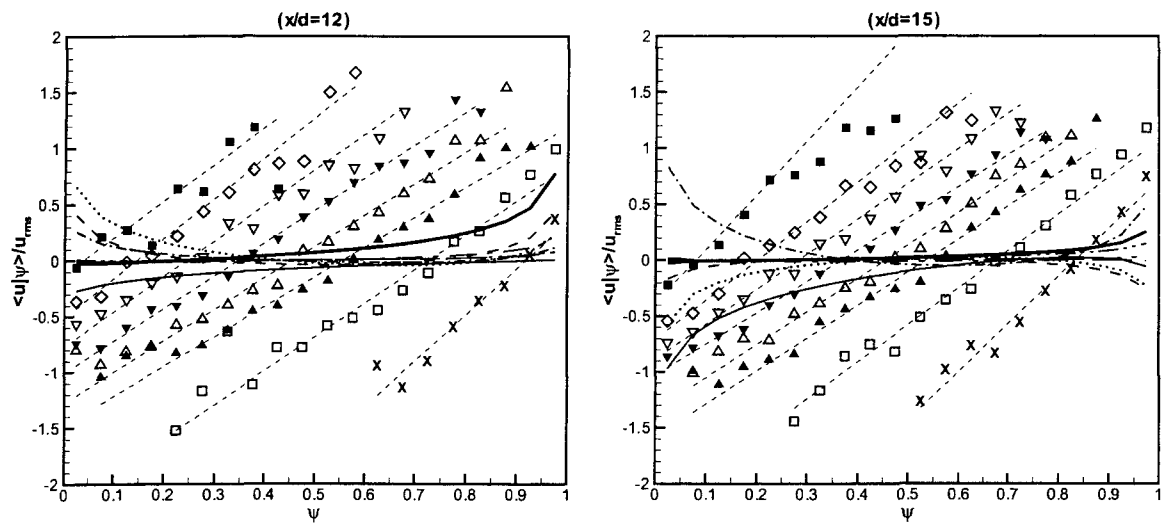


Figure 6.11 The comparison of conditional mean streamwise velocity from the experimental data (symbols) and from the gradient PDF model (lines). Symbols and lines are the same as in Fig. 6.5. The thin dashed line are the results of the linear model.

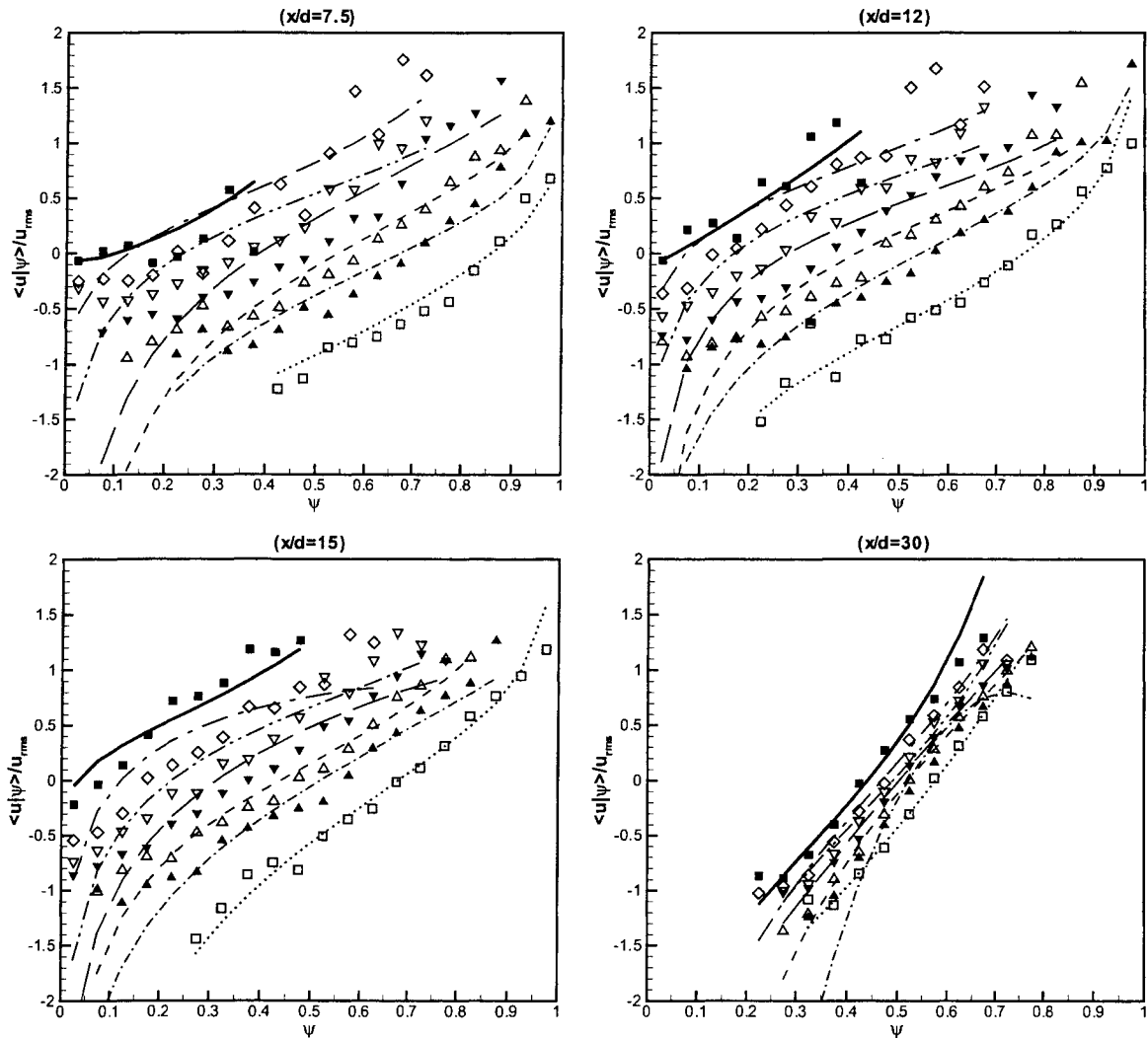


Figure 6.12 The comparison of conditional mean streamwise velocity from the experimental data (symbols) and from the improved gradient PDF model (lines). Symbols and lines are the same as in Fig. 6.5.

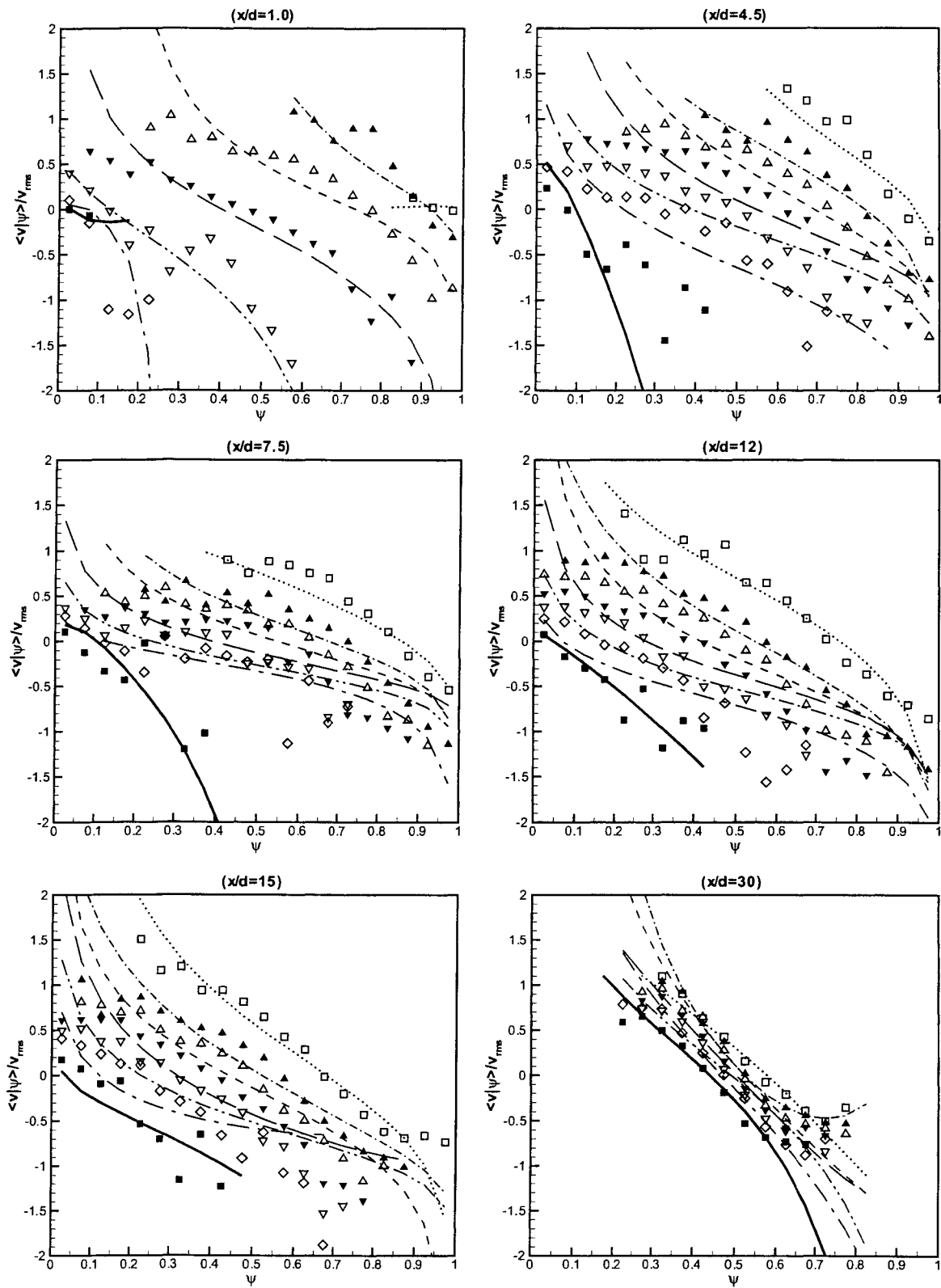


Figure 6.13 The comparison of conditional mean transverse velocity from the experimental data (symbols) and from the gradient PDF model (lines). Symbols and lines are the same as in Fig. 6.5.

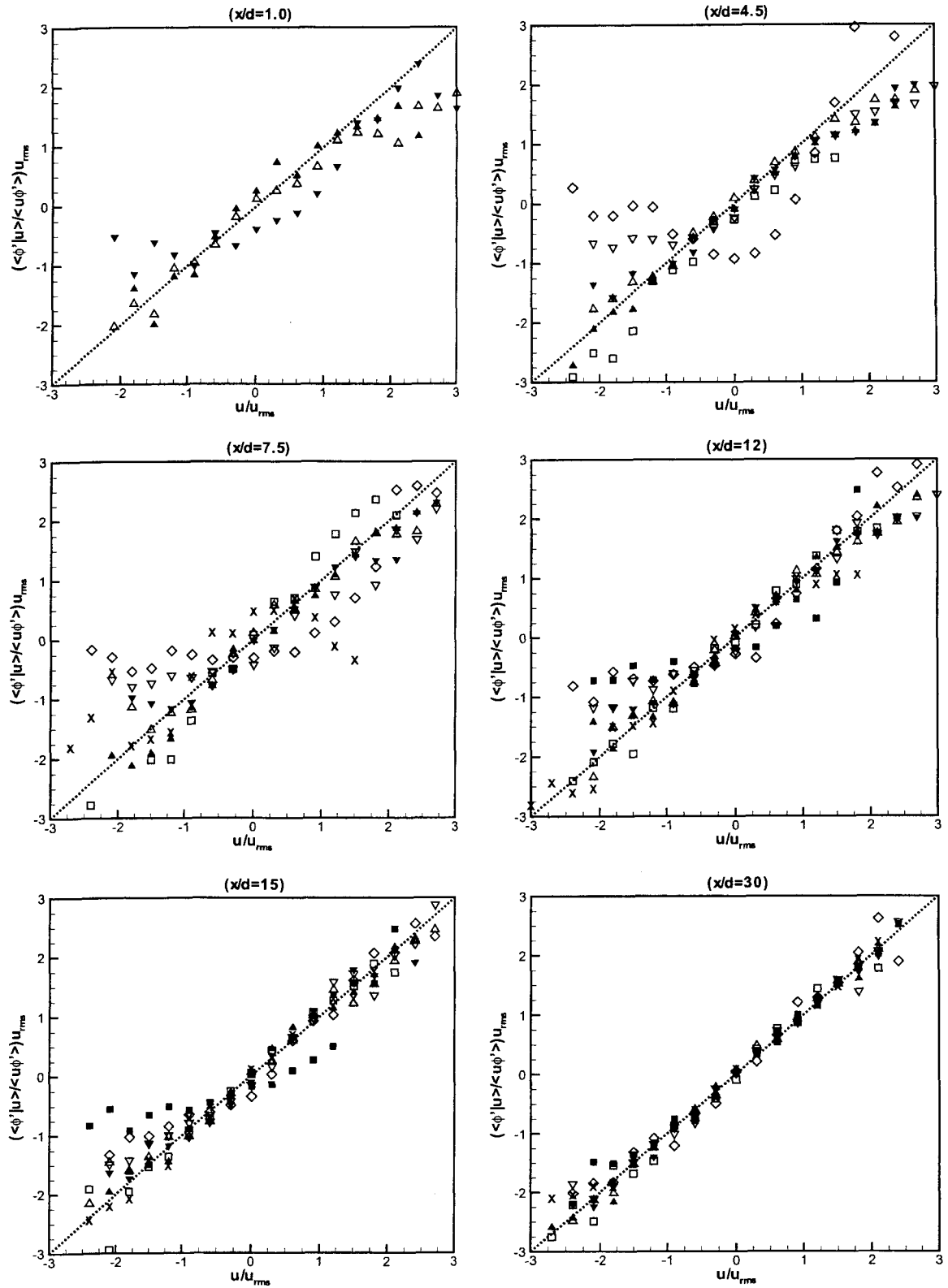


Figure 6.14 The mean scalar conditioned on the streamwise velocity at various positions normalized according to Eq.6.14. Symbols are the same as in Fig. 6.5.

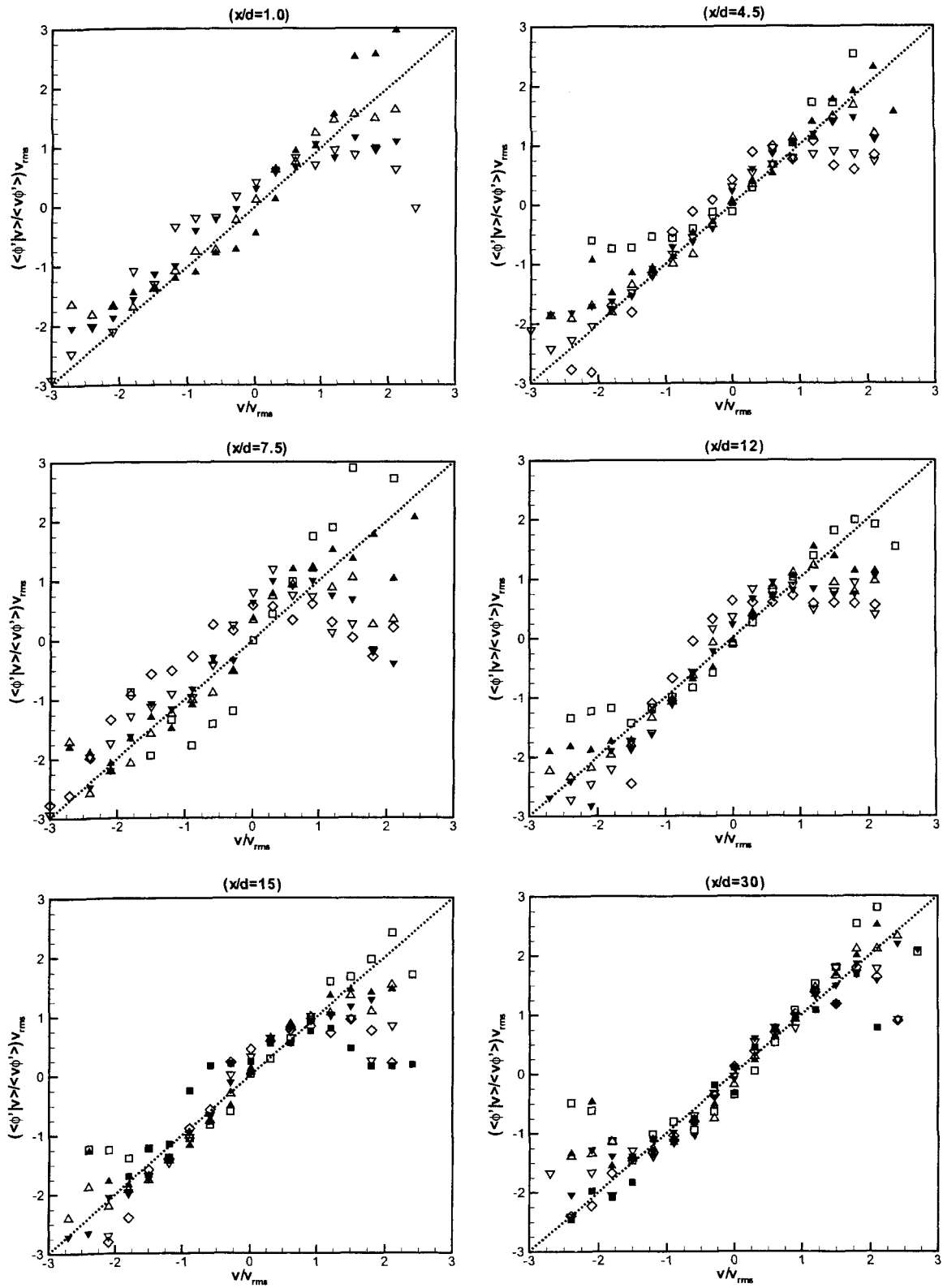


Figure 6.15 The mean scalar conditioned on the transverse velocity at various positions normalized according to Eq.6.14. Symbols are the same as in Fig. 6.5.

CHAPTER 7 CONCLUSIONS AND FUTURE DIRECTIONS

In this chapter, the important findings in this thesis work and the conclusions that can be drawn from the data are summarized. Future directions with the experimental investigation of the turbulent shear flows are also identified.

Summary and Conclusions

Confined Jet

In this thesis work, turbulent mixing in a confined rectangular jet was investigated using both non-simultaneous PIV and PLIF and simultaneous PIV and PLIF techniques. The Reynolds number of the jet was 50,000 based on the hydraulic diameter and the bulk velocity (or 10,000 based on the jet exit dimension and the velocity difference between streams). The Schmidt number of the fluorescence dye is 1,250. Instantaneous velocity and concentration fields were measured at seven representative downstream locations. It was found that the results of the simultaneous PIV and PLIF measurements were remarkably consistent with those obtained by the non-simultaneous PIV and PLIF system, indicating that the combined PIV and PLIF system developed in this study was capable of acquiring high quality results.

Flow statistics, such as mean velocity, Reynolds stresses, turbulent kinetic energy, concentration mean and variance, were calculated and compared with CFD results. The turbulent dissipation rate was also estimated by computing the Reynolds-averaged SGS dissipation rate. Limited by the 2-D nature of the PIV measurements, two methods were tested to approximate the missing terms using known ones. These statistics revealed that there were two mixing layers growing symmetrically about the centerline of the test section from the tips of the splitter plates. The potential core in the center stream disappeared very quickly (at

about $x/d = 4.5$) and the flow continued its development towards channel flow. However, at the farthest observed downstream location, $x/d = 30$, the fluid was not yet fully mixed. The transverse distribution of the turbulent dissipation rate was symmetric around the centerline of the jet but inhomogenous in the test section. As expected, the distribution of the dissipation rate suggested strong correlation with the turbulent kinetic energy. Furthermore, the constraint of the jet resulted in some different characteristics of the profiles of the above flow properties from those in a free jet, indicating that the sidewalls affect the evolution of the jet significantly.

Self-similarity of the jet flow was then examined. In the potential-core region of flow, the profile of the normalized streamwise mean velocity was very different from the profile of the self-similar velocity. However the self-similarity persists up to $x/d = 30$ in the center region of the jet. The spreading rate was around 0.1, in good agreement with that of the planar jet [Gutmark and Wygnanski (1976); Pope (2000)]. However, unlike in free rectangular jets, the Reynolds stresses did not reach self-similarity. Although at some downstream locations, the $\langle u'u' \rangle$ and $\langle u'v' \rangle$ stresses appeared to approach somewhat self-similar states with comparable maximum values found for free jets [Krothapalli et al. (1981)], the stresses never actually reached self-similar states due to the constraint imposed by the side walls. Moreover, the Reynolds stresses exhibited significant anisotropy, as revealed both by the shear stress and by the differences in the normal stresses.

The combined PIV and PLIF technique permitted the measurement of turbulent fluxes. The streamwise turbulent flux was found to be symmetric about the centerline, whereas the cross-stream turbulent flux was antisymmetric. Velocity-concentration correlation coefficients were also determined. In the potential core of each stream, the fluctuating velocity and concentration were uncorrelated. At the farthest observed location, the measured coefficients appeared to converge to a constant value of approximately 0.55. Based on the turbulent-viscosity hypothesis and the gradient-diffusion hypothesis, the turbulent viscosity and the turbulent diffusivity in the rectangular jet have been characterized. Consistent with the existing literature (Lemoine *et al.* 1999), both of these transport coefficients increased with downstream dis-

tance. The cross-sectional distributions show that these transport coefficients were larger in the shear-layer regions than in either the center region of the jet or in the boundary layers near the sidewalls. The results for turbulent Schmidt number were consistent with the existing body of experimental data, showing spatial variation in Sc_T and an average around 0.8.

Another important finding was that the orientation of the turbulent flux vector was nearly uniform around 30° with respect to the streamwise direction in this jet flow. Since the mean concentration gradient was in the transverse direction, the angle between the mean gradient and the turbulent flux was about 120-degrees. Therefore, the simple gradient transport model using a scalar turbulent diffusivity cannot represent the behavior of the turbulent flux in this flow, and the non-diagonal components should be nonzero, as proved by the results computed with the experimental data.

Spatial correlation fields of turbulent fluxes and concentration were also studied. The $R_{u'\phi'}$ correlation was elliptical in shape with a major axis tilted downward with respect to the streamwise axis, whereas the $R_{v'\phi'}$ correlation was a horizontally oriented ellipse. Negative regions of $R_{u'\phi'}$ were observed in the outer streams, and these negatively correlated regions decayed with downstream distance and finally disappeared altogether. The $R_{\phi'\phi'}$ correlation field was found to be an ellipse with the major axis inclined at about 45-degrees with respect to the streamwise direction.

Linear stochastic estimation was used to interpret spatial correlation data and to determine conditional flow structures. A vortex street near the splitter plate was responsible for the negatively correlated region observed in the $R_{u'\phi'}$ spatial correlations of turbulent fluxes (This was proved in the wake study). A positive concentration fluctuation event was observed to correspond to a finger of nearly uniform concentration fluid reaching out into the free stream, whereas a negative event corresponds to a pocket of nearly uniform fluid being entrained from the outer stream into the center jet region. Large-scale vortical structures were observed in the conditional velocity fields with an elliptical shape and a streamwise major axis. The growth of the structure size increased linearly initially but then grew more slowly as the flow transitioned towards channel flow.

Confined Wake

Similar non-simultaneous and simultaneous PIV and PLIF systems as described in the jet study were employed to investigate a confined rectangular wake flow with a Schmidt number of 1,250 and a Reynolds number of 37,500 based on bulk velocity and hydraulic diameter. Instantaneous velocity and concentration fields were measured at seven representative downstream locations. Flow statistics such as the mean velocity, Reynolds stresses, turbulent kinetic energy, concentration mean and variance were calculated from the PIV and PLIF data. The PDF of the concentration at some representative positions in the flow as well as the turbulent dissipation rate were estimated from the experimental data. The PDF of the concentration was found to be well approximated by beta-PDF. These statistics have been compared with CFD results.

It was observed that the two wakes formed by the two splitter plates grew quickly such that the potential core in the center stream disappeared at $x/d = 4.5$ where the two wakes met. The wakes had completely decayed by $x/d = 30$. The mean velocity profile in the wake was found to tend to reach an equilibrium state. However, unlike in a free wake, the distribution of the velocity defect at the edges of the wake was very different due to the interaction of the two wakes and the effect of boundary layers growing along the side walls.

The turbulent fluxes were measured with results obtained using the simultaneous PIV and PLIF system. The streamwise turbulent flux was found to be symmetric about the centerline of the test section, whereas the transverse turbulent flux was antisymmetric about the centerline with the same magnitude of the other turbulent flux. Unlike in the confined jet, the orientation of the turbulent flux vector varied in the flow and only remained uniform in some regions, where the angle was a constant of -140° . However, the mean concentration gradient was still in the cross-stream direction, as in the confined jet. Therefore, the turbulent flux vector was not aligned with the mean gradient so that the simple gradient transport model using a scalar diffusivity cannot completely describe the behavior of the turbulent flux in the wake flow as well. Two components of the turbulent diffusivity tensor were then evaluated, and as expected the non-diagonal component of the tensor was significantly non-zero. The diagonal component

was nearly constant in streamwise direction. The dimensionless turbulent viscosity was initially around 0.002 and increased in the streamwise direction. The results for the turbulent Schmidt number were consistent with the existing body of experimental data [Brethouwer (2005); Feng et al. (2006)], showing spatial variation and an average around 0.8.

Spatial correlations of the turbulent fluxes and concentration fluctuations were evaluated with the simultaneous velocity and concentration data. In the $R_{u'\phi'}$ correlation field, there were a positive and a negative vertically-oriented-elliptical correlation region, which were symmetric around the basis point. Similar results were found in regions near the splitter plates in the confined jet, although the negative correlation region disappeared in farther downstream locations in the jet. The $R_{v'\phi'}$ correlation region was a horizontally oriented ellipse with negative values of the correlation coefficient. The correlation field of $R_{\phi'\phi'}$ was also an ellipse with horizontal major axis.

The results of linear stochastic estimation revealed the presence of a vortex street in the estimated velocity fields. The rotation of the vortex was counterclockwise corresponding to a positive concentration fluctuation, and clockwise corresponding to a negative event. It was found that a positive concentration fluctuation event signified a finger of unmixed fluid reaching out from the center stream into the outer stream and vice versa. In both cases, the finger advected fluid from one stream into the other horizontally. The growth of the structure size increased linearly initially at a rate of 0.075 but then grew more slowly as the flow transitioned towards channel flow.

Conditional Statistics

Sawford (2004) noted that, to his knowledge only that of Li and Bilger (1994) included a partial set of the conditional statistics from experimental results for model testing. Therefore, the conditional statistics of the experimental data obtained in this thesis work are expected to be of great importance for developing and validating CFD models.

It was found that the PDF of the scalar (concentration) was accurately described by beta-PDF at each observed positions. Consequently the joint velocity-scalar PDF was not jointly

Gaussian, although the scalar PDF however became more Gaussian at further downstream locations. The conditional mean velocity was found to agree with a linear model when the scalar is close to the local mean value. However, another commonly used model for the conditional velocity, the gradient PDF model, gave poor predictions for the streamwise conditional velocity, as the streamwise gradient of PDF was very small in this flow. By replacing the scalar turbulent diffusivity by a tensor, the gradient PDF model was improved so that both the predicted streamwise and transverse conditional velocities agreed well with the experimental data. On the other hand, the scalar fluctuations conditioned on velocity were presented and analyzed against a linear model, showing that the linear model only obtained good approximations of the experimental data when the joint velocity-scalar PDF approached nearly jointly Gaussian.

Future Directions

It is well-known that the initial and boundary conditions are crucial in CFD studies. However, since both the Komolgorov scale and the Batchelor scale were small in regions near the inlet of the test section and near the side walls, the current measurement system could not resolve the smallest eddies in the flow. Therefore, it would be necessary to carry out more zoomed-in measurements for these regions if more accurate initial and boundary conditions are needed for CFD studies.

In this thesis work, limited by the 2-D nature of the PIV measurement, the out-of-plane velocity (w) and the gradient in spanwise (z -) cannot be measured. When evaluating the turbulent kinetic energy and the dissipation rate, the missing terms were assumed to be in the same magnitude of the corresponding y - terms. Although this assumption is valid for some planar jet and wake flows [Pope (2000)], in the confined rectangular jet and wake flows this assumption may cause significant errors, especially for further downstream locations where the flow is far from the 2-D state. Therefore, one long term goal of the laboratory should be the development of a stereo-PIV system capable of the measurements of three velocity and gradient components.

Another suggestion for future work is to carry out measurements of reacting shear flows in

this flow system using reactive PLIF technique. Such a future investigation would be a logical continuation of the work presented in this thesis.

BIBLIOGRAPHY

- Aanen, L., Telesca, A. and Westerweel, J. (1999). Measurement of turbulent mixing using PIV and LIF. *Machine Graphics and Vision*, 8, 529-543.
- Adrian, R. J. (1991). Particle-imaging techniques for experimental fluid mechanics. *Annual Review of Fluid Mechanics*, 23, 261-304.
- Adrian, R. J. (1994). Stochastic estimation of conditional structure: a review. *Applied Scientific Research*, 53, 291-303.
- Adrian, R. J., Jones, B. G., Chung, M. K., Hassan, Y., Nithianandan, C. K. and Tung, A. T.-C. (1989). Approximation of turbulent conditional averages by stochastic estimation. *Physics of Fluids A*, 1, 992-996.
- Adrian, R. J. and Yao, C. S. (1983). Pulsed laser technique application to liquid and gaseous flows and the scattering of seed material. *Applied Optics*, 24, 42-52.
- Agrawal, A. and Prasad, A. K. (2002). Organizational modes of large-scale vortices in an axisymmetric turbulent jet. *Flow, Turbulence and Combustion*, 68, 359-377.
- Aksevoll, K. and Moin, P. (1996). Large eddy simulation of turbulent confined coannular jets. *Journal of Fluids Mechanics*, 315, 387-400.
- Ali, S. F. and Ibrahim, E. A. (1996). Coincidence of turbulent-nonturbulent interface and hot-cold interface in a plane turbulent wake. *Mechanics Research Communications*, 23, 91-102.
- Anselmet, F., Djeridi, H. and Fulachier, L. (1994). Joint statistics of a passive scalar and its dissipation in a turbulent flow. *Journal of Fluid Mechanics*, 280, 173-197.

- Antonia, R. A., Browne, L. W. B., Rajagopalan, S. and Chambers, A. J. (1983). On the organized motion of the turbulent plane jet. *Journal of Fluids Mechanics*, 134, 49–66.
- Antonia, R. A., Satyaprakash, B. R. and Hussain, A. K. K. M. F. (1980). Measurements of dissipation rate and some other characteristics of turbulent plane and circular jets. *Physics of Fluids*, 23, 695–700.
- Baldyga J. (1994). A closure model for homogeneous chemical reactions. *Chemical Engineering Science*, 49, 1985–2003.
- Baldyga, J. A. and Bourne, J. R. (1999). *Turbulent mixing and chemical reactions*. New York: John Wiley & Sons.
- Baldyga, J. A. and Pohorecki R. (1995). Turbulent micromixing in chemical reactors: a review. *Chemical Engineering Journal*, 58(2), 183–195.
- Batchelor, G. K. (1949). Diffusion in a field of homogeneous turbulence. *Australian Journal of Science Research A*, 2, 437–450.
- Batchelor, G. K. (1953). *The theory of homogeneous turbulence*. Cambridge, UK: Cambridge University Press.
- Batchelor, G. K. (1959). Small-scale variation of convected quantities like temperature in turbulent fluid. Part 1. General discussion and the case of small conductivity. *Journal of Fluid Mechanics*, 5, 113–133.
- Beguier, C. I., Dekeyster, I., Launder, B. E. (1978). Ratio of scalar and velocity dissipation time scales in shear flow turbulence. *The Physics of Fluids*, 21, 307–310.
- Bilger, R. W. (1980). Turbulent reacting flows. In: Libby, P. A. and Williams, F. A. (Eds.), *Topics in Applied Physics Number 44*, New York: Springer.
- Bilger, R. W. (1993). Conditional moment closure for turbulent reacting flow. *Physics of Fluids A*, 5, 436–444.

- Bilger, R. W., Saetran, L. R. and Krishnamoorthy, L. V. (1991). Reaction in a scalar mixing layer. *Journal of Fluid Mechanics*, 233, 211–242.
- Brethouwer, G. (2005). The effect of rotation on rapidly sheared homogeneous turbulence and passive scalar transport. Linear theory and direct numerical simulation. *Journal of Fluid Mechanics*, 542, 305–342.
- Brown, G. L. and Roshko, A. (1974). On density effects and large structure in turbulent mixing region. *Journal of Fluid Mechanics*, 64, 2775–2814.
- Browne, L., Antonia, A. and Shah, D. 1987. Turbulent energy dissipation in a wake. *Journal of Fluid Mechanics* 179, 307–326.
- Cantwell, B. J. (1981). Organized motion in turbulent flow. *Annual Review of Fluid Mechanics*, 13, 457–515.
- Cantwell, B. and Coles, D. (1983). An experimental study of entrainment and transport in the turbulent near wake of a circular cylinder. *Journal of Fluid Mechanics*, 136, 321–374.
- Carter, C. D., Donbar, J. M. and Driscoll, J. F. (1998). Simultaneous CH planar laser-induced fluorescence and particle imaging velocimetry in turbulent nonpremixed flames. *Applied Physics B*, 66, 129–132.
- Chakrabarti, M., Kerr, R. M. and Hill, J. C. (1997). First order closure theories for a series-parallel reaction air in a simulated homogeneous turbulence. *AIChE Journal*, 43, 902–912.
- Chen, H. C. and Patel, V. C. (1988). Near-wall turbulence models for complex flows including separation. *AIAA Journal*, 26, 641–648.
- Christensen, K. T. (2004). The influence of peak-locking errors on turbulence statistics computed from PIV ensembles. *Experiments in Fluids*, 36, 484–497.
- Crimaldi, J. P. and Koseff, J. R. (2001). High-resolution measurements of the spatial and temporal scalar structure of a turbulent plume. *Experiments in Fluids*, 31(1), 90–102.

- Dahm, W. J. A. and Dimotakis, P. E. (1987). Measurements of entrainment and mixing in turbulent jets. *AIAA Journal*, 25, 1216–1223.
- de Bruyn Kops, S. M. and Mortensen, M. (2005). Conditional mixing statistics in a self-similar scalar mixing layer. *Physics of Fluids*, 17, 095107-1–11.
- Durbin, P. A. and Petterson Relif, B. A. (2001) *Statistical Theory and Modeling for Turbulent Flows*, West Sussex: John Wiley & Sons Ltd.
- Elavarasan, R. and Meng, H. (2000). Flow visualization study of role of coherent structures in a tab wake. *Fluid Dynamics Research*, 27, 183–197.
- Elsener, J. W. and Elsner, W. (1996). On the measurement of turbulence energy dissipation. *Measurement science & technology*. 7, 1334–1348.
- Eswaran, V. and Pope S. B. (1988). Direct numerical simulations of the turbulent mixing of a passive scalar. *Physics of Fluids*, 31, 506–520.
- Feng, H., Olsen, M. G., Hill, J. C. and Fox, R. O. (2006). Simultaneous velocity and concentration field measurements of passive-scalar mixing in a confined rectangular jet. Submitted to *Experiments in Fluids*.
- Feng, H., Olsen, M. G., Liu, Y., Fox, R. O. and Hill, J. C. (2005). Investigation of turbulent mixing in a confined planar-jet reactor. *AIChE Journal*, 51, 2649–2664.
- Fiedler, H. E. (1987). Coherent structures. In: Comte-Bellot, G., Mathieu, J. (Eds.), *Proceedings of the First European Turbulence Conference*, Lyon, France. Berlin: Springer-Verlag, 320–336.
- Fox, R. O. (1996) Computational methods for turbulent reacting flows in the chemical process industry. *Revue de l'Institut Francais du Pétrol*, 51, 215–243.
- Fox, R. O. (1998). On the relationship between Lagrangian micromixing models and computational fluid dynamics. *Chemical Engineering Progress*, 37, 521–535.

- Fox, R. O. (2003). *Computational Models for Turbulent Reacting Flows*. Cambridge: Cambridge University Press.
- Friberg, P. C. and Hjertager, B. H. (1999). Simulation of a 3-Dimensional Large-Scale Fermenter with Four Rushton Turbines. *2nd International symposium on two-phase flow modeling and experimentation*.
- Fukushima, C., Aanen, L. and Westerweel, J. (2000). Investigation of the mixing process in an axisymmetric turbulent jet using PIV and LIF. *proceedings of 10th International Symposium on Application of Laser Techniques to Fluid Mechanics*, Lisbon, Portugal.
- George, W. K. (1989). The self-preservation of turbulent flows and its relation to initial conditions and coherent structures. In: George, W. K. and Arndt R. (Eds.), *Advances in Turbulence*, New York: Hemisphere, 39–73.
- Ghosal, S. and Rogers, M. M. (1997). A numerical study of self-similarity in a turbulent plane wake using large-eddy simulation. *Physics of Fluids*, 9, 1729–1739.
- Gordeyev, S. V. and Thomas, F. O. (2000). Coherent structure in the turbulent planar jet. Part I. Extraction of proper orthogonal decomposition eigenmodes and their self-similarity. *Journal of Fluid Mechanics*, 414, 145–194.
- Grant, H. L. (1958). The large eddies of turbulent motions. *Journal of Fluid Mechanics*, 4, 149–190.
- Girimaji, S. S. (1991). Assumed β -pdf model for turbulent mixing: Validation and extension to multiple scalar mixing. *Combustion Science and Technology*, 78, 177–196.
- Guillard, F., Fritzon, R., Revstedt, J., Trägårdh, C., Aldén, M. and Fuchs, L. (1998). Mixing in a confined turbulent impinging jet using planar laser-induced fluorescence. *Experiments in Fluids*, 25, 143–150.
- Gutmark, E. and Wygnanski, I. (1976). The planar turbulent jet. *Journal of Fluid Mechanics*, 73, 465–495.

- Harvey, A. D. (2003). Generalized turbulent reacting flow code: 1. Equations and numerics. *Midland, MI: The Dow Chemical Company Hydrocarbons Research, LAD 2003-008.*
- He, G. and Hsu, A. (1999). The effect of Schmidt number on turbulent scalar mixing in a jet-in-crossflow. *International Journal of Heat and Mass Transfer*, 42, 3727–3738.
- Hughes, T. J. R., Mazzei, L., Oberai, A. A. and Wray A. A. (2001). The multiscale formulation of large eddy simulation: Decay of homogeneous isotropic turbulence. *Physics of Fluids*, 13, 505–512.
- Jayesh and Warhaft, Z. (1992). Probability distribution, conditional dissipation, and transport of passive temperature fluctuations in grid-generated turbulence. *Physics of Fluids A*, 4, 2292–2307.
- Jiménez J., Linan A., Rogers M. M. and Higuera F. J. (1997). A priori testing of subgrid models for chemically reacting non-premixed turbulent shear flows. *Journal of Fluid Mechanics*, 349, 149–171.
- Johnson, D. A. and King, L. S. (1985). A mathematically simple turbulence closure model for attached and separated turbulent boundary layers. *AIAA Journal*, 23, 1684–1692.
- Jones, W. P. and Launder, B. E. (1972). The prediction of laminarization with a two-equation model of turbulence. *International Journal of Heat and Mass Transfer*, 15, 301–314.
- Kailasnath, P., Sreenivasan, K. R. and Saylor, J. R. (1993). Conditional scalar dissipation rates in turbulent wakes, jets, and boundary layers. *Physics of Fluids A*, 5, 3207–3215.
- Kawaguchi, Y., Segawa, T., Feng, Z. and Li, P. (2002). Experimental study on drag-reducing channel flow with surfactant additives - Spatial structures of turbulence investigated by PIV system. *International Journal of Heat and Fluid Flow*, 23(4), 700–709.
- Keane, R. D and Adrian, R. J. 1992. Theory of cross-correlation analysis of PIV images. *Applied scientific research*, 49, 191–215.

- Kim, I. S. (2004). Conditional moment closure for non-premixed turbulent combustion. *Ph.D. dissertation*, University of Cambridge.
- Kiya, M. and Matsumura, M. (1985). Turbulence structure in the intermediate wake of a circular cylinder. *Bull. JSME*, 28, 2617–2624.
- Klimenko, A. Y. (1990). Multicomponent diffusion of various admixtures in turbulent flows. *Fluid Dynamics*. 25, 327–334.
- Krothapalli, A., Baganoff, D. and Karamcheti, K. (1981). On the mixing of a rectangular jet. *Journal of Fluid Mechanics*. 107, 201–220.
- Kolmogorov, A. N. (1941). The local structure of turbulence in incompressible viscous fluid for very large Reynolds numbers. *Dokl Akad Nauk SSSR*, 30, 299–303.
- Kompenhans, J., Raffel, M. and Willert, C. 1998. *Particle Image Velocimetry - A Practical Guide*. Berlin: Springer-Verlag.
- Kothnur, P. S. and Clemens, N. T. (2001). Experimental investigation of the relationship between strain and scalar dissipation in gas-phase turbulent jets. *AIAA paper*. No. 2001–1023.
- Langford, J.A. and Moser, R. D. (1999). Optimal LES formulations for isotropic turbulence. *Journal of Fluid Mechanics*. 521, 273–294.
- Launder, B. E. and Sharma, B. I. (1974). Application of the energy-dissipation model of turbulence to the calculation of flow near a spinning disc. *Letters in Heat and Mass Transfer*, 1, 131–138.
- Law, A. W. and Wang, H. 2000. Measurement of mixing processes with combined digital particle image velocimetry and planar laser induced fluorescence. *Experimental thermal and fluid science*, 22, 213–229.

- Lemoine, F., Antoine, Y, Wolff, M. and Lebouch, M. (1999). Simultaneous temperature and 2D velocity measurements in a turbulent heated jet using combined laser-induced fluorescence and LDA. *Experiments in Fluids*, 26, 315–323.
- Lesieur, M., Comte, P. and Métais, O. (1995). Numerical simulation of coherent vortices in turbulence. *Applied Mechanics Reviews*, 48, 121–147.
- Li, J. D. and Bilger, R. W. (1994). A simple theory of conditional mean velocity in turbulent scalar-mixing layer. *Physics of Fluids*, 6, 605–610.
- Liu, Y., Feng, H., Olsen, M. G., Fox, R. O. and Hill, J. C. (2006). Turbulent mixing in a confined rectangular wake. Submitted to *Chemical Engineering Science*.
- Liu, Y. and Fox, R. O. (2006) Predictions for chemical processing in a confined impinging-jets reactor. *AIChE Journal*, 52, 731–744.
- Liu, Y., Raman, V., Fox, R. O. and Harvey, A. D. (2004). Scale up of gas-phase chlorination reactors using CFD. *Chemical Engineering Science*, 59, 5167–5176.
- Lubbers, C. L., Brethouwer, G. and Boersma, B. J. (2001). Simulation of the mixing of a passive scalar in a round turbulent jet. *Fluid Dynamics Research*, 28, 189–208.
- Ma, X., Karamanos, G. S. and Karniadakis, G. E. (2000). Dynamics and low-dimensionality of a turbulent near wake. *Journal of Fluid Mechanics*, 410, 29–65.
- Ma, B. and Warhaft, Z. (1986). Some aspects of the thermal mixing layer in grid turbulence. *Physics of Fluids*, 29, 3114–3120.
- Mankbadi, R. R. (1992). Dynamics and control of coherent structure in turbulent jets. *Applied mechanics reviews*, 45, 219–247.
- Mehta, R. V. and Tarbell, J. M. (1987). An experimental study of the effect of turbulent mixing on the selectivity of competing reactions. *AIChE Journal*, 33(7), 1089–1101.

- Meyer, K. E., Özcan, O. and Larsen, P. S. (2000). Point and planar LIF for velocity-concentration correlation in a jet in cross flow. *proceedings of 10th International Symposium on Application of Laser Techniques to Fluid Mechanics*, Lisbon, Portugal
- Mi, J., Zhou, Y. and Nathan, G. J. (2004). The effect of Reynolds number on the passive scalar field in the turbulent wake of a circular cylinder. *Flow, Turbulence and Combustion*, 72, 311–331.
- Moin, P. and Mahesh, K. (1998) Direct numerical simulation: A tool for turbulence research. *Annual Reviews of Fluid Mechanics*, 30, 539–578.
- Mortensen, M. (2005). Consistent modeling of scalar mixing for presumed, multiple parameter probability density functions. *Physics of Fluids*, 17, 018106-1–4.
- Nakagawa, S., Nitta, K. and Senda, M. (1999). An experimental study on unsteady turbulent near wake of a rectangular cylinder in channel flow. *Experiments in Fluids*, 27, 284–294.
- Oakley, T. R., Loth, E. and Adrian, R. J. (1996). Cinematic particle image velocimetry of high-Reynolds-number free shear layer. *AIAA Journal*, 34, 299–308.
- O'Brien, E. E. and Jiang, T. L. (1992). The conditional dissipation rate of an initially binary scalar in homogeneous turbulence. *Physics of Fluids A*, 3, 3121–3123.
- Olsen, M. G. and Dutton, J. C. (2002). Stochastic estimation of large structures in an incompressible mixing layer. *AIAA Journal*, 40(12), 2431–2438.
- Olsen, M. G. and Dutton, J. C. (2003). Planar velocity measurements in a weakly compressible mixing layer. *Journal of Fluid Mechanics*, 486(12), 51–77.
- Ong, L. and Wallace, J. (1996). The velocity field of the turbulent very near wake of a circular cylinder. *Experiments in Fluids*, 20, 441–453.
- Overholt, M. R. and Pope, S. B. (1996). Direct numerical simulation of a passive scalar with imposed mean gradient in isotropic turbulence. *Physics of Fluids*, 8, 3128–3148.

- Panchapakesan, N. R. and Lumley, J. L. (1993). Turbulence measurements in axisymmetric jets of air and Helium. Part 2. Helium jet. *Journal of Fluid Mechanics*, 246, 225–247.
- Patel, V. C., Rodi, W. and Scheuerer, G. (1985). Turbulence models for near-wall and low Reynolds number flows: A review. *AIAA Journal*, 23, 1308–1319.
- Penzkofer, A. and Leupacher, W. (1987). Fluorescence behavior of highly concentrated Rhodamine 6G solutions. *Journal of luminescence*, 37, 61–72.
- Pipino, M. and Fox, R. O. (1994). Reactive mixing in a tubular jet reactor: A comparison of PDF simulations with experimental data. *Chemical Engineering Science*, 49(24), 5229–5341.
- Pope, S. B. (1976). The probability approach to the modeling of turbulent reacting flows. *Combustion and Flame*, 27, 299–312.
- Pope, S. B. (1985). PDF methods for turbulent reactive flows. *Progress in Energy and Combustion Science*, 11, 119–192.
- Pope, S. B. (1998). The vanishing effect of molecular diffusivity on turbulent dispersion: implications for turbulent mixing and the scalar flux. *Journal of Fluid Mechanics*, 359, 299–312.
- Pope, S. B. (2000). *Turbulent flows*. Cambridge, UK: Cambridge University Press.
- Prasad, A. K., Adrian, R. J., Landreth, C. C. and Offutt, P. W. (1992). Effect of resolution on the speed and accuracy of particle image velocimetry interrogation. *Experiments in Fluids*, 13, 105–116.
- Prasad, A. K. and Gonuguntla, P. V. (1996). Turbulence measurements in nonpenetrative thermal convection. *Physics of Fluids*, 8, 2460–2470.
- Raman, V., Fox, R. O., Harvey, A. D. and West, D. H. (2001). CFD analysis of premixed methane chlorination reactors with detailed chemistry. *Industrial & Engineering Chemistry Research*, 40, 5170–5176.

- Raman, V., Fox, R. O., Harvey, A. D. and West, D. H. (2003). Effect of feed-stream configuration on gas-phase chlorination reactor performance. *Industrial & Engineering Chemistry Research*, 42, 2544–2557.
- Raman, V., Fox, R. O. and Harvey, A. D. (2001). Hybrid finite-volume/transported PDF simulations of a partially premixed methane-air flame. *Combustion and Flame*, 136, 327–350.
- Ranade, V. V. (2002). *Computational Flow Modeling for Chemical Reactor Engineering*. San Diego: Academic Press.
- Ren, Z., Subramaniam, S. and Pope, S. B. (2002) Implementation of the EMST mixing model. <http://eccentric.mae.cornell.edu/~laniu/emst>.
- Richardson, L. F. (1920). The supply of energy from and to atmospheric eddies. *Proceedings of the Royal Society of London, Series A*, 97, 354–373.
- Rodi, W. and Mansour, N. N. (1993). Low Reynolds number $k - \epsilon$ modeling with the aid of direct simulation data. *Journal of Fluid Mechanics*, 250, 509–529.
- Rogallo, R. S. and Moin, P. (1984). Numerical simulation of turbulent flows. *Annual Reviews of Fluid Mechanics*, 16, 99–137.
- Rogers, M. M., Mansour, N. N. and Reynolds, W. C. (1989). An algebraic model for the turbulent flux of a passive scalar. *Journal of Fluid Mechanics*, 203, 77–101.
- Saarenrinne, P. and Piirto, M. (2000). Turbulent kinetic energy dissipation rate estimation from PIV velocity vector fields. *Experiments in Fluids, Suppl*, s300–s307.
- Sawford, B. L. (2004) Conditional scalar mixing statistics in homogeneous isotropic turbulence. *New Journal of Physics*, 6, 1–30.
- Sardi, K., Taylor, A. M. K. P. and Whitelaw, J. H. (1998). Conditional scalar dissipation statistics in a turbulent counterflow. *Journal of Fluid Mechanics*, 361, 1–24.

- Sharp, K. V., Kim, K. C. and Adrian, R. J. (1998) Dissipation estimation around a Rushton turbine using particle image velocimetry. *Proceedings of the 9th International Symposium on Application of Laser Techniques to Fluid Mechanics*.
- Sharp, K. V. and Adrian, R. J. (2001). PIV study of small-scale flow structure around a Rushton turbine. *AIChE Journal*, 47, 766–778.
- Sheng, J., Meng, H. and Fox, R. O. (2000). A large eddy PIV method for turbulence dissipation rate estimation. *Chemical Engineering Science*. 55, 4423–4434.
- Shih, T. H. and Mansour, N. N. (1990). Modeling of near-wall turbulence. *Engineering Turbulence Modeling and Experiments*, edited by Rodi, W. and Ganić, E. N. Amsterdam: Elsevier.
- Simones, S. and Ayrault, M. (1994). Concentration flux measurements of a scalar quantity in turbulent flows. *Experiments in Fluids*, 16, 273–281.
- Sinai, Y. G. and Yakhot, V. (1989). Limiting probability distribution of a passive scalar in a random velocity field. *Physical Review Letters*, 63, 1962–1964.
- Smagorinsky, J. 1963. General circulation experiments with the primitive equation. I. The basic experiment. *Monthly Weather Review*, 91, 99–164.
- Sohankar, A., Davidson, L. and Norberg, C. (1999). A dynamic one-equation sub-grid model for simulation of flow around a square cylinder. *Engineering Turbulence Modeling and Experiments-4*, , 227–236
- Soria, J. (1996). An investigation of the near wake of a circular cylinder using a video-based digital cross-correlation particle image velocimetry technique. *Experimental Thermal and Fluid Science*, 12, 221–233.
- Spalding, D. B. (1971). Concentration fluctuations in a round turbulent free jet. *Chemical Engineering Science*, 26, 95–107.

- Sreenivasan, K. R. and Antonia, R. A. (1978). Joint probability densities and quadrant contribution in a heated turbulent round jet. *AIAA Journal*, *16*, 867–868.
- Stanislas, M., Okamoto, K., Kähler, C. J. and Westerweel J. (2005). Main results of the Second International PIV Challenge. *Experiments in Fluids*, *39*, 170–191.
- Subramaniam, S. and Pope, S. B. (1998) A mixing model for turbulent reactive flows based on Euclidean minimum spanning trees. *Combustion and Flame*, *115*, 487–514.
- Subramaniam, S. and Pope, S. B. (1999) Comparison of mixing model performance for non-premixed turbulent reactive flow. *Combustion and Flame*, *117*, 732–754.
- Tavoularis, S. and Corrsin, S. (1981). Experiments in nearly homogenous turbulent shear flow with a uniform mean temperature gradient. Part 1. *Journal of Fluid Mechanics*, *104*, 311–347.
- Taylor, G. I. (1921). Diffusion by continuous movements. *Proceedings of the London Mathematical Society*, *20*, 196–212.
- Tennekes, H. and Lumley, J. L. (1972). *A first course in turbulence*. Cambridge, MA: MIT Press.
- Thomas, F. O. and Goldschmidt, V. W. (1986). Structural characteristics of a developing turbulent planar jet. *Journal of Fluid Mechanics*, *163*, 227–256.
- Tirtowidjo, M. (1997). Fundamental kinetic modeling of industrial reactors. *AIChE Annual Meeting, paper 78b*
- Townsend, A. A. (1956). *The Structure of Turbulent Shear Flow*. Cambridge, Cambridge University Press.
- Triantafyllou, G., Triantafyllou, M. and Chryssostomidis, C. (1986). On the formation of vortex streets behind stationary cylinders. *Journal of Fluid Mechanics*, *170*, 461–477.
- Tritton, D. J. (1988). *Physical Fluid Dynamics*, 2nd edition. Oxford, Oxford University Press.

- Tso, J. and Hussain, A. K. M. F. (1989). Organized motions in a fully developed turbulent axisymmetric jet. *Journal of Fluid Mechanics*, 203, 425–448.
- Tsuchiya, Y., Horikoshi, C. and Sato, T. (1986). On the spread of rectangular jets. *Experiments in Fluids*, 4, 197–204.
- Tsurikov, M. S. and Clemens, N. T. (2002). The structure of dissipative scales in axisymmetric turbulent gas-phase jets. *proceedings of 40th Aerospace Sciences Meeting, AIAA paper*, 2002-0164.
- Unal, M. and Rockwell, D. (1988). On vortex shedding from a cylinder. Part 1. The initial instability. *Journal of Fluid Mechanics*, 190, 491–512.
- Vernet, A., Kopp, G. A., Ferré, J. A. and Giralt, F. (1997). Simultaneous velocity and temperature patterns in a homogeneous plane of a cylinder-generated turbulent far wake. *Transactions ASME: Journal of Fluids Engineering*, 119, 493–496.
- Villiermaux, J. and Devillon, J. C. (1972). Representation de la coalescence et de la redispersion des domaines de segregation dans un fluide par un modèle d'Interaction Phénoménologique. *Proceedings of the 2nd International Symposium on Chemical Reaction Engineering*, 1–13. New York, NY: Elsevier.
- Vreman, B., Geurts, B. and Kuerten, H. (1997). Large-eddy simulation of the turbulent mixing layer. *Journal of Fluid Mechanics*, 339(), 357–390.
- Wang, L. and Fox, R. O. (2004). Comparison of micromixing models for CFD simulation of nanoparticle formation. *AIChE J.* 2004, 50, 2217–2232.
- Westerweel, J. 1993. *Digital particle image velocimetry: theory and application*. Delft, The Netherlands: Delft University Press.
- Wilcox, D. C. (1998). *Turbulence Modeling for CFD*. 2nd Edition. La Cañada, CA: DCW Industries Inc.

- Wynanski, I., Champagne, F. and Marasli, B. (1986). On the large-scale structures in two-dimensional, small-deficit, turbulent wakes. *Journal of Fluid Mechanics*, *168*, 31–71.
- Yeung, P. K., Xu, S. and Sreenivasan, K. R. (2002). Schmidt number effects on turbulent transport with uniform mean scalar gradient. *Physics of Fluids*, *14*, 4178–4191.
- Zhou, Y. and Antonia, R. A. (1995). Memory effects in a turbulent plane wake. *Experiments in Fluids*, *19*, 112–120.

ACKNOWLEDGEMENTS

My sincere thanks go to the National Science Foundation and the Dow Chemical Company for their generous financial support that made it possible to complete this dissertation. To Dr. Michael G. Olsen, for his help in providing excellent research direction and training, constructive criticism and motivation throughout my graduate work at Iowa State University. To Dr. Rodney O. Fox and Dr. James C. Hill, your insights and words of encouragement have often inspired me and renewed my hopes for completing my graduate education. To Dr. Francine Battaglia and Dr. Richard H. Pletcher, I appreciated your commitment in evaluating and providing positive critique of my research work.

To fellow graduate students in the Mechanical Engineering Department and the Chemical and Biological Engineering Department, thank you all for your unconditional support. To my parents, my wife and friends, thank you for your love and support.